



HAL
open science

Modeling of the manufacturing process of lithium-ion batteries : the link between electrolyte impregnation and electrochemical performance

Abbos Shodiev

► **To cite this version:**

Abbos Shodiev. Modeling of the manufacturing process of lithium-ion batteries : the link between electrolyte impregnation and electrochemical performance. Chemical engineering. Université de Picardie Jules Verne, 2021. English. NNT : 2021AMIE0064 . tel-03941301

HAL Id: tel-03941301

<https://theses.hal.science/tel-03941301v1>

Submitted on 16 Jan 2023

HAL is a multi-disciplinary open access archive for the deposit and dissemination of scientific research documents, whether they are published or not. The documents may come from teaching and research institutions in France or abroad, or from public or private research centers.

L'archive ouverte pluridisciplinaire **HAL**, est destinée au dépôt et à la diffusion de documents scientifiques de niveau recherche, publiés ou non, émanant des établissements d'enseignement et de recherche français ou étrangers, des laboratoires publics ou privés.



Thèse de Doctorat

Mention : Chimie
Spécialité Chimie de Solides et Sciences des Matériaux

présentée à l'Ecole Doctorale en Sciences Technologie et Santé (ED 585)

de l'Université de Picardie Jules Verne

par

Abbos SHODIEV

pour obtenir le grade de Docteur de l'Université de Picardie Jules Verne

*Modeling of the manufacturing process of lithium-ion batteries:
the link between electrolyte impregnation and
electrochemical performance*

Soutenue le 14/10/2021, après avis des rapporteurs, devant le jury d'examen :

| | | |
|-------------------------------|--|---------------------------|
| M. P. Johansson, | Professeur, Chalmers University of Technology | Rapporteur |
| M. Y. Bultel, | Professeur, Grenoble INP | Rapporteur |
| M^{me} Y. Yin, | Scientist, Saft Groupe S.A. | Examineur |
| M. B. Lestriez, | Professeur, IMN Nantes | Examineur |
| M. M. Gaberscek, | Professeur, National Institute of Chemistry | Examineur |
| M. V. Seznec, | Maître de Conférences, UPJV, Amiens | Examineur |
| M. J. Li, | Senior Scientist, ORNL | Examineur |
| M. A.A. Franco, | Professeur, UPJV, Amiens | Directeur de thèse |



Acknowledgments

This work was supported by the European Union's Horizon 2020 research and innovation programme for the funding support through the European Research Council (grant agreement 772873, "ARTISTIC" project).

First, I want to thank the members of the jury of my PhD defence for having found the time to read my thesis.

Foremost I would like to express the sincerest gratitude to my supervisor, Prof Alejandro Franco, who has supported me throughout my thesis with his patience and knowledge at the same time allowing me the room to work in my own way. I also would like to thank him for having the confidence for giving me the opportunity to be involved in different collaborations.

I am also indebted to fellow colleagues Anne Charbonnier, Nathalie Saulnier and Daphne Boursier for the working atmosphere and invaluable the support I had in the last three years. Either administration duties, work travels or adaptation in the lab and France, you have made as easy as possible. Merci aussi pour votre aide à améliorer mon français et ma compréhension de la culture française.

My sincere thanks go to J. Li, M. Gaberscek, M. Morcrette, Ch. Delacourt, C. Davoisne, and Dominique Larcher for insightful comments and valuable discussion on my research activities during my thesis.

I would also like to thank each and every member of the ARTISTIC project who have together made this group what it is. We have a friendly, supportive and most important caring team.

Also, I want to thank all the Ph.D students of the LRCS lab. I had a great time with you guys.

My family have always supported my dreams and aspirations, and I'd like to thank them for all they have done for me. Love all of you.

Preface

The thesis is based on the following articles.

I. 4D-resolved model for Electrochemical Impedance Spectroscopy of $\text{Li}(\text{Ni}_{1-x-y}\text{Mn}_x\text{Co}_y)\text{O}_2$ -based cathodes in symmetric cells: Consequences in tortuosity calculations, Abbas Shodiev, Emiliano N Primo, Mehdi Chouchane, Teo Lombardo, Alain C Ngandjong, Alexis Rucci, Alejandro A Franco *J, Power Sources, (2020)*

II. Investigating electrode calendaring and its impact on electrochemical performances by means of a new discrete element method model: Towards a digital twin of Li-Ion battery. Alain C Ngandjong, Teo Lombardo, Emiliano N Primo, Mehdi Chouchane, Abbas Shodiev, Oier Arcelus, Alejandro A Franco *J, Power Sources, (2020)*

III. Insight on electrolyte Infiltration of Lithium-Ion Battery electrodes by Means of a New Three-Dimensional-resolved Lattice Boltzmann Model, Abbas Shodiev, Emiliano Primo, Oier Arcelus, Mehdi Chouchane, Markus Osenberg, André Hilger, Ingo Manke, Jianlin Li, Alejandro A Franco, *Energy Storage Materials, (2021)*

IV. Machine Learning 3D-resolved prediction of electrolyte infiltration in battery porous electrode, Abbas Shodiev, Marc Duquesnoy, Oier Arcelus, Mehdi Chouchane, Jianlin Li and Alejandro A. Franco, *J, Power Sources, (2021)*

V. Deconvoluting benefits of porosity distribution in layered electrodes in layered electrodes on electrochemical performance of Li-ion batteries, Abbas Shodiev, Mehdi Chouchane, Miran Gaberscek, Oier Arcelus, Jiahui Xu, Hassan Oularbi, Jia Yu, Jianlin Li, Mathieu Morcrette and Alejandro A. Franco, *Energy Storage Materials (2022)*

Reprints were made with permission from the respective publishers.

Table of contents

| | |
|--|----|
| CHAPTER I: Introduction..... | 11 |
| 1.1. Energy and environment contexts | 13 |
| 1.2. Batteries for energy storage..... | 14 |
| 1.2.1 Primary batteries..... | 15 |
| 1.2.2 Secondary batteries | 16 |
| 1.3. Lithium ion batteries..... | 18 |
| 1.3.1 Working principle and key parameters..... | 18 |
| 1.3.2 Components | 21 |
| 1.4. Lithium ion battery manufacturing..... | 29 |
| 1.4.1. Electrode manufacturing..... | 29 |
| 1.4.2 Cell assembly..... | 30 |
| 1.4.3 Cell finishing | 31 |
| 1.5. Digital twins of battery fabrication process..... | 33 |
| 1.5.1 ERC-Artistic: the fusion of models, data and AI to create digital twin..... | 34 |
| 1.5.2 Scope of the thesis | 36 |
| CHAPTER II: 4D-resolved Physical Model for Electrochemical Impedance Spectroscopy in Symmetric Cells: Consequences in Tortuosity Calculations..... | 37 |
| 2.1. Introduction | 39 |

| | |
|---|--------|
| 2.2. Theory | 41 |
| 2.2.1 Electrode structures generation | 41 |
| 2.2.2 Electrochemical model | 42 |
| 2.2.3 Simulation procedure | 43 |
| 2.3. Experimental methodology | 48 |
| 2.4. Results and discussions | 49 |
| 2.4.1. Parameters influencing on the EI spectrum shape | 49 |
| 2.4.2 Carbon binder domain..... | 53 |
| 2.4.3 Ionic conductivity | 58 |
| 2.4.4 Effect of calendaring | 61 |
| 2.4.6 Effect of AM amount and tortuosity factor calculations..... | 63 |
| 2.5. Conclusion | 68 |
| CHAPTER III: Optimized electrode power density without reducing the energy density with layered electrode architecture | 73 |
| 3.1. Introduction..... | 75 |
| 3.2. Methodology | 76 |
| 3.2.2 Pore size distribution and Pore network | 76 |
| 3.2.3 EIS and Discharge models and Simulation procedure | 77 |
| 3.3. Experimental methodology | 77 |
| 3.4. Results and Discussions | 79 |

| | |
|--|------------|
| 3.4.1 Isolating ionic resistance from electronic resistance contributions in EIS | 79 |
| 3.4.2 Understanding electrode porosity effects on ionic resistance by EIS | 82 |
| 3.4.3 Designing heterogeneous electrode architectures with improved performance | 86 |
| 3.5. Conclusion | 95 |
| CHAPTER IV: Insight on electrolyte infiltration by means of a new three dimensional resolved Lattice Boltzmann model..... | 99 |
| 4.1. Introduction | 101 |
| 4.2. Experimental methodology..... | 103 |
| 4.3. Workflow and model description | 103 |
| 4.3.1 Workflow..... | 103 |
| 4.3.2 Model description | 106 |
| 4.4. Results and discussions | 111 |
| 4.4.1. Stochastically generated electrodes | 111 |
| 4.4.2 Calendering effect | 113 |
| 4.4.3 Electrolyte infiltration direction in full cells | 121 |
| 4.4.3 In silico electrochemical performance evaluations | 1223 |
| 4.5. Conclusion..... | 126 |
| CHAPTER V: Machine learning 3D resolved of electrolyte infiltration in LIB..... | 131 |
| 5.1. Introduction | 133 |
| 5.2. Computational procedure | 135 |

| | |
|---|-----|
| 5.3. Results and discussions | 139 |
| 5.3.1 Machine learning predictions..... | 139 |
| 5.3.2 Comparison of LBM simulations and predicted based on ML..... | 141 |
| 5.3.3 Parameters influencing the saturation and their physical interpretation | 143 |
| 5.4. Conclusions..... | 147 |
| CHAPTER VI: General conclusions and outlooks..... | 149 |
| Abbreviations | 153 |
| Bibliography..... | 155 |
| Résumé développé de la thèse en Français (Summary in French) | 173 |

CHAPTER – I

General Introduction

1.1. Energy and environmental contexts

The ability to create and use tools is one of the significant parameters that set our species apart from most other animals. While this allows us to extend our abilities, it also requires a proportional energy supply. Therefore, energy was and still is one of the main interests of humankind, and our survival as species depends on it. During most of history, traditional biomass was the main source of energy, as it was sufficient for powering all our technological demands. The 1st industrial revolution introduced the use of fossil fuels for energy supplies (**Figure 1**), but fossil fuels have drawbacks such as limited reserves, air pollution, greenhouse gas emissions, unsustainable extraction processes and unethical practices causing geopolitical tension. Accordingly, fossil fuel dependency is an untenable and suboptimal destination for the future; it is critical to shift to renewable energy sources if sustainability is our goal.

Possible alternative sources of energy are nuclear, hydropower, solar photovoltaic and wind power. One of the most used low-carbon energy sources is hydropower. While it can store 210 times more energy than was needed to build it, its application is limited due to its strict geological constraints. Currently, solar and wind are the fastest-growing domains of renewable energy sources, and some developed countries are already accounting for more than 25% of total electricity production at the same price per kWh hour as electricity produced using fossil fuels. Photovoltaic panels are used to convert sunlight into electricity and wind turbines generate it from airflow.[1] Nevertheless, both technologies lack constant electricity output as the sun does not shine 24 hours per day and air does not always blow. Integrated energy storage devices are required to overcome these variabilities and fluctuations. Among the different types of energy storage, batteries are prevalent where volume and weight are critical parameters, for example, phones, laptops, cameras and almost all electronic devices.

Batteries also have applications in the transportation sector, where fossil fuels are still dominant. It is essential to note that the share of electric vehicles (EV) in the market has been aggressively increasing in the last few years and, hopefully, will continue to increase to reach 100%.[2] Many parameters must be fulfilled to achieve this state and one of them is its cost: it must be comparable to the one of internal combustion cars to making EVs attractive and affordable for consumers. The cost of an EV has the highest positive correlation with the price of the battery inside it, which could roughly be estimated as the sum of its material performance, production volume, production

efficiency and second life. Material performance can be improved by finding new chemistries, volume production is optimized by manufacturing in big scales, such as in the Tesla Company Giga factory, and production efficiency could be enhanced by experimentation in controlling the different process parameters. All three are time consuming and expensive processes, which could be aided, and in some cases replaced, by creating a digital twin of the fabrication process based on experimental measurements. To this end, understanding the physical processes behind manufacturing in the aim of creating its digital twin will be a precious commodity for the society.

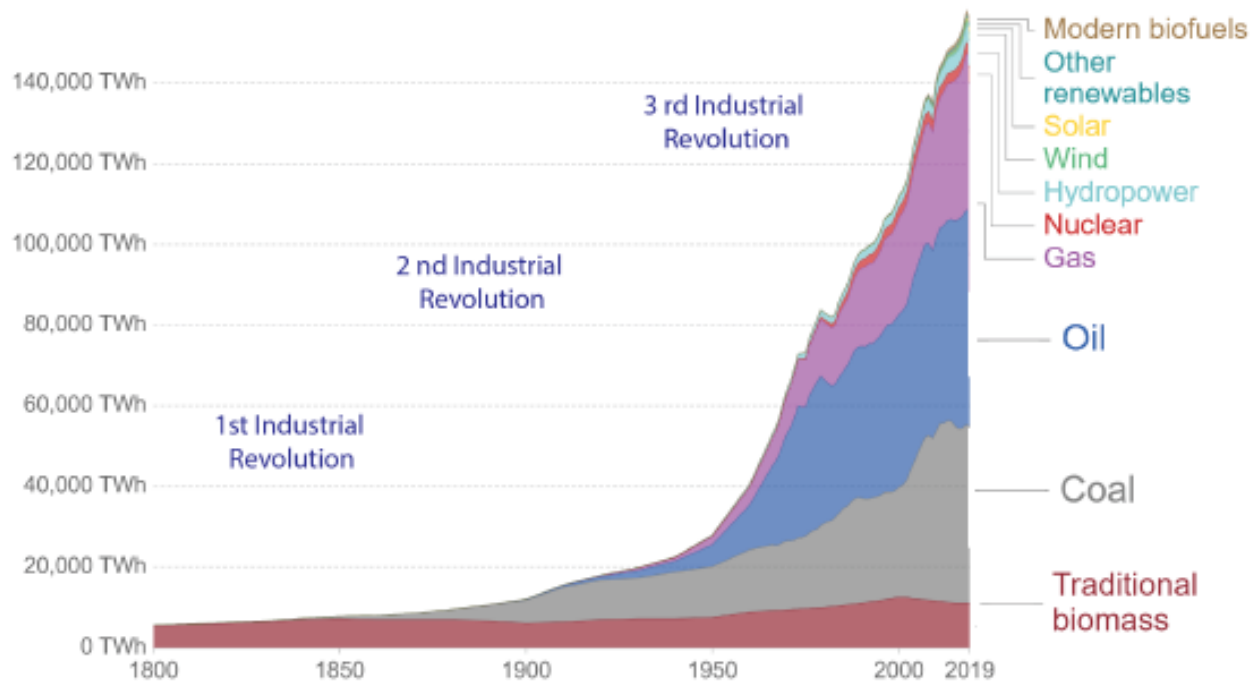


Figure 1: Energy consumption and its primary sources since the first industrial revolution.[3]

1.2. Batteries for energy storage

A battery is an electrochemical system that converts chemical energy into electric energy by the oxidation-reduction reaction. Usually, a battery consists of several electrochemical cells. The cell is a basic unit to provide electrical energy from chemical energy.[4] There are three major components of the cell, the negative (anode) electrode, positive (cathode) electrode and electrolyte. The negative electrode releases electrons to the external circuit and an oxidation reaction takes part. The positive electrode, on the other side, receives electrons from the external circuit and is reduced. The electrolyte is located between these two electrodes and serves as an ion conductor.[5]

Generally, the cells are classified as primary, non-rechargeable, where the reaction is irreversible, and secondary, electrically rechargeable, where the reaction is reversible.

1.2.1 Primary batteries

The first primary battery was introduced around 200 years ago by Alessandro Volta as the ‘Volta pile’ in his letter to the Royal Society of London.[6] His cell consisted of two different metals, zinc as the anode and copper as the cathode, separated by a piece of cloth soaked with bromine, and produced a flow of current when a coil externally connected with the two metals. The term for battery in French ‘la pile’ is derived directly from his cell. A bit later, in 1836, John Daniell, from England, introduced his new cell with 1.1V, which was able to give enough magnitude to find itself useful for some applications.[7] For example, the invention of this primary battery, known as the Daniell cell, allowed the rapid commercialization of telegraphic systems.

In 1866, the French chemist Leclanchè introduced a primary battery that could deliver a small uninterrupted current at 1.5V. In his cell design, he replaced the zinc rod with a zinc can, which can be used as anode and as a container at the same time, and the liquid electrolyte by its paste form, which restricted its displacement. The Leclanchè cell was a game-changer for primary batteries that expanded further their penetration into different industry domains such as mobile radios, flash lamps and clocks. This kind of cell format served till mid of 20 century and is known as the ‘dry cell’.[5]

The electrochemistry behind the Leclanchè cell was straightforward and simple, reducing manganese dioxide into manganese as a cathode and simple oxidation of zinc metal as an anode. But under high load, the system suffers from the side reaction of Zn^{2+} hydrolysis, which produces H^+ and decreases the zinc metal's pH. The deterioration of the zinc electrode corrosion leads to an increase in pressure within the cell and ultimately breaks down the battery. In the mid-20th century, the ammonium chloride electrolyte used in the Leclanchè cell was replaced by a zinc chloride solution to overcome this problem, and the modern ‘zinc chloride’ cell was born. This cell can serve three times longer with a more constant potential during the discharge.[8]

During the last 50 years, many new chemistries were developed for primary batteries such as magnesium, aluminum, alkaline, zinc oxide, cadmium oxide, silver oxide, zinc-air, lithium and

solid electrolytes. All of them find their usage depending on their electrochemical performance, service life, design and cost.[5]

1.2.2. Secondary batteries

French chemist Gaston Planté invented the first functioning rechargeable cell in 1859.[9] The battery consisted of two lead sheets separated by porous materials soaked in diluted sulfuric acid. Even though the output was 2 volts, it gave a tiny amount of current. But after several cycles, current gradually increased. This behavior is well known as a formation step in the manufacturing of batteries. We will briefly discuss the formation step in the battery fabrication chapter briefly.

It is well known that the automobile industry laid down the foundation for the evolution of modern infrastructure and the development and improvement of new technologies. In 1881, regardless of twenty years of cars' invention, they were still started by hand cranking. Camille Fauré, a French engineer, took the Gaston Planté cells and coated electrodes with a paste of lead dioxide and sulfuric acid to solve the problem.[5] As a result, she obtained a battery capable of starting the car engine with a higher capacity and decreased formation steps from several months to hours. This was the foundation of basic lead-acid technology.

At the end of the 19th century and the beginning of the 20th century, Waldemar Jungner in Sweden and Thomas Edison in the USA developed independently alkaline secondary batteries. Both cells had 1.2V, both of them had nickel cathode material and the only difference between them was pure iron versus iron mixed with cadmium anode material. Further, during the 20th century, this technology was improved several times and was the foundation for the more recent nickel-metal-hydrate batteries. These inventions radically increased the cell's power capability and functioning temperature range and had lower the manufacturing cost. One of the significant drawbacks of the battery is the hydrogen evolution at the anode electrode.

The development of Lithium-Ion Battery (LIB) started during the oil crisis in the 1970s. Researching on materials for semiconductors, Stanley Whittingham designed an energy-rich lithium battery that was subsequently refined by his fellow Nobel laureates John B. Goodenough and Akira Yoshino, who improved the technology by replacing the cathode and anode with lithium cobalt oxide and graphite, respectively.[10] Since the first commercial LIB in 1991, the world has seen a boom in mobile electronics, long-range electric vehicles and the possibility of acting as an accumulator for renewable sources such as solar and wind power. In this sense, Lithium-ion batteries (LIBs) are widely used as energy storage devices in electronic gadgets, electric vehicles,

and stationary applications; due to their high power and energy densities and good cycle life.[11],[12],[13].

Currently, alternative ion (sodium, calcium, potassium) batteries and metal (lithium, zinc, magnesium) air batteries are under development as post lithium ion battery technologies.[14,15][16,17] The other ion based devices are interesting as a substitute to lithium ion technology due to their abundance in nature.[18,19] The rise of interest in metal-air batteries founded on its vast theoretical capacity. The concept of using oxygen of air as an active material grants it with this enormous plausible capacity. Among other metals, more particularly Li-air technology has received an increased research interest because of its very high theoretical energy density.[20] Nevertheless, many unsolved and poorly understood research challenges block this technology from reaching its full potential. All the above discussion on secondary batteries energy and power capabilities are summed up in the Ragone plot (**Figure 2**).[21]

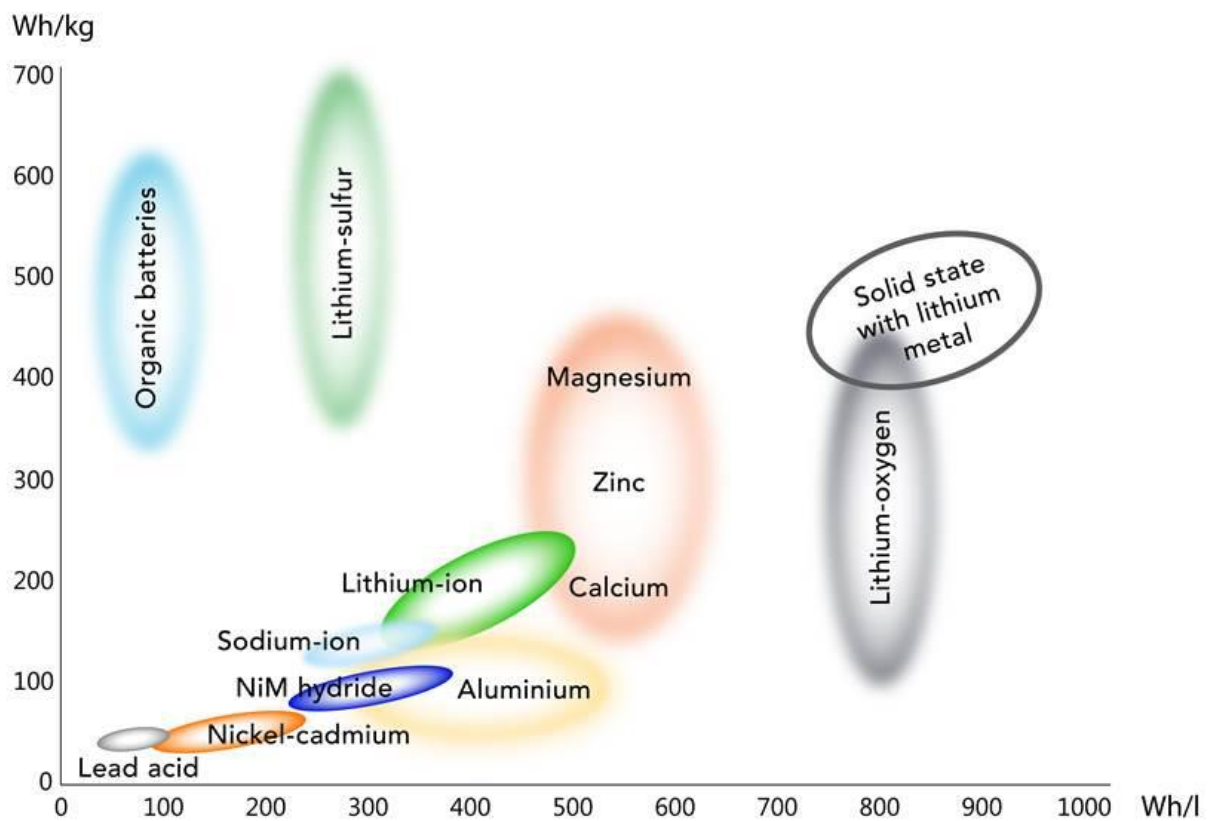
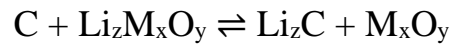


Figure 2: Ragone plot, for various electrical energy storage devices.[21]

1.3. Lithium Ion Batteries

1.3.1 Working Principle and Key Parameters

The development of Lithium-Ion Battery (LIB) started during the oil crisis in the 1970s. Researching on materials for semiconductors, Stanley Whittingham designed an energy-rich lithium battery that was subsequently refined by his fellow Nobel laureates John B. Goodenough and Akira Yoshino, who improved the technology by replacing the cathode and anode with lithium cobalt oxide and graphite, respectively.[22] Currently LIBs are one of the most widespread rechargeable batteries due to their high energy densities and cycle lives of several 1000 cycles.[23] Energy storage in LIB is based on Li^+ ion migration accompanied by redox reactions taking place in the electrodes, as (Figure 3). Li^+ is used as a charge carrier due to its low standard electrochemical potential and its small ionic radius, resulting in a small volume expansion of the host structure. During battery operation, Li^+ intercalates/de-intercalates into the crystal structure of the LIB material.[13] The reaction taking place within the cell can be summarized as follows,



Cell potential:

As the reaction progresses, the free energy of the system decreases. It can be expressed by Gibbs (ΔG°) free energy,

$$\Delta G^\circ = -nFV^\circ \tag{1}$$

Where F is the Faraday constant, n is the number of electrons involved in the stoichiometric reaction and V° is the standard potential. The standard potential of the cell is determined by the type of active materials used, and can be calculated from free energy data or obtained experimentally. The standard potential of the cell is the sum of the anode (oxidation) and cathode (reduction) standard potentials,

$$V_{cell}^{\circ} = V_{cathode}^{\circ} + V_{anode}^{\circ} \quad (2)$$

The overall cell voltage (V_{cell}) depends on the concentration of electroactive species (C_i), absolute temperature (T) and gas constant (R) as expressed in Nernst equation,

$$V_{cell} = V_{cell}^{\circ} - \frac{RT}{nF} \ln \frac{C_{ox}}{C_{Red}} \quad (3)$$

Capacity

The electrode or full-cell performance can be characterized by its specific discharge capacity Q_d (in Ah) as a function of current I within the discharge period T_d with equation (4),

$$Q_d = \frac{1}{m} \int_0^{T_d} I(t) dt \quad (4)$$

Energy and power density

The most important parameter characterizing a full cell's performance is its specific discharge energy (in Wh/kg). The specific discharge energy depends heavily on the charge-discharge rate, which in turn depends on the current or power applied during cycling. It is therefore essential to consider both the specific energy E_d and specific power P_d of the cell simultaneously,

$$E_d = \frac{1}{m} \int_0^{T_d} V(t) I(t) dt \quad (5)$$

$$P_d = \frac{E_d}{T_d}$$

(6)

Stability and Cycle life

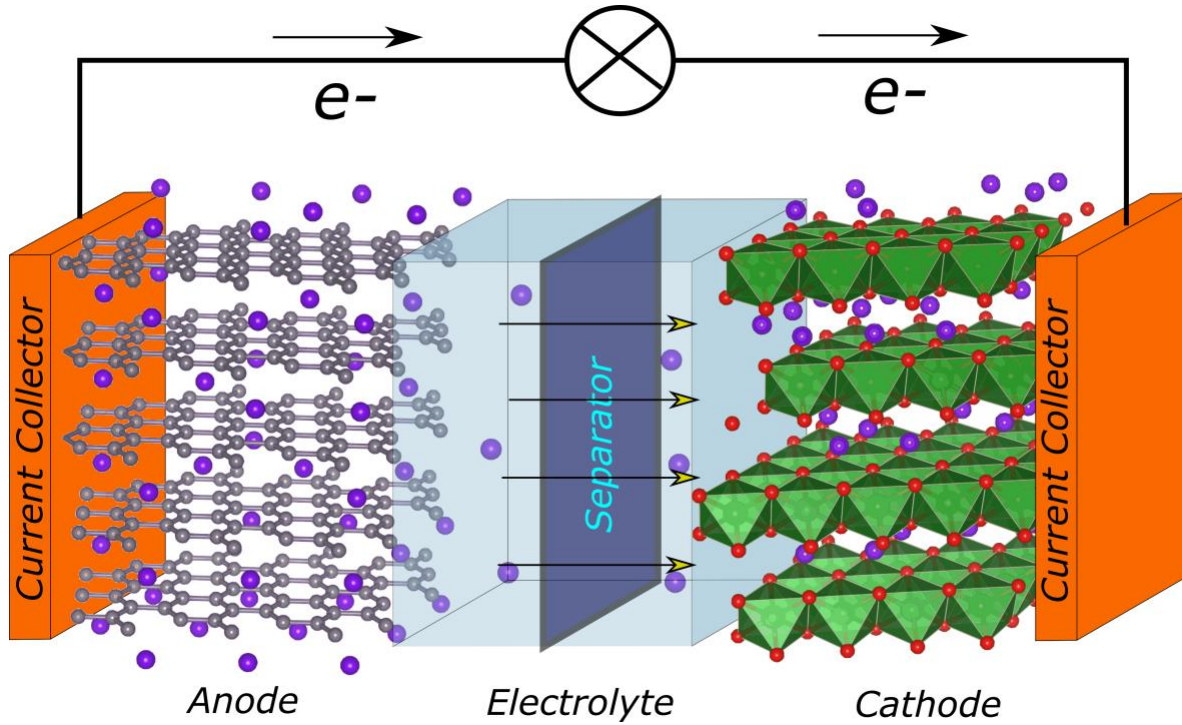


Figure 3: Schematic representation of the Li-ion cell, with a Li_2C anode and Li_2MxO_y cathode.[24]

Many variables can affect the electrode and the cell stability. The most common parameter used to describe cell stability is the specific discharge capacity/energy as a function of the cycle number. A cell's usual (but not absolute) cycle life estimation is the number of cycles in which 20 % of the maximum discharge capacity/energy is lost. Another stability parameter is the Coulombic efficiency (η), defined for any cycle as the ratio of discharge over charge capacity,

$$\eta = \frac{Q_{\text{cathodic}}}{Q_{\text{anodic}}}$$

(7)

Where Q_{anodic} and $Q_{cathodic}$ represent the charge inserted and extracted from the cell, respectively. Coulombic efficiency is a useful parameter to characterize the charge loss in the cell. The cell instability originates from several different factors like electrolyte degradation or the volume expansion of LIB materials. This capacity loss is also highly dependent on the electrode potential.

1.3.2. Components

Negative electrode materials

The electrodes in a LIB are produced by mixing active materials (AM) with conductive additives (CA) and binders. Initially, lithium metal was used as the negative electrode material because of its extraordinary high capacity of 3860 mAh/g and its high negative potential. This technology was quickly abandoned for industrial applications due to lithium dendrite growth, which leads to a short circuit. The metallic lithium was then replaced by lithium intercalating materials like graphite and lithium titanate (LTO) as anode materials.[25]

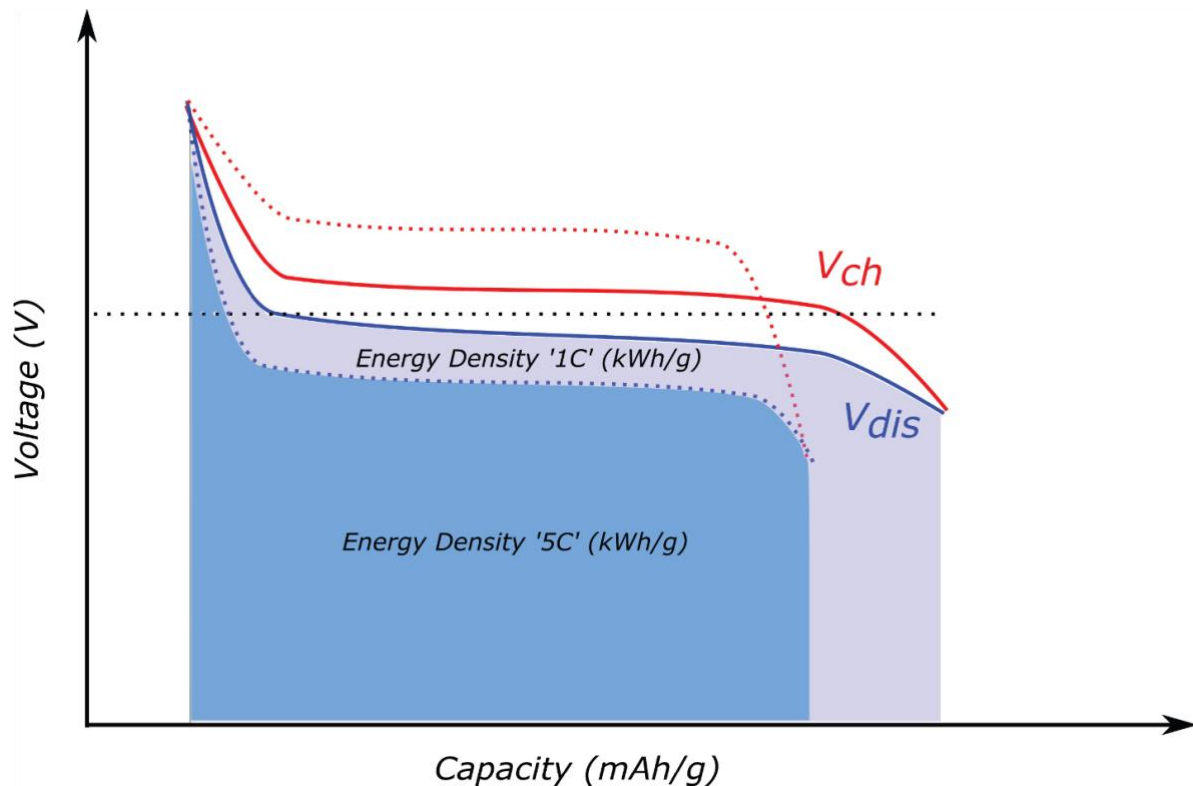


Figure 4: Schematic representation of the Capacity Voltage curves. Blue curves represent the charge curves whereas red ones represent discharge curves. Solid line for 1C rate and dashed line for 5C rate. Respectively, energy densities represented as the integrated area below the discharge curves.

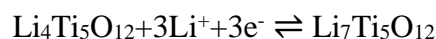
Graphite

Graphite is the most used anode active material in LIB. It is a semi-metal with high electronic conductivity and has a 372 mAh/g theoretical specific capacity. The intercalation of lithium cations into graphite takes part between 0.25 and 0.01V vs. Li/Li⁺. Such a low operational voltage gives the full cell high energy density but requires an electrolyte with a high potential stability window.[26] During cycling, electrolyte decomposition at the graphite surface leads to the formation of a solid electrolyte interphase (SEI), which accounts for the irreversible capacity in the first cycle This layer is crucial for reversible Li⁺ de-/intercalation as it prevents direct electronic contact between the graphite and the electrolyte and thus prevents further electrolyte decomposition. The SEI is strongly correlated with rate capability, energy density (initial charge loss) and cycle life.[27] After its formation, the lithium insertion reaction into graphite occurs,



LTO

Lithium titanate has a spinel crystal structure, which transforms salt structure into a rock with almost no volumetric changes during cycling. The resulting theoretical capacity is 175mAh/g and practical values of about 160 mAh/g can be achieved. The high voltage plateau vs. Li/Li⁺ lies within the stability window of the most used electrolytes and hence SEI development and electrolyte decomposition are not observed. However, the high potential and the lower capacity lead to lower energy compared to graphite electrodes.[28] The lithium intercalation into the LTO occurs according to the following reaction,



Positive electrode materials

In a typical LIB, the positive electrode active materials are transition metal oxides (M_xO_y). Positive electrode materials are divided into layered oxides, spinel materials with a three-dimensional framework and phosphates with an olivine structure. Layered materials are used as cathodes for high-energy systems, while spinel oxides and olivines are considered in the case of high-power Li-ion batteries.[25]

LiCoO₂

Lithium cobalt oxide (LiCoO₂, LCO) was the most used positive electrode material in industry. It consists of alternating layers of cobalt, oxygen, and lithium-ions and offers a practical capacity of around 155 mAh/g, good electronic and ionic conductivity, and a high potential voltage of 3.9 V. However, if LiCoO₂ is overcharged above a critical value (about 50% de-lithiation), the crystal structure becomes unstable and releases oxygen. Then formed oxygen then reacts with the electrolyte, leading to overheating and ignition of the electrolyte. Additionally, cobalt is a rare material with potential resources limitations. Therefore, intensive research was carried to partially or fully replace cobalt with another element. [29]

LiNi_{1-y-z}Co_yMn_zO₂

Nowadays, the most used cathode materials partially substitute cobalt with nickel and manganese (NMC) because of their high capacity, high operating voltage, low reactivity with the electrolyte and high rate performance. Nevertheless, NMC with high content of Ni might cause problems with cycle instability, thermal instability, and air instability. The origin of this phenomenon lies in nickel's instability in liquid organic electrolytes. As a result, it forms a solid electrolyte interphase on the surface of the positive electrode. Its operating voltage is 3.7V with 280 mAh/g specific capacity.[30,31]

LiMn₂O₄

Another alternative to LiCoO₂ is lithium manganese oxide (LiMn₂O₄, LMO). LMO is an environmentally friendly and cheap material with a spinel crystal structure with a three-dimensional network for Li-ion diffusion. The reversible lithium extraction from LMO occurs at a voltage range of 3.8 to 4.25 V vs. lithium, and its theoretical capacity upon complete Li⁺ extraction is 148 mAh/g. Nevertheless, only 0,8 Li⁺ ions per formula unit can be extracted reversibly.

Following Faraday's first law of electrolysis, this value corresponded to a specific capacity of about 120 mAh/g. The main drawback of LMO is its high rate of capacity fading during cycling, especially at elevated temperatures of about 50°C. This fade was extensively investigated in literature and several failure mechanisms were proposed. Fracture of the LMO surface is caused by the high concentration of lithium-ions located LMO particles' surface (Jan-Teller distortion) during deep discharge. Dissolution of Mn^{2+} into the electrolyte caused by intermediates developed at the carbon surface or due to fluoric acid formation through water contaminated $LiPF_6$ containing electrolytes, and the structural breakdown of the spinel lattice in highly de-lithiated state ($0.1 < x < 0.4$).[32]

$LiFePO_4$

The safest stable positive electrode material is lithium iron phosphate ($LiFePO_4$, LFP). It exhibits no oxygen evolution and no exothermic effects during charging/discharging, even at high charging/discharging rates, which makes cell ignition or explosion impossible. LFP is not toxic, is cheaper than LCO and NMC as iron is the second most common element on earth, and has an excellent cycle life.[33] This high cycle life is attributed to the high stability of the de-lithiated phase ($FePO_4$) and the low difference in the volume of lithium rich and lithium poor phases (lithium-poor phase has a 6,81% lower volume).[34] The Li^+ extraction reaction occurs at a voltage of 3.4 V vs. Li/Li^+ . A unique property of LFP is its extremely flat charging/discharging voltage profile, which enables LFP-based batteries to deliver a constant power during discharging (no DC-converter required). The theoretical capacity of LFP upon complete Li^+ -extraction is 170 mAh/g. However, the de-intercalation is generally limited to 0,6 Li-ions per formula unit LFP and therefore to a capacity value of about 100-110 mAh/g. This is mainly attributed to the low electron and Li^+ ionic conductivity of LFP. The latter can be circumvented by decreasing the LFP particle size to about 200 nm to ensure the short Li^+ ion diffusion paths. The electronic conductivity could be increased by additional carbon coating of the particles. With these modifications, a capacity of 165 mAh/g (0.97 Li-ions per formula unit) is possible.[35]

$LiMn_{0.67}Fe_{0.33}PO_4$

Partial replacement of Fe with Mn in the olivine LFP crystal increases the average Li-intercalation/de-intercalation voltage. The presence of Mn results in an additional voltage plateau at 4 V vs. Li/Li⁺. This leads to a higher cell voltage and an increase in energy density. Note that Mn and Fe display only a small difference in molar masses, and hence the capacity in mAh/g does not change significantly. As a transition metal in active materials, such as LMO and LMP, manganese is susceptible to dissolve in the electrolyte. LiMn_xFe_{1-x}PO₄ displays lower Mn²⁺ dissolution when $x \geq 0.3$, as Fe atoms on the metallic sites effectively block Mn diffusion into the electrolyte. This could be why the mixed Fe-Mn phosphate displays highly improved cycling stability at higher capacities than LiMnPO₄ ($x = 1$).[36]

Table 1 summarizes the electrochemical properties of the most common and well-studied of three classes of insertion compounds.

Table 1: Electrochemical properties of the most common cathodes for LIB.

| Framework | Compounds | Specific capacity (mAh/g) | Average potential (V) |
|-----------|-----------|------------------------------|--------------------------|
| Layered | LCO | 274 | 3.8 |
| Layered | LNMC | 280 | 3.7 |
| Layered | LNCA | 280 | 3.7 |
| Nasicon | LVP | 197 | 4.0 |
| Spinel | LMO | 148 | 4.1 |
| Spinel | LMNO | 148 | 4.7 |
| Olivine | LFPO | 170 | 3.4 |
| Olivine | LMFPO | 165 | 4.0 |

Electrolyte materials

The role of the electrolyte in a LIB is to act as an ionic conductor for transporting lithium ions between the anode and the cathode. LIB electrodes have porous structures, so electrolytes must be able to seep inside the media to transfer ions smoothly. In addition, electrolytes must also be inert to all cell components, be operational in a wide temperature range (meaning having low melting and high boiling points), and have a low enough viscosity to enable fast ion transport and efficient

filling on the production line.[37] Further, the electrolyte must be able to dissolve lithium salts to acceptable concentration and have a high operating electrochemical window. Currently, aprotic organic solvents where lithium salts are dissolved are used as electrolytes for commercial LIBs.[38,39] Some of the organic solvents used in industry are ethylene carbonate (EC), propylene carbonate (PC), dimethyl carbonate (DMC), ethyl methyl carbonate (EMC), and diethyl carbonate (DEC). Another critical part of the electrolyte is the supporting salts. There are quite a lot of publications on electrolyte additives, but there has been very little attention given to new salts.[40] Usually, salts for LIB must have anions that are stable towards oxidation and reduction at both electrodes, be inert to the other components of the cell, and should be able to dissolve in the solvent while allowing Li ions to transfer through the solution. The most well-known salt that might be able to fill all the criteria is LiPF_6 [40] and is currently the most used salt in the market. Other possibilities include LiClO_4 , LiAsF_6 , LiBF_4 and LiAlCl_4 .[41]

Table 2: Physical properties of most common solvents in commercial LIB.[42]

| Solvent | Density (g/cm^3) | Dielectric Constant | Viscosity (cP at 25°C) | Melting Temperature (°C) | Boiling Temperature (°C) |
|---------|---------------------------------------|------------------------|---------------------------|-----------------------------|-----------------------------|
| EC | 1.327 | 89.78 | 1.9 | 36.4 | 248 |
| PC | 1.200 | 64.92 | 2.53 | -48.8 | 242 |
| DMC | 1.063 | 3.107 | 0.63 | 4.6 | 91 |
| DEC | 0.969 | 2.805 | 0.77 | -74.3 | 126 |
| EMC | 1.006 | 2.958 | 0.65 | -53.0 | 110 |

The state of the art in both academic and industrial research is focused on developing solid electrolytes which are attractive due to safety concerns and the potential of using metallic lithium. In addition, other ionic liquid electrolytes are being developed as an alternative to liquid organic carbonates. Ionic liquids are attractive due to their high conductivity at room temperature and high thermal stability but suffer from lower operational potential windows and the possibility of reacting with the cell's current collectors. Nonetheless, such electrolytes are at a stable potential range for LFP cathodes and LTO anodes.

Conductive additives for electrodes

Carbon conductive additives are mixed with both positive and negative active materials to make the electrodes. The primary role of the conductive additive is to increase electronic conductivity by optimizing the contact between the redox-active particles within the electrodes. Even when added in small amounts, it has a massive influence on slurry's rheology during the manufacturing process, and directly influences the mechanical stability of the electrodes. A variety of graphites (KS15, SFG15, and MX15) and carbon black (Acetylene black, Denka™ SUPER P Li, C65) are applied to both electrodes. The graphite and carbon black show complementary properties, and the choice depends on the cell requirements, electrode formulation and type of active electrode material. They have the dimensional differences of the primary particles where carbon is smaller by a factor of about ten than graphite, with considerable differences in surface area, dispersibility and conductivity. Usually, conductive additives with low polymer and electrolyte absorption allow for good mechanical stability, high electrolyte penetration, and good electrochemical performance.

Binders for electrodes

As mentioned above, LIBs use nonaqueous electrolytes with lower ionic conductivity. Therefore, to have a high current output electrodes must be thinner and broader compared to those of other secondary batteries, making the use of binders crucial for LIBs. Accordingly, binders must have excellent adhesion to the active material, wide potential range, high melting point, low swelling rate, good electronic and ionic conduction. Unfortunately, a binder which can fill all the requirements does not exist and only three binders that comply have been found. Currently, polyvinylidene fluoride (PVDF) and styrene-butadiene rubber (SBR) are deployed for negative electrodes and PVDF and polytetrafluoroethylene (PTFE) for the positive electrodes. The amount of added binder is crucial role in the electrochemical performance of the electrode. The less binder used, the higher the active material density, which provides higher capacity. On the other hand, adding more binders increases the power capability and mechanical stability under different electrode conditions. The binder is usually formulated based on the type of active material and on the battery design, for example, more is needed in electrodes designed to be rolled. Depending on the fabrication process, binders can have a film or an agglomerate form. The amount of binder can significantly influence the slurry formation, casting, calendaring, and electrolyte filling steps during manufacturing. Overall, the binder is essential for both the electrochemistry of the cell and the batteries' fabrication.

Separators

A separator is a porous membrane placed between electrodes permeable to ionic flow but prevents electric contact of the positive and negative electrodes. The suitable separator prevents short electrical circuits, allows fast ionic transport, and has good mechanical and dimensional stability. Currently, popular separators (Celgard, HiPore, Teklon and Solupur) are based on polyethylene (PE) and polypropylene (PP) compositions. Celgard's separators are by far the best characterized and the most used battery separators in the literature. Usually, separators are composed with 40% porosity, up to 25 μm thickness, and 150° C melting temperatures. One of their critical requirements is their pore size distribution.

Current collectors

The role of current collectors is to connect electrodes with an external circuit. Requirements for current collectors are high electronic conductivity and electrochemical stability window. Copper and aluminum are the most common current collectors used in the LIB industry. Copper is used for an anode electrode due to its up to 3V vs. Li/Li⁺ stability. Aluminum is used for cathode electrodes due to its lower price and good stability in the range of cathode material. It can not be used as a current collector with anode as at 0.3V vs. Li/Li⁺ reacts with lithium and forms Li-Al alloy. The potential problems with all current collectors are corrosion and adhesion with electrodes due to mechanical stress during the fabrication. Carbon-based current collectors might be used as an alternative in the future and are promising with good flexibility.

1.4. Lithium Ion Battery manufacturing

The main steps in LIB manufacturing consist in fabricating the cell components (electrode, separator, etc.), cell assembly, and cell finishing (**Figure 5**). Manufacturing different parts of the battery and the assembly of the cell are independent of its design (pouch, cylindrical, prismatic, etc.), however, the last step, cell finishing, firmly depends on the design of the final product.

1.4.1 Electrode manufacturing

Electrode fabrication plays one of the most significant role in manufacturing. It consists of six steps: dry and wet mixing, coating, drying, calendaring, slitting and vacuum drying.[43] The first step is also known as the slurry preparation step. The slurry is prepared by dry mixing of two or

three materials (active material, carbon black and binder) and progressed to liquid form by adding solvent. Sometimes, the process is performed under vacuum conditions to escape gas inclusions. The quality of the slurry depends on mixing time, mixing temperature and dispersing sequence. The mixing time can take from 20 min up to 5 hours under room temperature.[44] The prepared slurry is coated on the current collector foil using a doctor blade, slot die, anilox roller, etc. The slurry is usually double coated (on both sides) on the foil sequentially. Indeed, the slurry is coated on one side of the foil and transferred to the drying process. After the first drying step, the current collector turn over to coat the slurry on the other side then it is dry again. The overall coating thickness, homogeneity, surface quality and adhesion between the coating and the substrate are influenced by the coating speed, coating width, application tools (slot die, comma bar, anilox roller) and precision of the slurry pump parameters. The next step is drying, or removing solvent from the slurry by heating. The slurry coated foil is introduced on a roller system into the heating chamber, which consists of several chambers that allow to homogenously increasing the temperature. The drying quality depends on drying speed parameters (35 m/min-80 m/min), length of the dryer (up to 100 m), temperature profile inside the chamber, and foil pretension choice.[45] In order to increase the rate capability and gain volumetric energy density, the double coated and dried electrodes are then compressed by a pair of rotating rollers to calender them. Then, two bottom and top rollers ensure the application of a precisely defined pressure.[46] Consistent gap between the rollers, calendaring speed, constant applied pressure, roller temperature, and cleanliness of the roller are crucial to obtain electrodes with defined porosity, good surface texture, and good contact between coating and substrate. The next step is slitting, where rolling knives are used to divide the wide fabricated electrodes into smaller ones (from 60 mm to 300 mm) depending on the battery's design (Pouch, Prismatic or Cylindrical). Before cell assembly, the electrodes are kept in a vacuum oven (from 12h to 30h) for further drying (60°C to 150°C).[45]

1.4.2. Cell assembly

The dried roll of separated electrodes is stacked in a cycle of the anode, separator, cathode, separator, anode, etc. The manufactured stack is fixed with adhesive tape. There are several ways of stacking the anode, cathode and separator sheets together, such as Z shape, lamination and pocket stacking. To pouch the battery, the current collector tabs are connected using ultrasonic or laser welding. The welded cells are inserted into the case for a further sealing step. Usually, all the parts of the case are sealed except the side where electrolyte insertion takes place. The bottom part

is left open for the pouch cell format and the top for the cylindrical cell format. Controlled sealing temperatures and pressures are very important for keeping low contact resistances. During the electrolyte filling, a distinction between the two sub-processes, “filling” and “wetting”, must be made. During filling, a high-precision dosing needle is used to fill the cell with electrolyte under vacuum. The cell initially contains inert gas which is removed by applying a pressure profile, generating vacuum in its place. The electrolyte injection and gas evacuation activate the capillary effect for electrolyte penetration.[47] The evacuation and partial filling are repeated several times to ensure full wetting of the cell. The last part of the cell is sealed afterward to close the compartment completely. The degree of wetting, accurate distribution of the electrolyte in the sealed cell and tightness depend on working pressure, number of cycles, dryness of environment, control of electrolyte quantity, and electrolyte transport system. The electrolyte filling step is the same for all kind of battery designs and so far no alternative ways are used in series production.[48]

1.4.3. Cell finishing

After the electrolyte filling step, roll pressing sometimes takes place for the pouch cell format. The cell is clamped on a carrier with a gripper while two rollers apply pressure. This step ensures optimum distribution and absorption of the electrolyte, and helps avoid unwetted zones, which might create electrochemically inactive areas. It also allows for good development of the Solid Electrolyte Interface (SEI) layer during the formation step, which describes the first charging and discharging processes of the battery. The cell is then charged and discharged to define the current and voltage curves and to form the electrode-electrolyte interface. The first charge is done at around 0.1 C - 0.5 C rates between 20 % and 80% state of the charge, and could take up to 24 hours. The quality of SEI formed depends on the process temperature, pressurization and orientation of the cell. It is well-known that a strong gas evolution occurs during the first charging, therefore, degassing is performed after the formation step. During degassing, the gas bag is pierced in a vacuum chamber and the escaping gases are pulled away. The cell is then finally sealed under vacuum. The pressing of the cells during degassing is the most influential parameter for this step. The final step in manufacturing batteries is cell aging. During the aging stage, the cell Open Circuit Voltage (OCV) is measured continuously for up to three weeks under changing temperature conditions. Usually, cells undergo high temperature (30°C - 50°C) and room temperature (22°C) aging. The lack of significant changes in the cell properties during aging indicates good cell quality

and a fully functioning state. Self-discharge rate during the aging period is one of the indicators of quality. The batteries also go through an EOL test as most products before going to the market.

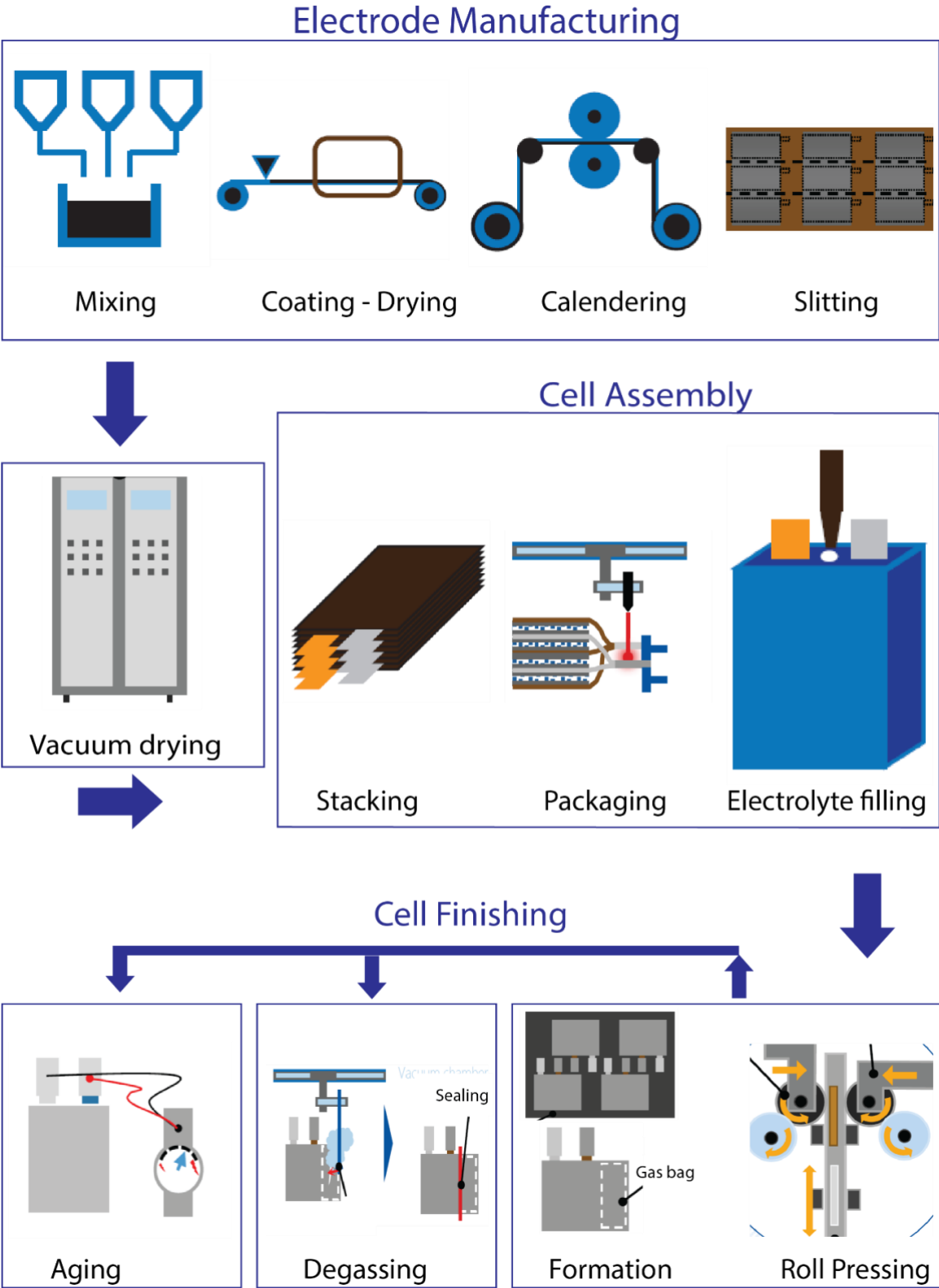


Figure 5: Schematic representation of typical LIB manufacturing process for pouch cell format.[49]

1.5. Digital twins of battery fabrication process.

1.5.1 ERC-Artistic: the fusion of models, data and AI to create the digital twin

This thesis was part of the ERC-ARTISTIC project, a highly innovative and multidisciplinary project devoted to improve the current fabrication process and ensure rechargeable battery technologies with emerging chemistries achieving reliability. It has three global objectives and three tools in hand to reach them (**Figure 6**).

Motivations and objectives of the project

The first objective is developing a multiscale modeling platform that rationalizes the formulation and fabrication process of well-controlled battery electrode design and efficient operation. The demonstration of its reliability will be achieved by comparing it to experiments on conventional material chemistries for LIBs. This needs the establishment of a workflow coupling multiple simulation techniques and artificial intelligence (machine/deep learning) algorithms, providing insights on self-organization mechanisms of material mixtures in slurries and on the relationships between the properties of the material such as texture, surface chemistry and wettability, to the whole fabrication process layout and the arising electrode mesostructure and electrochemical performance. The second objective is to examine and improve the platform's robustness and flexibility by applying it to new electrode chemistries chosen as test cases based on experimental data. The third objective consists of developing an online, open access and integrative multiscale computational tools devoted to provide users with an interactive quantitative evaluation of how the electrode formulation and fabrication parameters relate to the battery cell performance. Such a tool will permit the optimization of electrode designs and will support direct and reverse engineering approaches, *i.e.*, it will allow predictions on how fabrication parameters impact the cell performance, but also recommendations on the most appropriate fabrication process (*e.g.*, temperature to be applied in the solvent drying step) to fabricate electrodes with the desired performance targets.

ARTISTIC PROJECT PILLARS

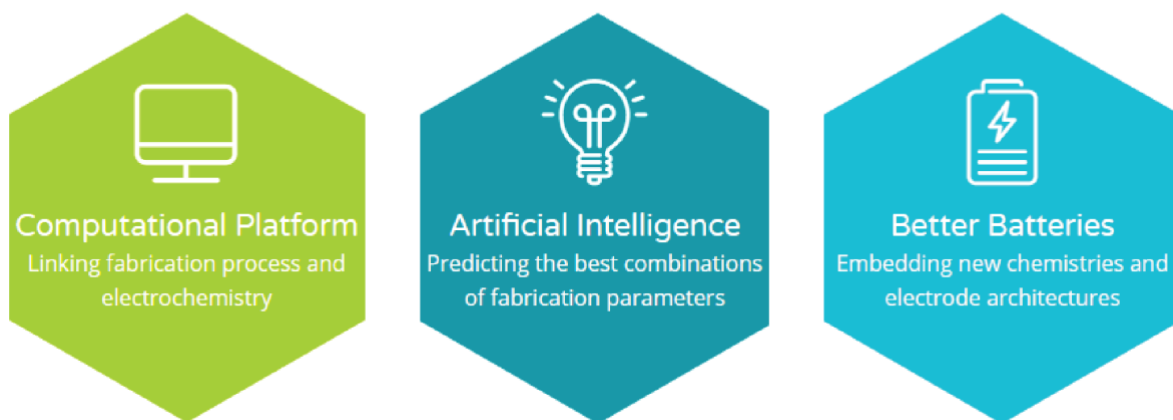


Figure 6: ERC-Artistic project pillars.[50]

The architecture of the project

A computational platform is established by connecting discrete particle models with continuum models. The discrete particle models allow predicting the electrode mesostructure as a function of the fabrication parameters, whereas the continuum models allow predicting the performance at the cell level as a function of the electrode mesostructure. The resulting computational platform will allow performing both direct and reverse engineering: it will not only allow predictions on how fabrication parameters impact the cell performance, but also recommendations on the most appropriate fabrication process (e.g., temperature to be applied in the solvent drying step) to fabricate electrodes with the desired performance targets.

The first step namely the development of modeling tools allowing the simulation of the different steps of the fabrication process. Coarse-Grained Molecular Dynamics (CGMD) and Discrete Element Method techniques are used to predict the self-organization of the slurries and of the electrode mesostructure during the solvent evaporation and calendaring steps as a function of the chemistry of the materials and fabrication parameters (slurry composition, particle sizes distribution, type of solvent used, drying temperature and time, etc.). These simulation tools aim to be universal regarding the materials chemistry and are first tested for NMC, LiFePO_4 and graphite, silicon and Li-rich materials as the active materials. Multiple binders (e.g., PVDF), carbon additives (e.g. Super P[®]), slurry solvents (both aqueous and non-aqueous) and dispersants are also

considered. The generated electrode is then exported to the Lattice Boltzmann Method (LBM) model to simulate the electrolyte invasion dynamics in the porous electrode. The LBM model is used to simulate electrolyte filling and obtain advanced insights on the impact of the electrode mesostructure on the speed of electrolyte impregnation and wetting, highlighting the importance of porosity, pore size distribution and pores interconnectivity on the filling dynamics. After LBM simulations, the cells are exported to performance models (electrochemical impedance spectroscopy and charge/discharge) to carry out electrochemical tests.

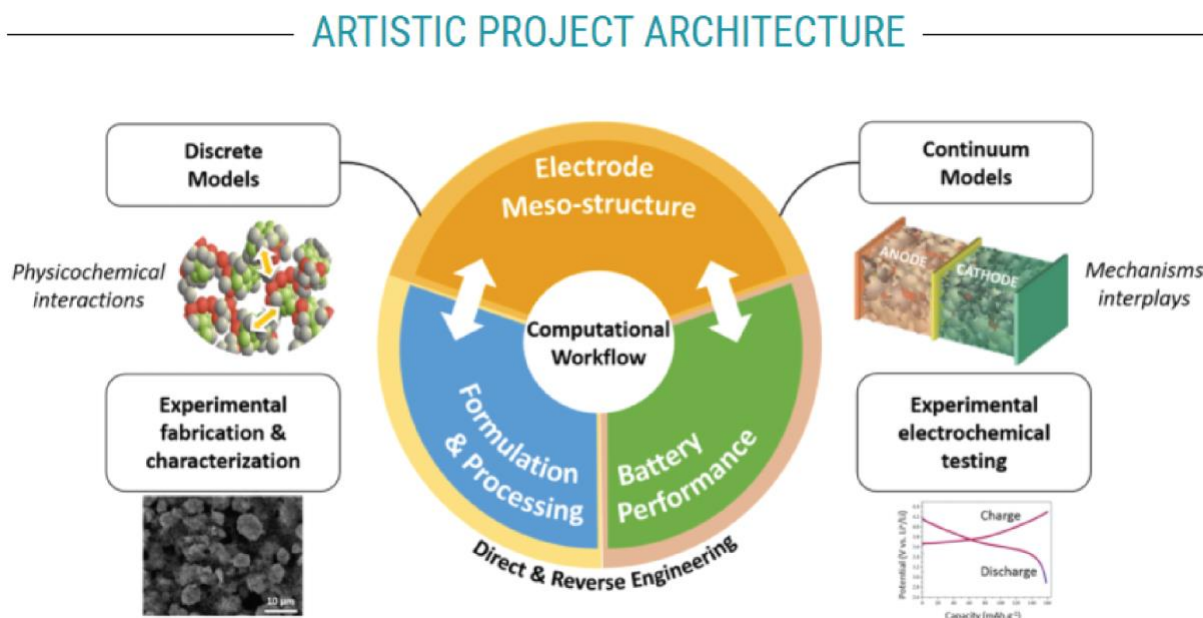


Figure 7: ERC-artistic project architecture.[50]

For experimental validation, the electrodes and cells are fabricated using the prototyping facilities available at the Laboratoire Réactivité et Chimie des Solides (LRCS) that mimic industrial processing conditions. Fabricated components and cells include the optimized electrode architectures arising from the cell performance simulations. To validate the CGMD models, slurries are characterized regarding their properties (*e.g.*, viscosity), while the electrode microstructural characterization is carried out by different complementary techniques, including gas adsorption porosimetry (porosity and tortuosity), X-ray tomography and 3D FIB/SEM. The electrical conductivities and mechanical properties of the various coatings are also characterized. The fabricated electrodes, including those with the most promising architectures generated from the computational data outputs, are finally experimentally tested at the lab scale from an

electrochemical viewpoint (*e.g.*, charge/discharge curves, GITT and EIS) through advanced characterization tools (*e.g.*, potentiostat coupled to *in operando* XRD).

1.5.2 The scope of the thesis

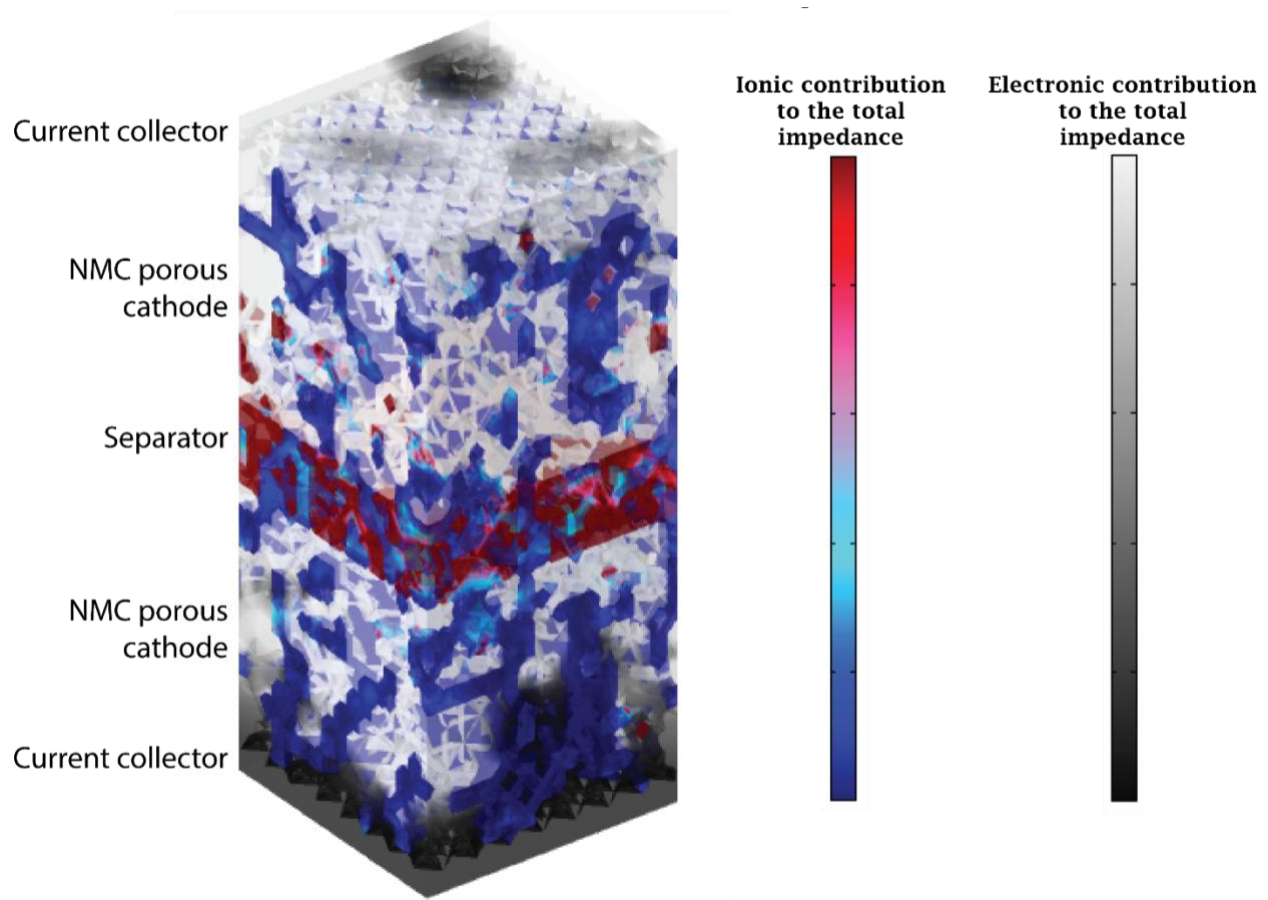
This thesis focuses on developing an understanding of the physics governing the propagation of the electrolyte in porous electrodes during the impregnation step. This is strongly dependent on the chemistry of the materials constituting the electrode (active material, carbon aggregates, polymer binder), determining the wettability of the pores, and the textural properties (porosity and tortuosity) which in turn depends on the level of calendaring of the electrodes.

The first part of the thesis consists of developing an electrochemical impedance model to characterize symmetrical electrochemical cells. The 3D EIS model to characterize symmetrical electrochemical cells which was accompanied by experimental validation. The model must also validate the output of different structures generated by the Coarse grained molecular dynamics model, stochastically generated electrodes, and electrodes obtained by experimental tomography.

The second part of the work consists of developing models based on the Lattice Boltzmann method to simulate the electrolyte propagation in the electrode mesostructures as obtained by different sources. The model must capture the electrolyte impregnation and the physics of the applied external pressure at a 3D level. Some experimental research should still be carried out for the validity of the model.

Chapter -II

4D-Resolved Physical Model for Electrochemical Impedance Spectroscopy in Symmetric Cells: Consequences in Tortuosity Calculations



2.1. Introduction

Since the first commercial LIB in 1991, the world has seen a boom in portable electronics, long-range electric vehicles and the possibility of acting as an accumulator for renewable sources such as solar and wind power. In this sense, optimization studies are still required to improve LIB electrochemical performance and to decrease their cost.[51] Generally, the former depends on the chemistry of the active materials and electrode mesostructure characterized by its porosity (ε) and pore size distribution, electronic and ionic conductivity and tortuosity. Except for the latter, all the other properties can be determined experimentally through simple characterization techniques. On the contrary, there is not a direct way to determine the tortuosity, which expresses the ratio of the average pore length between two random points within an electrode mesostructure and the geometrical shortest path between the points (in Cartesian coordinates, a straight line). This is an important property controlling the effective transport capabilities towards lithium ions in porous electrodes. Recently, Tjaden *et al.* have thoroughly reviewed different definitions of tortuosity and measurement schemes allowing to access to its value, and made an analysis in the limitations of each one.[52]

In the battery field, one of the most straightforward ways of obtaining the value of the tortuosity factor (τ) is through the MacMullin number (N_M), where $N_M = \tau/\varepsilon = X/X_{eff}$ being X the electrolyte bulk conductivity or diffusion coefficient and the subscript *eff* refers to its effective value within the porous electrode.[53–55] The effective ionic conductivity of electrodes can be determined through Electrochemical Impedance Spectroscopy (EIS) using the so-called transmission line model (TLM)[56], through which the ionic resistance of the electrolyte in the porous structure is obtained in the mid-frequencies 45° slope region. Although this constitutes a rather simple way to estimate how the electrode morphological properties affect the τ of the porous mesostructure, the main limitation of this approximation is that it considers all the pores as a collection of parallel identical cylindrical reservoirs of electrolyte with constant conductivity through the z direction, *i.e.* the electrode thickness.[57] Several authors have addressed this issue by using more complicated TLMs and/or explicit transport equations to describe the ionic and electric current in the porous electrode. Within the first approach, embedded TLMs were used for modelling fractal distribution of pores[58], a TLM with a normal distribution of pore radius and density per unit surface was added to study the impact of pore size distribution [59] and a multiscale TLM-electrical circuit model was used to distinguish nano- and micro-scale interparticle pore

contributions[60]. As to the second approach, Cooper *et al.* developed a series of steady-state ion transport equations in the frequency domain applied to several 2D pore morphologies and pseudo-3D and 3D electrode structures.[61] Kant and Singh proposed a theory that combines the diffuse layer dynamics at the electrode mesoscale, through the Debye-Falkenhagen model of electrical double layer relaxation, and micropores dynamics by employing a TLM.[57] This model was applied to arbitrary shaped mesostructures with embedded heterogeneous micropores. Although they provided valuable insights as to how the EIS profile changes when taking into account more complicated pore size distributions, they all simplify the electrode micro/mesostructure into arbitrary morphologies (in the case of electrical circuit studies they actually do not take into account any electrode morphology) and/or do not explicitly consider all the phases present in a conventional electrode, *i.e.*, the active material, the conductive carbon, the binder and the void between them that is filled with electrolyte. It is worth mentioning that despite its limitations, TLMs have been applied for studying τ and electrolyte ionic resistance within the pores (R_{ion}) in graphite-based anodes,[62–64] LiNiO_2 ,[65] LiFePO_4 [53] and $\text{LiNi}_{1/3}\text{Mn}_{1/3}\text{Co}_{1/3}\text{O}_2$ [53] cathodes.

It is also common to see in literature Newman-type 1D or pseudo-2D physical models to simulate LIB electrode performance, which are based on the homogenization of the active material (AM) and carbon-binder domain (CBD) into one solid phase.[23,66,67] Such homogenization does not allow to investigate how the spatial location of the carbon-binder domain (CBD) and different interfaces affects the overall electrode performance.

In a recent publication we have reported a 4D (3D in space + time) LIB cell physical model which captures the impact of the spatial location of CBD and interfaces on the overall electrochemical performance upon discharge.[68,69] Our model allows to minimize input parameters and geometrical assumptions (by considering explicitly AM, CBD and pore phases) and to carry out very precise studies about the electrode texture.[69]

In the present work an extension of that model is used to investigate EIS features of LIB porous electrodes characterized in a symmetric cell configuration. To the best of our knowledge, the use of multiphase geometries for EIS simulations is introduced for the first time ever. Here, the porous electrode consists of three distinct phases: the NMC active material, the CBD and the void between them, which is filled with the electrolyte. This gives several advantages, namely, the possibility of assigning different physics to each phase and taking into account explicitly the double layer contribution of each one.[70–72] First, we introduce the model main features and assumptions.

Second, a detailed analysis of the EI spectra main features is carried out, by changing the physics of the different phases and comparing with *in house* experimental results. Finally, a general discussion is performed around the limitation of this EIS methodology for the calculation of τ in porous electrodes. We believe that, because of the explicit consideration of the electrode micro/mesostructure, our modeling approach can be used to decrease the gap between modeling and experiment and to help resolving existing controversies in regards of the experimental EIS data interpretation.

2.2. Theory

2.2.1. Electrode structures generation

The workflow for the generation of the 3D-resolved electrode mesostructures has been already presented in following works.[73,74] Briefly, the generation of the electrodes starts by modeling the slurry preparation through a Coarse-Grained Molecular Dynamics (CGMD) simulation. At this stage, beads representing NMC and carbon-binder domain (CBD) particles are randomly placed in the simulation box and then allowed to equilibrate through a MD simulation (NPT ensemble).[73] The force field used to model the particles interactions is derived from a combination of Lennard-Jones and Granular-Hertzian potentials and was parametrized and validated with experimental NMC slurries. The drying step was performed by shrinking through MD simulation (at NPT) the effective CBD particles to a final diameter lower than the one in the slurry state, in order to mimic the loss of the solvent.[75] At the second stage, post-CGMD obtained electrode structures were meshed by using our voxelization algorithm INNOV in MATLAB environment and imported into Comsol Multiphysics 5.4 software (**Figure 1**).[68] The last stage is to apply appropriate material properties and physical models to the 3D multi-phase mesh and to calculate the EI spectra by using the Lithium-Ion Batteries and Transport of Diluted species modules in Comsol Multiphysics.

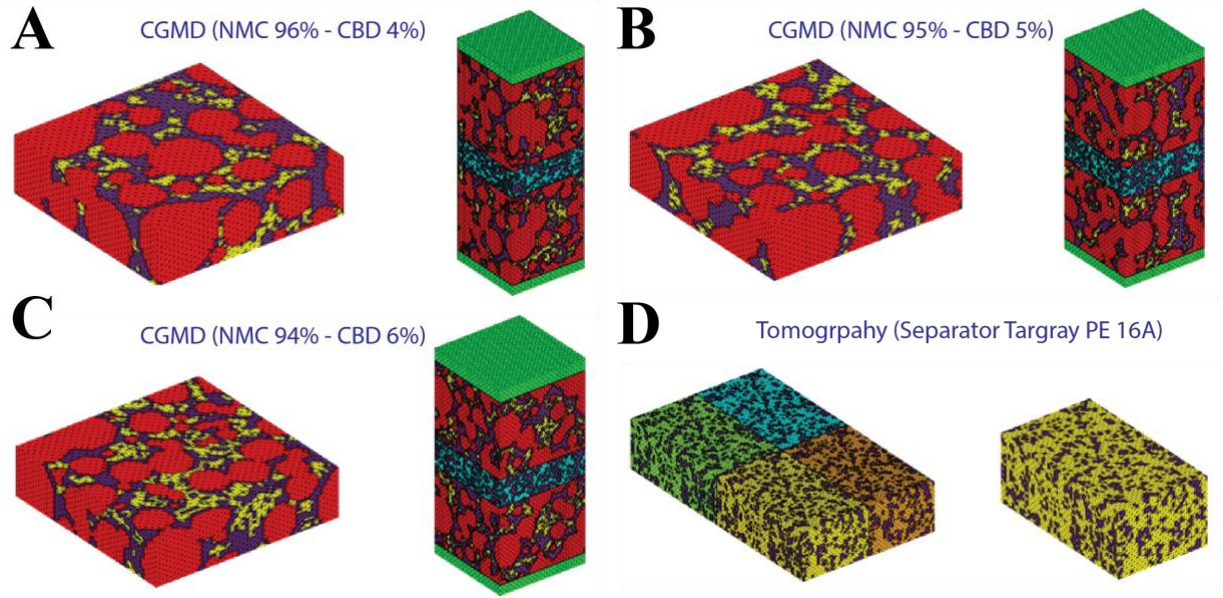


Figure 1. Electrode cut-view (left) and full symmetrical cell (right) for the composition (A) NMC 96% - CBD 4%, (B) NMC 95% - CBD 5%, (C) NMC 94% - CBD 6%, and (D) Tomography separator Targray PE 16A.

2.2.2 Electrochemical model

The imported volumetric multi-phase mesh consists in five sub-domains: NMC and CBD particles, separator, current collector and electrolyte. The full physics behind the 3D EIS model and geometry subdomains are provided in **Figure 2** and **Table 1**.

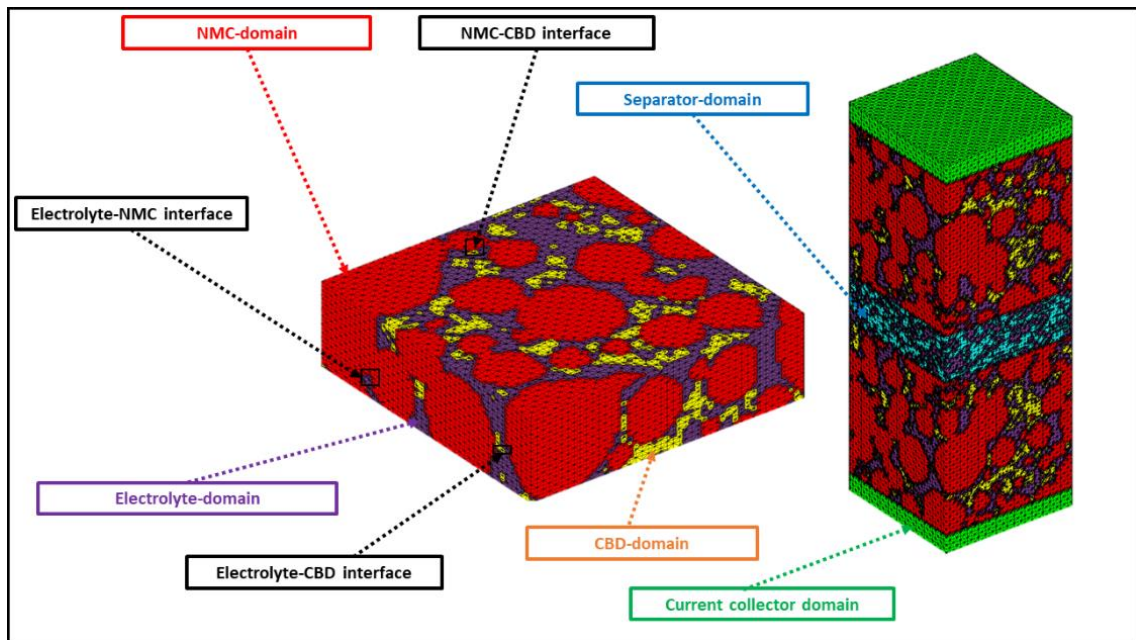


Figure 2. Scheme of the simulated symmetric cell.

Table 1. List of equations for the EIS modeling.

| <i>NMC-domain governing equations</i> | |
|--|--|
| $\nabla(j_{NMC}) = 0$ (Eq. 1) | Bulk electrode current source |
| $-K_{NMC} \cdot \nabla\phi_{NMC} = j_{NMC}$ (Eq. 2) | Ohm's law for electronically conducting matrix |
| <i>Electrolyte-domain governing equations</i> | |
| $\frac{\partial C_{el}}{\partial t} = -\nabla(N_{el})$ (Eq. 3) | Diluted solution binary electrolyte mass transport |
| $\left(-D_i \nabla C_i - \frac{D_i}{RT} F C_i \nabla \phi_{el}\right) = N_i$ (Eq. 4) | Mass transport in electrolyte due to diffusion and migration |
| $\nabla(j_{el}) = 0$ (Eq. 5) | Bulk electrolyte current source |
| $j_{el} = -\sigma_{el} \cdot \nabla\phi_{el}$ (Eq. 6) | Ohm's law for diluted solution binary electrolyte |
| <i>CBD-domain governing equations</i> | |
| $\frac{\partial C_{el}}{\partial t} = -\nabla(N_{el})$ (Eq. 7) | Diluted binary solution electrolyte mass transport in the CBD domain |
| $j_{el} = -\sigma_{el} \cdot \nabla\phi_{el}$ (Eq. 8) | Ohm's law for diluted binary solution of the electrolyte in the CBD |
| $\left(-D_i^{eff} \nabla C_i - \frac{D_i^{eff}}{RT} F C_i \nabla \phi_{el}\right) = N_i$ (Eq. 9) | Mass transport of the electrolyte due to diffusion and migration in the CBD |
| $D_{el}^{eff} = \varepsilon_{el}^{1.5} D_{el}$ (Eq. 10) | Effective Bruggeman diffusion parameter of the electrolyte inside the CBD |
| $\sigma_{el}^{eff} = \varepsilon_{el}^{1.5} \sigma_{el}$ (Eq. 11) | Effective Bruggeman conductivity parameter of the electrolyte inside the CBD |
| $-K_{CBD}^{eff} \cdot \nabla\phi_{CBD} = j_{CBD}$ (Eq. 12) | Ohm's law for solid effective conducting matrix of CBD |

| | |
|---|---|
| $K_{CBD}^{eff} = \varepsilon_{el}^{1.5} K_{CBD}$ (Eq. 13) | Effective Bruggeman solid conductivity parameter of CBD |
| $\nabla(j_{CBD}) = 0$ (Eq. 14) | Bulk CBD solid current source |
| <i>Current collector domain equations</i> | |
| $\nabla(j_{cc}) = 0$ (Eq. 15) | Bulk current collector current source |
| $-K_{cc} \cdot \nabla\phi_{cc} = j_{cc}$ (Eq. 16) | Ohm's law for electronically conducting matrix in the current collector |
| <i>Electrolyte-NMC interface</i> | |
| $-\mathbf{n} \cdot \mathbf{j}_{el} = 0$ (Eq. 17) | No current density flow between NMC and electrolyte phase |
| $-\mathbf{n} \cdot \mathbf{j}_{NMC} = 0$ (Eq. 18) | |
| <i>Electrolyte-CBD interface</i> | |
| $\left(\frac{\partial(\phi_{CBD} - \phi_{el})}{\partial t}\right) \cdot (C_{dl}) = j_{dl}$ (Eq. 19) | Double layer current |
| <i>CBD volumetric double layer</i> | |
| $j_{dl} \cdot A_{dl} = j_{v,dl}$ (Eq. 20) | Total volumetric double layer current |
| <i>Applied perturbation</i> | |
| $\phi_{app} = \Delta\phi e^{-i\omega t} = 10 \text{ mV}$ (Eq. 21) | |
| <i>Electric Ground</i> | |
| $\phi_s = 0$ (Eq. 22) | |
| <i>Formulation of the variables in the frequency domain</i> | |
| $a = a_0 + Re(\tilde{a} \cdot e^{2\pi f \cdot it})$ (Eq. 23) | |

2.2.a. Electrode level

The AM particles consist of a solid matrix, where the Ohm's law is used to describe the electronic conductivity (Eq. 2). Since the AM specific surface area is normally two orders of magnitude lower than the one of carbon additive, the current density coming from the double layer formation comes mainly from the latter. Therefore, it was assumed that the NMC surface in contact with the

electrolyte does not form a double layer (Eqs. 18 and 19). Moreover, and for simplifying the model, no interfacial resistance between AM and CBD was considered.

It is known that conductive carbon black is added to ensure good electrical connection between the current collector and the resistive NMC AM phase.[76,77] Furthermore, being a small and high surface-to-volume ratio material, it contributes to a large extent to the final electrode ε and τ . In our model, the CBD particle is a mixture of solid electronic conductor (with a certain volume fraction) and electrolyte permeable phase in order to mimic the microporosity present in carbon/binder mixtures. On one hand, it is known that the binder allows the transport of ions and swells upon impregnation with the electrolyte.[78]

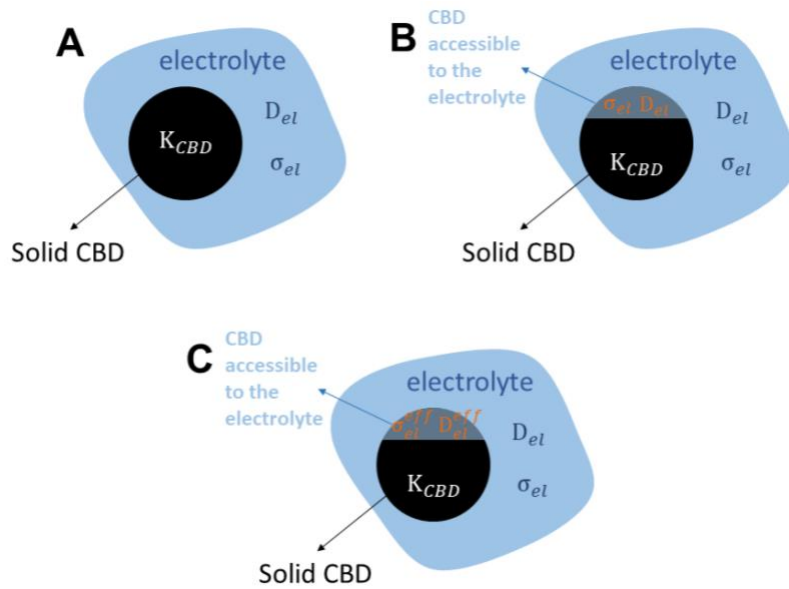


Figure 3. Schemes for the physical treatment of both ionic and electronic conductivity within the CBD phase. (A) 100 % solid CBD with no volume fraction accessible to the electrolyte. (B) CBD phase with 80% of its volume fraction treated as a solid and 20% accessible to the electrolyte. (C) CBD phase with 80% of its volume fraction treated as a solid and 20% accessible to the electrolyte. Its ionic conductivity and diffusion coefficient were corrected using Bruggeman relation.

On the other, the carbon additive particles are normally of ~ 50 nm diameter, generating an interconnected porous hierarchical microstructure within the electrode. In the case of CBD-solid subdomain, modified Ohm's law was used. The electrolyte-permeable subdomain was represented as a phase with 20% of its volume accessible to the electrolyte (Eqs. 10 and 11), with effective σ_{el}^{eff} and D_{el}^{eff} corrected by the Bruggeman relation, and 80% of it as conductive solid (Eq. 13). As mentioned above double layer formation takes place on the surface of CBD so a capacitive double layer current density term was included in the CBD-electrolyte interphase (Eq. 20), assuming its

formation is homogenous. A volumetric double layer was also added to take into account the contribution of the effective microporosity of the CBD phase (Eq. 20).

2.2.b. Separator level

The used Targary PE 16A separator 3D microstructure was taken from open source tomography data.[79] The information about geometry and ϵ of separator are given in Table 2 and the meshed structure is shown in the **Figure 1D**.

2.2.c. Electrolyte level

One of the assumptions of the model is that the electrolyte fills the void between all the solid domains. The electrolyte is non-intercalating in order to avoid faradaic processes, and diluted to keep as small as possible the ratio between the ionic and electronic resistance.[80] Nernst-Planck equations are used to describe ionic transport in the diluted electrolyte (Eqs. 3 and 4).[81,82] It was assumed constant temperature across the cell and no convection taking place. For the electrolyte subdomain within CBD, transport parameters were corrected by using the effective Bruggeman relation (Eqs. 10 and 11).

2.2.d. Current collector level

The current collector consists of a full solid domain, where the Ohm's law for electronically conducting materials is used to describe its properties (Eqs. 15 and 16). In this work no electrode-current collector interface resistance was considered.

2.2.3. Simulation procedure

The EI spectra were calculated in Comsol Multiphysics 5.4 environment, using the Battery Module.[83] The impedance was calculated at 10 frequencies per decade, ranging from 1 to 10^7 Hz. A sinusoidal perturbation of 10 mV was applied and the resulting current output model equations were linearized. By applying a Laplace transformation, the response was expressed in the frequency domain. The EIS 4D heterogeneous model simulations were performed using an Intel® Xeon® E5-2609 CPU @ 1.9 GHz (2 processors) with 32 GB of RAM and Intel® Xeon® E5-4627 Cache @ 3.30 GHz with 264 GB of RAM. Each simulation took approximately between 8 and 20 hours depending on input parameters and the electrode structure. All the cell parameters and constants used for the EIS simulation are listed in Table 2.

For the calculation of τ on simulated electrodes using GeoDict® software.

Electrode tortuosity and tortuosity factor calculations

Electrode tortuosity (τ_{EIS}) values were calculated through EIS data from the graphical method according to Landesfeind *et al* with the following expression:

$$\tau_{EIS} = \frac{R_{ion} A \epsilon k}{2d} \quad (24)$$

where R_{ion} is the ionic resistance within the electrode extracted from impedance data, A is the surface area of the electrode, ϵ is the electrode porosity, k is the bulk ionic conductivity of the electrolyte and d is the thickness of the electrode.[53,84]

The calculation of tortuosity factors (τ_{Factor}) were performed using TauFactor application in MATLAB environment. In this case, an applied concentration gradient was modeled by setting a concentration difference on the two opposing faces of the structure in the direction of the applied concentration gradient. Effective diffusivity of the porous media is a value between 0 and 100 representing the percentage of the diffusivity of the fluid phase. (τ_{Factor}) was defined as:[61]

$$\tau_{Factor}^2 = \frac{Porosity}{Effective\ diffusivity} \quad (25)$$

Table 2. Symmetric cell dimensions and model inputs.

| AM 96% - CBD 4% symmetric cell dimensions | |
|--|--|
| Simulation Box | $99.60 \times 35.3 \times 35.30 \mu\text{m}^3$ (293172 tetrahedrons in mesh) |
| Electrode | $38.8 \times 35.3 \times 35.3 \mu\text{m}^3$ |
| Current collector | $5 \times 35.3 \times 35.30 \mu\text{m}^3$ |
| Separator | $12 \times 35.3 \times 35.3 \mu\text{m}^3$ |
| AM 95% - CBD 5% symmetric cell dimensions | |
| Simulation Box | $92 \times 37.8 \times 37.8 \mu\text{m}^3$ (215607 tetrahedrons in mesh) |
| Electrode | $35 \times 37.8 \times 37.8 \mu\text{m}^3$ |

| | |
|--|---|
| Current collector | $5 \times 37.8 \times 37.8 \mu\text{m}^3$ |
| Separator | $12 \times 37.8 \times 37.8 \mu\text{m}^3$ |
| AM 94% - CBD 6% symmetric cell dimensions | |
| Simulation Box | $121 \times 40 \times 40 \mu\text{m}^3$ (236002 tetrahedrons in mesh) |
| Electrode | $49.5 \times 40.1 \times 40.1 \mu\text{m}^3$ |
| Current collector | $5 \times 40.1 \times 40.1 \mu\text{m}^3$ |
| Separator | $12 \times 40.1 \times 40.1 \mu\text{m}^3$ |
| Electrolyte properties | |
| Concentration | 10 mM |
| Bulk ionic conductivity | $3.749 \times 10^{-2} \text{ S m}^{-1}$ [measured] |
| Diffusion coefficient | $7.5 \times 10^{-11} \text{ m}^2 \text{ s}^{-1}$ [85] |
| NMC properties | |
| Bulk electrical conductivity | $1.06 \times 10^{-3} \text{ S m}^{-1}$ [86] |
| CBD properties | |
| Bulk electrical conductivity | 760 S m^{-1} [87] |
| Surface double layer capacitance | 0.2937 F m^{-2} [83,88] |
| Aluminum current collector properties | |
| Bulk electrical conductivity | $3.774 \times 10^7 \text{ S m}^{-1}$ [89] |
| Separator properties | |
| Porosity | 40% |

2.3. Experimental methodology

LiNi_{1/3}Mn_{1/3}Co_{1/3}O₂ (NMC) was supplied by Umicore. C-ENERGY™ super C65 carbon black was supplied by IMERYYS. Solef™ Polyvinylidene fluoride (PVdF) was purchased from Solvay and N-methylpyrrolidone (NMP) from BASF. Tetrabutylammonium perchlorate (TBAClO₄) was from Alfa Aesar. All the other reagents were battery grade and were used without further purification.

The slurry solid components NMC, C65 and PVdF were premixed with a soft blender. Afterwards, NMP was added until reaching the desired ratio between solvent and solid components. The total mass of solid components was always 65 g. The mixture was performed in a Dispermat CV3-PLUS high-shear mixer for 2 h in a water-bath cooled recipient at 25 °C. The slurry was coated over a 22 μm thick Aluminum current collector using a comma-coater prototype-grade machine. The calendaring of the electrodes was done with a prototype-grade calender. The electrodes analyzed in this work were NMC 96% - C 2% - PVdF 2%, NMC 95% - C 2.5% - PVdF 2.5% and NMC 94% - C 3% - PVdF 3%. The thicknesses and porosities for each electrodes are, respectively, $174.7 \pm 0.9 \mu\text{m}/45 \pm 2\%$, $169 \pm 1 \mu\text{m}/46 \pm 2\%$ and $164 \pm 3 \mu\text{m}/49 \pm 2\%$.

All EIS tests were performed in 2035 coin cells assembled in a dry room ($\text{H}_2\text{O} < 15 \text{ ppm}$). NMC cathodes were punched into 13 mm electrodes and were assembled into the coin cells (both at the positive and negative side) using Celgard 2500 as separator (thickness = 25 μm , porosity = 55%). The electrolyte was a 10 mM TBAClO₄ solution, prepared in a 1:1 wt mixture of ethylenecarbonate:dimethylcarbonate. The EIS were performed with a MTZ-35 impedance analyzer (BioLogic, Seyssinet-Pariset, France) in the range of $10^{-1} - 10^5 \text{ Hz}$ with a potential perturbation of 10 mV. All measurements were carried out at $25 \pm 1 \text{ }^\circ\text{C}$.

2.4. Results and discussion

2.4.1. Parameters influencing on the EI spectrum shape

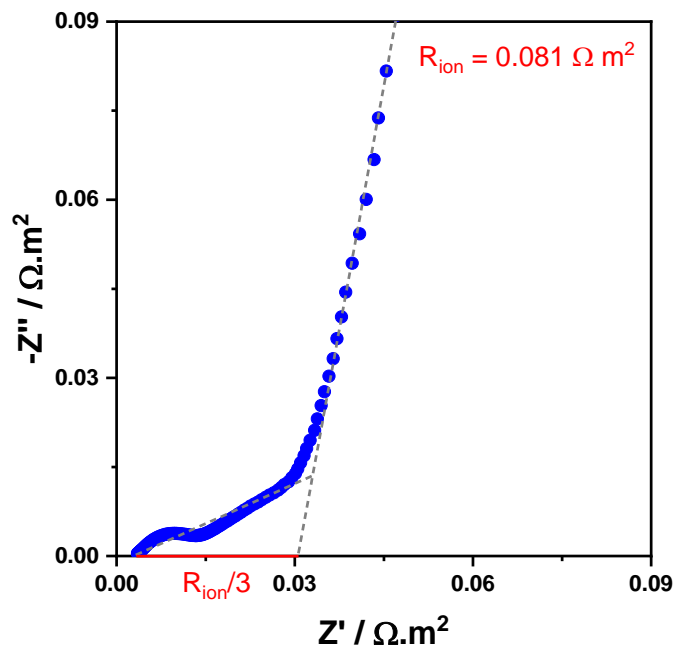


Figure 4. Experimental Nyquist plot for the NMC 96% - C 2% - PVdF 2% electrode. The lines represent the extrapolation towards low and high frequencies with which the graphical method for obtaining the total ionic resistance can be extracted from, according to Landesfeind et al.[53]

The HF intercept on the real axis of the Nyquist plot is generally associated to the resistivity/conductivity of the electrolyte. In the case of our symmetric cell, it corresponds to the resistance of the electrolyte within the separator (R_{sep}), which can be calculated as [62]:

$$R_{sep} = \frac{\ell_{sep}}{\frac{\varepsilon_{sep}}{\tau_{sep}} \sigma_{el}} \quad (26)$$

, where ℓ_{sep} is the separator thickness and ε_{sep} and τ_{sep} are the separator porosity and tortuosity. From the slope of the graph in **Figure 4**, τ_{sep} can be extracted using the data provided in Table 2 for ℓ_{sep} and ε_{sep} . This outputs $\tau_{sep} = 3.81$.

Nyquist and Bode plots for the experimental NMC 96% - C 2% - PVdF 2% electrode are displayed in **Figure 5 A** and **B**, respectively. There are three different regions with characteristic impedance behavior: an almost vertical straight low frequency (<1 Hz), a sloping mid frequency (1-10² Hz) and a curved high frequency (>10³ Hz) region. The low frequency part, which has a phase angle ~ 65° (slope = 77°), corresponds to the double layer formation in the electrolyte-electrode interface. Surface roughness or an inhomogeneous current distribution alter the ideally polarizable behavior of the electrodes, rendering phase angles lower than 90° for capacitive phenomena.[90,91] The second sloping mid-frequencies region has an angle ranging from 25 to 18° (slope = 32°) and is associated to the electrolyte ionic resistance within the porous electrode, as in this frequency zone the penetration length is in the order of the ion diffusion length.[61] Furthermore, since the blocking electrolyte ensures that no faradaic current is flowing during the EI experiment, the high frequency curved EI response cannot be related to charge transfer processes. Nevertheless, TLM predicts a 45° slope and no semi-circle even in the high-frequency limit. The origin of these deviations has been studied in last years by many authors and several hypotheses have been proposed. Among them we can highlight the contact resistance between the electrode and the

current collector,[55,92] the anomalous electronic transport effects in the conductive carbon phase within the porous electrode mesostructure,[93] the homogeneous [59] and heterogeneous [57,94] pore size distribution and the different pore shapes,[61] the hierarchical organization of macro/meso/microporosity,[58,60] and the non-uniform current distribution over the pore section (resulting in smaller virtual pore radii, compared to the real pore dimensions).[95] Here, with the help of our 4D-resolved simulations, we shed light to this issue.

Nyquist and Bode phase plots of the simulated AM 96% - CBD 4% electrode are displayed in **Figure 5 C** and **D**, respectively. By comparing with the experimental Bode phase plot it can be seen that both profiles are very similar in terms of shape, although in simulated spectra the characteristic frequencies are shifted towards higher values. This is due to the fact that all electronic/ionic phenomena within the simulated electrode occurs faster than the experimental one. Furthermore, the mid frequency region (with a 32° slope) is shorter than the experimental one, which is related to the small size of the electrode slab used in the simulation. To reduce the calculation time, we worked with electrode slabs of 38.8 μm, which makes a total cell thickness of 99.6 μm, while the typical thickness of an experimental symmetric cell is around 416 μm. Thinner electrodes means shorter ionic paths for conduction rendering smaller R_{ion} . Experimental EI spectrum for a symmetric cell with a thinner electrode (43 μm) confirms this (**Figure 3**), rendering only a curved response in the mid-to-high frequency region. The low frequency part in the simulated spectra is parallel to the imaginary axis and has ~90° phase angle as the interfaces were treated as ideally polarizable.

Figure 6 A and **B** shows the ionic (electrolyte within the pores and CBD) and electronic (NMC and CBD) contribution to the total impedance of a cross-sectional cut at half the electrode thickness. Panel C depicts the location of CBD, AM and pores phases for reference. The cross-sectional 2D plots for the ionic contribution to the impedance from 10^3 to 10^5 Hz reveal that the impedance on the electrolyte is very low and almost constant while the ionic contribution in the CBD phase increases with the frequency. This is related to the fact that the penetration depth sampled by the alternating signal grows with the frequency and therefore the concentration of the ionic species penetrates deeper into the pores within the phase.[61] In our simulations, the electrolyte transport within CBD pores is modelled with effective diffusion and ionic conductivity coefficients D_{el}^{eff} (Eq. 10) and σ_{el}^{eff} (Eq. 11), respectively. In this sense, the 3D explicit consideration of CBD phase with a different physics than the one adopted for the AM particles

enables a detailed analysis of the electrochemical phenomena, in contrast to all the previously reported models.[66,67,96,97] As stated above, the high-frequency curved region (which can be seen both in the experimental and simulated EI spectra) was linked, among others, to the current collector-electrode contact resistance [53], AM-CBD contact resistance or anomalous electronic transport.[93] Within the formalism of our model there is no contact resistance between the current collector and the electrode and between the AM and CBD phases so these possibilities can be excluded.

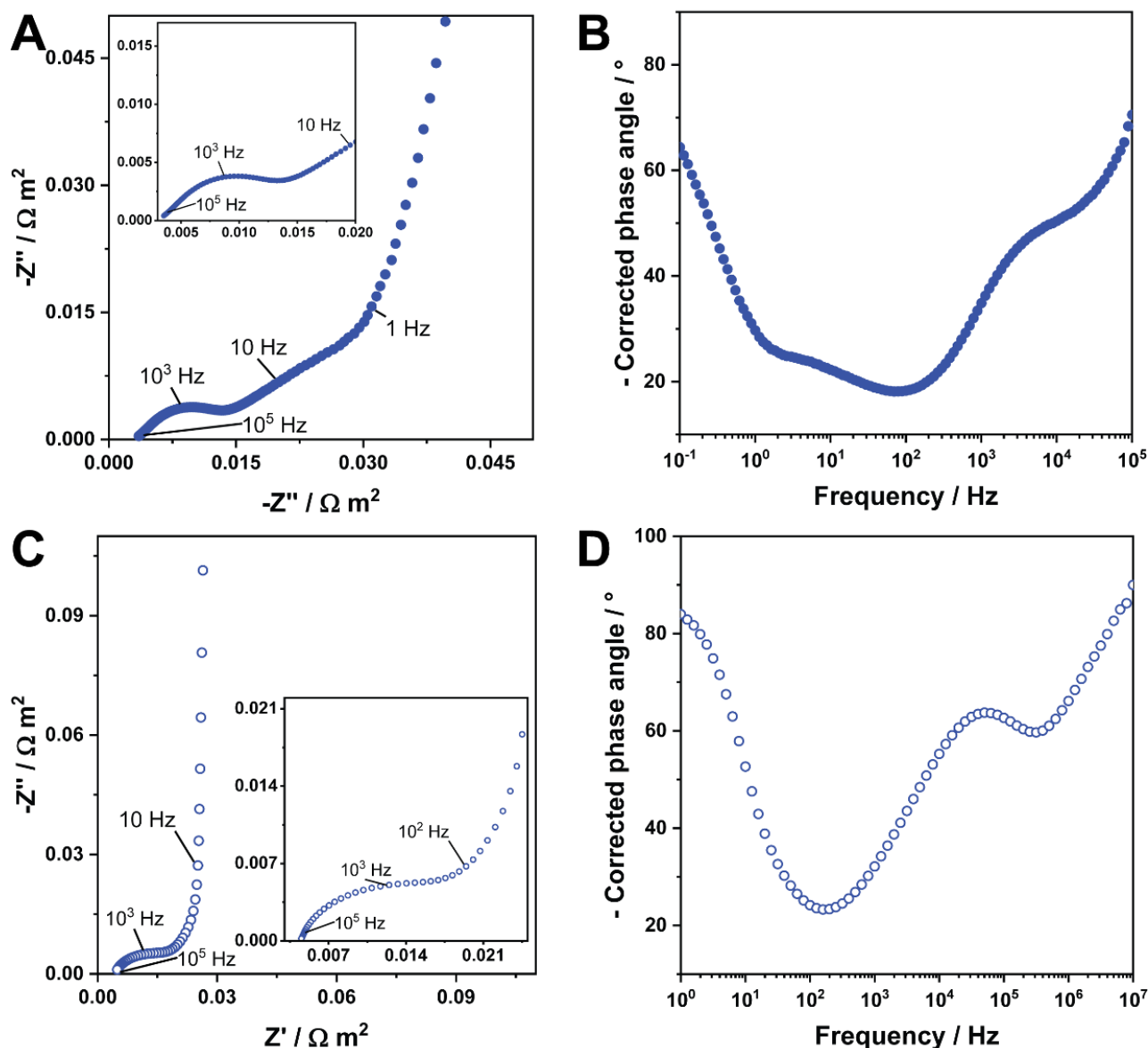


Figure 5. Experimental (A, B) and simulated (C, D) Nyquist (A, C) and Bode (B, D) plots of a NMC 96% - C 2% - PVdF 2% and NMC 96% - CBD 4% symmetric cell, respectively.

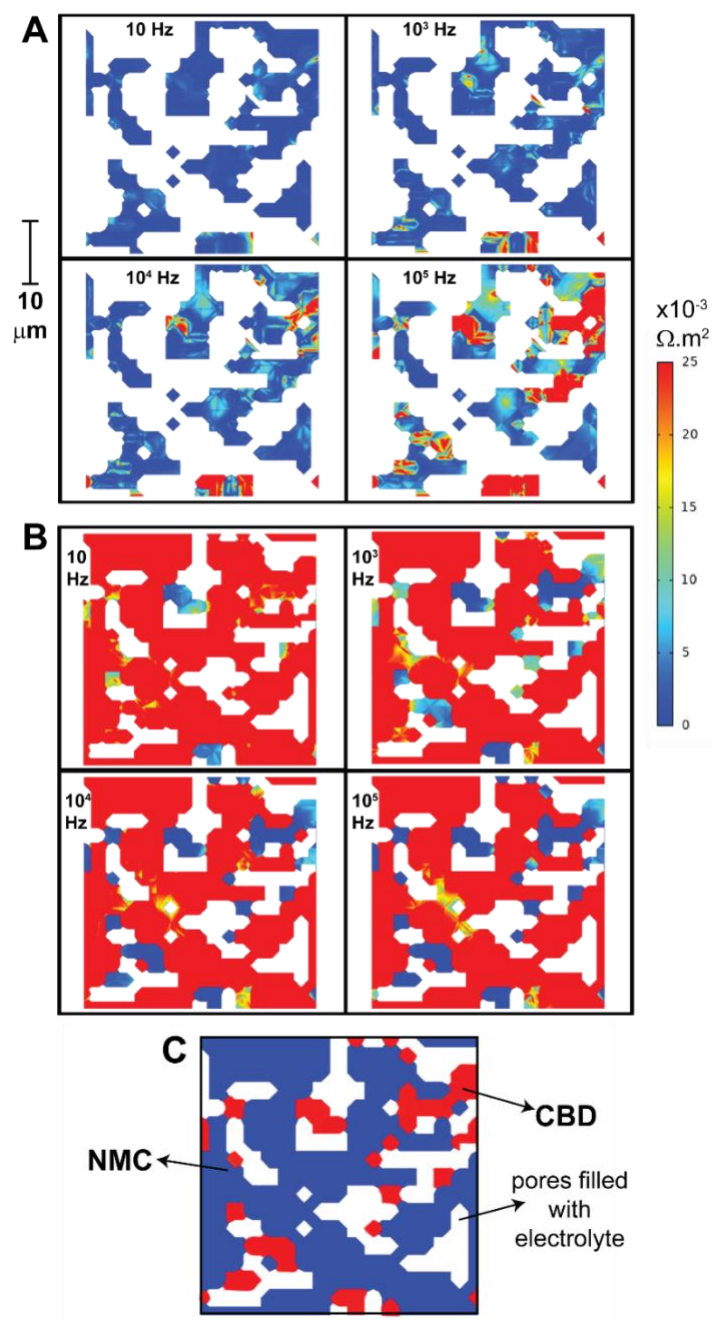


Figure 6. Simulated NMC 96% - CBD 4% electrode cross-sectional impedance 2D plots corresponding to the ionic (A) and electronic (B) contribution to the total measured impedance, at selected frequency values. Note that due to our model formality, impedance on CBD moiety appear in both ionic and electronic 2D plots. (C) Scheme of the cross-section cut, where each phase is explicitly tagged with different colors. The cut-views were done at half the electrode thickness.

2.4.2 Carbon binder domain

To further understand the phenomena associated to the curved high frequency region we focus the analysis on the properties of the CBD phase. Namely, the physics behind CBD phase will be changed in order to understand its impact on the EI spectra. **Figure 7 A** and **B** present the Nyquist and Bode plots, respectively, for the simulated AM 96% - CBD 4% in the cases of 100% solid CBD particles and with 20% of its volume fraction accessible to the electrolyte, with and without the Bruggeman correction of σ_{el} and D_{el} (**Figure 3** displays a scheme of the different physics taken into account, for better comprehension). When considering a 100% solid CBD phase, the high frequency curved region increases its size. In the case of the CBD that can be accessed by the electrolyte and without Bruggeman correction, the high frequency curved region decreases its size and tends to be more straight line-like with a slope equal to 25°. In terms of the total accessible volume to the electrolyte, the 100% solid CBD case has $3.37 \times 10^{-14} \text{ m}^3$ while for the electrolyte-accessible CBD the volume is $3.56 \times 10^{-14} \text{ m}^3$. Therefore, upon reducing the volume accessible to the electrolyte the high-frequency region tends to curve. Moreover, when comparing the 20% inner-porous CBD phase (same accessible electrolyte volume) the effective Bruggeman correction outputs smaller σ_{el}^{eff} and D_{el}^{eff} which in time makes the high frequency region to curve. The 2D ionic contributions to the impedance heat maps of **Figure 4 C** reveal that, for the same frequency (in the range between $10 - 10^5 \text{ Hz}$), the impedance of the electrolyte in the pore regions remains unchanged.

The main changes are seen in the electrolyte within the CBD phase. For the 10^4 and 10^5 Hz 2D plots, the ionic contribution to the impedance is higher for the Bruggeman corrected CBD phase. Summing up, the total volume available for electrolyte impregnation and the influence of porosity on its properties (namely, σ_{el} and D_{el}) are some of the factors that determine the presence of a curved high frequency region. The increase in total accessible volume tends to decrease the size of the curved region. On the contrary, the consideration that CBD inner porosity causes a reduction in electrolyte effective parameters, compared to its bulk σ_{el} and D_{el} , generates the opposite effect. It is generally considered that the effect of the solid phases conductivity on the high to middle frequencies is almost non-existent, especially if a diluted electrolyte is used for the symmetric cell experiments.[84] **Figure 8 A** and **B** depict the Nyquist and Bode plots, respectively, for the simulated AM 96% - CBD 4% with different values of CBD and NMC phases conductivities (K_{CBD}

and K_{NMC} , respectively): 760 and 1.06×10^{-3} , 760 and 1.06×10^{-5} , and 0.076 and $1.06 \times 10^{-3} \text{ S m}^{-1}$. The decrease in K_{NMC} at constant K_{CBD} (green vs. black dotted curves in **Figure 8**) causes the Nyquist plot to curve in the low frequency region while the sloping mid frequency region reduces its size. The decrease of K_{CBD} at constant K_{NMC} (violet vs. black dotted curves in **Figure 8**) makes the high frequency intercept on the real axis to upshift, while the curved region reduces its size and flattens, with a slope of 20° . Furthermore, the characteristic frequency of the curved region downshifts to lower values. All the above indicates that solid phase properties also shape the EI response. The charge balance equations ensure that the ionic current coming from the electrolyte in the pores and CBD is counterbalanced by the electronic charge coming from the CBD and NMC phases. The decrease in their conductivities causes a change in the kinetics of the double layer formation which produces an increase in the frequency. The latter can also be seen in the cross-sectional 2D plots corresponding to the ionic contribution to the total impedance, depicted in panel C of **Figure 8**.

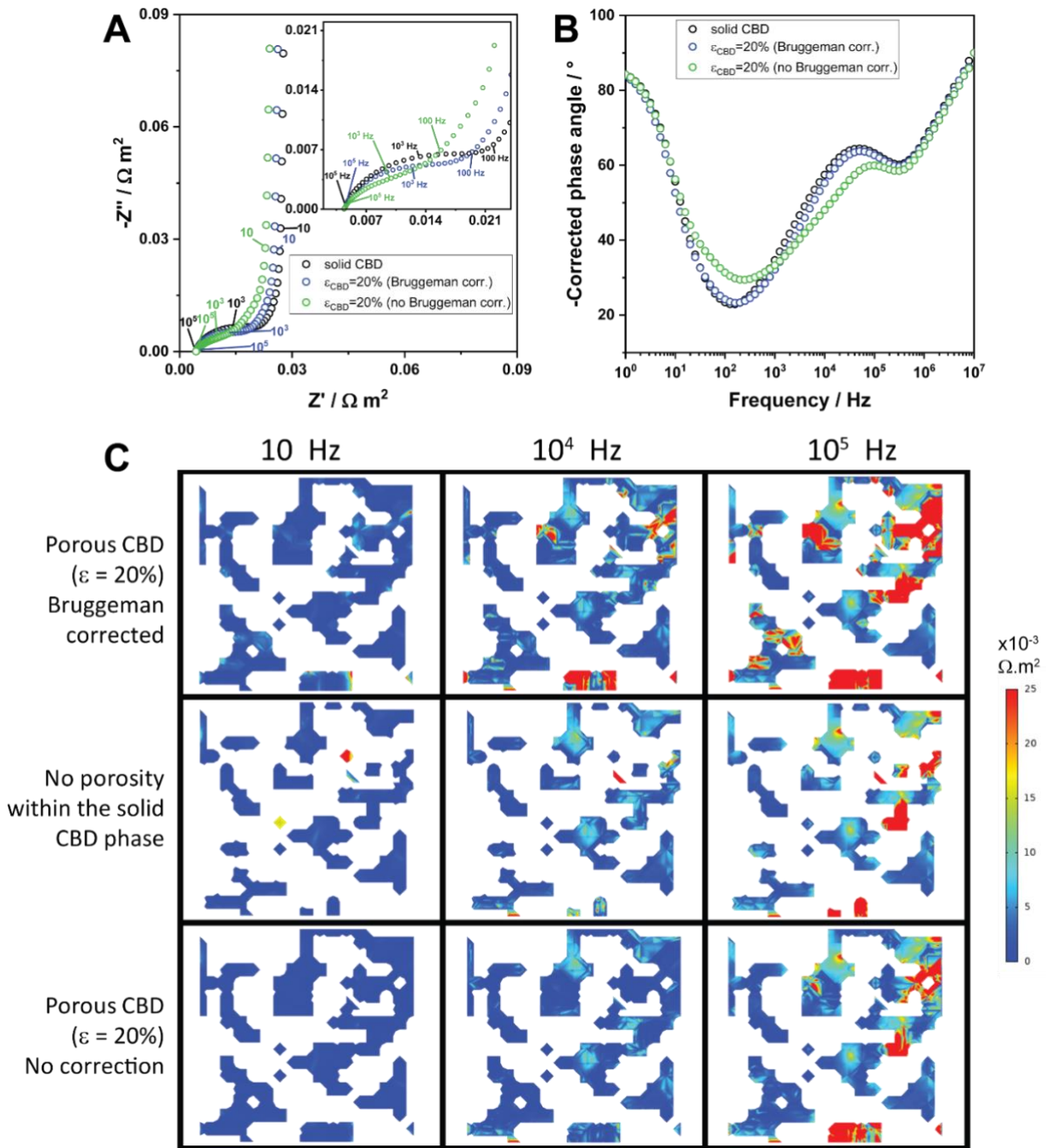


Figure 7. Simulated Nyquist (A) and Bode (B) plots for NMC 96% - CBD 4% symmetric cell, in which CBD is treated as a solid non-porous phase (black circles) and 20% porous CBD with σ_{el} and D_{el} equal to their bulk values (green circles) and with Bruggeman-corrected σ_{el}^{eff} and D_{el}^{eff} . (C) Electrode cross-sectional impedance 2D plots corresponding to the ionic contribution to the total measured impedance, at selected frequency values. The scheme of the cross-section cut is the same as in Figure 6 C.

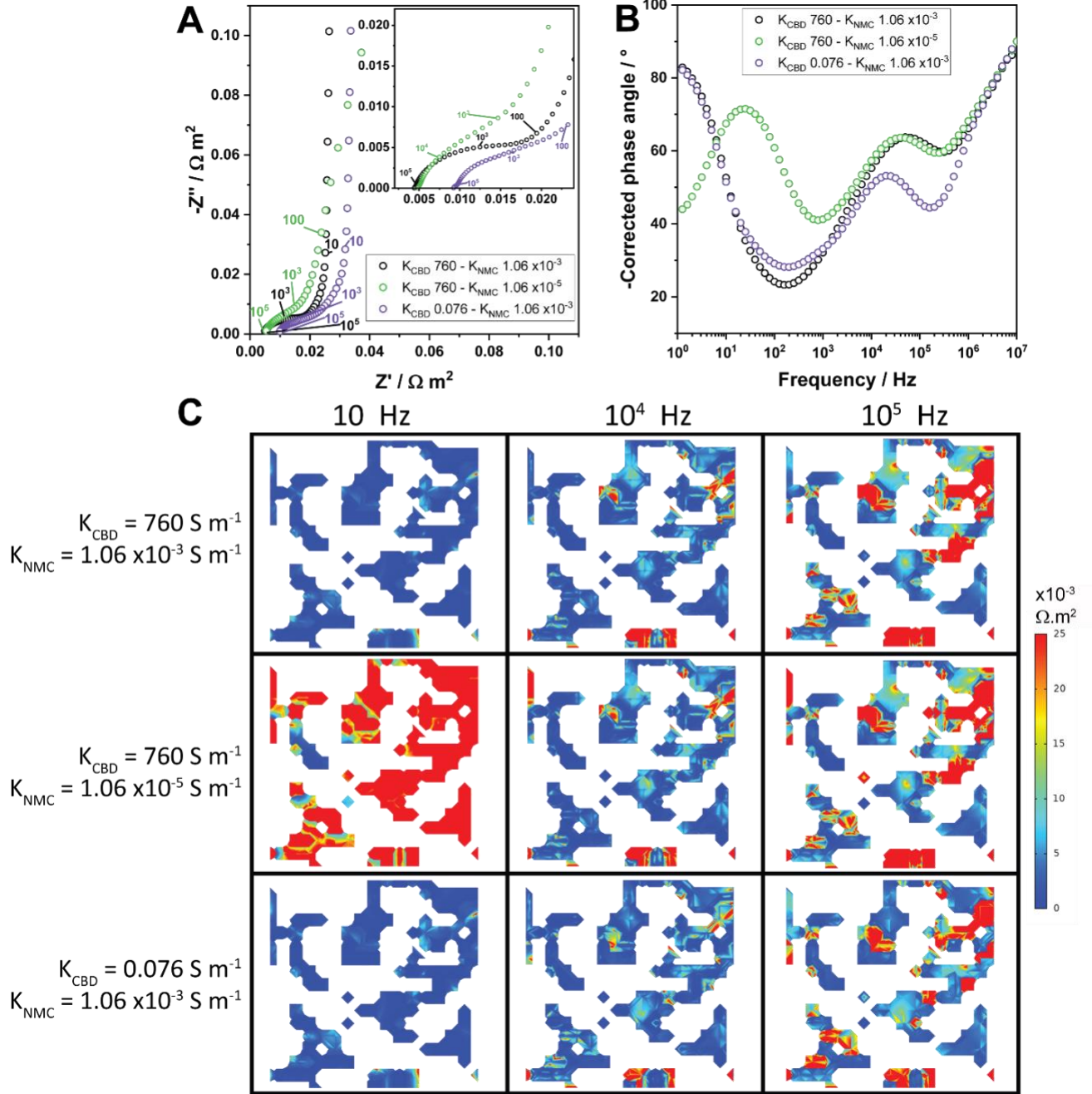


Figure 8. Simulated Nyquist (A) and Bode (B) plots for NMC 96% - CBD 4% symmetric cell, for different conductivities of CBD (K_{CBD}) and NMC phases (K_{NMC}), respectively: 760 and 1.06×10^{-3} (black dots), 760 and 1.06×10^{-5} (green dots), and 0.076 and 1.06×10^{-3} S m⁻¹ (violet dots). (C) Electrode cross-sectional impedance 2D plots corresponding to the ionic contribution to the total measured impedance, at selected frequency values, for each of the EI spectra of panels A and B. The scheme of the cross-section cut is the same as in Figure 6 C.

2.4.3 Ionic conductivity

To compare the influence of electrolyte conductivity on the EI response, simulations were done at various electrolyte concentrations (*i.e.* at different σ_{el}) and are shown in **Figure 5 A and B**. As the electrolyte conductivity decreases from 0.473 S m^{-1} to 4.19×10^{-3} the high-to-mid frequency region evolves to a more curved profile while its characteristic frequency downshifts. Furthermore, the high frequency intercept on the real axis decreases with σ_{el} . This value represents the electrolyte resistance within the separator and has an inversely proportional relation with σ_{el} . [62] In this sense, the tortuosity factor of the separator (τ_{sep}) can be extracted from the slope of a high frequency real axis intercept vs. electrolyte resistance plot (**Figure 10**). In our case, $\tau_{sep} = 3.8$ which is in good agreement with the expected values of tortuosity for commercially available separators. [53,98] The occurrence of the curved region in the high-to-mid frequency region can be interpreted by analyzing the electrode cross-sectional impedance 2D plots corresponding to the ionic contribution to the total measured impedance depicted in panel C of **Figure 9**. At constant frequency, as the concentration of the electrolyte increases, the ionic contribution to the total impedance reduces its value. Furthermore, while at 200 mM ionic contribution remains very low in all the reported frequencies, at 10 mM the main increase at high frequencies comes from the electrolyte within the CBD. When $C_{electrolyte} = 1 \text{ mM}$, and compared to the 10 mM at 10^4 Hz , the ionic contribution comes from the electrolyte in the electrode and not exclusively from the one within the CBD phase, with effective properties lower than the bulk ones.

All the previous analyses performed on the general shape of the simulated EI spectra suggests that the ionic resistance region depends not only on the effective value of the electrolyte conductivity within the porous electrode but also in the characteristic times at which each region of the porous electrode is accessed as a function of the frequency. For the case of NMC cathodes, the low K_{NMC} values makes the system extremely sensitive to the total volume accessible to the electrolyte, K_{CBD} and the impact of CBD microporosity (which in our simulations was modeled through a Bruggeman correction of σ_{el} and D_{el}). Some studies on porous electrodes have pointed out that not all the electrolyte accessible volume can be sampled within the same time frame and the characteristic frequencies will depend upon the distribution of σ_{el}^{eff} and D_{el}^{eff} and the conductivity of the solid phases. [99,100]

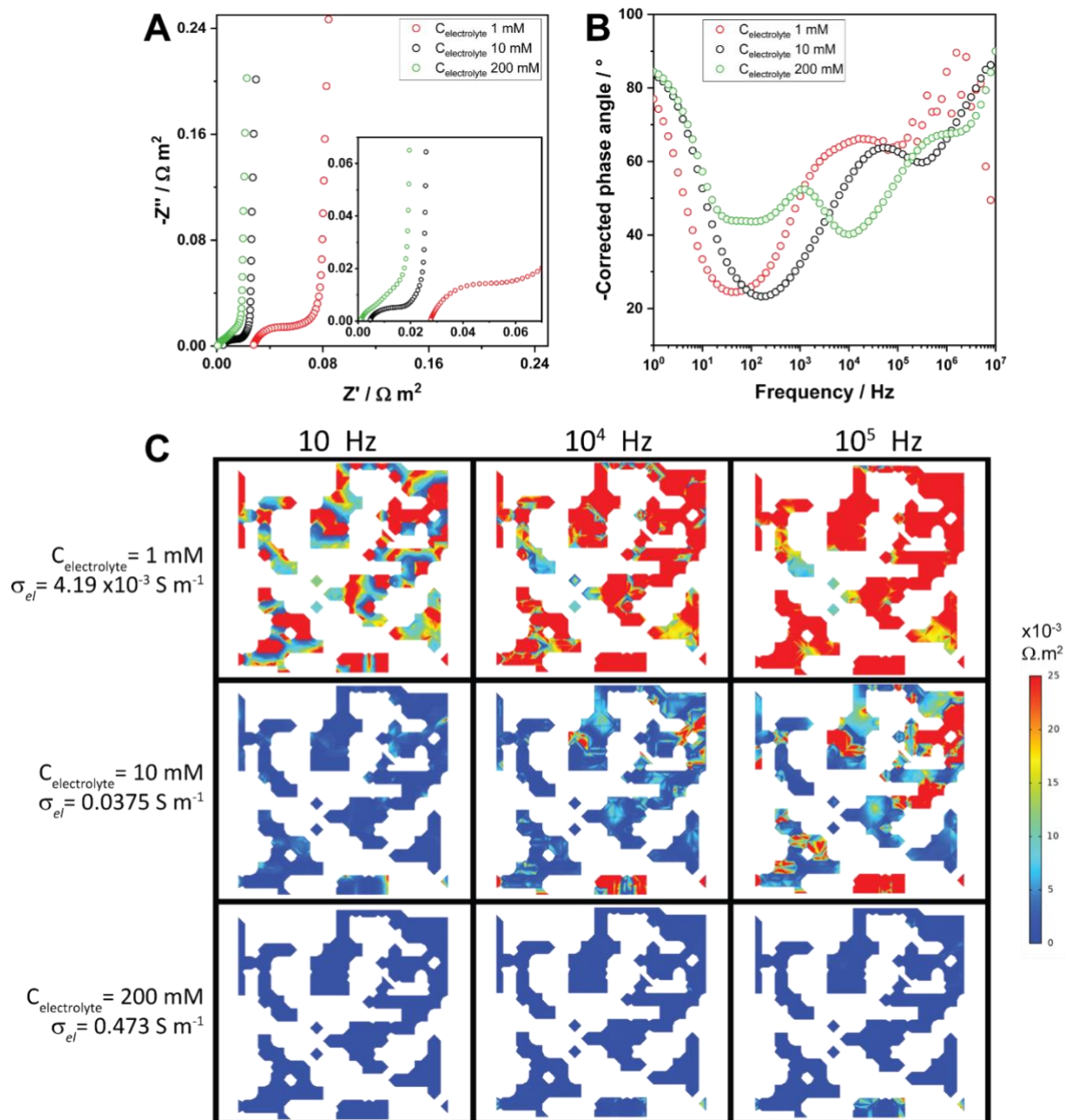


Figure 9. Simulated Nyquist (A) and Bode (B) plots for NMC 96% - CBD 4% symmetric cell, for different TBAClO₄ electrolyte concentrations: 1 mM ($\sigma_{el} = 4.19 \times 10^{-3} \text{ S m}^{-1}$, red dots), 10 mM ($\sigma_{el} = 0.0375 \text{ S m}^{-1}$, black dots) and 200 mM ($\sigma_{el} = 0.473 \text{ S m}^{-1}$, green dots). (C) Electrode cross-sectional impedance 2D plots corresponding to the ionic contribution to the total measured impedance, at selected frequency values, for each of the EI spectra of panels A and B. The scheme of the cross-section cut is the same as in Figure 6 C.

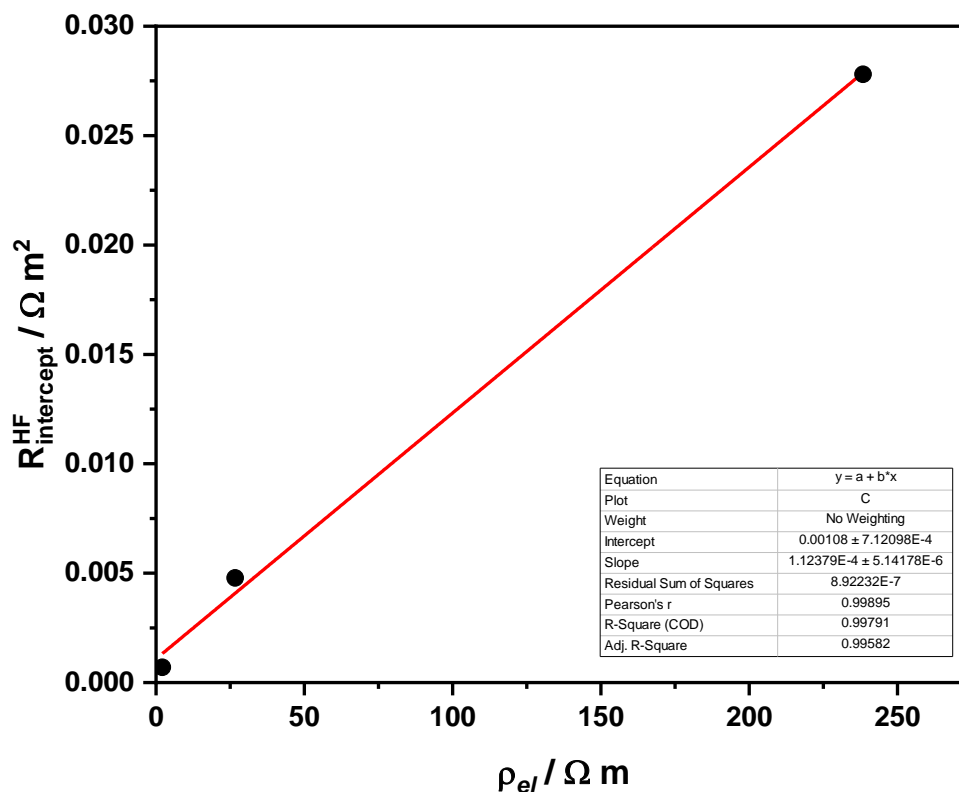


Figure 10. Intercept on the real axis Z' at high frequency ($R_{\text{intercept}}^{\text{HF}}$) as a function of the resistivity of the electrolyte ($\rho_{\text{el}} = 1/\sigma_{\text{el}}$), taken from the Nyquist plots from **Figure 8**. The red line represents the linear fitting performed to the data.

The diffusion rates of ions into and within the different electrode moieties with different effective parameters will vary with the frequency, which directly impacts the response times of the double layers established on the surface of the pores.

Figure 11 presents a summary of the found contributions of each parameter to the EI spectra of symmetric cell NMC cathodes. Our time resolved 3D electrochemical model with explicit consideration of AM and CBD phases allows to analyze in a systematic way the impact of each phase properties on the EI spectrum features. The versatility of it resides in the fact that no assumptions were made on the conductivity of the solid phase (unlike the reported works with equivalent electric circuits) and the possibility of considering different ion/electric transport regimes in the different electrode phases (as opposed to the Newman time-resolved simulations with homogenization of the solid phase).

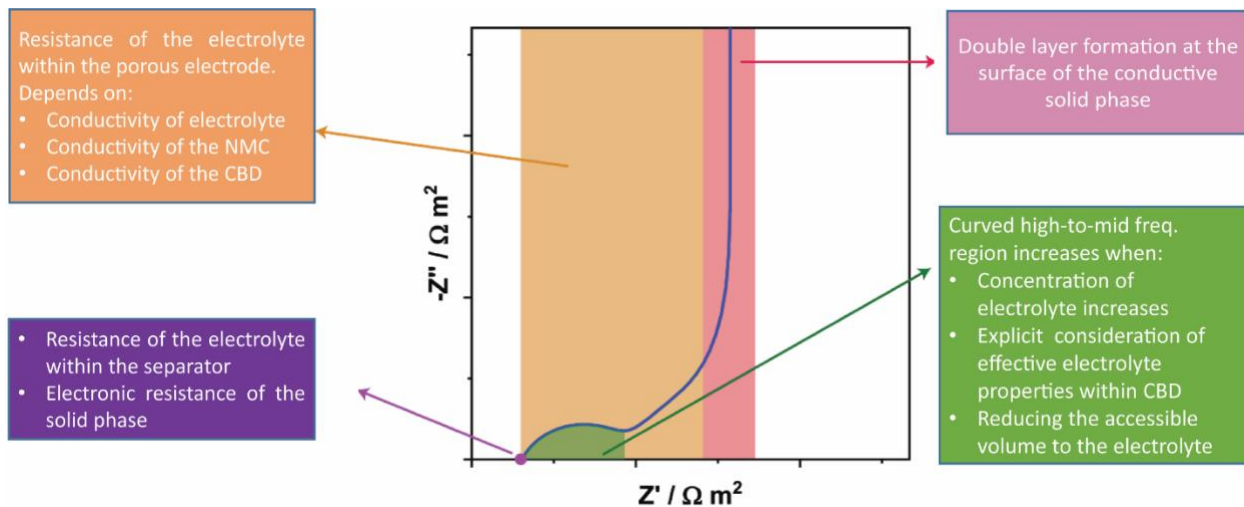


Figure 11. Schematic Nyquist plot showing the contribution of the electrolyte and solid phases parameters on the different regions of the EI spectrum.

2.4.4. Effect of calendaring

Figure 12A shows that by increasing the applied calender pressure the high frequency intercept shifts to lower values, indicating lower electronic resistance of the solid phase.[101] Additionally, the low-frequency region shows an ideal 90° behavior because the CBD/electrolyte interface was treated in the model as ideally polarizable, with constant double-layer capacitance. The length of the mid-frequency sloping region increases by increasing the calendaring pressure, indicating an increase of the effective electrolyte ionic resistance upon calendaring.[53,101,102] The latter is directly linked to the decrease in the electrode porosity and pores size distribution, which slows down the migration and diffusion rate of ions within pores.[101] Moreover, the length of this region is directly linked to the EIS tortuosity factor (τ_{EIS}), whose calculated values (Table 3) are in agreement with the ones obtained through GeoDict diffusivity methodology. **Figure 12B** displays the ionic contribution to the overall impedance of a cross-sectional cut at half the electrode thickness at 100 Hz. Within our models formality, CBD has 47% of inner porosity treated as a region permeable to the electrolyte diffusion. The effective ionic diffusion coefficient is corrected through a Bruggeman relation. Therefore, in the 2D plots of **Figure 12B**, the ionic contribution comes from the electrolyte within the pores and the accessible region within the CBD phase. In this sense, as the contact between the CBD particles increases and the porosity decreases upon calendaring, the ionic contribution to the total impedance grows.

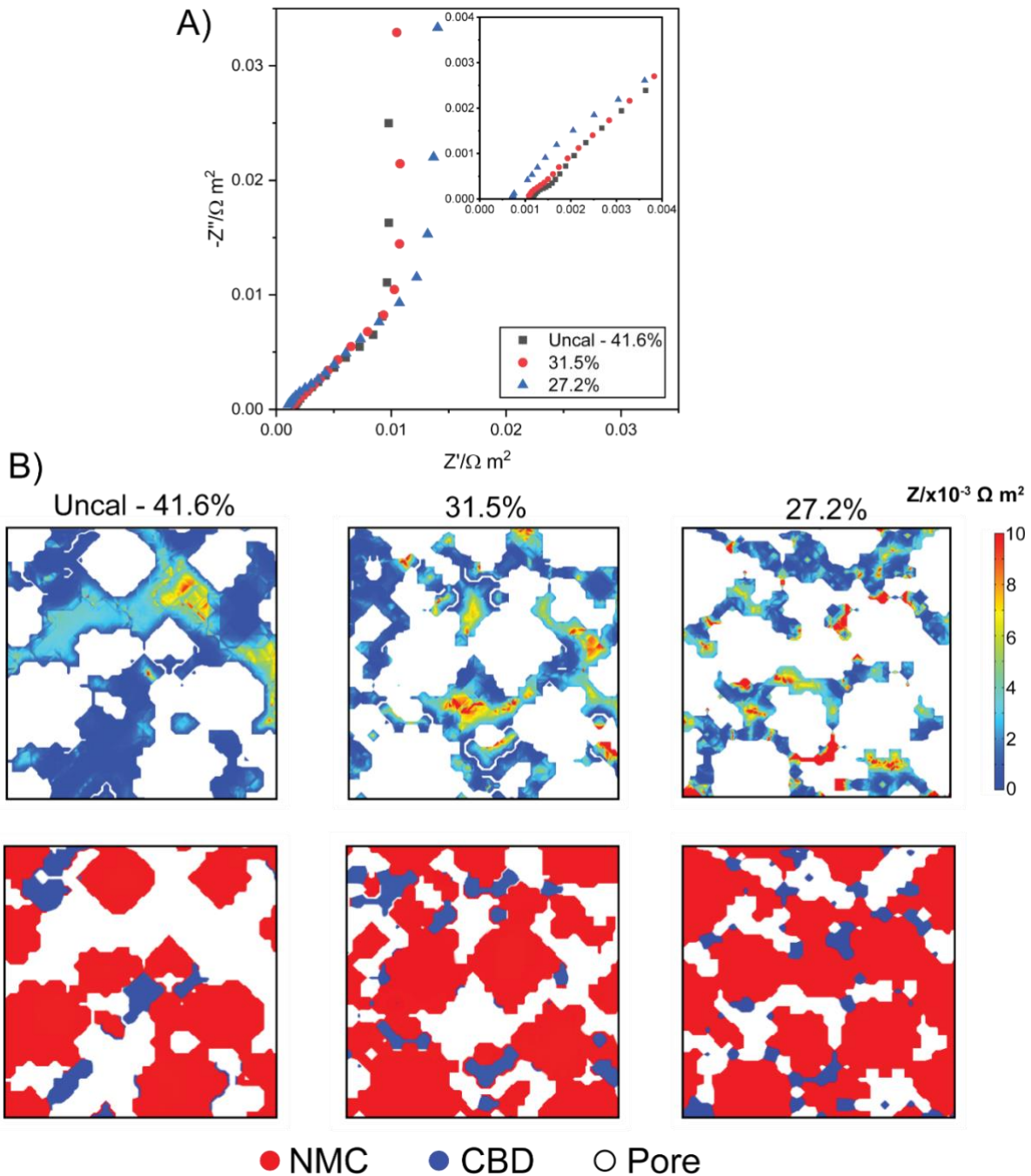


Figure 12. (A) Simulated Nyquist plots for un-calendered and calendered electrodes in symmetric cell configuration. (B) (Top row) Electrode cross-sectional impedance 2D plots corresponding to the ionic contribution to the total measured impedance at half the electrode thickness at 100 Hz. (Lower row) Scheme reporting the distribution of AM, CBDs and pore phases

Table 3. Ionic resistances (R_{ion}) of the electrolyte within the porous electrode and associated tortuosity factors (τ_{EIS}) Eq. (25) calculated according to the Transmission Line Model proposed by Landesfeind *et al.*[53]

| | R_{ion} ($\Omega \text{ m}^2$) ^a | τ_{EIS} ^b |
|-------------|---|---------------------------|
| Uncal-41.6% | 0.02595 | 1.3676 |
| 31.5% | 0.02913 | 1.3808 |
| 27.2% | 0.04014 | 1.7527 |

^aObtained from the graphical interpolation of the high-to-mid frequency region on the EI spectra.

^b EIS-derived tortuosity obtained through the graphical method according to Landesfeind *et al.*[53]

2.4.5. Effect of AM amount and tortuosity factor calculations

Figure 12 presents the experimental (A, B) and simulated (C, D) Nyquist and Bode spectra for symmetric cells with different AM/CBD compositions: NMC 96% (black dots), NMC 95% (red dots) and NMC 94% (blue dots). Regardless the fact that the simulated spectra do not exactly reproduce the experimental spectra, as simulated symmetric cells are thinner than the experimental ones, the main features resemble and the trends as a function of the electrode composition are maintained. In both the experimental and simulated EI response it can be seen that the sloping and curved mid-to-high frequency parts reduce their size and the frequencies of the different phenomena upshift when going from NMC 96% to NMC 94% electrodes. Furthermore, the cross-sectional views of the three different NMC composition electrode for the ionic contribution to the total impedance (**Figure 7**) show that as the frequency increases, the impedance is higher for the electrolyte inside the porous CBD phase.

Table 4 shows that the volume fraction accessible to the electrolyte increases with the amount of CBD in the electrodes. As shown in **Figure 11**, the reduction in the curved high frequency region is related to the increase in the accessible volume for the electrolyte. Furthermore, when comparing NMC 96% - 95% high frequency intercept on the real axis to the one in NMC 94% electrode the drastic reduction in this value is due to the higher amount of conductive CBD phase which also causes an upshift in the frequency of the processes (Bode plot of **Figure 13 D**). However, the increase in the CBD amount would also increase the ionic impedance contribution due to higher contributions of the lower effective values σ_{el}^{eff} and D_{el}^{eff} , as seen in the second column of Table

5. We determined above that the fact of performing a Bruggeman correction to the electrolyte properties within the CBD phase causes an increase in the curved high frequency region. In this case, we see the opposite behavior when decreasing the amount of NMC in the simulated electrode because the effect that dominates is the increase in the electrode conductivity as a consequence of the higher amount of CBD conducting phase.

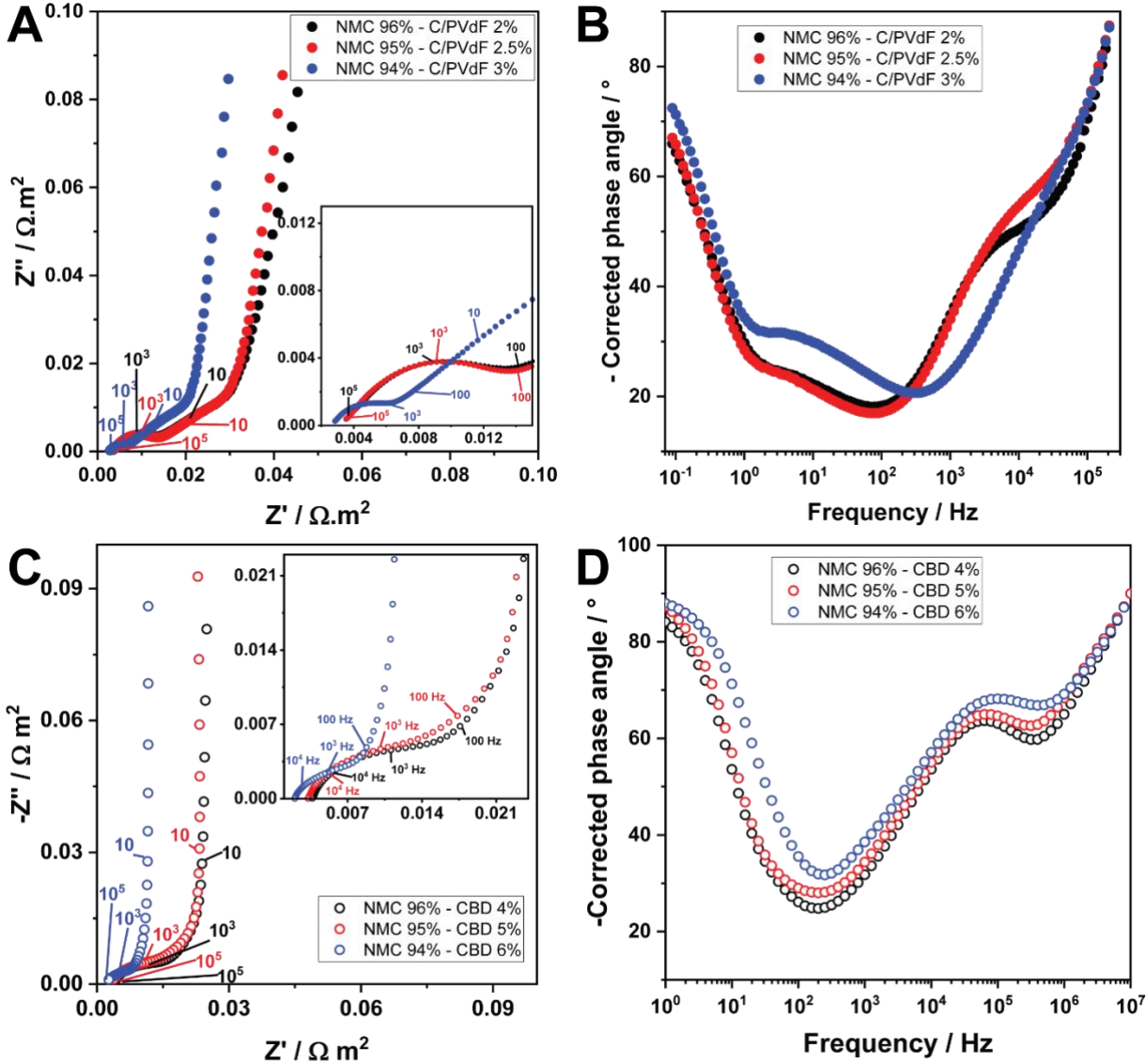


Figure 13. Experimental (A, B) and simulated (C, D) Nyquist (A, C) and Bode (B, D) plots of a NMC 96% - C 2% - PVdF 2% / NMC 96% - CBD 4% (black dots), NMC 95% - C 2.5% - PVdF 2.5% / NMC 95% - CBD 5% (red dots) and NMC 94% - C 3% - PVdF 3% / NMC 94% - CBD 6% (blue dots) symmetric cell, respectively.

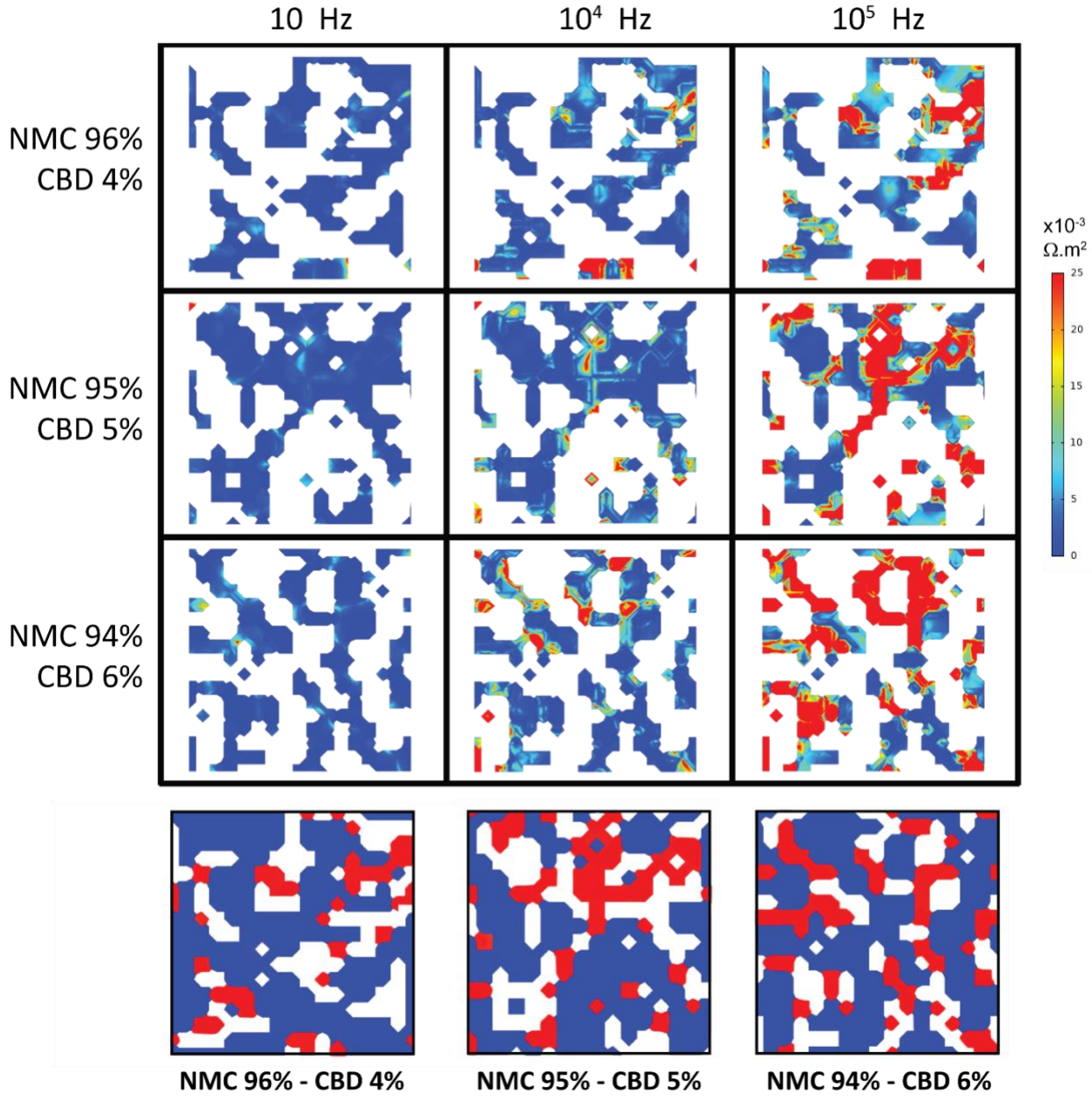


Figure 14. Electrode cross-sectional impedance 2D plots corresponding to the ionic contribution to the total measured impedance, at selected frequency values for the NMC 96% - CBD 4%, NMC 95% - CBD 5% AND NMC 94% - CBD 6% electrodes. The schemes of the cross-section cut, where each phase is explicitly tagged with different colors, are shown in the lower part of the figure. The cut-views were done at half the electrode thickness.

Table 4. Selected geometric features of the simulated electrodes at the three NMC compositions.

| Composition | Percentage of electrolyte volume within the CBD phase(%) ^a | Volume fraction accessible to the electrolyte(%) ^b | τ_{diff} ^c |
|------------------|---|---|----------------------------|
| NMC 96% - CBD 4% | 5.3 | 34.0 | 1.54 |
| NMC 95% - CBD 5% | 6.3 | 34.7 | 1.60 |
| NMC 94% - CBD 6% | 7.1 | 36.3 | 1.61 |

^a Calculated as the ratio between the CBD volume accessible to the electrolyte and the total volume of the electrode. ^b Calculated as the ratio between the total volume accessible to the electrolyte (CBD + pores) and the total volume of the electrode. ^c Calculated with GeoDict[®].

Table 5. Solid phase electronic conductivities ($\sigma_{electronic}$), ionic resistances (R_{ion}) of the electrolyte within the electrode pores, $R_{ion}/R_{electronic}$ Eq. (26) ratios and tortuosities (τ_{EIS}) Eq. (25) calculated according to Landesfeind *et al.*[53].

| Composition | $\sigma_{electronic}/S\ m^{-1}$ ^a | $R_{ion}/\Omega\ m^2$ ^b | $R_{ion}/R_{electronic}$ ^c | τ_{EIS} ^d |
|-----------------------|--|------------------------------------|---------------------------------------|---------------------------|
| NMC 96% - C/PVdF 2% | 0.261 | 0.0815 | 60 | 3.93 |
| NMC 95% - C/PVdF 2.5% | 0.521 | 0.0799 | 127 | 4.08 |
| NMC 94% - C/PVdF 3% | 0.785 | 0.0512 | 122 | 2.87 |

^a Measured. ^b Obtained from the graphical interpolation of the high-to-mid frequency region on the experimental EI spectra (**Figure 13**). ^c $R_{electronic}$ was obtained as $\ell/\sigma_{electronic}$, where ℓ is the electrode thickness. ^d EIS-derived tortuosity factor was obtained through the graphical method according to Landesfeind *et al.*[53]

The fact that the mid-to-high frequency region is due only to ionic transport within the porous medium comes from the assumption that electrolyte ionic resistance is at least two orders of magnitude higher than solid electrode electronic resistance. Recently, Landesfeind *et al.*[84] pointed out that if this condition is not met, then both of the conducting phenomena will play a role in the total resistance measured by impedance. To corroborate this condition, $\sigma_{electronic}$ of the experimental NMC electrodes soaked with the 10 mM TBAClO₄ electrolyte were measured. Table 4 presents these values for the three experimental NMC electrodes, along with the ionic resistances

(calculated by the graphical method proposed by Landesfeind *et al.* using EI data [53]). The calculated $R_{\text{ion}}/R_{\text{electronic}}$ show that for the NMC 96% electrode the ratio is smaller than 100 which would imply that the effective electrolyte conductivity cannot be derived from the EI spectra. Furthermore, and although for NMC 95% and 94% this condition is met, the appearance of the curved high-to-mid frequency feature and the fact that the mid frequency part has a slope of 34° points out that the TLM cannot be used to calculate the tortuosity factors as the conditions for applying it are not met. Once again, the complex interplay between the pore size distribution (and its impact in the electrolyte effective parameters) and the different conductivities for the solid phase generates a distribution in the frequencies at which the ionic resistance of the electrolyte is sampled. Furthermore, the calculated values of τ_{EIS} do not follow a clear trend when increasing the amount of conductive carbon and binder. It is expected that τ should increase when going from NMC 96% to NMC 94% as a result of: (i) adding more conductive carbon and the consequent increase in the electrode microporosity; and (ii) adding more binder, which would generate thicker layers of polymer over the solid particles.[53,63,64,103]

To fully compare the τ coming from EI experiments with the ones calculated from the diffusivity (using DiffuDict[®] module of GeoDict[®] software on the simulated electrode structures), EI simulations were performed on thicker NMC 96% - CBD 4% cathodes. The Nyquist plot (**Figure 12**) shows that for a 148.7 μm thick electrode the sloping mid frequency region dominates the high-to-mid frequency region (with a slope of 45°). Nevertheless, at very high frequencies the EI spectra features a curved region as in the previous thinner simulated electrodes. The comparison with the same electrode but considering a fully solid CBD (no permeability to the electrolyte) shows that in thicker electrodes the mid-to-high curved region now represents a smaller part of the Nyquist plot. For this electrode, the τ_{EIS} coming from the graphic interpolation of the impedance spectrum outputs a value of 12.5 while the τ_{diff} derived from GeoDict[®] software is 1.79. A straightforward way to validate if each methodology captures correctly the τ is to compare these values with an electrode which has been calendered. In this case, the application of a pressure generates a reduction in the pore size/porosity and an increase in the contacts between the conducting particles [103–105] which normally is associated with an increase in τ . For the calendered simulated NMC 96% - CBD 4% cathode (**Figure 12**) $\tau_{\text{EIS}} = 4.6$ while $\tau_{\text{diff}} = 1.84$. The τ_{diff} shows the expected trend whereas τ_{EIS} does not. Note also that τ_{diff} successfully disclosed the rise in the tortuosity for the

electrodes with increasing amount of CBD (fourth column of Table 3 for the simulated electrodes NMC 96%, NMC 95% and NMC 94%). As a general remark, it is expected that τ_{diff} outputs lower tortuosity factors than the EIS-based method, as it does not take into account the inner CBD porosity.

All the above points out the complexity of the phenomena that determines the impedance response of electrode pores filled with a diluted, non-intercalating electrolyte. The approximation that the electrolyte effective ionic conductivity can be derived from the mid-to-high frequency region works only if one effective parameter comes out of the measured response. Our physical model for the calculation of EI spectra in three-phase simulated electrodes enabled to understand that the physics that explains the observed response is not as simple as a decrease in the electrolyte effective properties. This comes from the fact that NMC phase is a poor electronic conductor that represents 60%, 57% and 53% of the electrodes total volume for NMC 96%, 95% and 94%, respectively. In this sense, the electron conduction takes place mainly at the CBD phase, which in time has inner porosity that constraints the electrolyte effective properties. Furthermore, the TLM model assumes no limitations on the solid electronic conductivity, while it is known that conductivity in porous media depends on the percolation and spatial distribution of the conductive particles.[106] Therefore, this kind of systems are quite sensitive to the spatial location of the CBD phase and the degree at which the latter affects the electrolyte properties. It is not surprising then that the reported electrodes at which EIS methodology was used to derive the electrode tortuosity factor are mainly graphite-based anodes.[53,62–64] In the latter, both the carbon additive and the AM are good electronic conductors so there are no limitations on the solid phase side in terms of the electronic conductivity.

As it has been discussed in Cooper *et al.* work [107], there is still much debate around the best way to acquire a representative τ value for porous electrodes. In this work we discussed EIS-based technique but the most widely used methodologies, such as geometric- and diffusivity-derived, lack of information regarding to microporosity (as they rely on tomography results for the calculation) and they are highly anisotropic (meaning that they can measure τ either in the x, y or z direction of the electrode structure).[103]

2.5. Conclusions

In this chapter, a 4D (3D in space + time) physical model was successfully used to simulate and analyze EI spectra of symmetric cells based on simulated NMC cathodes for the evaluation of their tortuosity. The results were compared and validated with experimental *in house* EI spectra acquired on real NMC cathodes. The electrochemical 4D model explicitly considers the three electrode phases (*i.e.* AM and CBD particles and the pores filled with electrolyte) along with distinctive physics for the electron and ion conduction within them.

In the first part of the work the general features of the EI were discussed: **Figure 6** provides a good summary of them. It was found that, unlike TLM used for the interpretation of spectra, the high-to-mid frequency region deviated from a 45° slope and a curved region at high frequency appears, both in simulated and experimental cases. The possibility of analyzing each variable at a time enabled to conclude that these deviations from the “ideal TLM” features are related to the characteristic times at which each region of the porous electrode is accessed as a function of the frequency. The fact that our model considers a Bruggeman-corrected ion diffusion/conduction of electrolyte within the porous CBD phase and different electronic conductivities for AM and CBD, proved to be a successful strategy for the interpretation of EI spectra in symmetric cells.

In the second part, the main limitations for the calculation of NMC-based cathodes τ from symmetric cell-EI experiments were analyzed. The comparison of electrodes with different NMC/CBD compositions both simulated and experimental revealed that τ_{EIS} , which comes from the electrolyte effective ionic conductivity, output values and trends which are not the expected ones. Although all the methodologies for the τ calculation have their limitations and assumptions, for the case of porous electrodes in which the AM is not a good electronic conductor, EI-symmetric cell may output erroneous results. Nonetheless, our 4D explicit model helped to understand this matter as we could compare τ values coming from two independent methodologies for the same electrode structure.

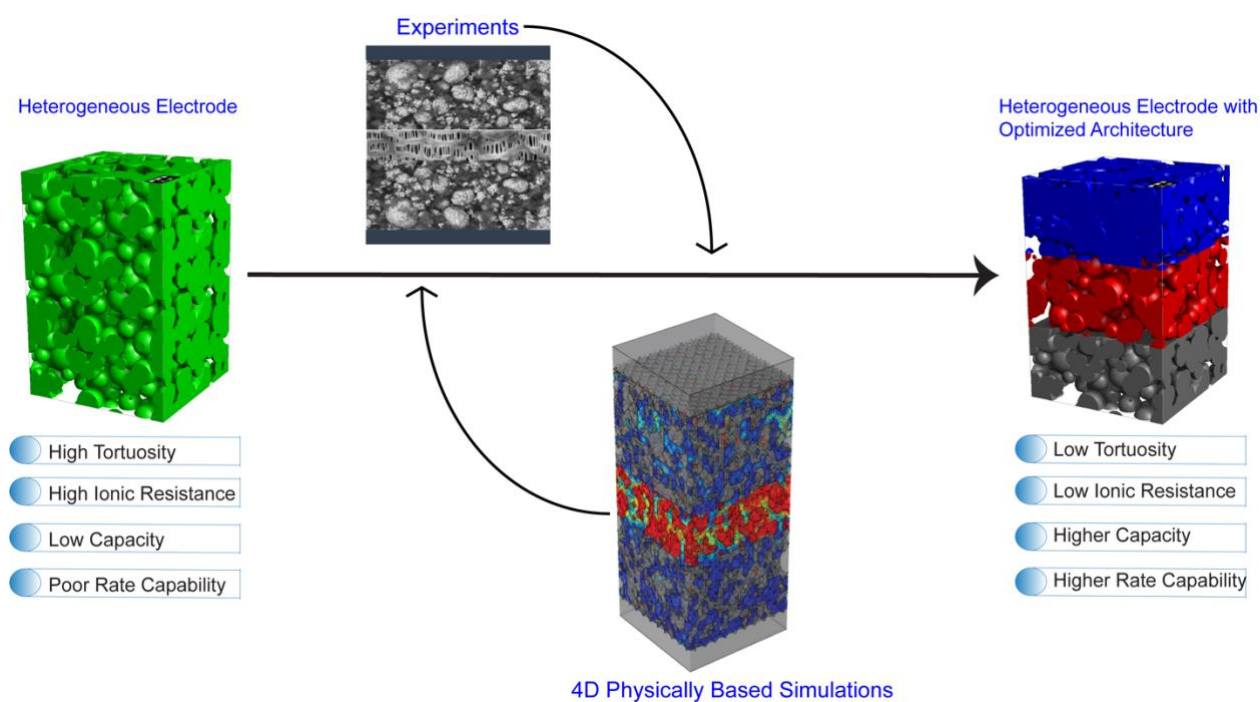
Nomenclatures

| | |
|------------------|--|
| EIS | Electrochemical impedance spectroscopy |
| NMC | $\text{Li}(\text{Ni}_{1/3}\text{Mn}_{1/3}\text{Co}_{1/3})\text{O}_2$ |
| PVdF | Polyvinylidene fluoride |
| C | Carbon black |
| CBD | Carbon-binder domain |
| AM | Active material |
| CGMD | Coarse-grained molecular dynamics |
| MD | Molecular dynamics |
| ε | Porosity |
| τ | Tortuosity factor |
| N_M | MacMullin number |
| <i>eff</i> | Effective value |
| TLM | Transmission line model |
| R_{ion} | Ionic resistance |
| A_{dl} | Double layer area |
| j_{dl} | Double layer current density |
| <i>a</i> | Variable |
| N | Flux density |

| | |
|--------------------|--|
| a_0 | Variables solution for the average field |
| n | Normal vector |
| C_{el} | Electrolyte concentration |
| R | Universal gas constant |
| C_{dl} | Double layer capacitance |
| T | Temperature |
| D | Diffusion coefficient |
| t | Time |
| F | Faraday's constant |
| ϕ | Potential |
| j | Current density |
| σ | Ionic conductivity |
| i | i th species |
| ε_{el} | Electrolyte volume fraction within CBD |
| f | Frequency |
| K | Electronic conductivity |
| $\dot{J}_{v,dl}$ | Volumetric double layer current density |
| ℓ | Electrode thickness |

Chapter – III

Optimized Electrode Power Density Without Reducing the Energy Density with Layered Electrode Architecture



3.1. Introduction

Developing optimized energy conversion and storage devices has led to an unprecedented growth of the sustainable energy industry during the last three decades. Particularly, lithium-ion batteries (LIBs) have enabled consumer electronic technologies as well as the incipient electric vehicle (EV), due to their high energy and power densities, and long cycling stability [108]. Nevertheless, continuous improvements such as increasing energy density and decreasing manufacturing costs are still required to unlock their full potential.[109] State-of-the-art chemistries are well engineered and capable of fast charging, yet electrodes need to be relatively thin leading to low energy densities and high costs.[110] Increasing electrode thickness and mass loading is a common approach to enhance the LIB energy density.[111,112] However, even if the lithium ion migration in a liquid electrolyte is several orders of magnitude higher than lithium diffusion in the solid phase, it is still the rate-limiting factor in a thick electrode and for electrodes under high C-rate.[113] Additionally, thick electrodes might also suffer from poor electrode wetting and dysfunctional heterogeneity in the mesostructure.[114] These variations may lead to heterogeneous current distributions, increased ionic impedance, and fast electrolyte decomposition under high storage temperatures,[16,17] resulting in lower energy and power capacities with accelerated cell degradation.[47] Therefore, optimizing thick electrode architectures becomes crucial for overcoming the limitations of current distributions in LIBs.[115]

Some experimental works have recently reported the interplay between energy and power density and electrode properties, such as areal loadings, porosities, and electrode architectures.[116–120] However, some electrode properties are challenging to engineer due to time, costs and instrument limitations.[121] In this regard, physical modelling serves as an efficient tool to address the electrochemical performance of LIBs, where optimization processes based on experimental trial and error become expensive and cumbersome.[116,122] For instance, several modeling studies

were recently reported to quantify and address the heterogeneity issue at a single particle level and full electrode level.[123] [124] All these discharge models were built to describe how electrode heterogeneities affected Li intercalation at different rates, and to assess its consequences on the overall performance of the LIB.[125–127] However, the ion migration limitation in the electrolyte phase of a porous electrode determines the battery performance under high C-rate operation, which, up to the authors' knowledge, was not independently and systematically studied in the works mentioned above.

Electrochemical impedance spectroscopy (EIS) is one of the dominant tools to measure ionic resistance in the battery field. The experimental setup to measure the ionic resistance of porous electrodes was first proposed by Ogihara *et. al.* using a symmetric cell configuration.[65] Additionally, EIS constitutes a simple way to calculate the electrode tortuosity factor. Several authors already used symmetric cell configurations to measure the tortuosity factors of a graphite anode, a LFP cathode, and a NMC cathode.[84,128,129] Moreover, in a recent publication, we have reported for the first time a 4D (3D in space + time) physical model of a NMC electrode symmetric cell, which captures the impact of the spatial location of carbon-binder domain (CBD), to simulate the EIS.[101] Our model allows assigning different physics to NMC, CBD and pores and explicitly considering the electrochemical double layers at the NMC/electrolyte and CBD/electrolyte interfaces, which sets up a perfect ground for the characterization of ionic resistances on heterogeneous porous electrodes.

The present work reports a systematic assessment of the ionic resistances on heterogeneous porous electrodes with different active material chemistries. The study first shows the methodology for the experimental measurements, the stochastic generation of heterogeneous electrode mesostructures, and the description of the EIS simulations. Secondly, the main trends for the

obtained experimental and simulated EIS were analyzed and compared. Lastly, the role of electrode heterogeneities on ionic resistances across the thickness of electrodes was investigated via experiments and simulations by calculating tortuosity factors. On top of that, half-cell discharge simulations and experiments were carried out to study overall electrode performance. We believe this study will assist in the conception of thick electrodes with reduced ionic resistance and improved charge and discharge rate capabilities for LIBs.

3.2. Methodology

Electrode structures generation

Previously we reported both stochastic and physics-based generation of electrodes in our works.[46,130] In this work, the stochastic way of generation electrodes was chosen to have electrodes with controlled porosity and the same time keeping all other parameters constant. The details of the technique can be found in following publication.[68] Active Material (AM) particle size distribution and AM/CBD dry weight ratio measurements were used as inputs. To generate electrodes. The obtained electrode mesostructures are meshed by our voxelization algorithm INNOV in MATLAB environment and imported into COMSOL Multiphysics 5.4 platform.[68]

Pore size distribution and pore network

The pore phase of the generated electrodes was further segmented into individual pores using the watershed method.[131] Specifically, the PoroDict library was used as part of the GeoDict[®] software package. Due to the discrete voxelated nature of the studied mesostructures, over-segmentation of the pore space is a common artifact induced by watershed-based methods. Many post-processing methods exist to alleviate the effect of such artifacts. In GeoDict[®] this is solved by reconnecting the initially segmented pores only if the percentage of surface area that is shared between them is bigger than a chosen value.[103,132] A low threshold value results in many pores being reconnected, while the contrary happens when a high threshold value is selected. In this

work, an intermediate value is carefully selected so that non-physical artifacts are eliminated. Once the pore space is labeled, the diameters of equivalent volume spheres are calculated and arranged in a histogram. The histogram is further normalized to account for the non-uniform selection of the number of histogram bins.

Experimental methodology

As-received materials were used including LiNi_{1/3}Mn_{1/3}Co_{1/3}O₂ (NMC, Umicore), Lithium iron phosphate (Aleees), C-ENERGY™ super C65, C45 carbon black and GHDR 10-4 graphite (IMERYYS), Solef™ Polyvinylidene fluoride (PVdF, Solvay), Carboxymethyl Cellulose (CMC, ACROS Organics), N-methyl pyrrolidone (NMP, BASF), Tetrabutylammonium perchlorate (TBAClO₄, Alfa Aesar) and Poly (vinylidene fluoride-co-hexafluoropropylene) (PVdF-HFP, Kynar Flex2801, Arkema).

The electrode with controlled porosity and the bi-porous electrodes were prepared by the Bellcore process.[133] The solid components, including active material, carbon black, and binder, were premixed with a soft blender. Furthermore, a solvent was added until reaching the desired ratio between solvent and solid components. The mixture was performed in a Dispermat CV3-PLUS high-shear mixer for two hours in a water-bath cooled recipient at 25 °C. The slurry was then coated over a 22 μm thick aluminum current collector using a comma-coater prototype-grade machine. The solid components were ground with an agate mortar and then moved to a glass container.

Table 1. List of analyzed electrodes

| Name | Active material (dry mass %) | Carbon black (dry mass %) | Binder (dry mass %) | Porosity (%) | Thickness (μm) |
|------|---------------------------------|------------------------------------|---------------------------|-----------------|-------------------|
| | | | | | |

| | | | | | |
|------------------------------|---|----------------|--------------------|-------|-----|
| Uncalendered- NMC-96 | LiNi _{1/3} Mn _{1/3} Co _{1/3} O ₂ (96%) | C65 (2%) | PVdF (2%) | 49% | 144 |
| Uncalendered- LFP-96 | LiFePO ₄ (96%) | C45 (2%) | PVdF (2%) | 64% | 122 |
| Uncalendered- Graphite-96 | GHDR 10-4 (94%) | C45 (2%) | CMC/SBR (2%) | 55% | 108 |
| Calendered- NMC-96 | LiNi _{1/3} Mn _{1/3} Co _{1/3} O ₂ (96%) | C65 (2%) | PVdF (2%) | 28% | 73 |
| Calendered- LFP-96 | LiFePO ₄ (96%) | C45 (2%) | PVdF (2%) | 37% | 64 |
| Calendered- Graphite-96 | GHDR 10-4 (94%) | C45 (2%) | CMC/SBR (2%) | 32% | 75 |
| NMC-PVDF- HFP-C45 | LiNi _{1/3} Mn _{1/3} Co _{1/3} O ₂ (73%) | C45 (7%) | PVdF (20%) | 55.6% | 127 |
| NMC-PVDF- HFP-C45 | LiNi _{1/3} Mn _{1/3} Co _{1/3} O ₂ (72.7%) | C45 (19.5%) | PVdF-HFP (7.8%) | 44% | 85 |

Different volumes of dibutyl phthalate, calculated according to the volume ratio, were added as a porogen agent. Acetone was added as a solvent, and the mixture was well mixed with a magnetic stirrer at high speed. The slurry was then deposited on a Mylar foil by doctor blading. The films detached from the Mylar foil were dried in ambient temperature and combined to one electrode under 10 Pascal at 130 °C. The bi-porous electrode was then soaked 3 times during 15 min in ether to remove the porogen agent. The analyzed electrodes in this work are listed in **Table 1**.

3.4. Results and discussion

3.4.1. Isolating ionic resistance from electronic resistance contributions in EIS.

It is frequent practice to represent EIS response as Nyquist plots. The typical shape of a the high frequency points of Nyquist plot for symmetric cells is about 45° slope line followed by about 90° vertical line at low frequencies. The high-frequency intercept on x-axis acts as a pure resistor while the response at lowest frequencies tends to a vertical line representing a purely capacitive behavior. Between these two regions, slopes with 45° represent the resistance caused by ion migration inside the porous electrode.[62,134,135] Furthermore, sometimes a semicircle shaped spectrum shows up in mid-high frequency intervals for some electrode materials. Since the blocking electrolyte ensures that no faradaic current flows during the EIS experiment, this arc-like EIS response cannot be related to a charge transfer process, as usually observed in LIB electrodes.

In the present lithium-less symmetric cells, this semicircle is ascribed to the contact electronic resistance at the current collector/composite electrode interface, consistent with our previous experimental studies.[136] In this case, the capacitive element originates from the double layer capacitance that occurs at the current collector/electrolyte interface (i.e. the electrolyte phase inside the pores of composite that wets the current collector substrate). The phenomenon can be predicted from our recent review article, which shows a general EIS response of insertion battery composites (see Figs. 4A and D in conjunction with equations (4)-(6) in that paper).[137] On top of that, the electronic conductivity of the AM generates a semicircle too. As Landesfeind *et al.* pointed out, if a high electronic conductivity condition is not met, both ionic and electronic effects will play a role in the total resistance measured by impedance, which hinders the measurement of pure ionic resistances.[63,101]

Figure 1 shows experimentally obtained EIS plots for uncalendered and calendered NMC, LFP, and Graphite electrodes in symmetric cell configurations. As discussed above, uncalendered NMC

and LFP (**Figure 1A**) electrodes with low electronic conductivities present a semicircle at the mid-high frequency region (10^6 Hz to 10^2 Hz). The LFP electrode, which has a lower electronic conductivity when compared to the NMC based electrode, shows an even bigger semicircle region and total resistance.[138] On the other hand, the graphite electrode does not show the curved mid-high frequency impedance values, due to its higher intrinsic electronic conductivity. One way of experimentally increasing electronic conductivity and decreasing the contact resistance is to perform electrode calendaring. **Figure 1B** illustrates the EIS spectra of calendared Graphite, NMC and LFP electrodes. Electrode calendaring makes the semicircle region (electronic/contact resistance) drastically decrease and ensures the isolated measurement of ionic resistances. Given that the electronic contribution to the resistance was virtually suppressed due to calendaring, the total resistance of the LFP electrode decreased (62.5%) from 0.04 to $0.025 \Omega\text{m}^2$. The same change was observed for NMC electrodes after the calendaring step. In contrast, the overall resistance for the graphite electrode increased after calendaring, which is due to an increase in the ionic resistances only, given that the electronic resistances are not a limiting factor for graphite electrodes.

Furthermore, before carrying out further EIS simulations, correct conductivity values for the AM must be found to correctly calibrate the model. In order to find out the exact value above which the electronic conductivity stops being a limiting source of impedance of the system, several EIS simulations were carried out by setting different bulk electronic conductivity numbers.

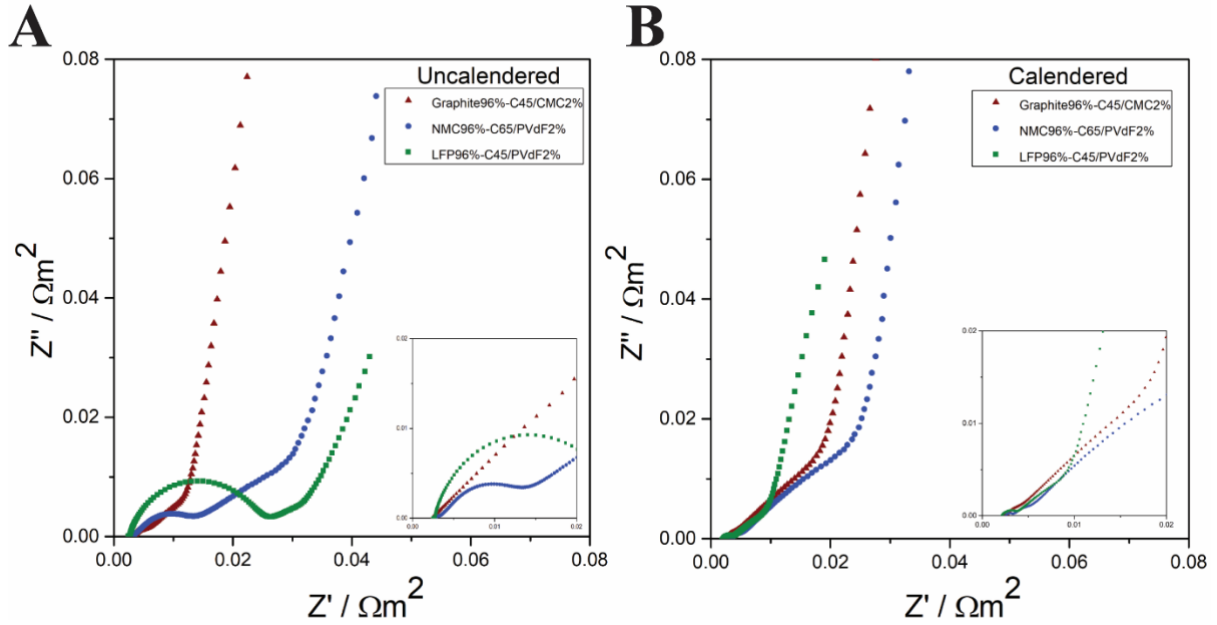


Figure 1. Experimental, Nyquist plots of (A) Uncalendered and (B) Calendered, Graphite 96% - C45/CMC 2% (red), NMC 96% - C65/PVdF 2% (blue) and LFP 96% - C45/PVdF 2% (green) electrodes in symmetric cells.

Figure 2A shows a cut view of the simulated 3D symmetric cell. **Figure 2B** and **2C** show the Nyquist and Bode plots obtained by simulations. When the electronic conductivity of the AM was set to be of 0.001 S/m (as experimentally measured for NMC electrodes),^[101] the EIS simulations were consistent compared to the experimentally measured ones (**Figure 1A**). However, when setting a higher electronic conductivity (1 and 760 S/m) in the model, the electronic resistance coming from AM disappeared (semicircle region), and only ionic resistance (45° slope line) was measured. The simulated EIS spectra with high electronic conductivity values are consistent with the experimentally obtained calendered electrodes (**Figure 1B**). In short, the above analysis shows that by sufficiently increasing the electronic conductivity of the composite AM, we ensure the dominating presence of the 45° slope line appearing between 10⁵ Hz to 10 Hz in **Figure 2B**. This impedance feature corresponds to the electrolyte resistance due to ionic migration limitations in the porous electrode.^[13] Additionally, the Bode plot (**Figure 2C**) shows that, for AM

conductivities of 1 S/m and 760 S/m , the corrected phase angles remain between 43° and 50° (10⁵ Hz to 10 Hz) as theoretically expected.

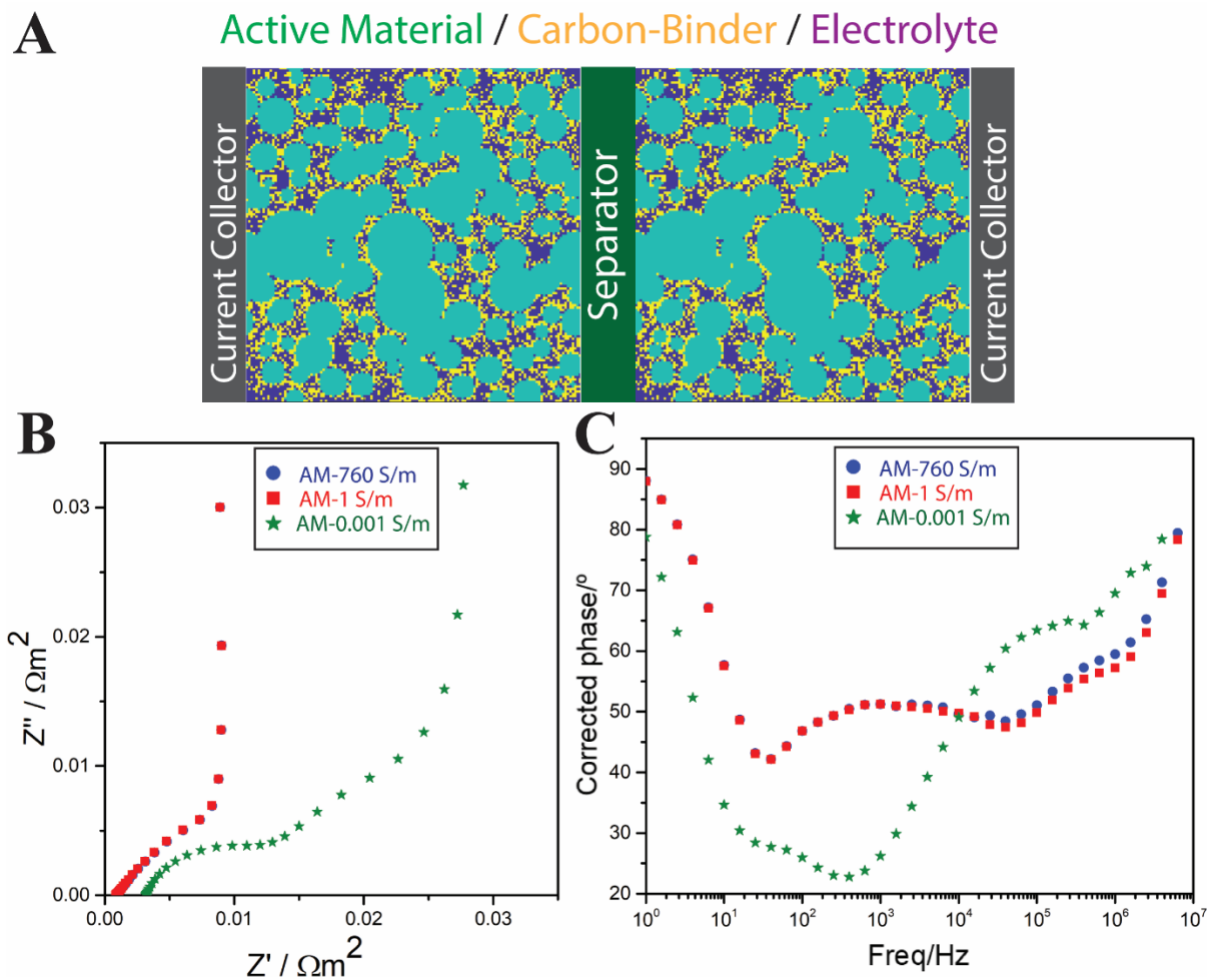


Figure 2. (A) 2D cut view of the simulated symmetric cell. (B) Simulated Nyquist and (C) Bode plots of a NMC 96% - CBD 4% symmetric cells with different electronic conductivities of the NMC active material.

Consequently, all contact resistances are neglected and bulk electronic conductivity of AM domain was set to 1 S/m (higher than in reality) in our model. These assumptions ensure isolating electronic and ionic contributions to the electrode’s impedance response, and allow us to simulate the ionic resistance of the porous electrode.

3.4.2. Understanding electrode porosity effects on ionic resistance by EIS

Once our EIS model is correctly calibrated to isolate the ionic resistance contributions from our 3D model electrodes, the influence of electrode porosity on overall ionic resistance and tortuosity was studied. For this, three electrodes with 30%, 35% and 45% porosities were generated and simulated by symmetrical EIS model. The schematics of the symmetric cells **(A)** and their corresponding pore size distributions (PSD) **(B)**, EIS simulations in Nyquist **(C)** and Bode **(D)** plots are shown in **Figure 3**.

Usually, PSD of the electrodes changes simultaneously when changing electrode porosity. Therefore, PSD of the electrodes was calculated to quantify exactly how much pore sizes changed by decreasing the electrode porosity. **Figure 3B** shows that an electrode with 45% porosity has the broadest PSD among the three electrodes with 1.5 μm to 3.5 μm equivalent diameter. The smallest standard deviation of PSD was found for the electrode with 30% porosity, as expected. Still, it is clear from the results that the differences in the pore size distributions between different electrodes is slim. These small differences allow us to isolate and systematically study the effect of electrode porosity independently.

In the Nyquist plot (**Figure 3C**), the sloping region (mid-to-high frequency) increases when the electrode porosity is reduced from 45% to 30%, ascribing to the higher resistance caused by the low amount of electrolyte and a longer migration path for ions. In addition, the resistance of the electrode increases from 0.0025 to 0.0045 Ωm^2 when the electrode porosity decreases from 45% to 30%. Furthermore, it is crucial to notice that high porosity electrodes lead to double layer formation at higher frequencies faster than the electrodes with lower porosities, which can be explained by an easier path for ions to reach the surface of the electrode.

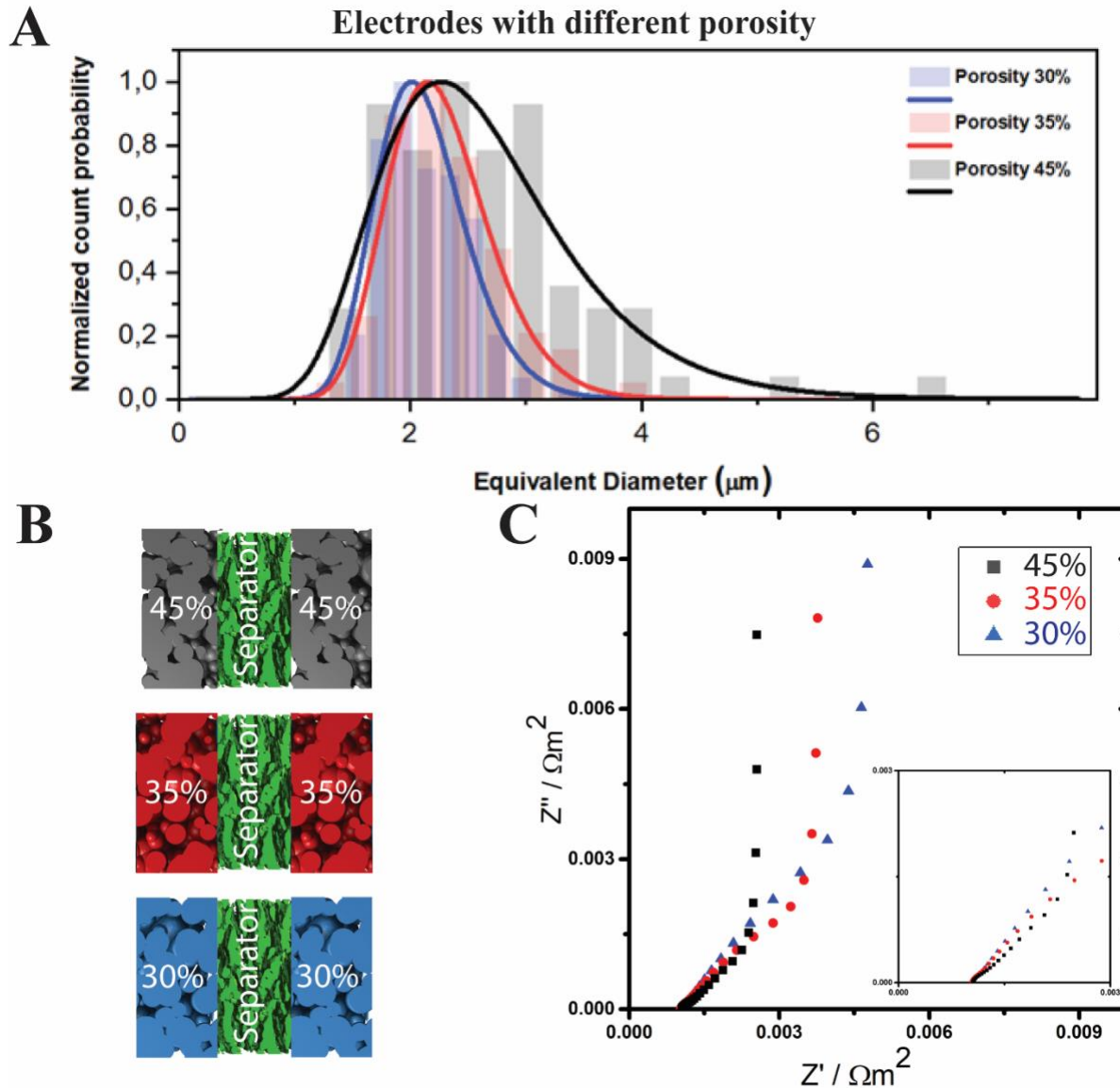


Figure 3. (A) Normalized pore size distribution of stochastically generated AM 96% - CBD 4% electrodes with porosities 30%, 35% and 45%. (B) Schematics of the electrodes with different porosities in symmetric cells. (C) Simulated Nyquist AM 96% - CBD 4% symmetric cells with different electrode porosities

Figure 4 shows the ionic impedance of a cross-sectional cut at half of the thickness of the electrode, parallel to the surface at 10^2 Hz. The illustration shows that pores are better connected at higher porosities, which allows easier ionic transport. According to the cross-sectional 2D cut plots (**Figure 4A**), the electrolyte resistance inside the electrode increased when the electrode porosity

decreased. Furthermore, higher resistance regions (blue zones) are observed for the CBD domain for the electrode with lower porosity.

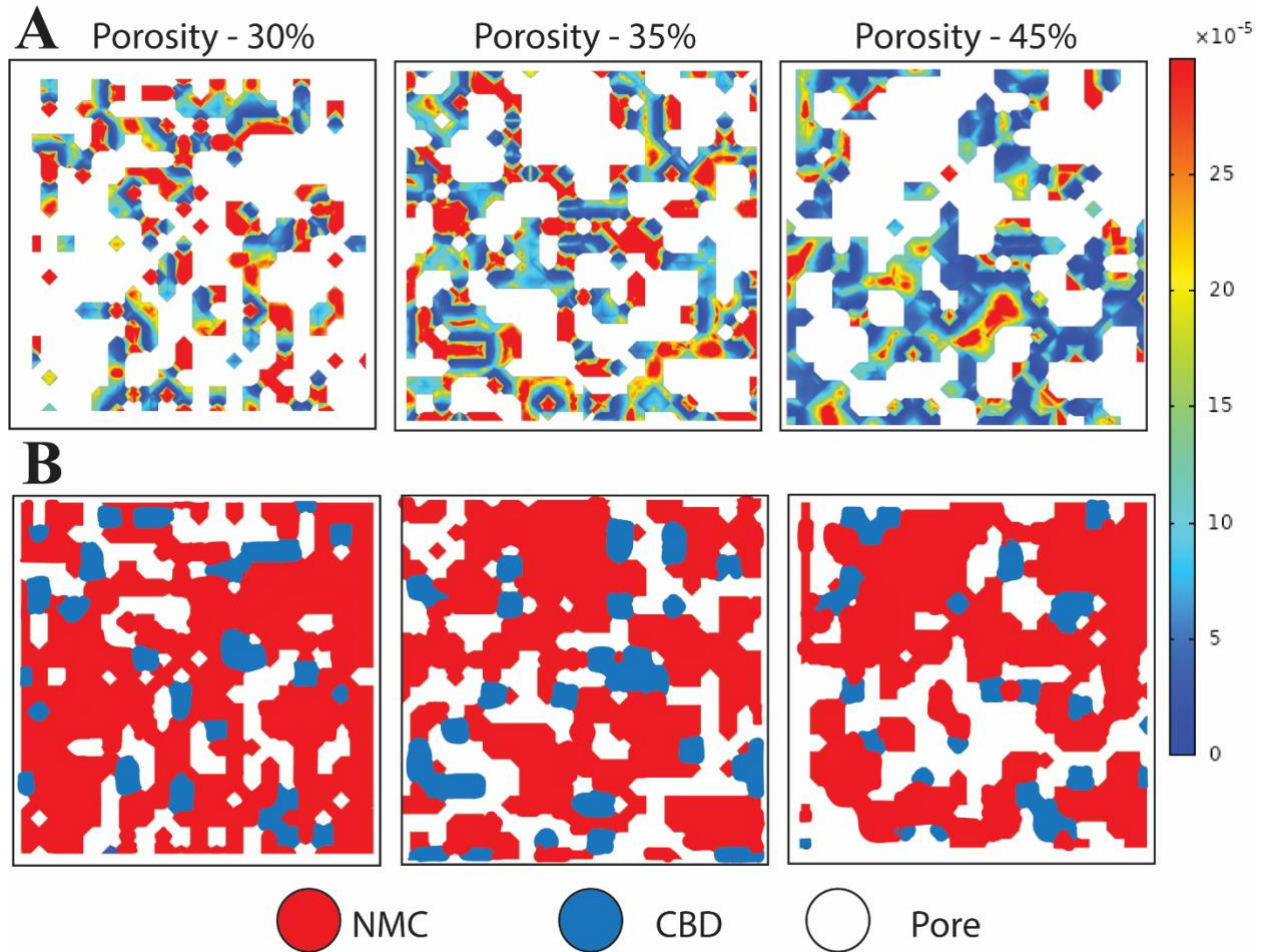


Figure 4. (A) Simulated NMC 96% - CBD 4% electrode cross-sectional impedance 2D plots at 100 Hz frequency, corresponding to the ionic contribution to the total measured impedance. Due to our model formality, impedance on CBD moiety appears in both ionic and electronic 2D plots. (B) Scheme of the cross-section cut, where each phase is explicitly tagged with different colors. The cut-views were done at half of the electrode thickness parallel to the surface.

Table 2 displays the calculated values of ionic resistances (R_{ion}) of the electrolyte within the porous electrode, the electrode tortuosities (τ_{EIS}) calculated through the graphical method according to Landesfeind *et al.*, and the diffusional tortuosity factors (τ_{Factor}). As expected, the lower the porosity, the higher the ionic resistance and higher the tortuosity values (τ_{EIS} and τ_{Factor}). Also, the

change in the tortuosity factors indicates a strong negative correlation between tortuosity values and porosity.

Table 2. Ionic resistances (R_{ion}) of the electrolyte within the electrode pores and tortuosity (τ_{EIS}) calculated according to Landesfeind et al.[128]

| | Porosity – 30% | Porosity – 35% | Porosity – 45% |
|--|----------------|----------------|----------------|
| Electrode thickness | 25 μ m | 25 μ m | 25 μ m |
| Tortuosity Factor (τ_{Factor}) | 2.15 | 1.89 | 1.59 |
| Tortuosity Factor (τ_{EIS}) | 3.3 | 2.8 | 1.8 |
| Ionic Resistance ($R_{ion}/\Omega\ m^2$) | 0.011 | 0.008 | 0.004 |

3.4.3. Designing heterogeneous electrode architectures with improved performance

In the last sections, we calibrated our EIS model to be able to capture ionic resistance contributions from EIS experiments by comparing experimental EIS spectra of calendered and uncalendered electrodes. Additionally, we studied the effect of the electrode porosity on the ionic resistances and electrode tortuosities. Overall, we find that highly porous electrodes are beneficial for achieving low ionic resistances which is crucial under high C-rate operation. However, a tradeoff exists between active mass loading and rate capability, which is basically a tradeoff between energy and power densities. Having therefore understood the principles of ionic resistance contributions in EIS, we envisioned electrode architectures that could optimize rate capabilities, for a fixed average porosity and thickness, by playing with their microstructural heterogeneities. To do this, electrodes with different porosities were assembled as one electrode to create heterogeneity of porosity across the electrode thickness (cartesian coordinate Z). Then, the constructed cells were studied systematically to create a complete map of the impact of heterogeneous porosity on total ionic resistance.

The obtained electrodes are shown in schematic form in **Figure 5A**. Their corresponding EIS simulation results are shown in **Figure 5B** and **C**, in the form of Nyquist and Bode plots, respectively. The calculated ionic resistance and tortuosity (τ_{EIS}) numbers for these cells are given in **Table 2**. Even though the four studied configurations have the same average porosity, the difference of the ionic resistances between them is significantly different, as shown in the Nyquist plots (**Figure 5B**).

Cell-1, with the highest porosity (45%) close to the separator, shows the lowest ionic resistance ($0.013 \Omega\text{m}^2$) with a minor tortuosity factor (τ_{EIS}) of 1.5. In contrast, Cell-2, with the lowest porosity (30%) close to the separator region, has the highest ionic resistance $0.024 \Omega\text{m}^2$ and tortuosity factor (τ_{EIS}) around 2.8. According to the results, adjusting the electrode porosity distribution can reduce the ionic resistance by almost 50% while maintaining the overall porosity. Furthermore, a second region close to the separator was studied. When comparing Cell-1 and Cell-4, we demonstrated that having a progressively decreasing porosity from the separator to the current collector can reduce ionic resistance, which results in a drastic improvement of the rate capability of the electrodes for the same areal loading. Additionally, the diffusional tortuosity factors, τ_{Factor} , for all four cells were calculated to have a value of around 1.81 (**Table 3**), which is in striking contrast with the calculated electrode tortuosity values (τ_{EIS}). These results show that diffusional tortuosity factors are inadequate when trying to characterize battery electrodes.[134]

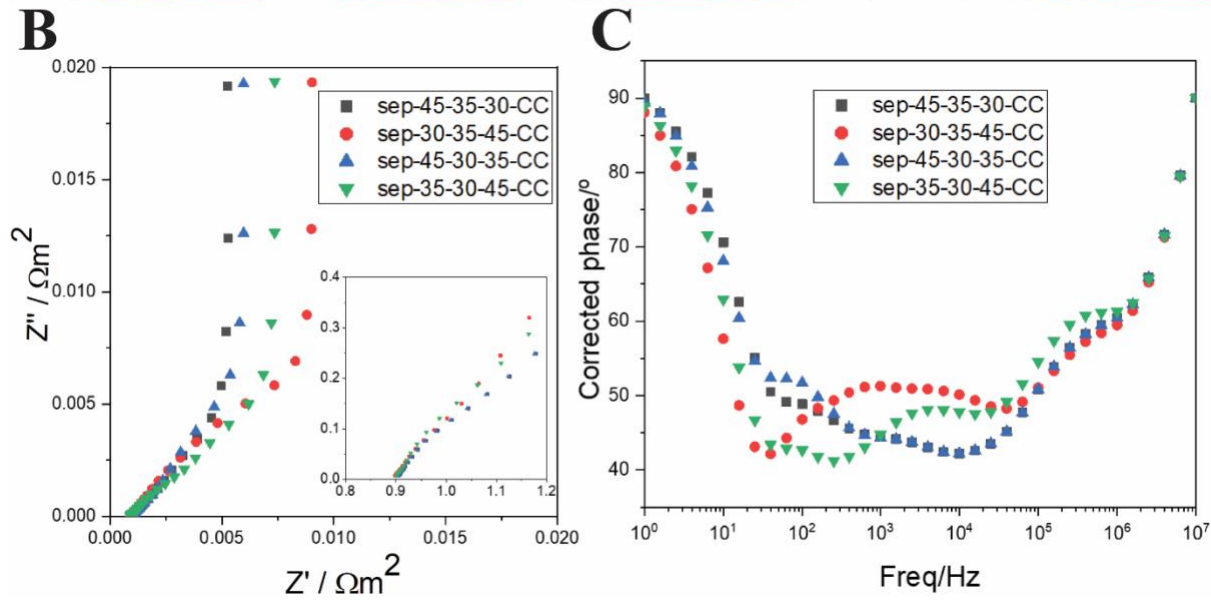
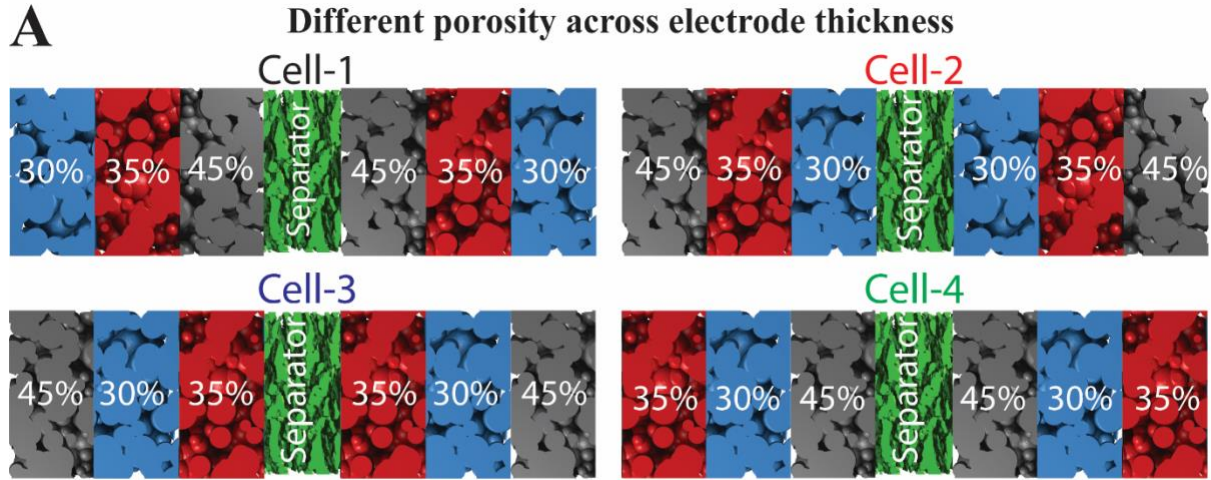


Figure 5. (A) Schematics of the different simulated symmetric cells with different porosity across the thickness. (B) Simulated Nyquist and (C) Bode plots for these symmetric cells.

| | Cell-1 | Cell-2 | Cell-3 | Cell-4 |
|---|--------------|--------------|--------------|--------------|
| | Sep-45-35-30 | Sep-30-35-45 | Sep-45-30-35 | Sep-35-30-45 |
| Electrode thickness | 75 μ m | 75 μ m | 75 μ m | 75 μ m |
| Tortuosity (τ_{Factor}) | 1.81 | 1.81 | 1.81 | 1.81 |
| Tortuosity (τ_{EIS}) | 1.5 | 2.8 | 1.7 | 2.2 |
| Ionic Resistance (EIS) $R_{ion}/\Omega m^2$ | 0.013 | 0.024 | 0.015 | 0.019 |

Table 3. Ionic resistances (R_{ion}) of the electrolyte within the electrode pores, tortuosities (τ_{EIS}) calculated according to Landesfeind et al.[128]

In order to apply the predicted simulation results, the bi-porous electrodes were prepared by the Bellcore process.[133] The bi-porous electrode consisted of two layers where each layer had a porosity of 40% and 55%. The manufactured porous and bi-porous electrodes were put in symmetric cell format for the EIS experiments. **Figure 6A** shows Nyquist plots of electrodes with different porosities. Consistent with the simulation results (**Figure 3C**), the electrode with 40% porosity showed higher resistance ($0.0085 \Omega\text{m}^2$) than the electrode with 55% porosity ($0.0055 \Omega\text{m}^2$). Furthermore, electrodes with different porosities were manufactured as one electrode to create heterogeneity of porosity across the electrode thickness (cartesian coordinate Z). **Figure 6B** shows the Nyquist plot where bi-porous electrodes were assembled to mimic the gradual porosity decreases/increases from the separator to the current collector side. The electrode with the highest porosity (55%) close to the separator shows the lowest ionic resistance $0.007 \Omega\text{m}^2$ and at the same time, the electrode with the lowest porosity (40%) close to the separator region has the highest ionic resistance $0.014 \Omega\text{m}^2$. According to the experiments, adjusting the electrode porosity distribution can reduce the ionic resistance by almost 50% while maintaining the overall porosity. This finding is in perfect agreement with simulation results.

In summary, EIS simulations predicted that the total ionic resistance is strongly correlated with electrode heterogeneity and these predictions were confirmed experimentally. Therefore, when keeping the same overall porosity, a desirable electrode mesostructure with a minimized impedance should have a porosity that gradually decreases from separator to current collector. This shows the significant impact of electrode design on electrochemical performance.

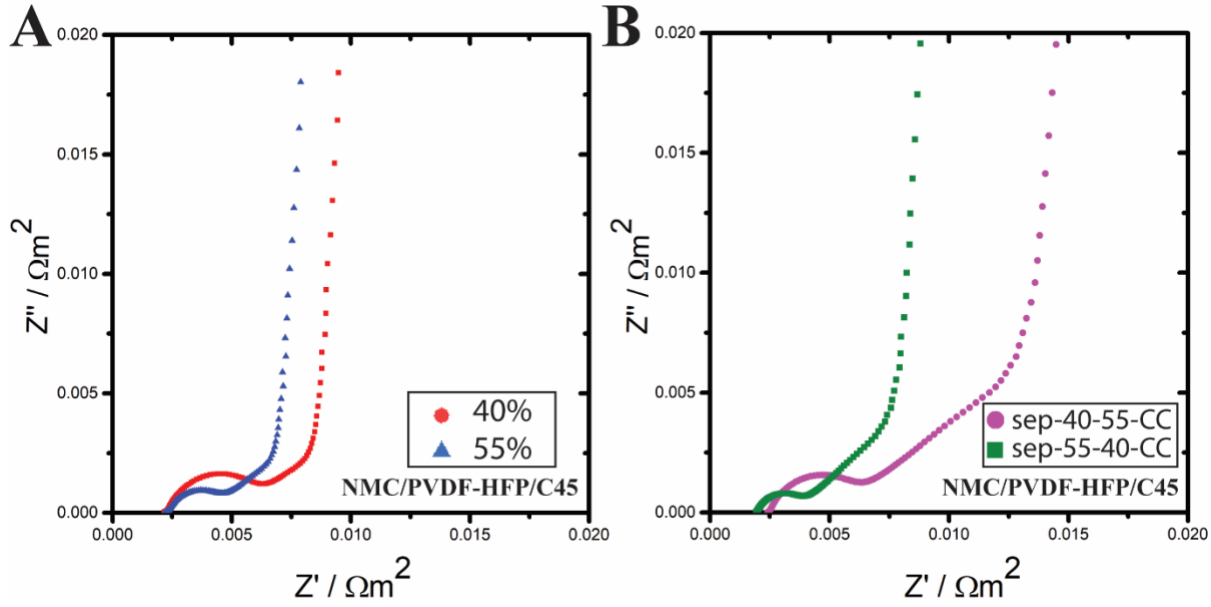


Figure 6. Nyquist plot of experimental symmetric cells (A) NMC/PVDF-HFP/C45 electrodes with 40% and 55% porosity. (B) NMC/PVDF-HFP/C45 Bi-porous electrodes consisted of two layers across the thickness (from the separator to the current collector side) where each layer had a porosity 40% and 55%

Besides the EIS simulations, discharge simulations for the same electrode mesostructures were carried out based on a half-cell configuration (**Figure 7A**). The simulations carried out at 5C, 3C and 1C rates for all the structures and the results of two electrodes, Halfcell-1 and Halfcell-2, with the most significant difference, are shown in **Figure 7B**. Both of the cells showed the same capacity (166 mAhg^{-1}) at 1C rate. Still, there is little difference in the overall potential between cells. However, when simulations carried under higher C rates (5C and 3C), Half-cell-1 with the highest porosity close to the separator exhibited the highest gravimetric discharge capacity, while Half-cell-2 with the lowest porosity close to the separator delivered the lowest gravimetric capacity among all the electrodes. The results of the discharge simulations at 3C rate for all the cells were given in **Figure 7D**. In agreement with our EIS simulations, discharge simulations showed the same trends for all the electrodes correspondingly. Electrode architecture with progressively

decreasing porosity from separator to current collector showed the best performance which is consistent with the EIS results.

Figure 8D and **E** represent the lithium concentration in the electrolyte phase at the end of discharge for Half-cell-2 and Half-cell-1, respectively. In Half-cell-2, the high concentration of lithium close to the separator dramatically decreases across the thickness of the electrode. On the other side, lithium concentration spreads more homogeneously across the thickness of the electrode in Half-cell-1, which has higher porosity close to the separator region. In Half-cell-1, with lowest porosity close to the separator reduces the contact surface of the NMC-electrolyte interface and limits the ion migration across the electrode, which reduces the utilization of the high porosity layer next to the current collector. Also, it is essential to mention that lower porosity near the current collector region ensures better contact between the electrode and the current collector, consequently allowing better electronic fluxes.

On top of the simulation calculations, comparable experiments were performed to reproduce the predictions. The same bi-porous electrodes, which mimic the gradual porosity, decrease/increase from the separator to the current collector side, were built in half-cell format against lithium metal to test the rate capability of the electrodes. Coherent with simulations, experiments were tested at 1C and 3C rates. The corresponding the discharge curves for two electrodes are given in **Figure 8**. Both electrodes had the same capacity (135 mAhg^{-1}) at 1C rate. Still, there is small difference in overpotential between electrodes as predicted by simulation results. By increasing the C rate from 1 to 3, the difference in capacity diverged between electrodes. Coherent with the simulation results, the electrode with higher porosity close to the separator exhibited the higher gravimetric discharge capacity, while the electrode with lower porosity close to the separator delivered the lower gravimetric capacity among two electrodes.

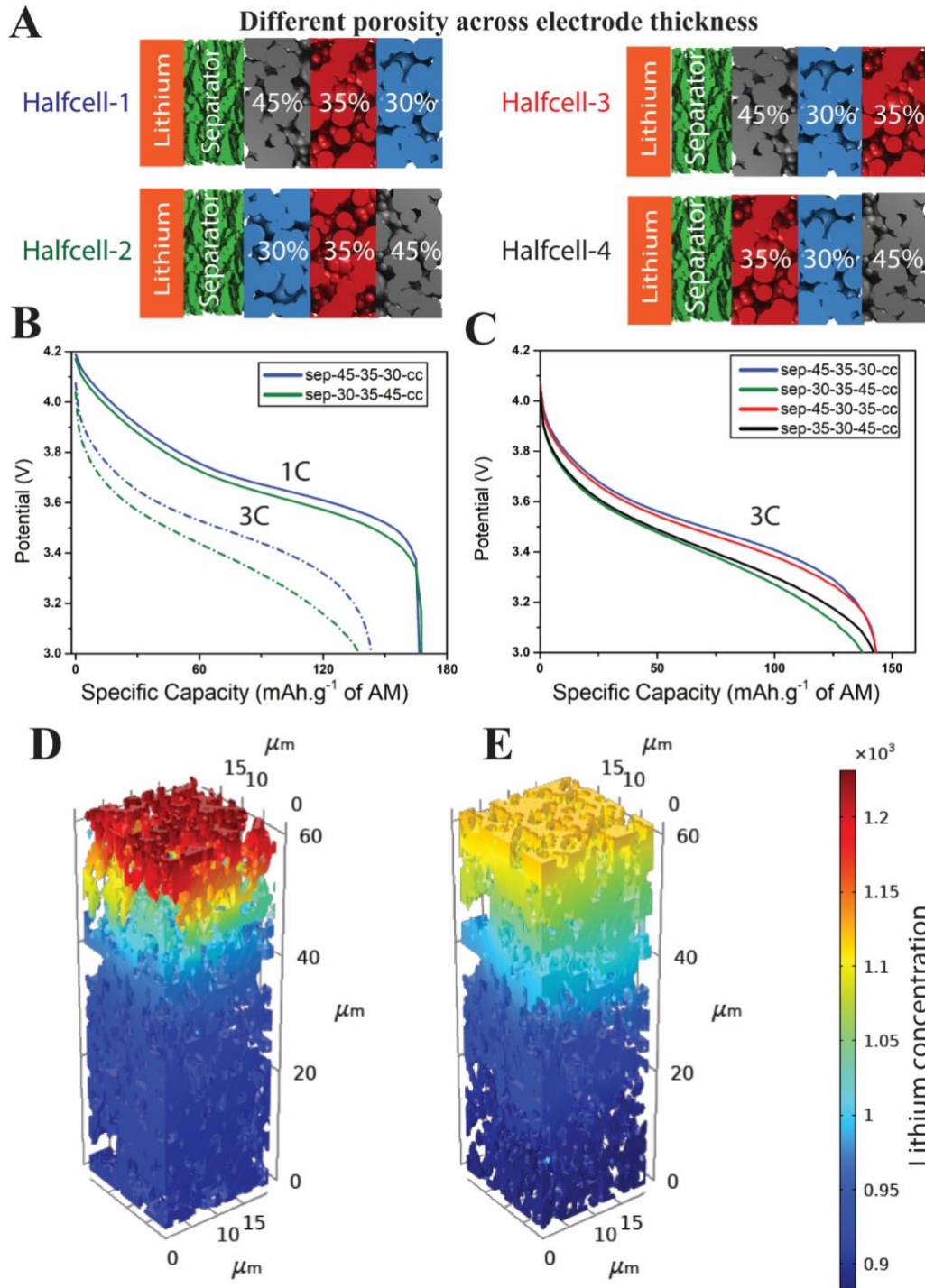


Figure 7. (A) Schematic of the simulated half cells with different porosity across the thickness (B). Simulated discharge curves for all the half cells at 3C rate. (C) and (D) representation of the lithium concentration in the electrolyte at the end of discharge simulation for Half-cell-2 and Half-cell-1, respectively (the separator and the current collector are located respectively at the top and bottom of the structures).

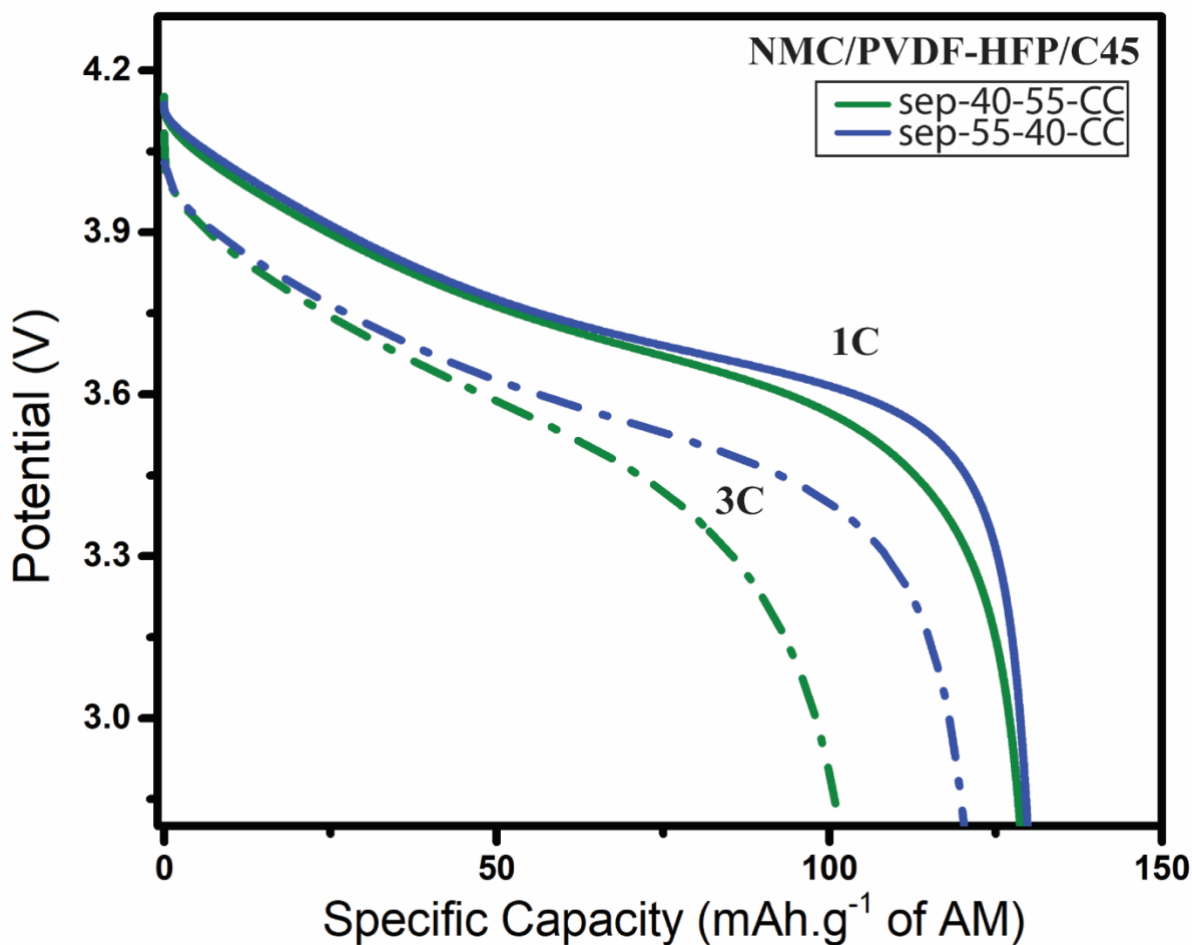


Figure 8. Experimental discharge curves for the half-cell format Lithium metal vs NMC/PVDF-HFP/C45 Bi-porous electrodes consisted of two layers across the thickness (from the separator to the current collector side) where each layer had a porosity 40% and 55% at 1C and 3C rates.

Three-phase, three-dimensional modeling gives an advantage not only to study different domains explicitly but also to create heterogeneity within the electrode across different directions. Therefore, in addition to previous studies, electrodes with heterogeneities of porosity across the surface were investigated. To our best knowledge, this is the first report on such a study. Accordingly, different electrodes were obtained by locating the electrodes with varying porosities across the surface (in Cartesian coordinates across X and Y). The setup of different test electrodes in symmetric cell and half-cell formats are shown in **Figure 9A** and **B**. In addition, the EIS

simulation results are given in **Figure 9C** in Nyquist plots. The simulation results indicate that the heterogeneity of porosity across the electrode surface does not affect the overall average ionic impedance.

Furthermore, all the EIS simulated cells' outcomes are closely overlapped, as shown in **Figure 9C**.

Accordingly, the same trend was observed during discharge simulations. **Figure 9D** shows half-cell discharge profiles, indicating that heterogeneity across thickness does not affect overall average electrode performance.

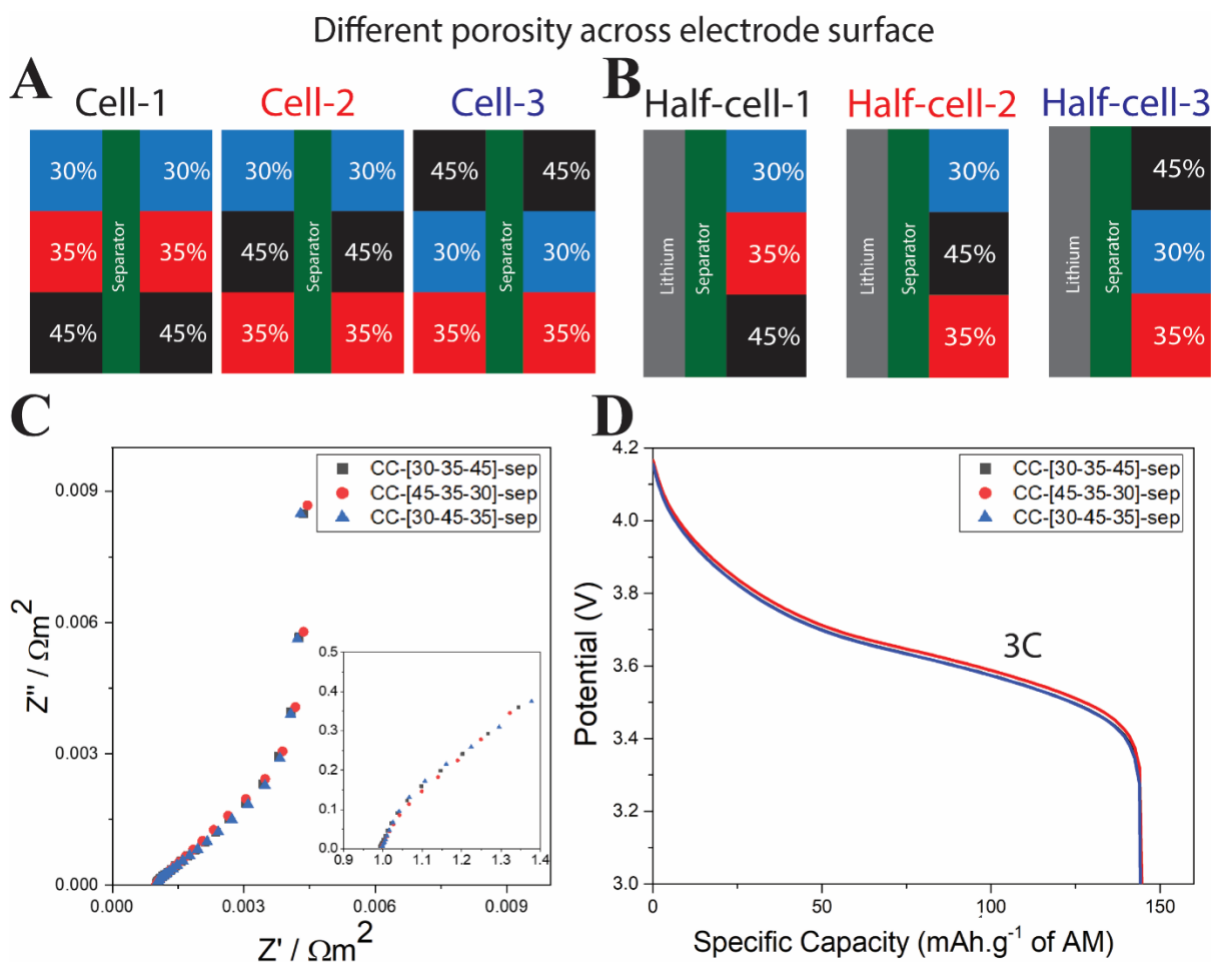


Figure 9. (A)Schematics of the different studied (A) symmetric cells and (B) half-cells with different porosity across the surface of the electrode. (C) Simulated Nyquist plots of the symmetric cells and (D) discharge profiles of the half-cells

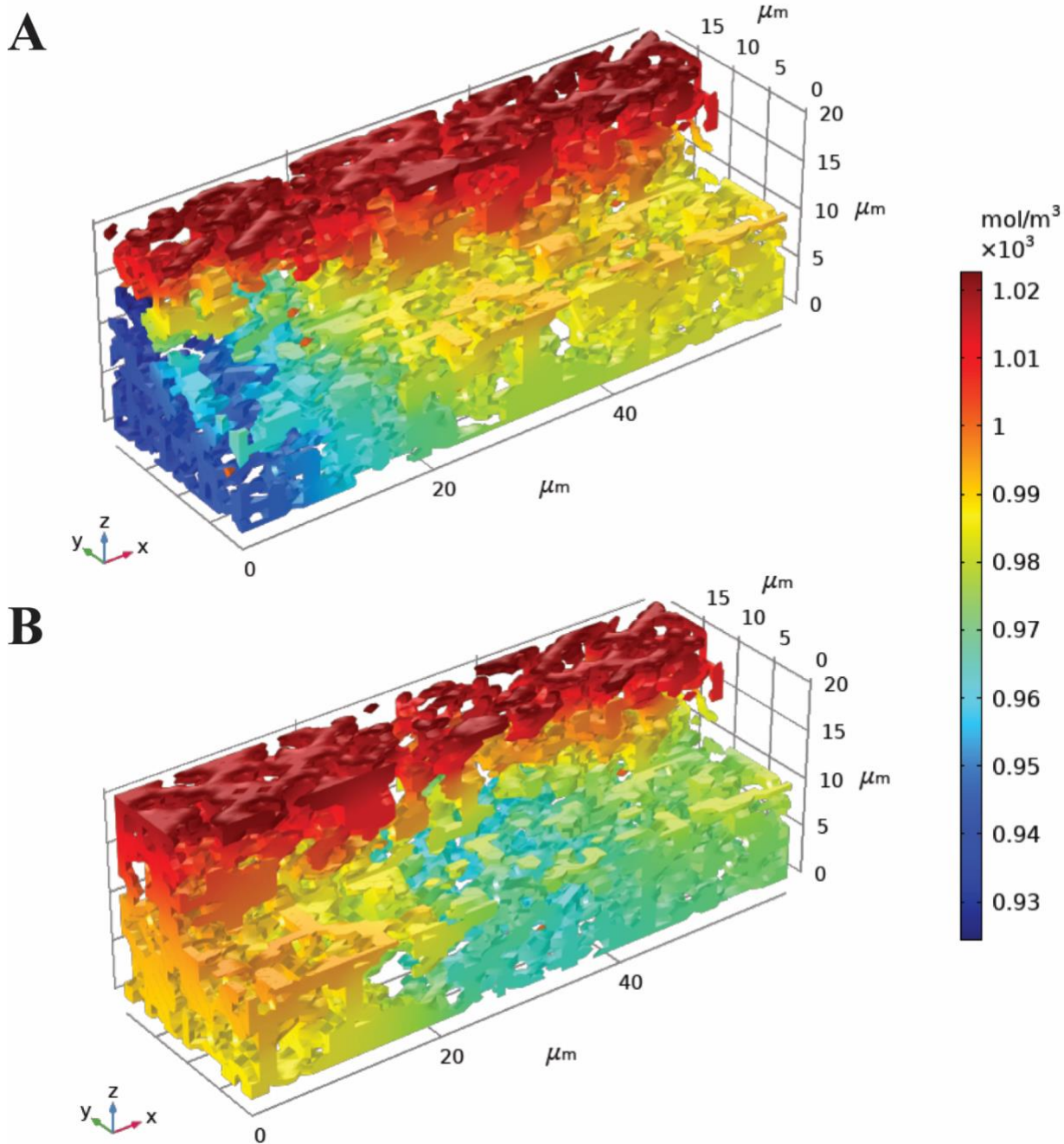


Figure 10. Representation of the lithium concentration in the electrolyte at the end of discharge simulation for (A). Half-cell-2 and (B). Half-cell-3, respectively (the separator and the current collector are located respectively at the top and bottom of the structures).

Even though average ionic resistance and gravimetric capacities are the same, different lithium concentration gradients can be observed in different electrode regions (**Figure 10**). **Figure 10** shows lithium concentration in the electrolyte within porous media at the end of discharge

simulation of Half-cell-1 and Half-cell-3. It can be seen from the map that the separator and electrode border for both cells show the same amount of lithium concentration. In contrast, with more depth of the electrode, lithium concentration profile across regions diverges.

3.5. Conclusion

In the scope of this work, a 4D (3D in space + time) physical model was successfully used to simulate and analyze the electrode porosity inhomogeneity effect on overall ionic resistance. Furthermore, the modeling results were compared and validated with experimental results. Different AM electrodes with different mesostructures were generated by *in house* INNOV application.

The first part of the study is devoted to a general discussion of the EIS spectra and mapping the role of ionic and electronic impedance experimentally by comparing NMC, LFP and Graphite electrodes with manufacturing conditions. On top of it, the simulations with different AM electronic conductivities were carried to eliminate electronic impedance and assess only ionic impedance.

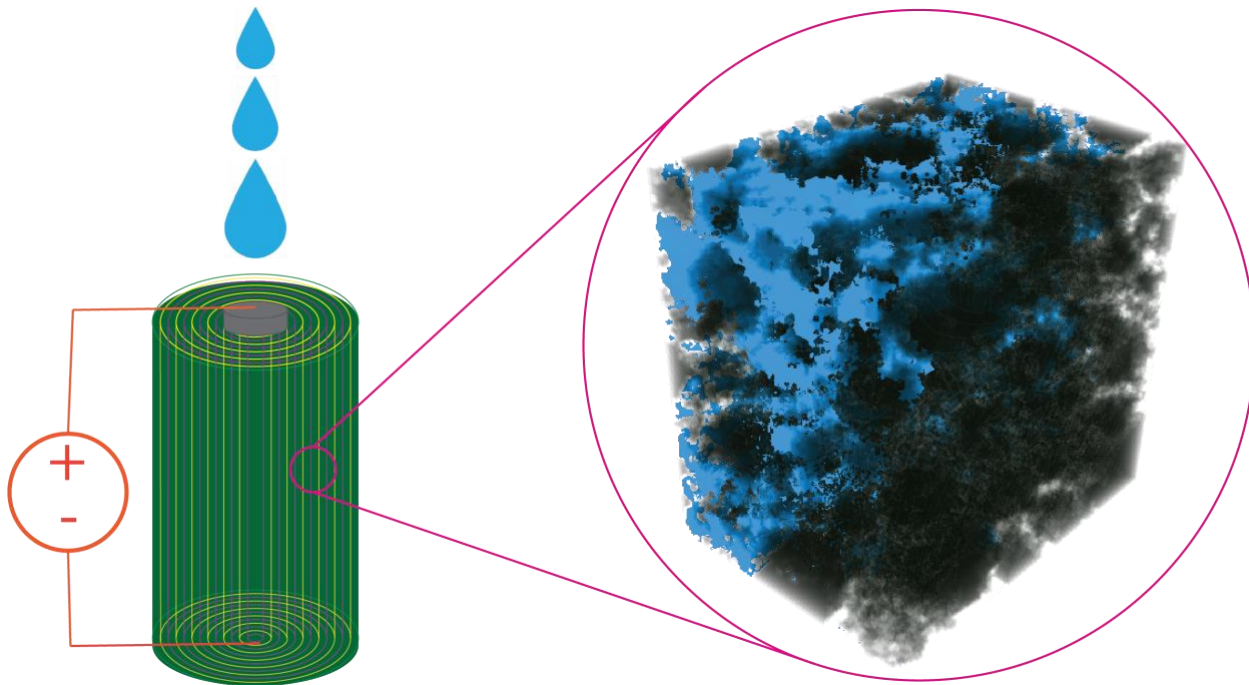
In the second part of the work, a comparison of electrodes with different porosities was performed based on simulations with EIS models. As expected, the results show that a lower porosity leads to a higher ionic impedance and electrode tortuosity. Tortuosity factors calculated by the EIS method (τ_{EIS}) and model based on diffusion (τ_{Factor}) were compared for all the simulations. Accordingly, the EIS method in symmetric cells suits better to calculate the electrode tortuosity (τ_{EIS}) than a method based on diffusion (τ_{Factor}) for battery electrodes.

Further electrodes with different porosities were built to study the effect of inhomogeneous porosity across thickness and surface directions. Furthermore, generated cells were studied systematically with EIS in symmetric cell configuration and discharge models in half cell setups.

The results coming from both simulation and experimental, showed that electrode inhomogeneity across thickness has a significant effect on the ionic impedance and capacity of the electrode. The study showed that the electrode region close to the separator side has the most prominent role in ionic impedance and tortuosity numbers which consequently influences the overall capacity. Therefore, to obtain the optimal structure with the best performance, electrode porosity must be constructed to decrease from the separator side to the current collector side.

Chapter –IV

Insight on Electrolyte Infiltration of Lithium-Ion Battery Electrodes by Means of a New Three-Dimensional-Resolved Lattice Boltzmann Model



4.1. Introduction

Alongside the massive improvement in cell chemistry,[139] it is critical to optimize the manufacturing process in order to improve its quality: one of the bottleneck steps in such manufacturing process is to ensure homogenous electrolyte impregnation within the electrode porous mesostructures.[48,140–142] There are several specific technical reasons behind this claim. Firstly, the electrolyte wetting of LIB cells takes a relatively longer time than other steps during manufacturing.[143] Secondly, since the charge transfer occurs at the electrolyte–electrode interface, the electrolyte infiltration determines the total electrochemically active surface area and, therefore, the cell energy and power capability.[16]·[17]·[144] Moreover, incomplete wetting can create "dead electrode zones" which may potentially lead to the formation of dendrites, inducing short circuits and reducing the battery cycle life.[145]·[146]·[147]

Davoodabadi *et al.* performed quantitative wettability measurements on NMC532-based cathodes, identifying two important parameters: the electrolyte penetrance coefficient and the solid permeability coefficient.[141] They found that the electrolyte with a greater value of the former wets faster the electrode, whereas the electrode with a greater value of the latter is more amenable to impregnation. Furthermore, studies performed by the same group revealed that the calendaring degree (*i.e.*, the porosity of the electrode after the calendaring), the wetting temperature, the nature of the solvent used to prepare the electrode slurry (*i.e.*, organic vs. aqueous) and the concentration of the electrolyte's salt play a key role in the wetting rate.[146] A ceramic coating on separator also improved the electrolyte wetting on the in-plane direction.[148] Günter *et al.* studied the impact of the amount of electrolyte on the performance of large-format LIB cells.[149] They analyzed the filling and the formation process and performed cyclability tests, finding interdependencies between the electrolyte quantity, the wetting rate, the cell capacity, and energy density. Working also with large-format LIB cells, Weydanz *et al.* used neutron imaging to visualize in real-time the electrolyte impregnation and analyzed the effect of using vacuum to reduce the wetting time.[150] It was also demonstrated that the electrode surface morphology, the separator material and the interphase between them affect the wetting kinetics.[151–153]

Despite the importance of the topic, reliable and broad scientific data does not exist in the literature.[145]·[154] There are several patent reports and scientific publications, but nevertheless, the electrode wetting process has not been sufficiently explored.[143] Electrolyte wetting has been evaluated experimentally by wetting balance and 2D in plane imbibition methods. However, the

experimental results cannot provide any information on how and what portion of the pores were filled.[141] The visualization favors a straightforward understanding of its profound nature.[155]·[156]·[157] However, it is a challenging task from an experimental perspective. The components of the cells, such as electrodes, separators, and housing, are not transparent to visible lights. Furthermore, the vacuum chamber, where usually electrolyte filled, does not allow doing *in situ* experiments. To the best of our knowledge, only a few papers are reporting the visualization of the liquid penetration by using transmission neutron and X-ray imaging.[157]·[158]·[159] The studies did not have the appropriate resolution to provide detailed information on how the pores were filled with electrolyte during the whole process, due to the limitations of the techniques.

Another path to address this puzzle is the utilization of computational methods to simulate porous media flow. Computational fluid dynamics based on finite element method (FEM) and finite volume methods (FVM) have been the most dominant tools to solve fluid dynamics problems.[160] Nevertheless, it cannot be applied in a straightforward way to 3D-resolved porous media phenomena where boundaries are complex and involve biphasic (gas/liquid) interface dynamics.[156]·[161] Recently, the increase in computational power and the development of the so-called Lattice Boltzmann Method (LBM) made possible to describe this process meticulously.[162]·[163]·[164] Compared to other techniques, the strength of the LBM is its mesoscopic nature based on the discrete kinetic theory. At the mesoscopic level, the LBM models combine microscopic dynamics, such as fluid-fluid and fluid-solid boundary interactions, and the macroscopic kinetic theory of fluids, like the Navier-Stokes equation in the bulk flow.[165] Moreover, several multiphase models reported recently advanced its capacity to simulate multiphase flow, becoming very attractive.[166] In spite of its advantages, LBM is a new tool, and few codes were developed compared to traditional computational fluid dynamics (CFD) methods.[167] Furthermore, LBM is computationally very expensive, which limits its deployment to an efficient and parallel usage of supercomputers.[156]·[168] Regardless these difficulties, Lee *et al.* implemented LBM to characterize electrolyte transport in the porous LIB electrode.[156]·[169] Despite the successful utilization and essential insights from the study, the model was only two dimensional, and flow was limited in some directions. Their simulation was based on an ideal case where only active material particles with perfectly spherical shape were considered. Furthermore, the inactive components, such as conductive additive and binder, which are known to significantly impact the AM active surface and pores structure,[156]·[169]·[170] were

not explicitly considered. Hence further studies on three-dimensional models are required to capture the full picture of the process.

For the first time, this study reports insights about the electrolyte filling dynamics in electrodes with three-dimensional resolution based on an innovative Lattice Boltzmann model where realistic geometries of electrodes were utilized. Furthermore, the impact of electrode porosity on electrolyte wetting dynamics was explored using electrodes generated by stochastic simulations, tomography characterizations and by the simulation of the electrodes manufacturing process. The separator's role and its surface contact with the electrode on electrolyte penetration was also characterized, and the electrolyte penetration was simulated in a full 3D LIB cell.

4.3. Workflow and model description

4.3.1 Workflow

The workflow of our study is summarized in **Figure 1**. Through LBM, the electrolyte impregnation simulations were performed over 3D electrode mesostructures of NMC-based cathodes and full LIB cell, including the graphite anode and the separator. The 3D NMC cathode mesostructures were generated through three different approaches. The first one is the stochastic generation by using our *in-house* INNOV code.[171] In short, spherical particles are placed randomly until the required amount of Active Material (AM) is achieved. Periodic boundary conditions and an experimental particle size distribution are applied. The conductive additives and binder (or Carbon Binder Domain -CBD-) inactive phase is added pixel per pixel with the only constraint that it has to be in contact with the solid phase (either active or inactive phase). The second electrode generation approach is our previously reported physical-based Coarse-Grained Molecular Dynamics (CGMD) and Discrete Element Method (DEM) models. The CGMD fully simulates the electrode mixing and drying steps, CGMD coupled with DEM mimics the calendaring step. Both simulations are based on experimental input data such as the active material (AM) particle size distribution and explicitly considers the carbon-binder domain (CBD). For further details about our CGMD model and its validation, the readers are referred to our previous publications.[172],[121] The third origin of the cathode mesostructures is micro X-ray tomography of real manufactured electrodes. The electrode consisted in NMC 111 (Umicore), carbon black additive (C-ENERGYTM super C65, Imerys) and PVdF (SolefTM, Solvay) with a weight composition of 96-2-2. Two different conditions were essayed: uncalendered ($\varepsilon = 47.8\%$) and calendered ($\varepsilon = 26\%$). The NMC

samples obtained by tomography were imported into INNOV for segmentation and the CBD domain added stochastically in a film form.[173] The micro X-ray tomographic measurements have been conducted at the P05 synchrotron imaging beamline, Desy, Hamburg (Germany).[174] The data acquisition setup consisted of a KIT CMOS camera combined with a 10 times optic and a 100 μm CdWO₄ scintillator yielding an effective pixel size of 0.642 μm . The samples have been measured in absorption contrast mode using a photon energy of 25 keV selected by a double multilayer monochromator. For each sample, 2401 projections have been measured with equidistant angle steps of 0.15° and an exposure time of 130 ms each. To reduce ring artefacts the center of rotation has been shifted by random but tracked values of up to 100 μm . The data has then been reconstructed using the filtered back projection algorithm and were further denoised using a 3D non-local means filter.[175] Finally, GeoDict software was used to generate graphite electrode mesostructures. We created a 1000×1000×1000 voxel domain with a voxel size of 100 nm to make a representative structure. A log-normal particle size distribution was generated by considering the D10, D50 and D90 values to be 8, 11, and 18 μm , respectively. The structure is built in two steps. First spherical particles are homogeneously distributed within the domain, where the total volume fraction that they should occupy is specified. Then the overlaps between the generated objects are removed to approach the specified volume fraction as much as possible. The porosity of the resulting structure without the addition of carbon-binder is 35%. The addition of carbon-binder (using the same algorithm as before) leads to the final porosity of 33%. All obtained geometries were imported into the INNOV program for the slicing and convert segmentation procedure into binary images, after which a DAT file is created and imported into the LBM simulations.[68]

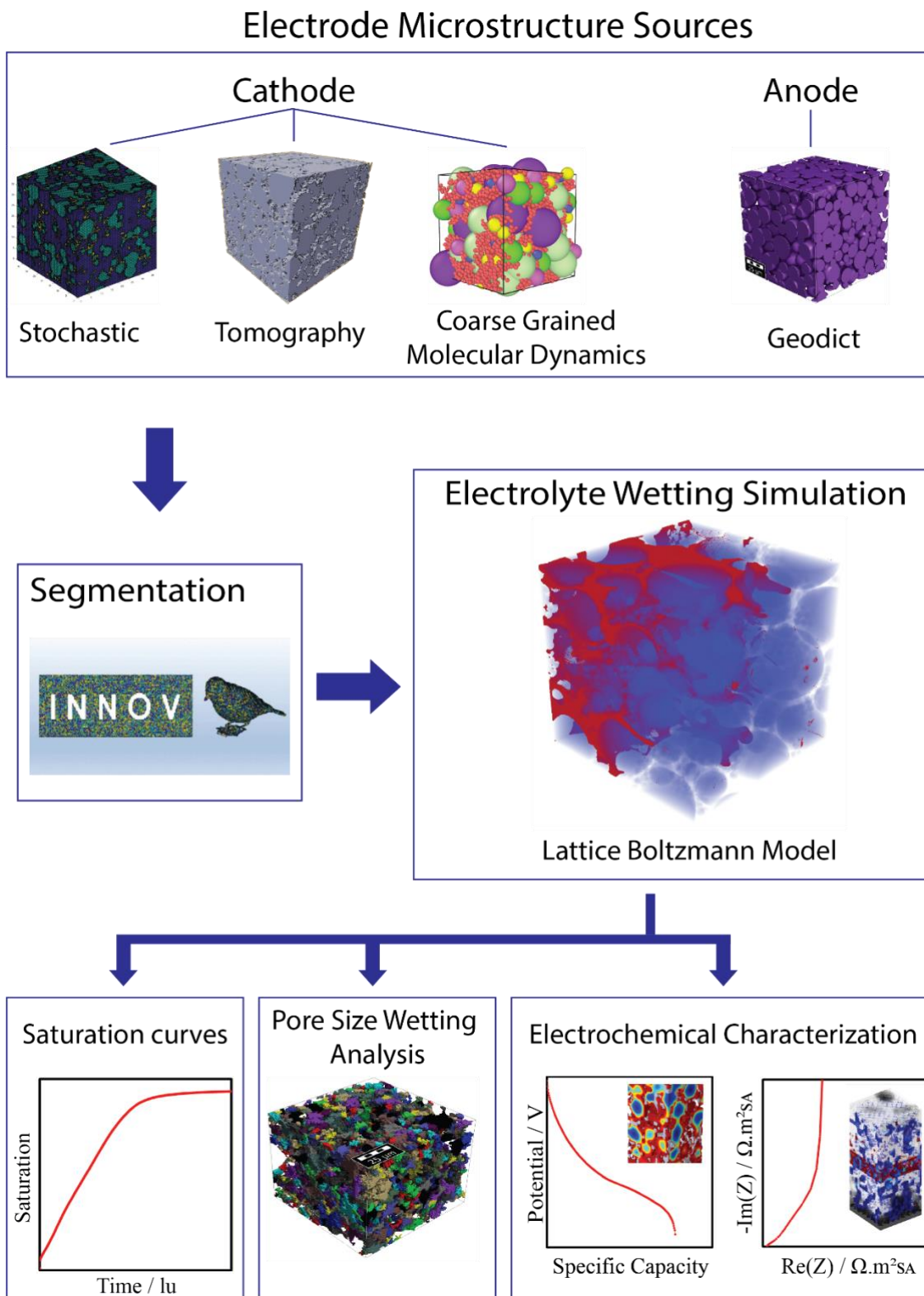


Figure 1. Schematic representation of the workflow used in the LBM simulation and its subsequent analysis.

4.2.1 Model Description

The LBM model developed for this study was based on three dimensional (D3Q19) cubic lattices using both an advection and a collision operator, where Q19 corresponds to fixed velocity vectors per fluid phase or component.[176]·[177] A scheme of the lattice structure is shown in **Figure 2**. The general LBM was initially developed by Shan and Chen and adapted in this work to describe three-dimensional interactions assuming an isothermal system.[178] In the proposed LBM model, motion and fluid-fluid interaction are defined by a set of particle distribution functions based on the Bhatnagar-Gross-Krook (BGK) collision operator where model constants can be used to characterize fluid density and velocity.[179] The left-hand side of equation (1) corresponds to a streaming term, and the right-hand side defines a collision term that together holds the system on Maxwellian equilibrium:[178]

$$f_i(x, t) - f_i(x + e_i \Delta t, t + \Delta t) = \frac{\Delta t}{\tau} [f_i(x, t) - f_i^{eq}(x, t)],$$

$$i = 0, 1, \dots, 18$$
(1)

In the equation above $f_i(x, t)$ is the particle distribution function which specifies the number of fluid particles at lattice location x and time t traveling in the i^{th} direction, e_i is a lattice velocity vector that corresponds to allowable directions of the velocity vector, Δt is a discrete time step and τ is the relaxation time. The relaxation parameter represents the rate of particle collisions which is related to the kinematic viscosity (ν) of the lattice $\nu = c_s^2(\tau - \frac{1}{2})$. In this kinematic viscosity expression c^s is the speed of sound of the lattice defined by $c^s = \frac{\Delta t}{\sqrt{3}}$ where $\Delta x = 1$ lattice length unit, lu .

As discussed above, the Navier-Stokes macroscopic kinetic theory was applied to describe fluid in the bulk flow at mesoscopic level in the LBM model.[180] The functional form of the equilibrium distribution $f_i^{(eq)} = f(\rho^n v^{n(eq)})$ has the following form for the purpose of recovering the Navier-Stokes equation:

$$f_i^{(eq)}(x, t) = w_i \rho \left[1 + \frac{e_i \rho^{eq}}{c_s^2} + \frac{1}{2} \left(\frac{e_i \rho^{eq}}{c_s^2} \right)^2 - \frac{1}{2} \left(\frac{e_i \rho^{eq}}{c_s^2} \right)^2 \right]$$
(2)

In the equation above w_i is the weight of each discrete velocity where $w_i = 1/3$ for $i = 0$, $w_i = 1/18$ for $i = 1, \dots, 6$ and $w_i = 1/36$ for $i = 7, \dots, 18$. The macroscopic values of density ρ is the density of $f_i(x, t)$ and macroscopic velocity u^{eq} is calculated by $u^{eq} = [u_x \quad u_y \quad u_z]$. [180]

The discrete velocities e_i are defined, with their representation given in **Figure 2**, [181]

$$\begin{aligned}
 & [e_0, e_1, e_2, e_3, e_4, e_5, e_6, e_7, e_8, e_9, e_{10}, e_{11}, e_{12}, e_{13}, e_{14}, e_{15}, e_{16}, e_{17}, e_{18}] \\
 = & c \begin{bmatrix} 0 & 1 & -1 & 0 & 0 & 0 & 0 & 1 & -1 & -1 & 1 & -1 & 1 & 1 & -1 & 0 & 0 & 0 & 0 \\ 0 & 0 & 0 & 1 & -1 & 0 & 0 & -1 & 1 & -1 & 1 & 0 & 0 & 0 & 0 & 1 & -1 & 1 & -1 \\ 0 & 0 & 0 & 0 & 0 & 1 & -1 & 0 & 0 & 0 & 0 & 1 & 1 & -1 & -1 & -1 & 1 & 1 & -1 \end{bmatrix}
 \end{aligned} \tag{3}$$

The density is obtained by summing the particle densities, $\rho = \sum_i f_i$ and the macroscopic velocity is obtained by summing the particle momentum and dividing by density, $u = \frac{\sum_i f_i e_i}{\rho}$. The external force (F_{ext}) is added to the macroscopic velocity as

$$u^{eq} = u + \frac{F_{ext} \tau}{\rho} \tag{4}$$

The two-phase fluid flow is simulated on the lattice by representing each fluid phase with its particle size distribution function as $f_i^\sigma(x, t)$, where $\sigma = w, nw$ is the index for each material particle distribution function. Another critical part of the system is the fluid-fluid interaction. In the Shan-Chen model, this interaction is described by interparticle forces ($F_{p,\sigma}$). Equation (5) represents the total fluid-fluid interaction where G_c is the interparticle strength: [180][182][183]

$$F_{p,\sigma}(x, t) = -G_c \rho_\sigma(x, t) \sum_i w_i \rho_{\bar{\sigma}}(x + e_i \Delta t, t) e_i \tag{5}$$

Only the nearest-neighbors lattices are active in the calculation of interparticle strength. By choosing the sign and magnitude properly, fluids can be separated to mimic immiscible flow behavior. As described above and shown in equation (6), $G_{ads,\sigma}$ is the interparticle adhesion strength between fluid and solid used to describe the wetting properties of the electrode with the adhesion force

$$F_{ads,\sigma}(x, t) = -G_{ads} \rho_{\sigma}(x, t) \sum_i w_i e_i \cdot s(x + e_i \Delta t, t) e_i \quad (6)$$

The negative (positive) values of $G_{ads,\sigma}$ can be used for wetting (non-wetting) fluids, respectively. At the fluid-solid interface, the solid is regarded as a phase with constant density. By carefully selecting the interparticle strength for each liquid-gas and solid phases, experimentally measured contact angle values were used as input for these studies.[141] The calculations of $G_{ads,\sigma}$ were based on

$$\cos \theta_w = \frac{G_{ads,nw} - G_{ads,w}}{G_c \frac{\rho_w - \rho_{nw/w}}{2}} \quad (7)$$

where ρ_w is the density of the wetting fluid and $\rho_{nw/w}$ is the dissolved density of the nonwetting fluid in the wetting fluid.[184] It is important to mention that the fluid-solid-interaction force exists only on the fluid-solid interface and it does not affect the macroscopic fluid equations.[185]

The adhesion force created by $G_{ads,\sigma}$ coefficients which are responsible for the wettability of the surface, are added in the model in the same way like the external forces:

$$u_{\sigma}^{eq} = u' + \frac{(F_{ads,\sigma} + F_{p,\sigma} + F_{ext,\sigma})\tau_{\sigma}}{\rho_{\sigma}} \quad (8)$$

The common velocity for the fluids is given by

$$u' = \frac{\sum_{\sigma} (\sum_i \frac{f_i^{\sigma} e_i}{\tau_{\sigma}})}{\sum_{\sigma} \frac{\rho_{\sigma}}{\tau_{\sigma}}} \quad (9)$$

The lattice pressure (P) at each node is calculated by the D3Q19 Shan-Chen LBM equation:[186];[187]

$$P = \frac{1}{3}[\rho_w + \rho_{nw}] + \frac{1}{3}[G_c \rho_w \rho_{nw}] \quad (10)$$

Initially, we assume all the pores within porous electrodes are filled with air for each LBM simulation. The electrolyte flow enters through the X-axis (thickness) and stops its motion when it reaches the end of the electrode. The periodic boundary condition across the Z and Y-axis (surface) were applied. As already mentioned, electrolyte parameters such as the density, contact angle with the solid phase, viscosity, and surface tension (equations 1, 6, 7) control the process of liquid injection within the electrode porosity. In this work, we considered an electrolyte composed of a 1M LiPF₆ solution in a 1:1 wt mixture of ethylene carbonate (EC) and diethyl carbonate (DEC) where the input parameters were experimentally measured with a BP100 bubble pressure tensiometer (surface tension), volume-changing method (contact angle) and AR 1000 rheometer (viscosity) as reported by one of the authors of the present article. [141] Evidently, selecting the electrolyte and active materials will alter the model's parameters, and exploring this parameter space is worth studying. For instance, using electrolytes with a higher concentration of salt, changes its viscosity, influencing the corresponding model parameters, such as kinematic viscosity (V) and ultimately hindering the electrolyte penetration process.[141] However, this systematic parametric study is beyond the scope of this work. Additionally, we must also note that other known effects that occur due to the electrolyte filling process, such as the swelling of the binder, were not taken into account in our model.

All the input parameters and sizes of simulation boxes are given in Table 7. The LBM simulations were carried out by using the open-source Palabos library version 1.0.[188] Each simulation took approximately two days to ten days, depending on the simulated system size. The tests were performed using a laboratory server with 256 Gigabytes of RAM.

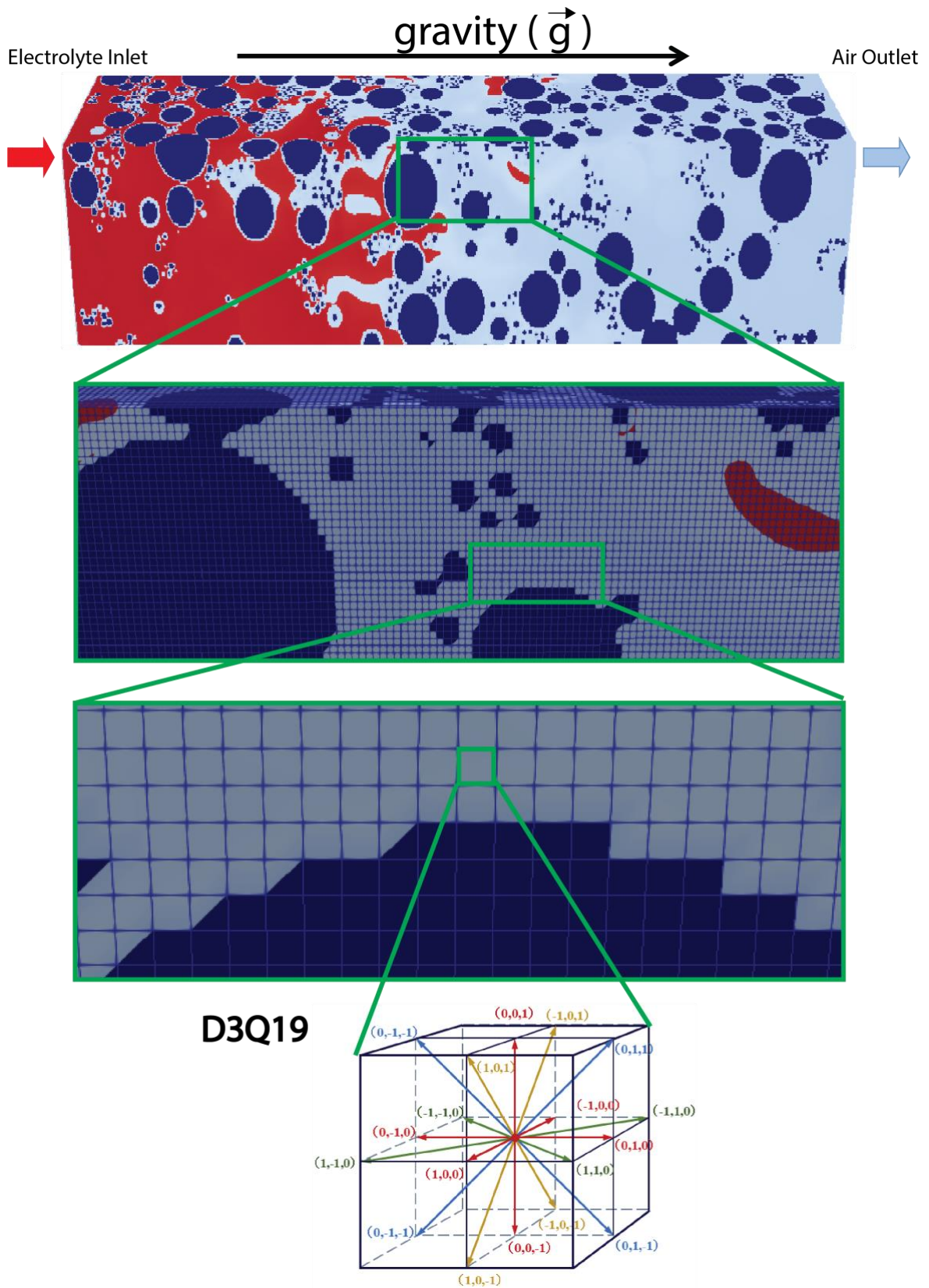


Figure 2. Lattice structure of three-dimensional fifteen velocity (D3Q19) model.

The PoroDict library (within GeoDict) was used to identify the 3D pore network. Pore space segmentation is done using the watershed algorithm.[131] It is known that the surface roughness on the images generally induces over-segmentation in watershed-based methods and many approaches exist to solve it.[132,189–191] In GeoDict, this is overcome by reconnecting the overly segmented pore-fragments back into a single pore, only if the shared interface percentage between the different pore fragments is larger than a chosen value. This interface threshold value is carefully selected so that the resultant pore sizes are not excessively large with respect to the original structure but are not overly segmented either. Once the pore space is labeled, we calculated the equivalent volume sphere's diameter for each pore and arranged them in a histogram. The histogram is further normalized to account for the non-uniform selection of the number of histogram bins.

In order to import LBM simulated electrodes into the electrochemical models, the NMC and CBD phases must be separated, as in the LBM workflow both phases are considered as one. Therefore electrodes with CBD and NMC phases were attained by transforming AM regions into CBD regions using the same stochastic algorithm mentioned above.

COMSOL Multiphysics environment was used to run electrochemical impedance spectroscopy (EIS) and galvanostatic discharge simulations. The 'Batteries & Fuel Cells' module for the discharge simulations and the 'Batteries & Fuel Cells' and the 'Transport of Diluted species' modules for EIS were implemented for the calculations.[68] The designs of the models and input parameters are identical to our previous reported papers.[68][69] The tests were performed using an Intel® Xeon® E5-4627 Cache @ 3.30 GHz with 264 GB of RAM. The discharge simulations took between 5 and 9 hours and the EIS tests 14 to 20 hours. Paraview, an open-source data analysis and visualization application, was utilized for the visualization of the data.[192]

The tortuosity factors were extracted by using GeoDict computational software. The first Fick's law and the MacMullin equation were applied to calculate the tortuosity factors. EIS tortuosity factors were calculated through the graphical method proposed by Landesfeind *et al.*.[55][128]

4.3. Results and discussions

4.3.1. Stochastically generated electrodes

Five cathode electrodes with different stochastic mesostructures and different porosities were generated for a first study on the mesostructure effect on the electrolyte penetration. As expected, by reducing the porosity, the tortuosity factor ($\tau_{GeoDict}$) increases, as reported in Table 1.[193]

Table 1. Tortuosity for stochastic electrodes with different porosities.

| Porosity | 25% | 30% | 35% | 40% | 45% | 50% |
|------------------|------|------|------|------|------|------|
| $\tau_{Geodict}$ | 2.20 | 1.90 | 1.70 | 1.53 | 1.48 | 1.36 |

Figure 3A shows the saturation curves for these mesostructures, where the saturation was quantified using the electrolyte volume ratio to the electrode's pore volume. All the cases display a profile with asymptotic growth, where saturation increases very fast at the early stages of impregnation. After a certain point, the gradient decreases and the higher the porosity, the faster the electrolyte penetrates through the porous mesostructure. Furthermore, the slope in the fast growth region tends to be smaller as the porosity decreases. The saturation curves for electrodes with porosities equal to 50% and 45% tend to rise monotonically and reach its maximum saturation before the other ones, indicating that the pore network is well connected and with less clogged areas. On the other hand, the impregnation for the mesostructures with 25% porosity displays slow electrolyte imbibition and reaches saturation at 1.5×10^5 lu (**Figure 3A**). The saturation curves derivatives, which describe the rate of electrolyte filling, are given in **Figure 3B**. It is clear from the figure that saturation rate tends to decrease with time for all the mesostructures, since the possible paths for fluid flow start to decline. The magnitude of the change in the rate is more significant for the electrodes with higher porosity (40% or higher). When electrode porosity is low, generally, the rate at which the electrolyte penetrates is monotone because the possible paths for fluid flow are limited. Overall, the graph clarifies that the rate of saturation is proportional to the structure's porosity. **Figures 3C** and **3D** represent the outgoing air at different time steps for the electrodes with 50% and 25% porosity, respectively. It further illustrates that the gas escape rate is much faster for the electrode with higher porosity. At 2×10^4 lu, all the electrode is already impregnated for the structure with 50 % porosity (**Figure 3C**), while for the one with 25 % porosity (**Figure 3D**), more than half of the air remained in the structure at that time step. We can also see some air trapped inside the electrode with 25 % porosity because there are several clogged pores within the geometry, explaining why the electrolyte saturation never reaches 100 %. This result confirms that decreasing the electrodes' porosity increases the wetting time and its unwetted regions.

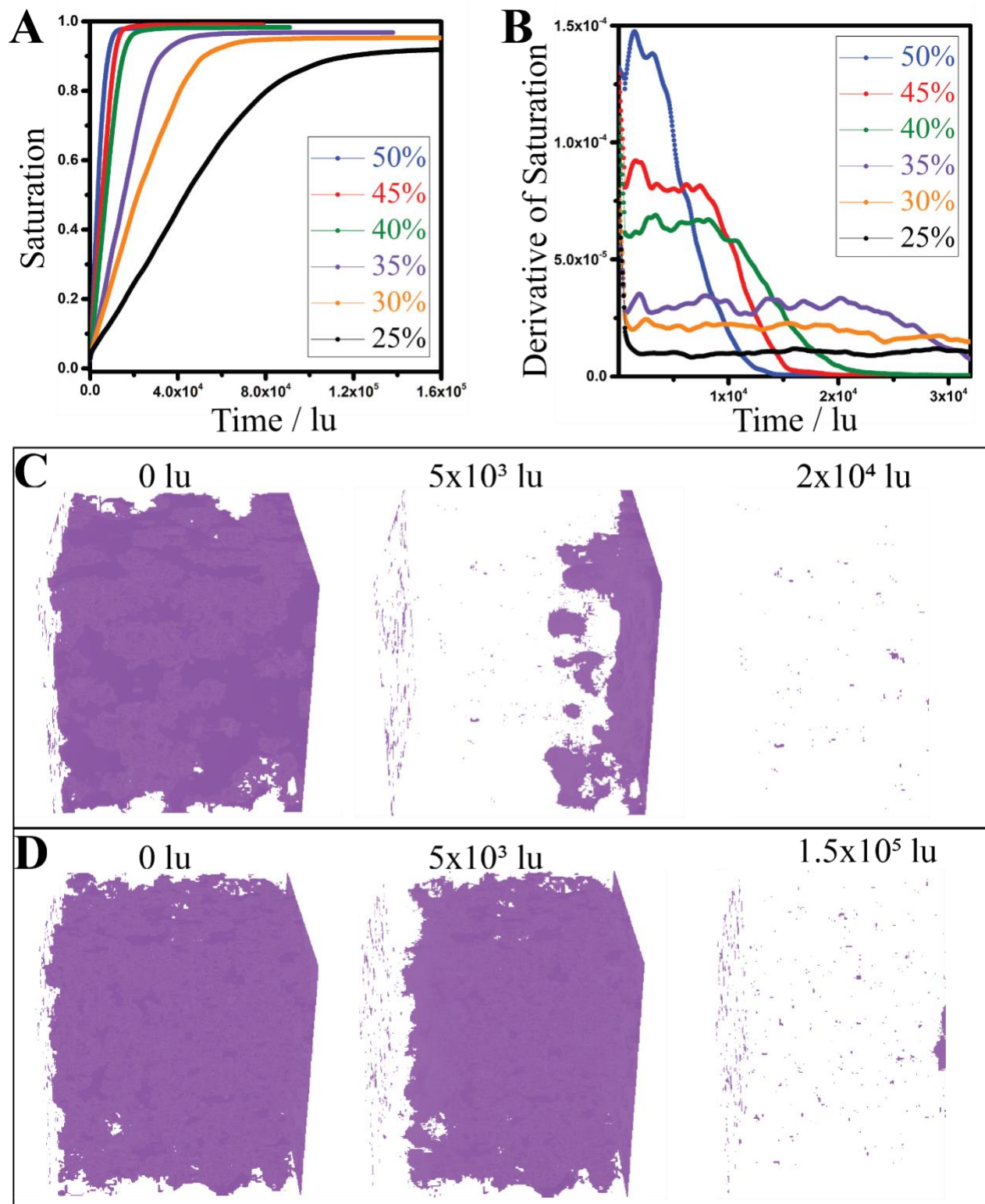


Figure 3. (A) Saturation profile of liquid electrolyte in the cathode with various porosities. (B) The first derivative of the saturation profile of liquid electrolyte in the cathode with various porosities. (C) The air output flow process (in purple) for the electrode with 50% porosity and (D) electrode with 25% porosity at different time steps.

4.3.2. Calendering effect

Usually, electrodes are calendered to maximize volumetric power and energy density. The calendering step changes the electrode's porosity, along with its pore size distribution and pore network.[194][43] However, this increased compactness of calendered electrodes might cause incomplete electrolyte wetting. Therefore, in this subsection, the objective is to study the calendering effect over the electrolyte filling on NMC111-based cathodes, obtained through both micro X-ray tomography and CGMD+DEM based simulations.

Table 3 shows the calculated tortuosity factors and porosities for all electrodes used in this subsection. The tortuosity factor increases from 1.53 to 2.89 and porosity decreases from 48 % to 25 % upon calendaring for tomography NMC cathodes. The same trend can be seen for CGMD+DEM-derived electrodes, where tortuosity changed from 1.53 to 1.92 and porosity decreased from 41.6 % to 27.2 %. The negative correlation between porosity and tortuosity factor is expected because electrode compaction leads to pores in general to a decrease of the pores interconnectivity.[195]

Table 2. Porosity and Tortuosity factor for the uncalendered and calendered NMC111 tomography-derived electrodes.

| | Uncalendered tomography | Calendered tomography | Uncalendered CGMD | Calendered CGMD+DEM |
|------------------|-------------------------|-----------------------|-------------------|---------------------|
| Porosity | 48% | 25% | 41.6% | 27.2% |
| $\tau_{Geodict}$ | 1.53 | 2.89 | 1.53 | 1.92 |

During the calendering step, the applied force leads to a change in pores size distribution (PSD) within the electrode, which is shown in **Figure 4A** for the NMC-based cathodes. After the calendering step, the mean pore size was reduced from 15 μm to 5 μm . The same behavior can be seen for CGMD electrodes (**Figure 4B**), where the mean pore size decreased from 8 μm to 4 μm . The uncalendered tomography electrode saturation curve (**Figure 4C**) increases rapidly because of more extended penetration paths and larger pore sizes, as demonstrated in **Figure 4A**. On the contrary, the wetting process rate for the calendered tomography one is reduced significantly and it never reaches 100% pore saturation, indicating dead pore zones with trapped air. **Figure 4D** presents the respective saturation curves for uncalendered CGMD and calendered CGMD+DEM electrodes. Equivalently, the saturation is faster for the uncalendered CGMD compared to

calendered CGMD+DEM. The difference comes from its higher porosity, lower tortuosity (Table 2), and higher pore size distributions (**Figure 4B**). As discussed above, higher porosity and PSD cause a better pore network connectivity, which opens a broad path for fluid flow. The saturation reaches its maximum at 0.99, and at a rate five times faster, for the uncalendered CGMD, when compared to a maximum of 0.96 for the calendered CGMD.

The better wettability and faster saturation nature of CGMD structures, when compared to the tomography ones, is found on the shape of the carbon additive and binder domain. CGMD simulations rely on the assumption that CBD has a spherical shape (due to the coarse-graining assumption in this simulation technique), but it is known that CBD forms a highly anisotropic phase. Due to this fact, electrodes coming from tomography have more geometrically intricate pores than CGMD electrodes. Nevertheless, there is only a three percent difference in saturation between calendered tomography and CGMD. The global trend for both uncalendered and calendered electrodes between CGMD and tomography cases showed the same pattern and are very closely allied.

The wetting process visualization for the uncalendered and calendered tomography electrodes is shown in **Figure 5A**. At the beginning of the simulation, there is a higher volume for electrolyte entrance in the uncalendered electrode. As the impregnation proceeds, the bigger and well-connected pores of the uncalendered electrode allow a uniform filling, as it can be seen in the almost plane cross-section electrolyte diffusion direction. The LBM simulations demonstrate the electrolyte occupies large pores first, which means the capillary forces, which result from the pressure difference between electrolyte and air phases, dominate the flow. The electrolyte chooses a preferential flow path within the 3D structure depending on local resistance forces. As a result, the flow is always directed towards a larger pore within the available options. Uncalendered electrode has higher PSD and higher porosity with all the big pores well connected to each other. Consequently, fluid flow is homogenous and fast as represented in **Figure 5A**. The calendered electrode with its smaller and less connected pores exhibits a non-uniform filling. This is validated by the air flow in **Figure 5B**, where air output flow is represented at different time steps for uncalendered and calendered tomography electrodes. It is easy to see the consistent homogenous airflow across all time steps for the uncalendered electrode. Also, at the end of the simulation, there is almost no air trapped within the porous structure.

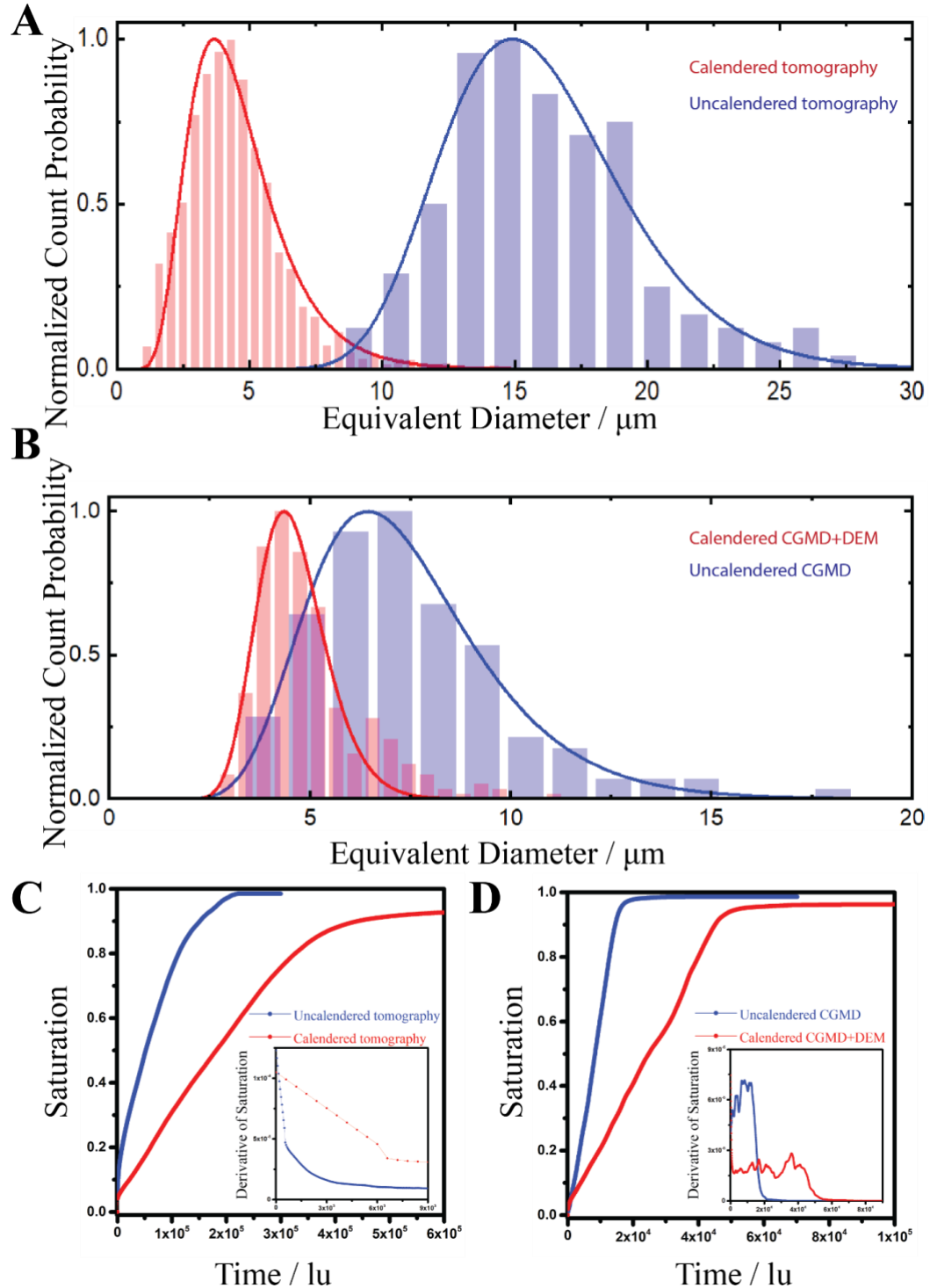


Figure 4. (A) Normalized pore size distribution for uncalendered and calendered tomography NMC 94% - CBD 6%. (B) Normalized pore size distribution for uncalendered and calendered CGMD+DEM. (C) Saturation profile and the first derivative (inset) of the saturation profile of liquid electrolyte for the calendered and uncalendered tomography NMC 94% - CBD 6% electrodes (D) Saturation profile and the first derivative (inset) of liquid electrolyte for the calendered CGMD+DEM and uncalendered CGMD.

On the contrary, air outflow is heterogenous and slower for the calendered electrode, and there are many air trapped volumes when simulation reaches convergence point. To better understand the nature of the un-filled pores, the geometrical analysis of the calendered electrode pores is performed with our INNOV application.[43] The study reveals the volume fraction of geometrically blocked pores equal to 5% of total volume and it is mostly responsible for creating unwetted zones. To better understand the impact of the PSD on the electrolyte impregnation process, the pores were split into three groups: big, medium, and small. Each group corresponds to one-third of the total pore volume. **Figures 7A and B** present the saturation curves for each pore group for the tomography uncalendered and calendered electrodes. For the former, big and medium pores show almost the same slope. On the other side, the saturation rate is slower for the small pores, and it does not reach its maximum, indicating that all the geometrically isolated un-wetted pores come from this group. In the case of the calendered tomography electrode, the saturation rate for all the groups decreased, compared to the uncalendered electrode, and none of them reached its maximum. Like tomography-derived electrodes, all big pores in the CGMD-based ones (**Figures 7C and D**) reached 100% saturation and the small pores have the lowest maximum saturation for both electrodes. We note also in **Figure 7C** contrary to the **Figures 7A, 7B and 7D** that the medium-pores group shows higher saturation rate compare to big-pores. We know that the electrolyte penetration rate depends on the porosity, tortuosity factor and pore size distribution of the electrode. The data shown in Table 2 shows that the uncalendered tomography (**Figure 7A**) and CGMD (**Figure 7C**) electrodes' porosity and tortuosity factors are almost similar. However, we hypothesize that this phenomenon's origin is related to the electrode's discontinuous pore network organization.[196] Across the thickness of the CGMD electrode, the three groups' population is not homogeneous, which leads to different groups dominating fluid flow across different parts of the thickness. We think that the fluid inlet is mainly populated with big pores, which leads to an increment of saturation at the early stage. When electrolyte reaches some depth in the electrode where pores with big size might be absent, flow is dominated by other groups. Even though average electrode properties are the same for both uncalendered tomography and uncalendered CGMD, their respective pore networks are not the same, which may explain this counter-intuitive behavior of **Figure 7C**. [197]

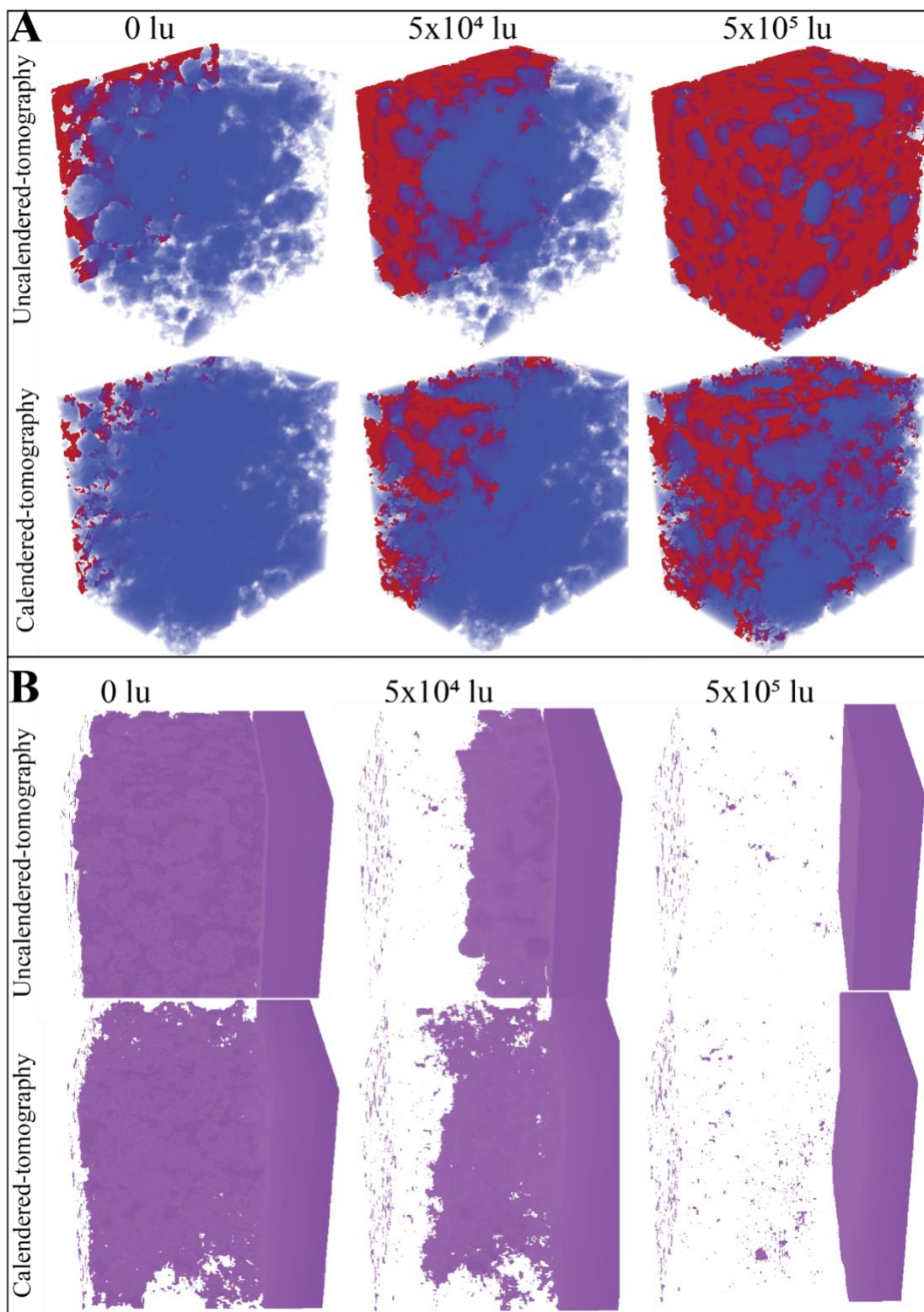


Figure 5. The wetting (red) process visualization for the (A) uncalendered and calendered tomography NMC 94% - CBD 6% (blue) at different time steps (B) the gaseous air (purple) in uncalendered and calendered tomography NMC 94% - CBD 6% electrode at different time steps.

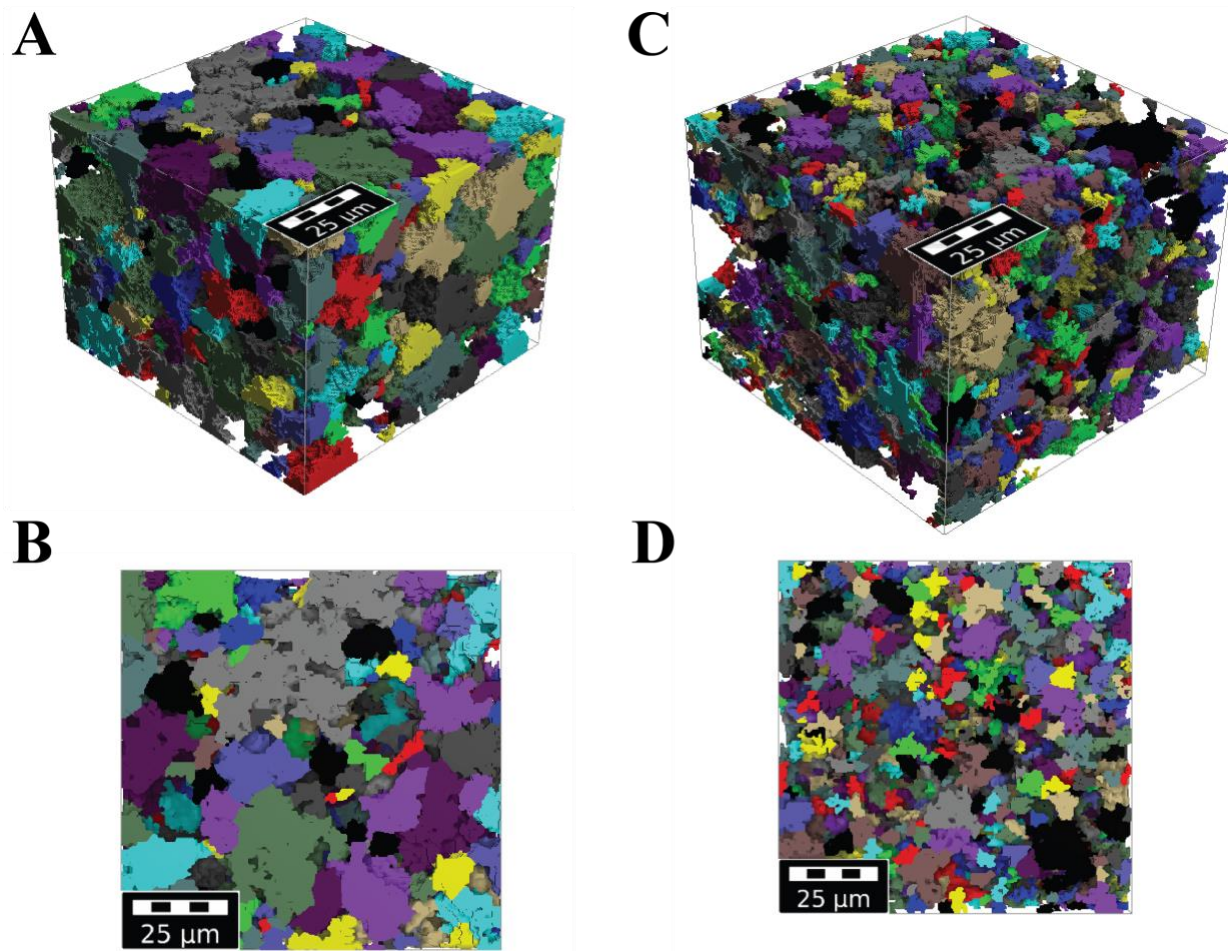


Figure 6. The extracted pore network from (A-B) uncalendered and (C-D) calendered tomography NMC 94% - CBD 6%.

As discussed above, the calendaring step decreases the electrode porosity and pore sizes, potentially creating more geometrically isolated pores. The idea that compressing the electrode creates clogged pores with a small size proved itself once more. These results suggest that calendaring the electrode to gain power density would be negatively correlated with the electrode's wettability which is consistent with the experimental results.[146] While the results are also in good agreement with intuition, our model allows providing quantitative results which have never been reported before, such as the correlation between saturation rate, processing conditions and micro structure. We believe that achieving optimally performing electrodes requires solving the compromise between the calendaring process and the electrolyte filling step. In short, better electronic conduction is achieved by calendaring, but it could result in clogged and poorly

connected pores that hinder the electrolyte penetration. Therefore, we recognize that keeping a well connected pore-network upon calendaring is vital.

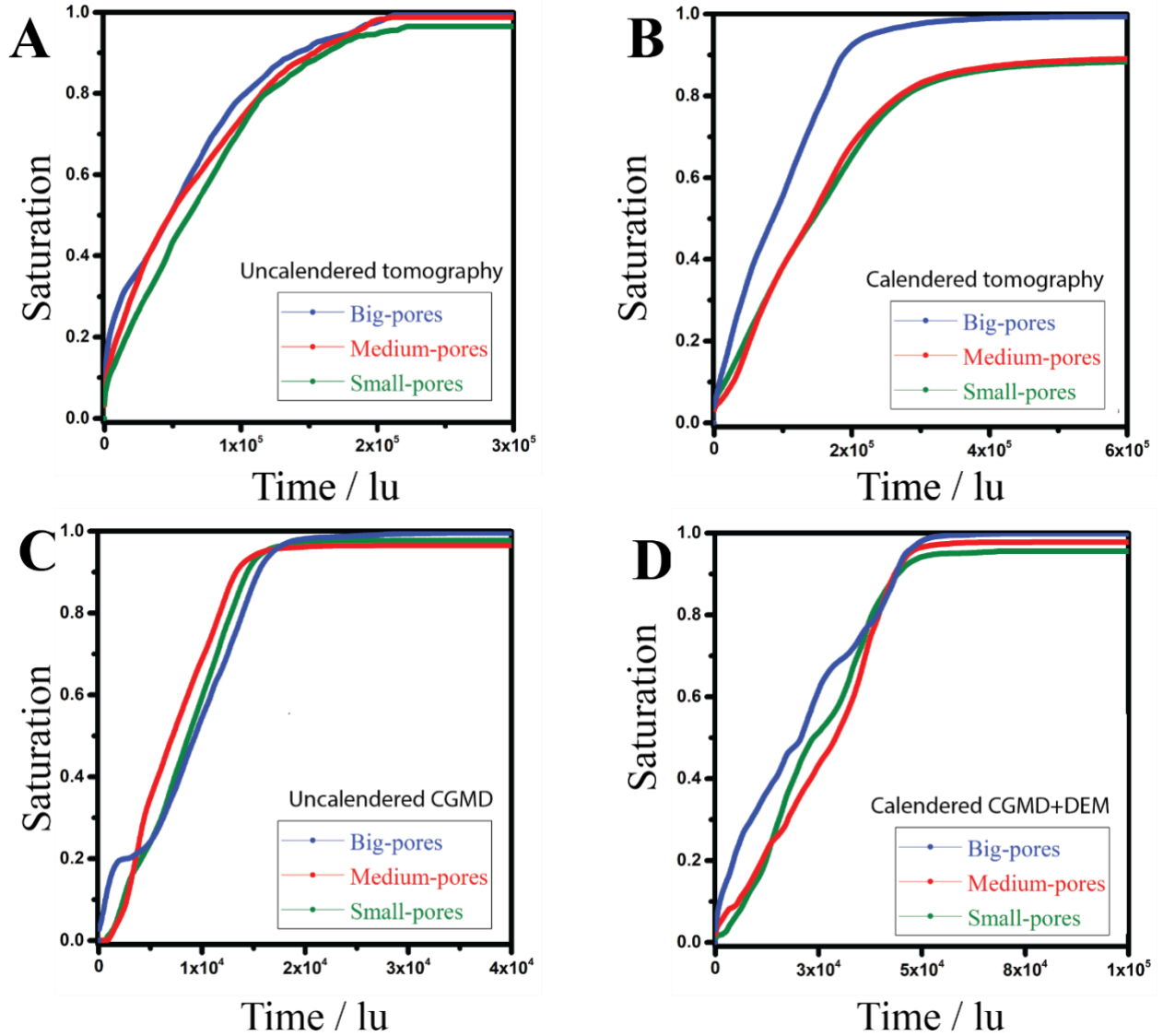


Figure 7. Saturation profile of liquid electrolyte three groups, big, medium, and small within (A) Uncalendered tomography NMC 94% - CBD 6% (B) Calendered tomography NMC 94% - CBD 6% (C) Uncalendered CGMD and (D) Calendered CGMD+DEM

4.3.3 Electrolyte infiltration direction in full cells

Conventionally, during LIB manufacturing process, the different parts of the cell are assembled in a sandwich format before filling with the electrolyte.[115][198] Therefore, NMC₁₁₁, Celgard2500, and Graphite electrodes were put together to construct the full LIB format and run LBM

simulations.[43] The porosities and tortuosity factors for the separator and the negative electrode are given in Table 3.

The saturation curves were the electrolyte inlet resides at two different sides of the full cell, is presented in **Figure 9A**. The saturation curves show several different plateaus and dynamic steps in both cases. When the electrolyte impregnation inlet is from the NMC the cell behaves precisely like the NMC electrode (**Figure 4C**). At around time step 4.5×10^4 lu the saturation speed increases when the electrolyte reaches the separator (**Figure 9B**). In it, the fluid goes relatively faster because the separator has a higher porosity and a very well interconnected porous structure, as seen in the **Figure 8**. At about 5.2×10^4 lu, the curve trend changes again as the fluid reaches the graphite electrode. The speed decreases drastically as the porosity of the negative electrode is smaller compared to the separator and the positive electrode, reaching the convergence at around 1.2×10^5 lu (**Figure 9B**). The graphite and separator structures are 100% wetted and all the unwetted zones are coming from NMC structure due to isolated pores as discussed above. The same three-step behavior can be observed for the cell setup where the electrolyte inlet is on the negative electrode. The origin of the three steps again comes from the microstructure and PSD of the three different components. The electrolyte impregnation speed is slower than in the previous case because the initial available space for the electrolyte entrance is smaller in the graphite electrode. The path of the electrolyte at different time steps is shown for both cells in **Figures 9C** and **9D**. Overall, the full cell studies showed the importance of the order of the components within the cell. Also, the initial electrolyte entrance location plays a crucial role in the LIB cell overall wetting time. It is worthy to note that electrolyte won't penetrate through the electrode stacks from anode to cathode or vice versa unless porous current collectors are used. Nevertheless, this result shows that the starting location of electrolyte injection can impact the overall electrolyte wetting process. This effect is under further investigation and will be reported in our future publications.

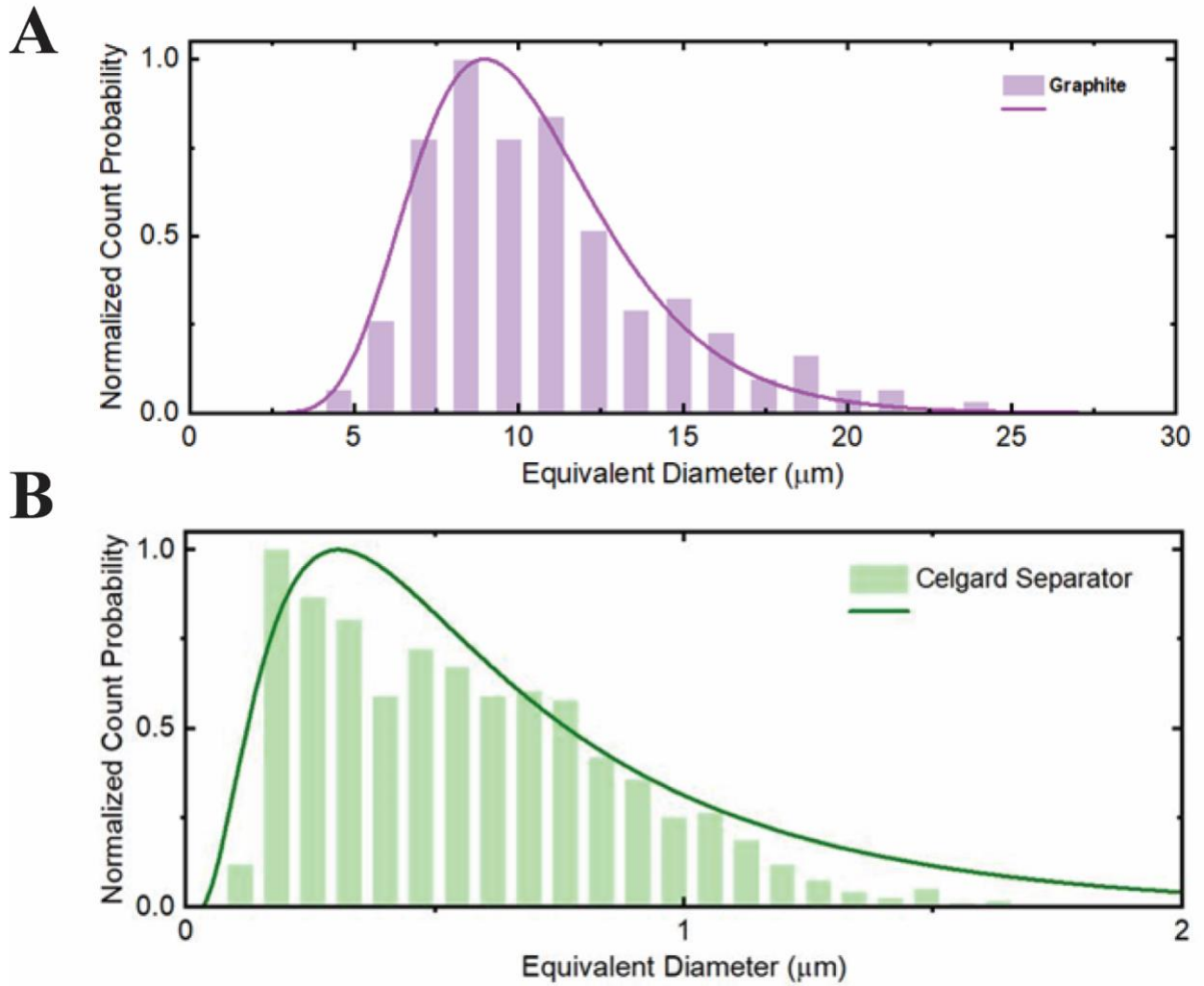


Figure 8. Normalized pore size distribution for (A) Graphite and (B) Celgard 2500 tomography.

Table 3. Porosity and tortuosity factor for graphite electrode and Celgard2500 separator.

| | Graphite | Celgard2500 | Un-calendered tomography |
|------------------|----------|-------------|--------------------------|
| Porosity | 31.5% | 55% | 48% |
| $\tau_{Geodict}$ | 1.63 | 1.49 | 1.53 |

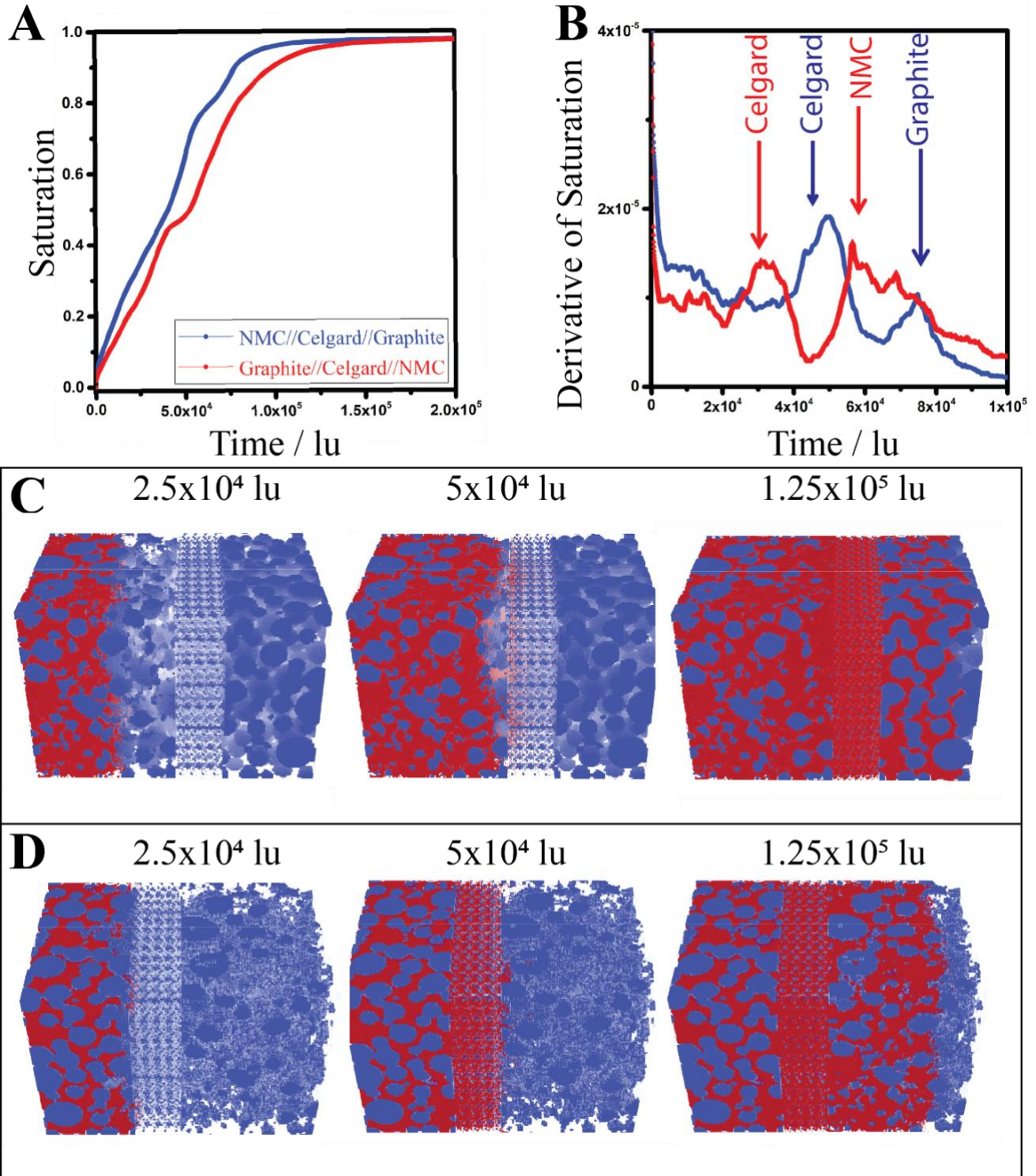


Figure 9. (A) Saturation curve for the NMC//Celgard//Graphite and Graphite//Celgard//NMC cells, (B) The first derivative of the saturation profile of liquid electrolyte in the cathode with various porosities, the wetting (red) process's visualization for the (C) NMC//Celgard//Graphite (blue) and (D) Graphite//Celgard//NMC (blue) at different time steps.

4.3.4 In silico electrochemical performance evaluations

In this section we study the electrolyte impregnation effect on the electrochemical performance of the electrode by means of continuum simulations. The electrochemical model is 4D-resolved (three spatial dimensions and time), and it accounts for the explicit location of AM and CBD in the electrode mesostructures. It resolves the intercalation electrochemistry at the NMC/electrolyte interface (for the case of the discharge simulation), the electrical double layer formation within CBD and at the CBD/electrolyte interfaces (for the case of EIS simulation), the lithium transport in the NMC (for the case of the discharge simulation), ionic transport in the electrolyte and in the CBD, electronic transport in both NMC and CBD. Related mathematical details and used parameters are described in our previous publications.[101][69] The following study was carried out for the case of the tomography-derived calendered NMC electrode.

Our 4D-resolved EIS model applied to an *in silico* symmetric cell setup already proved valuable to capture ionic and electronic resistance within the electrode.[101] We use it here to capture the effect of unwetted zones on the change in ionic resistance within the electrode. The symmetric cell consists of two identical electrodes, separated by a 12 μm thick Celgard separator based on the SEM images from the open-source data of Lagadec *et al.*[199] Two 5 μm thick aluminum current collectors were added at each electrode borne, and simulations were carried out by assuming a blocking electrolyte.[98] **Figure 10A** shows the Nyquist plots for the two cases: one assuming that all the pores are filled with electrolyte and another one corresponding to the wetted electrode according to LBM results. The corresponding response can be analyzed by dividing it into three regions. The high-frequency region ($>10^5$ Hz) is associated with the separator's resistance and the electrode's electronic resistance.[101,128] As the electrode architecture was not changed during the LBM simulation, both curves overlap in the high-frequency region plot. On the other side, the low-frequency ($< 1\text{Hz}$) region for both cases shows an ideal 90° behavior as the electrode/electrolyte interface is ideally polarizable, with constant electrical double layer capacitance.[200] Usually, the slopping mid-frequency (1- 10^5 Hz) region represents electrolyte ionic resistance within the porous electrode.[101][128] It can be seen that the length of the mid-frequency slope increases for the electrode with unwetted zones. This phenomenon's origin is that the ions have to take a longer path for the electrode with unwetted zones, as illustrated schematically in **Figure 11**. Moreover, the length of the slope directly links to the EIS tortuosity factor (τ_{EIS}).[128] Calculated tortuosity factors from the EIS (τ_{EIS}) are shown in Table 3.

The discharge curves for both electrodes at C/20 are reported in **Figure 10B**. The post-LBM electrode displays a lower specific capacity than the one entirely filled with electrolyte. This behavior is expected since it has been shown earlier that the unwetted zones will hinder the transport of ions and reduce the active surface area where Li^+ can intercalate (see **Figure 11**). The inset in **Figure 10B** represents the relative amount of intercalated Li in the AM at the surface in contact with unwetted areas to further prove the latter. In the post-LBM electrode case, this surface will be inactive and the only way Li can access these regions will be by diffusion through the AM. In the other case, Li^+ will intercalate at this surface, hence a higher lithiation state for the 100 % filled with electrolyte electrode compared to the post-LBM electrode case (100% and 64.7%, respectively). These heterogeneities in Li intercalation arising from the electrode filling will cause the electrode to have steeper Li concentration gradients, hence a higher polarization and a loss in capacity.[69] The combination of the two electrochemical models allowed us to characterize the wetting degree's impact thoroughly. The results demonstrated that the dry electrode mesostructure is not the only impactful parameter, but its degree of wettability is also crucial in its overall electrochemical performance.

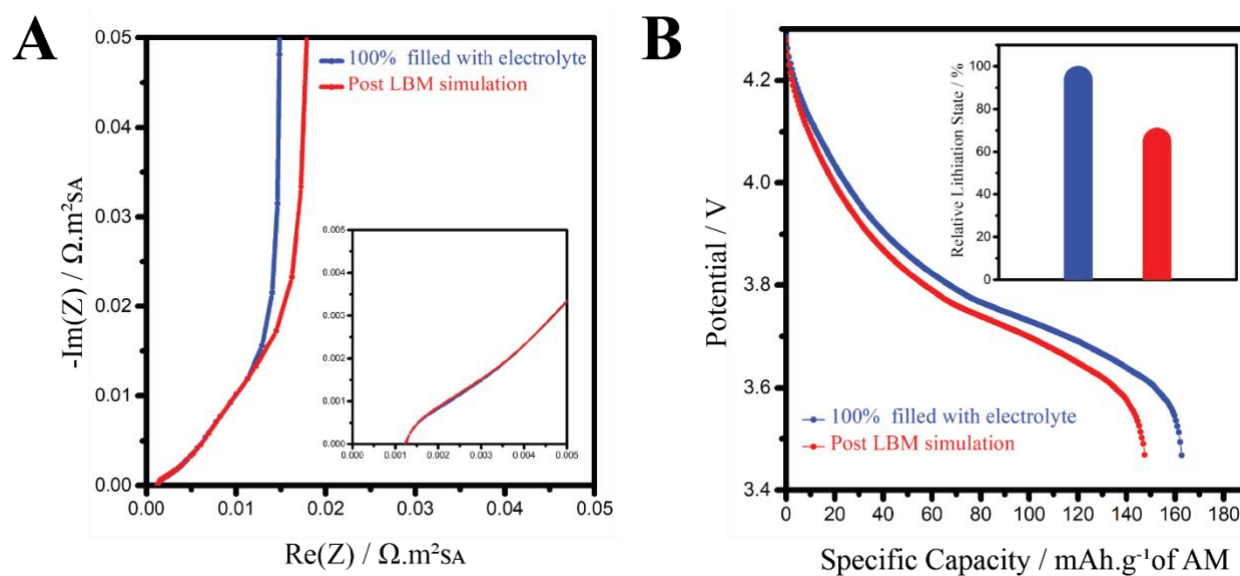


Figure 10. Simulated EIS and Discharge models for the calendared tomography NMC 96% - CBD 4% filled with 100% electrolyte and Post LBM simulated (A) Nyquist plots in the symmetric cell configuration, (B) Discharge curve at C/20 for the LBM output and the 100% filled electrode, the inset shows the average lithiation state of the AM surface in contact with the unfilled void at the end of discharge.

Table 5. Ionic resistances (R_{ion}) of the electrolyte within the porous electrode and associated tortuosity factors (τ_{EIS}) calculated according to the Transmission Line Model proposed by Landesfeind et al. [128]

| | R_{ion} ($\Omega \text{ m}^2$) ^a | τ_{EIS} ^b |
|------------------------------|---|---------------------------|
| 100% filled with electrolyte | 0.014 | 2.02 |
| Post LBM simulations | 0.0162 | 2.36 |

^a Obtained from the graphical interpolation of the high-to-mid frequency region on the EI spectra.

^b EIS-derived tortuosity obtained through the graphical method according to Landesfeind *et al.*

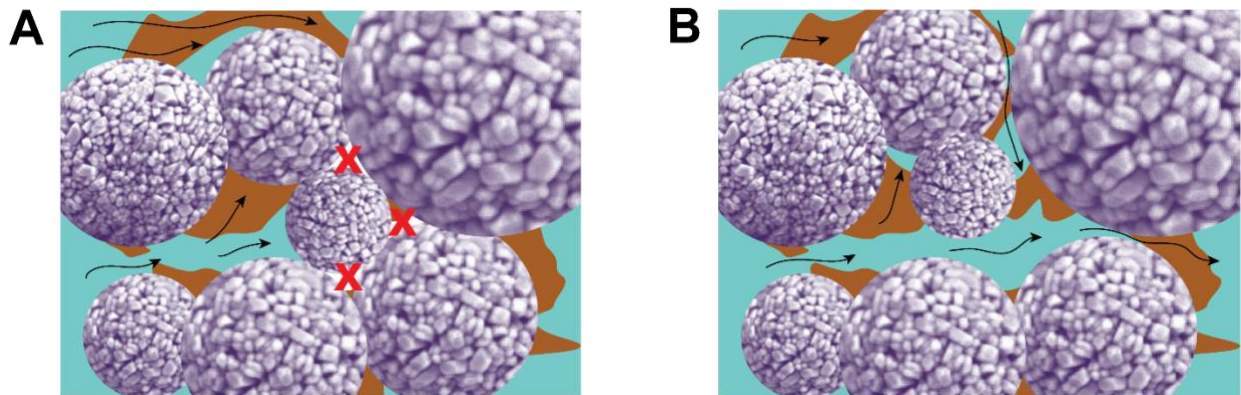


Figure 11. Schematics of ionic paths during the simulation of the electrochemical response (EIS or discharge) of the calendared tomography NMC 96% - CBD 4% electrodes for the case where the electrolyte does not fully fill the pores as calculated by the LBM for (A). The case where electrolyte is assumed to fill all the pores of the electrode (B). Blue colour represents the electrolyte while brown colours represents the CBD.

4.5. Conclusion

A novel three-dimensional LBM was developed to simulate electrolyte filling in different LIB cathode mesostructures and full cells. The LBM simulates unsteady fluid flow and two-phase (electrolyte and air) interface evolution during the electrolyte passage through the mesostructures. This model allowed us to visualize the electrolyte penetration and characterize the degree of wettability with a very high degree of detail. The electrodes from three different sources (stochastic, tomography, CGMD) were used in this simulation study.

The results indicate that porous electrodes' wettability is strongly linked to their porosity, pore size distribution, tortuosity factor and pore network organization. Also, the effect of calendaring on the wettability is found to be very significant. The studies further revealed that the geometrically isolated pores play a major role in electrodes' poor wettability. The full cell setup investigations demonstrated that the degree of electrolyte penetration in each electrode also strongly depends on the initial electrolyte droplets' location. Extension of this study to other setup configurations may give accurate suggestions to where to set the initial electrolyte inlet for optimal filling, but this is beyond of the present study's scope. Also, electrochemical simulations were performed to assess the effect of wettability on the positive electrode's overall performance. These simulations show that poor wettability leads to increased ionic resistance and inhomogeneous lithium intercalation, resulting in a lower capacity vs. the case where the electrolyte is supposed to fully fill the electrode pores, as typically assumed in many performance mathematical models in the literature. The simulation tool reported in this work is devoted to be integrated in the overall computational workflow of our ARTISTIC project simulating all the steps of the LIB electrode manufacturing process, including the electrode slurry, the coating, the drying, the calendaring, the electrolyte infiltration and the resulting electrochemical performance.[50]

Nomenclature

Table 6. Mathematical notations and list of symbols

| | |
|------------------|--|
| $f_i(x, t)$ | The distribution function of the fluid component |
| x | Lattice location |
| t | Traveling time |
| Δt | Discrete time step |
| i | i th direction |
| e_i | Lattice velocity vector |
| τ | The relaxation time |
| u^{eq} | Macroscopic velocity |
| e_i | Discrete velocities |
| F_{ext} | External force |
| ρ | Fluid density |
| ρ_w | Density of the wetting fluid |
| w_i | Weight of each discrete velocity i |
| c^s | Speed of sound |
| ν | Kinematic viscosity |
| $v^{n(eq)}$ | Equilibrium velocity |
| F^n | Total interaction force for fluid n |
| G_c | Interparticle strength |
| $G_{ads,\sigma}$ | Fluid-solid interparticle strength |
| P | Lattice pressure |

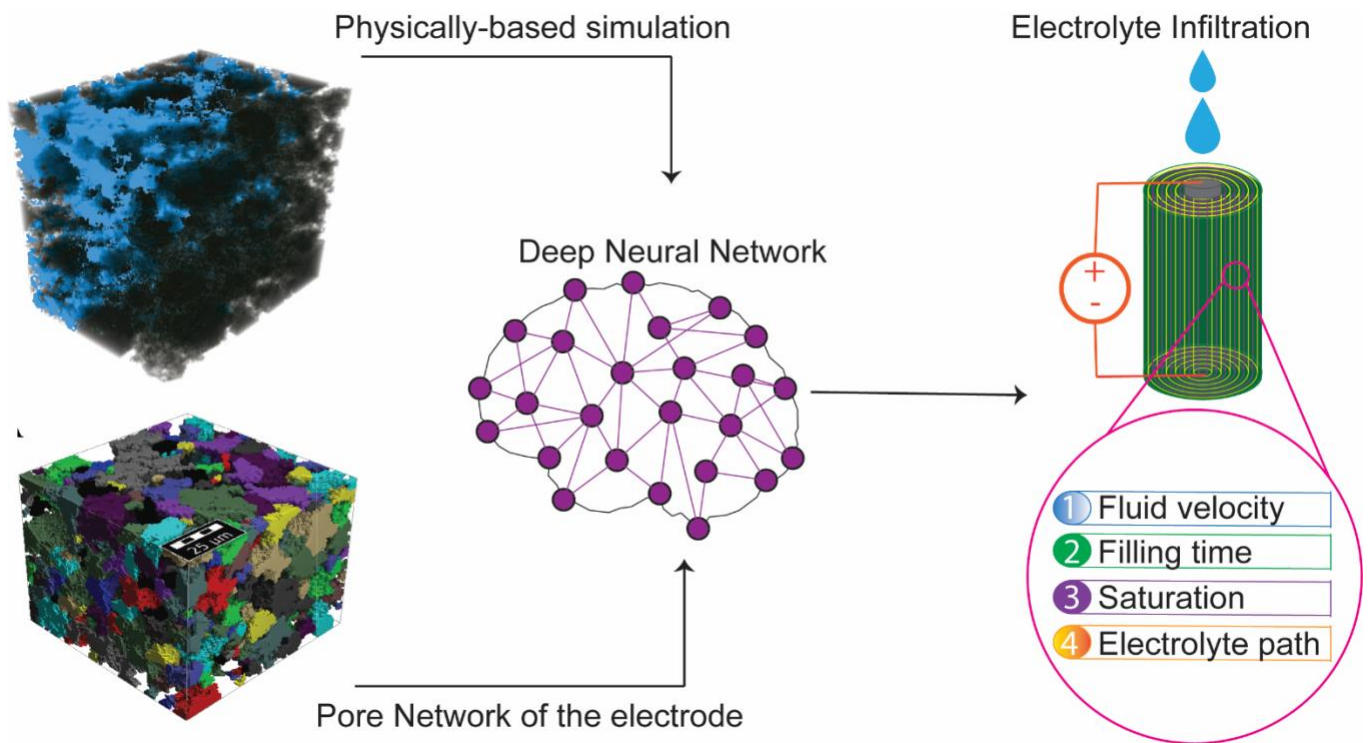
Table 7. Simulation inputs and geometry sizes.

| | | |
|---------------------------|------------------------|------------------------------|
| AM 96%-CBD 4% Porosity25% | 100 × 100 × 100 voxels | 50 × 50 × 50 μm ³ |
| AM 96%-CBD 4% Porosity30% | 100 × 100 × 100 voxels | 50 × 50 × 50 μm ³ |
| AM 96%-CBD 4% Porosity35% | 100 × 100 × 100 voxels | 50 × 50 × 50 μm ³ |

| | | |
|--|------------------------------------|---|
| AM 96%-CBD 4% Porosity40% | $100 \times 100 \times 100$ voxels | $50 \times 50 \times 50 \mu\text{m}^3$ |
| AM 96%-CBD 4% Porosity45% | $100 \times 100 \times 100$ voxels | $50 \times 50 \times 50 \mu\text{m}^3$ |
| AM 96%-CBD 4% Porosity50% | $100 \times 100 \times 100$ voxels | $50 \times 50 \times 50 \mu\text{m}^3$ |
| AM 96%-CBD 4% un-calendered tomography | $100 \times 100 \times 75$ voxels | $100 \times 100 \times 75 \mu\text{m}^3$ |
| AM 96%-CBD 4% calendered tomography | $100 \times 100 \times 75$ voxels | $100 \times 100 \times 75 \mu\text{m}^3$ |
| AM 96%-CBD 4% un-calendered CGMD | $107 \times 107 \times 603$ voxels | $107 \times 107 \times 60.3 \mu\text{m}^3$ |
| AM 96%-CBD 4% calendered CGMD+DEM | $107 \times 107 \times 474$ voxels | $107 \times 107 \times 474 \mu\text{m}^3$ |
| CelgardPP1615 | $100 \times 100 \times 25$ voxels | $100 \times 100 \times 25 \mu\text{m}^3$ |
| Graphite 95%-CBD 5% | $100 \times 100 \times 50$ voxels | $100 \times 100 \times 50 \mu\text{m}^3$ |
| Electrolyte denisty | 10 | $1300 \frac{\text{kg}}{\text{m}^3}$ |
| Gas denisty | 1 | $1.18 \frac{\text{kg}}{\text{m}^3}$ ([201]) |
| Contact angle | 0.357/1.643 | 90° [141] |
| Surface force (gas-liquid) | 0.1 | 7.28×10^{-2} ([141]) |
| t_0 | 1 <i>lu</i> | $1 \times 10^{-6} \text{s}$ |
| Reynolds number | 10^{-3} | 10^{-3} ([141]) |
| Capillary number | 10^{-5} | 10^{-5} ([141]) |

Chapter - V

Machine Learning 3D-resolved Prediction of Electrolyte Infiltration in Battery Porous Electrodes



5.1. Introduction

Lithium ion batteries (LIBs) can provide high energy and power densities with long cycle life,[202] constituting the technology of choice nowadays for electronic gadgets and electric vehicles.[23] Therefore, the demand for LIB increases rapidly and its cost becomes one of the critical issues to overcome. Generally, the price depends on the battery's cell chemistry and manufacturing process.[203] And the electrolyte infiltration in the battery cell is one of the bottlenecks in the manufacturing process.[48] It is crucial to optimize the electrolyte infiltration as it takes a relatively long time compared to the other manufacturing steps.[142] Moreover, it can also impact the electrochemical performance of the cell. Indeed, a poor electrolyte impregnation decreases the active surface area (active material/electrolyte interface), and creates an inhomogeneous SEI layer in LIB negative electrodes, which may lead to low energy and power densities, and shorter cycle life.[204];[47];[17];[101];[124]

Despite its importance, it is experimentally challenging to analyze electrolyte flow through the porous electrodes. Several attempts were made to capture the dynamic path of the infiltrating electrolyte by using 2D in-plane imbibition, transmission neutron and X-ray imaging.[158];[205];[141] Nevertheless, these studies lack appropriate resolution and detailed information due to the limitations of the techniques. In addition, the experimental results constitute average values, making very challenging the differentiation of the effect of various manufacturing conditions on electrolyte wetting. Moreover, performing high throughput experimental characterizations to unravel parameters interdependencies in the infiltration process is not a trivial task,[141];[146] since the experimental techniques reported in the literature are costly and require sophisticated tools.[115]

On the other side, a recent increase in computational power enables performing three dimensional (3D) fluid flow computational simulations to quantify the permeability of complex porous materials and electrolyte penetration, which can be carried out in electrode images obtained by micro-computer tomography (CT). One of the most prominent tools to evaluate the permeability of 3D mesostructures is the Lattice-Boltzmann Method (LBM).[47] The strength of this method comes from its mesoscopic nature based on the discrete kinetic theory, which straightforwardly includes biphasic interface dynamics. Thus, the LBM is an accurate numerical method to simulate physical phenomena in realistic electrode mesostructures. Typically, LBM simulations are

performed in representative elementary volumes (REVs), where relatively small sub-volumes of the bigger mesostructure are selected, such that the global mesostructural properties are preserved.[206]·[182] For the first time, we recently reported this approach to simulate electrolyte infiltration into LIB electrode mesostructures in 3D.[47] Results arising from LBM simulations are generally accurate, reliable and allow deep physical interpretation of the infiltration process. Nevertheless, performing routine calculations with LBM remains computationally expensive and time-consuming: typically, 48 to 120 hours are needed for simulating electrolyte infiltration in one electrode, running the code in a supercomputer. Still, LBM constitutes a great tool to produce big data for further analysis (100-300 Gigabytes per electrode), something which is not possible with current experimental tools. Still, the bottleneck of the LBM model is the inability to quickly screen a massive amount of electrode architectures and electrolyte types. Consequently, it remains crucial to speed up the simulation of the electrolyte infiltration process to pave the way towards the computational screening of the impact of electrolyte and electrode properties on the electrolyte infiltration dynamics and therefore envisage autonomous algorithms able to optimize the electrolyte infiltration for low required times.

Meanwhile, Artificial Intelligence (AI) has seen a tremendous rise in the last decade, becoming essential for modern industry and finance, among many other fields.[207] In LIBs, machine learning (ML) techniques have enabled tools that significantly reduce the slow time frames related to trial-and-error approaches or physics-based simulations for faster and more efficient data assessment.[130,208–210] Deep Neural Networks (DNNs) are the most popular technique in the AI field due to the good performances they show for modeling complex data structures with many non-linear relationships.[211]·[212] Particularly, Convolutional Neural Networks (CNNs), a type of DNN, are a perfect example, having outstanding performances in different applications involving many types of data such as images-to-images translations, image classification, or autonomous driving.[213–215] Such techniques have also been applied to datasets produced from LBM calculations in the geology domain through images-based prediction to obtain fluid flow properties in porous media.[206]·[216,217] They generally consist of supervised regression ML models, which reduce computational costs and predict relevant physical properties such as porosity or permeability from tomography (micro-CT) X-ray images.[218–220]

In the field of energy storage, DNN architectures have also become very popular to accelerate physical-based simulations and reduce trial-and-error efforts to optimize LIBs.[221]. Therefore,

our aim in this study is to report, for the first time to our knowledge, a ML model based on a multi layers perceptron model (MLP) that can describe the dynamics of the electrolyte infiltration process in 3D, given a particular mesostructure of a LIB electrode and its associated pore-network, while accounting for different external infiltration pressure conditions. The ML model was trained with the data coming from LBM simulations due to the lack of big data from the experimental side, but keeping in mind that the results of the LBM simulations are based on experimentally measured input parameters. Still, it is essential to notice that one more strength of the reported ML model is that it can be adapted for different sources of data (pure experimental or hybrid between experimental and simulated) as far as this concerns the same type of data. The manuscript is divided into three sections: first we present the different processing steps in obtaining the REV's using micro-CT X-ray tomography data coming from our previous work;[47] then we present the LBM simulation details to generate the data and the adopted MLP architecture; lastly, we present electrolyte infiltration prediction results from our ML model along with detailed sensitivity analysis on the effects of the pore-network properties and LBM simulation conditions on the predicted electrolyte infiltration dynamics. Finally, we discuss why this approach has the potential to pave the way towards fast computational screening of electrode architectures/electrolyte pairs for the accelerated optimization of electrolyte infiltration and LIB manufacturing process as a whole.

5.2. Computational procedures

Extraction of REV's:

From the full tomography dataset of the NMC 94% - CBD 6% electrode, eleven $100 \cdot 100 \cdot 75 \mu\text{m}^3$ sub-volumes of similar porosities were extracted with a maximal relative error of 5 %. The carbon binder domain (CBD) location in the REV's was resolved using an *in house* stochastic algorithm.[130]

Individual pore identification:

An accurate reconstruction of the three-dimensional pore spaces and the subsequent identification of individual pores was done by the PoroDict library within the GeoDict[®] software using the watershed algorithm. It is known that the surface roughness of 2D images (or 3D voxel data in our case) generally induces over-segmentation in watershed-based methods and many approaches exist to solve it.[222,223] GeoDict[®] handles this by reconnecting overly segmented pore-fragments back into a single pore only when the shared interface between the pore fragments is larger than a chosen value. For consistency, this interface threshold value is kept constant at 10 % for each of the

representative sub-volumes that were extracted and analyzed. Then, their volume, surface area, and surface area of contact with other pores were calculated based on a six neighbors approach.[68] Compared to other pore-network modelling approaches,[197,224,225] where the pores are approximated as spheres and cylindrical throats, the watershed algorithm identifies individual pores by labeling every voxel in the pore phase. This is especially useful when setting a one-to-one correspondence between the pore-wise labeled volumes and other voxel-based volumetric data coming from LBM simulations.

InPore-resolved saturation curves:

In the last section, how the pore domain's voxels are labeled into individual pores is introduced. Discrete pore-size distribution algorithms are particularly convenient to establish a one-to-one correspondence between the identified pores and the volumetric data coming from voxel-based physical simulations, particularly for our LBM simulations. To continue processing the data, both the 16-bit grayscale ‘.raw’ files and the time series data for electrolyte infiltration were converted into 3D NumPy arrays [226]. The time-series data is exported from Palabos as fluid density fields in VTK unstructured grid format and then further processed into NumPy arrays with the PyVista library.[188][227][228] Then, masked array operations are used into the voxels belonging to each distinct pore to obtain the pore-resolved saturation curves. Concretely, let us define an integer 3D array W such that its voxels are determined as

$$w_{ijk} = p: p = 1, \dots, N \quad (1)$$

where i, j , and k are the indices for the voxels in the array, p is the pore label, and N is the total number of pores in our pore domain. Then, let L_t be a 3D array for a snapshot of the LBM simulations at time t , such that:

$$l_{ijk}^t = \begin{cases} l_{solid} & \text{if } \rho_{ijk}^{LBM}(t) = 0 \\ l_{void} & \text{if } 0 < \rho_{ijk}^{LBM}(t) \leq \delta \\ l_{liquid} & \text{if } \rho_{ijk}^{LBM}(t) > \delta \end{cases} \quad (2)$$

where l_{solid} , l_{void} , and l_{liquid} are labels that indicate the voxels assigned to solid, void, and liquid phases, respectively; $\rho_{ijk}^{LBM}(t)$ is the density field at time step t , and δ is a threshold value for the

fluid density. Let \hat{x}_p be the set of voxels of W belonging to a pore with label p . Both W and L_t represent the same electrode mesostructure (**Figure 1**), so that voxels that belong to the set \hat{x}_p cover the same spatial domain within the microstructure. Then, the pore-resolved saturation (**Figure 1**) is defined as the ratio between the number of voxels l_{ijk}^t with label l_{liquid} in the set \hat{x}_p , and the size of the set \hat{x}_p itself, at time t .

LBM simulations:

Simulations were carried out using the open-source Palabos library version 1.0.[188] The model simulates the streaming and collision of particles on a grid. All the simulations are in the laminar flow regime. The Navier-Stokes macroscopic kinetic theory was applied to describe fluid in the bulk flow at the mesoscopic level. Further details of the model and its description can be found in our previous LBM publication.[47] All the input parameters such as the density, the fluid contact angle with the solid phase, the viscosity, the surface tension and the sizes of simulation boxes are given in Table 1. After, the outputs from the Palabos library were further treated using NumPy[226] with the PyVista library[227] in order to obtain the individual pore-resolved saturation curves.

ML model:

In this study, a sequential architecture is implemented to model the saturation curve values \bar{S} and the times of filling (T_{f0} and T_{f1} as seen in **Figure 1D**) for every pore in the tomographic REV's. The developed architecture follows a neural network-based model known as a MLP. The Python libraries, Tensorflow and Keras, are used in the backend to complete the architecture within a 3.7 version of Python. After training the modeling function, a sensitivity analysis is applied to analyze the effect of the input parameters on the uncertainty of the outputs. The architecture of the MLP comprises five hidden layers, with 80 nodes each, and one output layer containing 7 nodes. While no specific rule exists for selecting DNN hyperparameters,[229] this architecture was sufficient to fit the training data correctly and to obtain trustable predictions as shown in the results section.

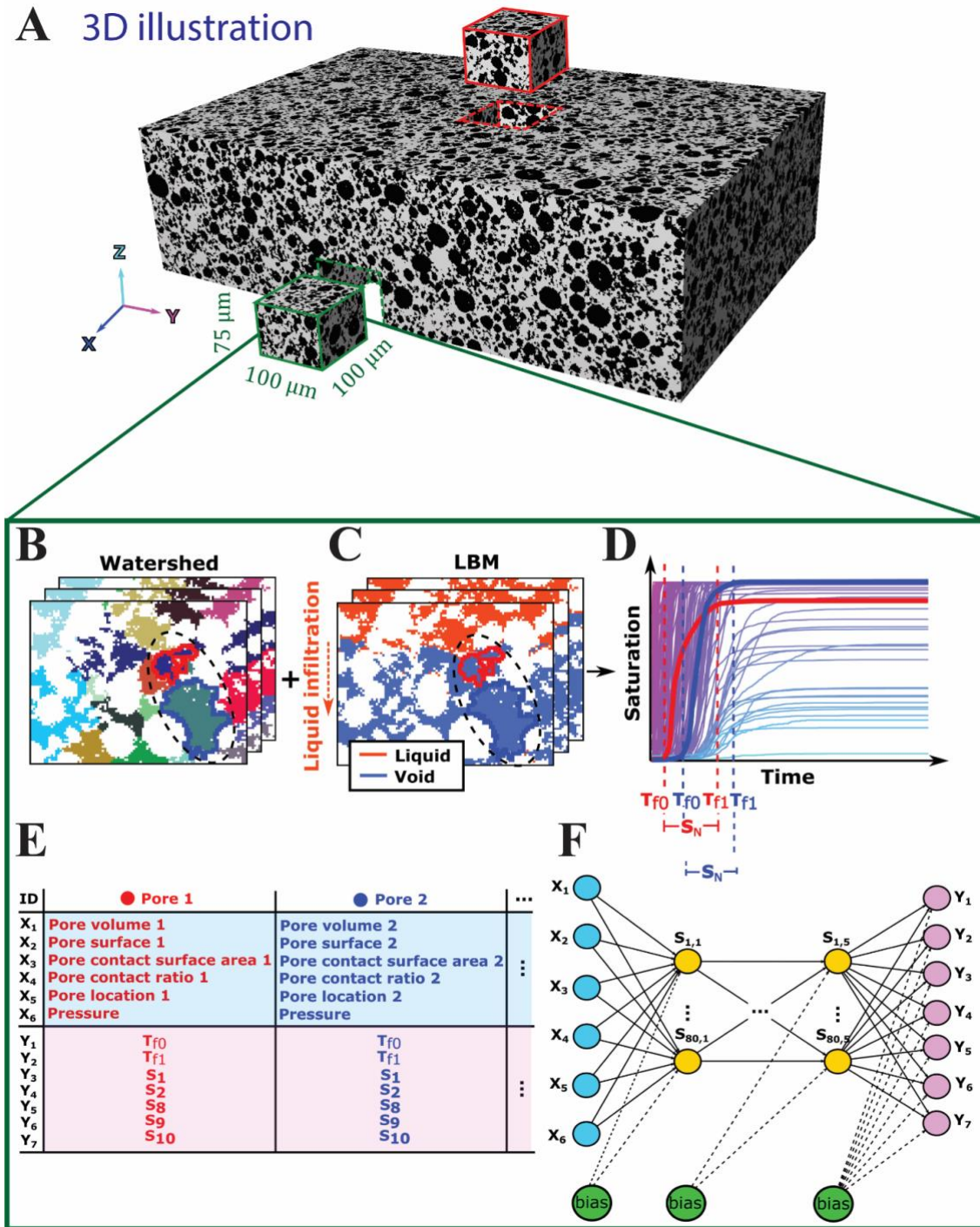


Figure 1. Summary of the data processing steps to be used as inputs in the ML model. (A) 3D micro-CT X-ray tomography data, colored rectangular parallelepipeds represent two examples of the different REVs that were extracted. (B) (left) Results from the watershed segmentation process, (C) (middle) volume data from LBM simulations with voxels labeled as liquid (orange), void (blue), and solid (white). (D) (right) Individual pore-resolved saturation curves. For clarity, two pores (blue and red) were highlighted, spanning the same spatial regions between the watershed and LBM voxel data. The respective pore-resolved saturation curves are also shown,

alongside their relevant features (\bar{S} , T_{f0} , and T_{f1}). (E) Structure of the data used for the training of the NN, columns enumerate each pore, while rows are divided into the inputs $(X_i)_{(i \leq 6)}$ (blue shaded region) and outputs $(Y_i)_{(i \leq 7)}$ (red shaded region). (F) Architecture of the neural network used for training, nodes in blue (red) represent the input (output) layers, respectively. Nodes in yellow represent the hidden layer nodes $S_{j,k}$ where k is the layer index, and j is the node index. Nodes in green represent the bias that is applied to each hidden layer.

The LBM model simulations were performed using an Intel® Xeon® E5-4627 Cache @ 3.30 GHz with 264 GB of RAM. Each simulation took approximately between 48 and 120 hours, depending on the input pressure parameter. The NN models' training took around 10 minutes by using 48 processors Intel® Xeon® Silver 4116 CPU @ 2.10 GHz with 64 GB of RAM. **Figure 1** illustrates the workflow that was used in this work.

5.3. Results and discussions

5.3.1. Machine learning prediction

The evaluation of the electrolyte infiltration dynamics was done by extracting the relevant features of pore resolved saturation curves as shown in **Figure 1D**. Specifically, we extracted the values of the times at which the pore filling starts (T_{f0}) and stops (T_{f1}), as well as the saturation values associated to ten in-between evenly spaced time steps, as the outputs of the MLP. The set of saturation points are defined as $\bar{S} = \{S_1, S_2, S_3, S_4, S_5, S_6, S_7, S_8, S_9, S_{10}\}$.

Figure 2 displays the critical features for the training and validation of the MLP. The complete dataset is randomly split into the training and testing dataset containing 80 % and 20 % of the total data, respectively. **Figure 2A** represents the evolution of the loss values (MSE) for the training data (80% of the total amount of data) and the validation data (the remaining 20%) during the training step of the MLP over 1000 training cycles. **Figure 2B** shows the average R^2 scores for the model compared with the mean square error (MSE) between the initial saturation curve and its discretization to define the saturation values outputs. In order to obtain a compromise between the global accuracy of the MLP and the error between the saturation curves and their associated discretized values, we successively retrained the MLP model after removing those saturation value outputs that were not properly fitted, thus reducing the number of outputs in the model. Particularly, this compromise is met by selecting $\bar{S} \setminus \bar{S}_{3-7} = \{S_1, S_2, S_8, S_9, S_{10}\}$ as the outputs of the MLP, along with T_{f0} and T_{f1} (as shown in **Figure 1E-F**). **Figure 2C** and **Figure 2D** display regression plots comparing the predicted values from the MLP model and the actual values from the LBM

simulations for the testing dataset, for the time at which the pore-filling starts (T_{f0}) and stops (T_{f1}), respectively.

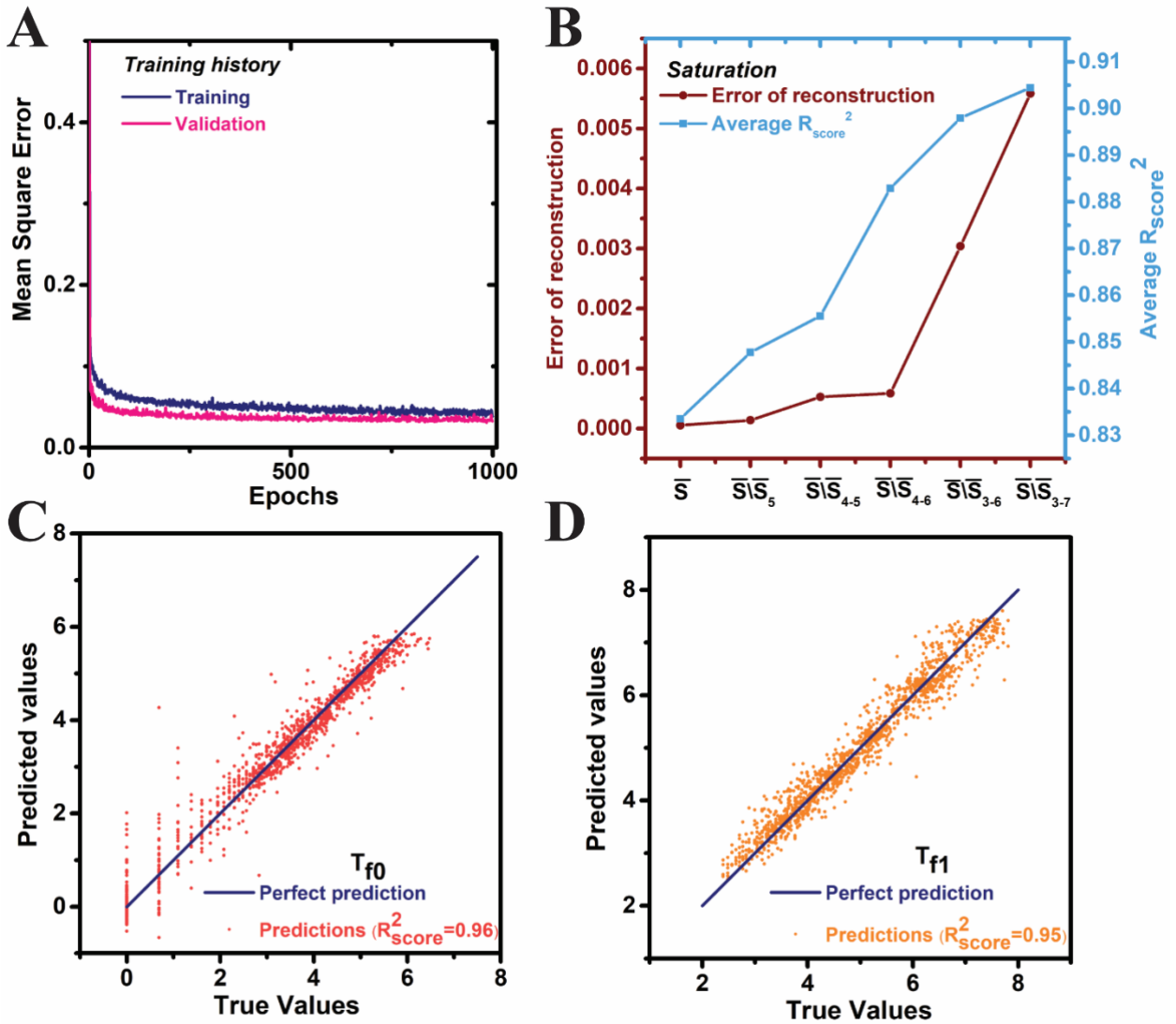


Figure 2. (A) MSE of the training and validation of the neural network, (B) R^2 scores (blue) and the MSE of the saturation curve reconstruction (garnet) as function of the set of saturation value ($\bar{S}|\bar{S}_i$) outputs predicted by the model, (C) Prediction of the starting times for electrolyte filling of individual pores (T_{f0}) and (D) Prediction of the full wetting times (T_{f1})

5.3.2. Comparison of LBM simulation and prediction based on ML

As mentioned above, our trained MLP can accurately predict the saturation, initial electrolyte entering and fully wetting time at an individual pore in the structure for the test dataset. In order to further compare and contrast our model, an additional REV was used, whose pore-network was not

part of neither the training nor testing datasets. After inputting the parameters of the brand-new pore-network in our MLP, the overall saturation curves were reconstructed from the obtained outputs, as shown in **Figure 3**. The obtained results closely match the saturation curves obtained with LBM, which gives a hint of the ability our ML model to perform well in a variety of electrode mesostructures.

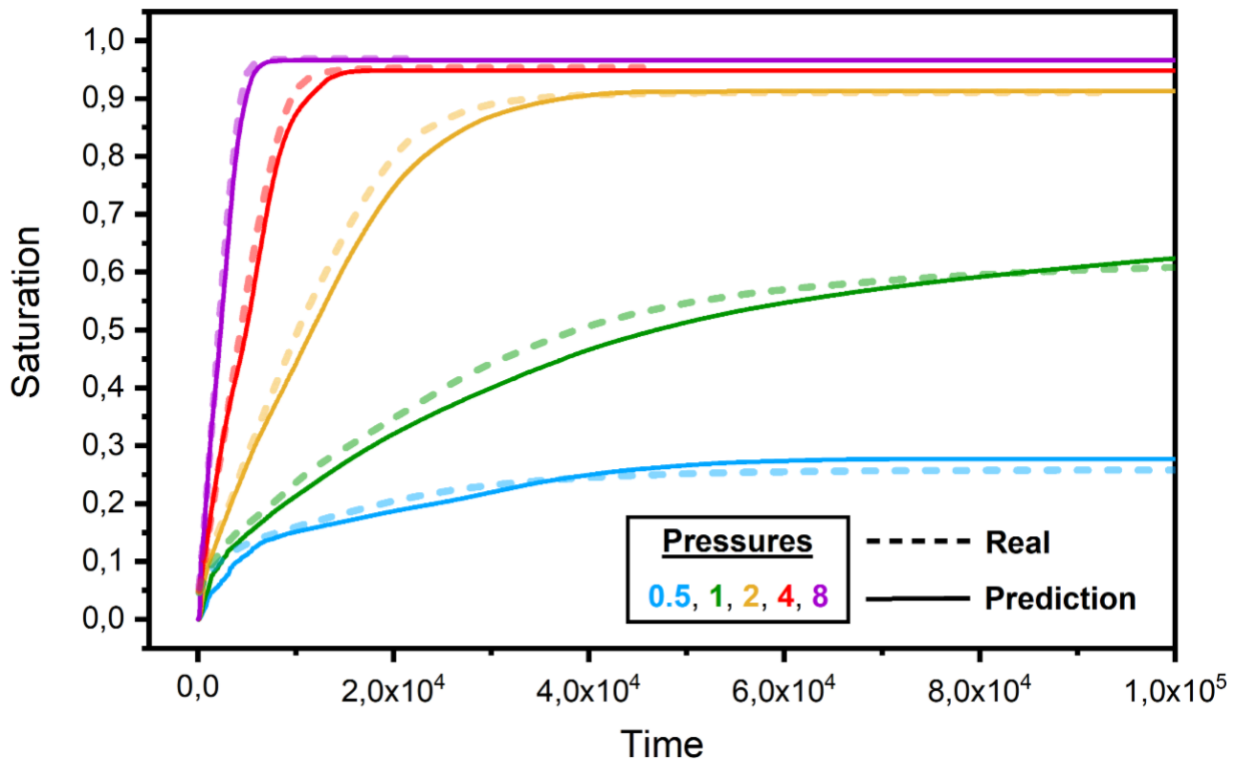


Figure 3. Saturation profile of liquid electrolyte from real (LBM simulated) and predicted (NN based) in the NMC 94% - CBD 6% cathode with various applied pressures.

Five different applied pressures were also used as input parameters to study and predict their effect on electrolyte penetration. Again, **Figure 3** shows the overall saturation curves simulated by LBM, and predicted by our MLP for different applied pressures. Generally, all saturation curves for both real and predicted cases show an asymptotic growth rate where the saturation curve increases steeply and slows down while it reaches the convergence point. Also, the wetting time for the electrode increases as applied pressure decreases for both real and predicted cases. Furthermore, the lower the applied pressure, the lower the overall saturation will be and the longer it will take to reach the convergence point. The saturation curves for real (LBM simulated) cases under the applied pressures p8, p4 and p2 tend to rise monotonically and reach complete wetted conditions.

For the lower pressure values (p_1 and $p_{0.5}$), the electrode wetting degrees are only 60% and 25%, respectively. In addition, the penetration rate, *i.e.* the rate at which the saturation will reach its convergence point, is slower for p_1 and $p_{0.5}$ compared to higher applied pressures. The predicted (MLP based) saturation curves agree with those from LBM simulated results, especially at high applied pressures where the predictions are extremely precise. In essence, the vital part is that the MLP can closely match the general simulation trends and is also able to precisely predict converging points, where the saturation degrees predicted by our MLP closely match those obtained by LBM simulations for high applied pressure inputs.

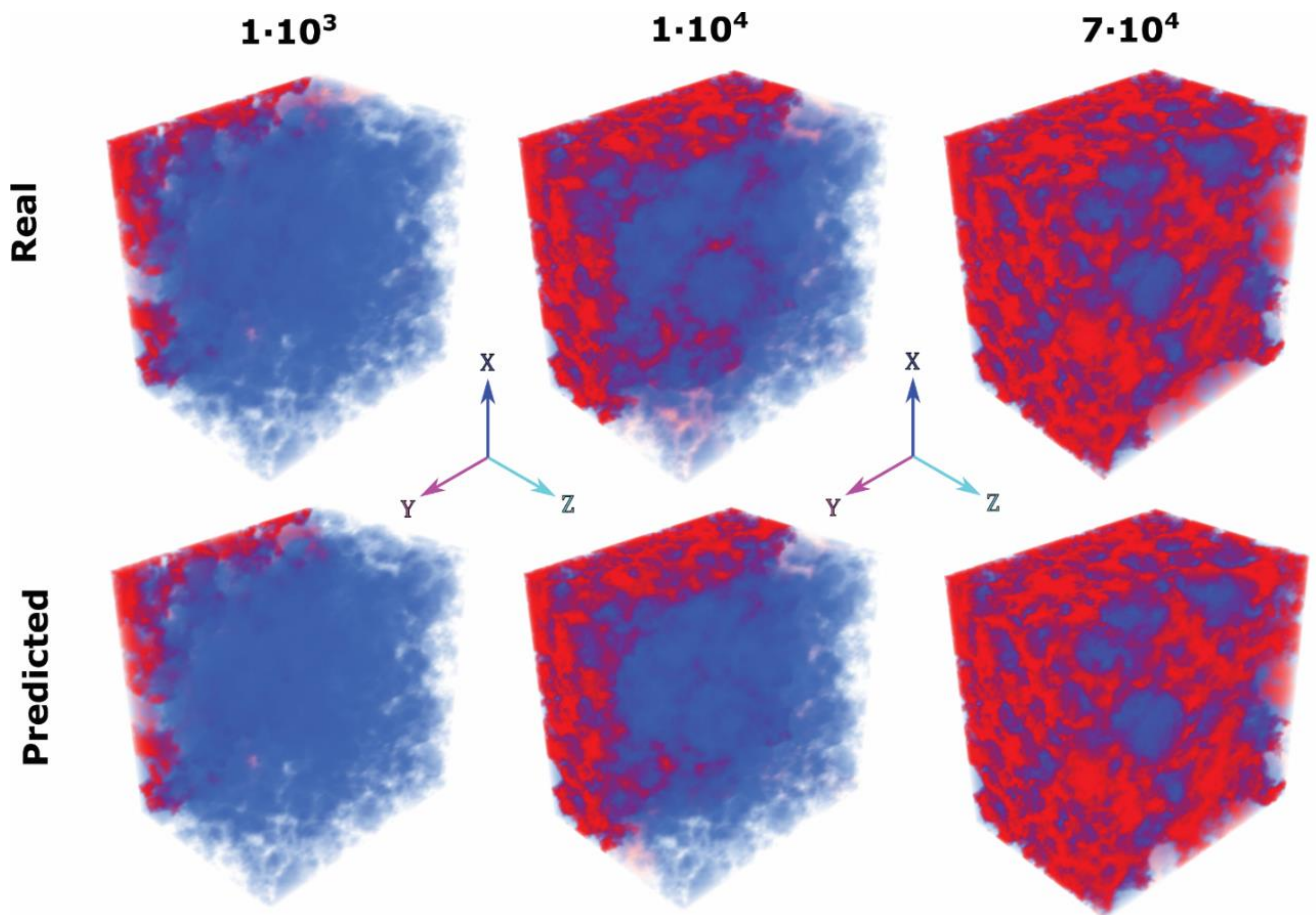


Figure 4. The wetting process visualization (electrolyte in red color) from real (LBM simulated) and predicted (MLP based) for the NMC 94% - CBD 6% electrode (blue) at different time steps. The electrolyte inlet is the yz plane at $x = 0$.

Our model also allows following the electrolyte wetting process in 3D, since its outputs depend on spatially resolved pore-networks. **Figure 4** shows the temporal evolution of the saturation degree of individual pores in the electrode mesostructure. It is known that electrolyte flows through the

porous electrode due to the pressure difference between the electrolyte and air phases, known as capillary forces, while local resistance forces drive the electrolytes path within the porous electrode. Usually, the electrolyte is always directed towards larger pores, as shown in our previous the LBM simulations.[47] **Figure 4** shows an excellent agreement between the MLP prediction and physical-based LBM model, in the path that the electrolyte takes within the porous electrode. There is a slight deviation at time step $1 \times 10^4 \text{lu}$, but the difference disappears at the converging point. The corresponding videos of the filling process as predicted by LBM and ML are available in website of ARTISTIC project.

5.3.3. Parameters influencing the saturation and their physical interpretation

Performing a sensitivity analysis of computational models is a clear and straightforward way to assess how the outputs of a model vary as a function of their inputs. In this work the *Sobol* indexes were extracted in order to evince the individual and total impact that the input parameters of the MLP model have on the seven outputs that we aim to predict, *i.e.* T_{f0} , T_{f1} and the saturation values \bar{S} . Additionally, the Sobol indexes corresponding to the initial ($S_{f0} = \{S_1, S_2\}$) and final ($S_{f1} = \{S_8, S_9, S_{10}\}$) saturation values are averaged out, which allows condensing the results in order to facilitate their physical interpretation (**Figure 5**). Let the decomposition of the total variance for one specific output (named Y) according to the Sobol decomposition be expressed as

$$V_{ar}[Y] = V(Y) = \sum_{i=1}^n V_i + \sum_{1 < i, j < n} V_{i,j} + \dots + V_{1, \dots, n} \quad (3)$$

where V_i is the conditional variance for Y over knowing X_i , and $V_{i, \dots, n}$ are the rest of conditional variances knowing different input parameters.

The Sobol indexes are the partial variances normalized by the total variance of the output, they are noted as $(Sob_i)_{(i \leq n)}$ and they are comprised between 0 and 1 (Eq. 3). They represent the individual effects (1st order Sobol indexes) of each input parameter:

$$Sob_i = \frac{V_i}{v} = \frac{V[E[Y|X_i]]}{v[Y]} \quad (4)$$

In this study, the Sobol index depends on the chosen output $(Y_j)_{(j \leq 7)}$, meaning that the equation above can be simplified as

$$Sob_{i,j} = \frac{V_i}{V_j} = \frac{V[E[Y \vee X_i]]}{V[Y_j]} \quad (5)$$

where $E[Y \vee X_i]$ is the conditional expectation of Y_j giving X_i .

By successively adding higher order terms to the indexes, we obtain the total effect for each input parameter

$$Sob_{T_i} = Sob_i + \sum_{i \neq j} Sob_{ij} + \sum_{j < k, i \neq j, i \neq k} Sob_{ijk} + \dots \quad (6)$$

where the different Sobol indexes Sob_{ijk} are related to the combination of various input parameters. Such indexes are calculated according to the Saltelli sampling method.[230,231] The latter global approach is very popular to obtain convergences when the number of samples varies significantly and represents the entire space of input parameters, whereas random sampling approaches may perform meaningless evaluations of sensitive indexes. Therefore, the Saltelli method extends the size of input parameters combinations for the resulting calculations, which are uniformly distributed over the full input parameters space. The variances calculated from Eq. 4 to Eq. 6 can be described as projections along the different ranges of input parameters. In this study, a batch of 14000 samples is used to evaluate the Sobol indexes for each output of the MLP.

Figure 5 shows the 1st order Sobol indexes regarding all possible combinations between inputs (geometrical properties of the pores and applied pressures) and outputs (T_{f0} , T_{f1} , S_{f0} and S_{f1}) in this study. We can see that the initial pore filling time (T_{f0}) highly depends on the pore volume with a Sobol index of 0.7 followed by the pore total surface area and its location with Sobol indexes of 0.3. The total wetting time of the pore (T_{f1}) is also influenced mainly by these three parameters. The pore volume has a major effect with a Sobol index of 0.6 and the second biggest factor is the pore surface area with Sobol index 0.4. It is intuitive that the bigger the pore size, the easier it is

for the electrolyte to occupy its volume. Also, other geometrical attributes such as pore location and pore surface area play a significant role in the pore filling start time (T_{f0}). Additionally, it is important to mention that all the input parameters have almost the same effect on the saturation values at the end of the pore filling (S_{f1}) with Sobol indexes about 0.45. The onset of saturation S_{f0} is, on the contrary, strongly influenced by the pore location with Sobol index around 0.7.

To sum up, the total electrode's wetting degree strongly depends on the pore network properties and applied pressure. The full wetting time (T_{f1}) is strongly affected by pore size distribution. Thus, to have optimal electrode mesostructures to reach complete wetting at the shortest possible time, pore size distribution and interconnectivity of the pores must be well designed during the manufacturing. This can be a challenging task with traditional manufacturing process, still it is achievable with alternative techniques such as SPS sintering and 3D printing.[114][232]

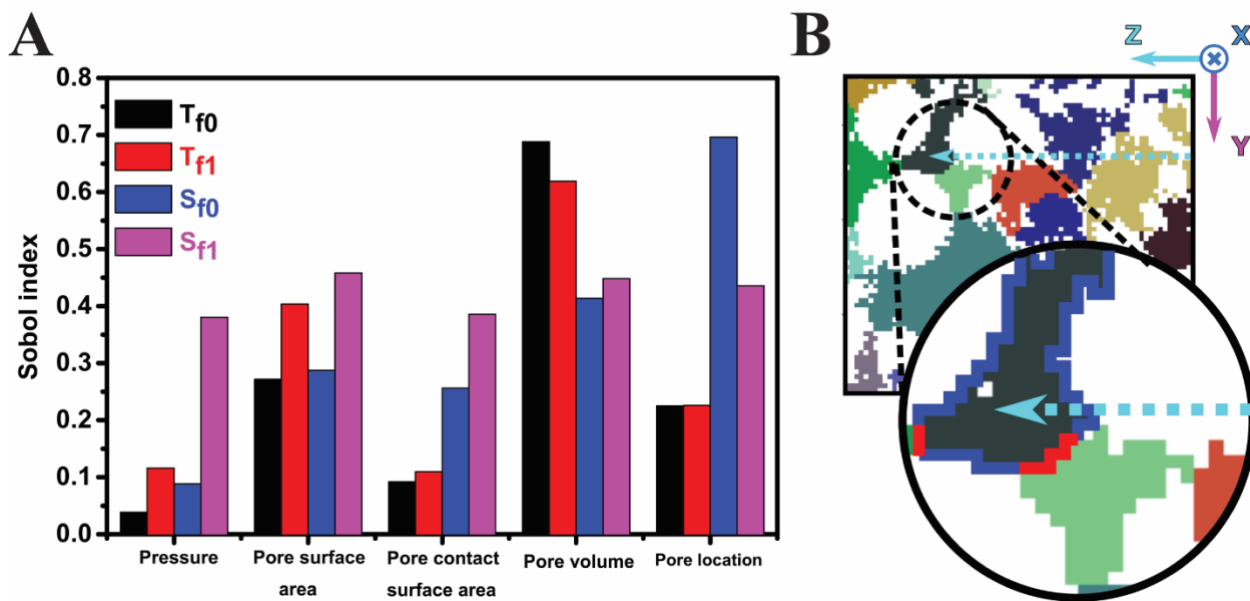


Figure 5. (A) Sobol indexes of the geometrical properties of individual pores and applied pressures, on the outputs T_{f0} , T_{f1} , S_{f0} , and S_{f1} . (B) Slice of the REV illustrating the geometrical properties of individual pores. The zoom region (black circle) illustrates the pore volume (grey zone), pore surface area (blue outline), pore contact surface area (red outline) and pore location (dotted turquoise arrow) of a given identified pore inside the REV.

5.4. Conclusions

In this work, we present an innovative ML model based on a multi layers perceptron (MLP) architecture, to predict electrolyte infiltration in porous NMC electrodes. The host structure of the NMC porous electrode was obtained experimentally by (micro-CT) X-ray tomographic measurements. The MLP was trained with data coming from physics-based 3D LBM model and extracted pore networks from (micro-CT) X-ray tomography. The neural network prediction results were compared and validated by 3D LBM simulations.

The trained MLP can generalize the flow problems to predict the rate of saturation and filling time in porous electrodes. Moreover, it can predict the direction of the fluid flow, total saturation, and filling time of the electrode accurately. Also, the predictions showed the same asymptotic trend as the physics-based LBM model for the saturation curve. Additionally, a systematic sensitivity analysis was carried out to unravel the spatial relationship between complex electrode pore shape, pore location, pore volume, the connection between other pores and applied external pressure on the overall predicted infiltration process characteristics, such as saturation degrees and filling times, among others.

Besides, the trained MLP accurately predicted examples of varying geometries and applied pressures in less than a second of computation on a desktop computer, while physics-based LBM simulations took several days (2-5) on a server with high computational power. Additionally, our ML model generates only around 10 Mb of data to be compared with the 50 - 200 Gb generated during the LBM simulations, saving data storage space and making post-processing fast and affordable. All the advantages mentioned above allow the model to quickly screen different electrode architectures and possible electrolyte properties as a part of a digital twin of battery manufacturing. Consequently, it serves as a vital tool to optimize the electrolyte infiltration process. Finally, this method can be used further on different domains where fluid flow through porous media takes part.

Table 1. List of input parameters for the LBM simulations

| AM 96%-CBD 4% un-calendered tomography | 100×100×75 voxels | 100 × 100 × 75 μm ³ |
|--|-------------------|--------------------------------|
| Electrolyte denisty | 10 | 1300 $\frac{kg}{m^3}$ |
| Gas denisty | 1 | 1.18 $\frac{kg}{m^3}$ |
| Contact angle | 0.357/1.643 | 90° [141] |
| Surface force (gas-liquid) | 0.1 | 7.28 × 10 ⁻² |
| t_0 | 1 <i>lu</i> | 1 × 10 ⁻⁶ s |
| Reynolds number | 10 ⁻³ | 10 ⁻³ |
| Capillary number | 10 ⁻⁵ | 10 ⁻⁵ |
| Pressure | 0.5 p | 151 988 Pascal |
| Pressure | 1p | 202 650 Pascal |
| Pressure | 2p | 405 300 Pascal |
| Pressure | 4p | 810 600 Pascal |

Chapter – VI

General Conclusion

The aim of the thesis was to create the models which describes electrolyte infiltration step of the manufacturing and its characterization by impedance spectroscopy model. The electrochemical impedance spectroscopy model should be developed based on Newman model. The Lattice Boltzmann Method must be used to describe the electrolyte infiltration process. All the models must be combined with experimental results. The thesis was part of the ERC-Artistic project.

The first stage of the thesis was devoted to develop the Electrochemical impedance Spectroscopy model. EIS constitutes an experimental technique used for the characterization of LIB porous electrodes tortuosities. For the first time, a 4D (3D in space + time) physical model is proposed to simulate EIS carried out on NMC porous cathodes, derived from the simulation of their manufacturing process, in symmetric cells. EIS is simulated by explicitly considering the NMC active material, carbon-binder domains and pores as spatially-resolved separated phases and assuming different physics for each of them. The calculated impedance responses are compared with *in house* experimental results arising from NMC-based cathodes prepared in a similar way. We investigate the influence of the physics assumed to describe the CBD behavior, the conductivity of the different solid phases and electrolyte, the relative amount of NMC and CBD and the impact of calendaring on the EI spectra, and we compare the results with the experimental EIS measurements. This methodology allows to understand the limitations of using EIS, electric circuit models and homogenized physical models for the determination of the tortuosity of NMC-based cathodes, revealing a complex interplay between the conductivity of the solid phases, the electrolyte properties and the cathode meso/microstructure.

Further, thick electrodes suffer from poor rate capability, high ionic impedance and heterogeneity in the mesostructure. Therefore, optimizing thick electrode architectures becomes crucial for overcoming these limitations. In the third chapter, a systematic assessment of the ionic resistance in heterogeneous porous electrodes through the combination of experimental measurements and computational simulations. The first part of the chapter is devoted to a general discussion of the EIS spectra, mapping the role of ionic and electronic impedance experimentally by comparing NMC, LFP and Graphite electrodes with different fabrication conditions. In the second part of the work, electrodes with different porosities are simulated to analyze the role of electrode porosity on ionic impedance. The results showed that a lower porosity leads to a higher ionic impedance and

electrode tortuosity factor. Furthermore, electrodes with different porosities were stacked and assembled to create heterogeneities of porosity across the thickness and surface of the electrode. The results showed that the electrode inhomogeneity across thickness has a significant effect on the ionic impedance and capacity of the electrode. The electrode architecture with progressively decreasing porosity from separator to current collector showed the best performance. Overall, we conclude that the ionic resistance in a thick electrode can be effectively reduced through proper tuning of the heterogeneous porosity. The proposed heterogeneous electrode architectures presented in our work could enormously help build thick electrode architectures for LIBs, therefore improving their performance under high C-rates.

The second stage of the thesis was devoted to development of the electrolyte infiltration process. Electrolyte filling takes place between sealing and formation in LIB manufacturing process. This step is crucial as it is directly linked to LIB quality and affects the subsequent time consuming electrolyte wetting process. Although having fast, homogeneous and complete wetting is of paramount importance, this process has not been sufficiently examined and fully understood. For instance, experimentally available data is insufficient to fully capture the complex interplay upon filling between electrolyte and air inside the porous electrode. We report here for the first time a 3D-resolved Lattice Boltzmann Method model able to simulate electrolyte filling upon applied pressure of LIB porous electrodes obtained both from experiments (micro X-ray tomography) and computations (stochastic generation, simulation of the manufacturing process using Coarse Grained Molecular Dynamics and Discrete Element Method). The model allows obtaining advanced insights about the impact of the electrode mesostructures on the speed of electrolyte impregnation and wetting, highlighting the important of porosity, pore size distribution and pores interconnectivity on the filling dynamics. Furthermore, we identify scenarios where volumes with trapped air (dead zones) appear and evaluate the impact of those on the electrochemical behavior of the electrodes.

Lastly, I present in the thesis an innovative machine learning model, based on deep neural networks, to fast and accurately predict fluid flow in three dimensions, as well as wetting degree and time for LIB electrodes. The ML model is trained on a database generated using a 3D-resolved physical model based on the Lattice Boltzmann Method. We demonstrate the ML model with a

NMC electrode mesostructure obtained by X-ray micro-computer tomography. The extracted pore network from tomography data was also used to train our ML neural network. The results show that the ML model is able to predict the electrode filling process, with ultralow computational cost (few seconds) and with high accuracy when compared with the original data generated with the physical model. Also, systematic sensitivity analysis was carried out to unravel the spatial relationship between electrode mesostructure parameters and predicted infiltration process characteristics, such as saturation dynamics, filling time among others.

The ML model can speed up the infiltration predictions by several orders of magnitude compared to the LBM model which usually requires several days of calculation. This paves the way towards massive computational screening of electrode mesostructures/electrolyte pairs to unravel their impact on the cell wetting and optimize the electrolyte infiltration conditions.

Perspectives:

Finally, the EIS, LBM and Machine learning models will be integrated into the ARTISTIC platform. The platform can be used to simulate, understand, and optimize battery manufacturing. The platform will be free of charge and all the data and codes will be available.

Also, future model development should be devoted to including swelling phenomena in the LBM simulations. For example, it is known that the electrode swells after contact with the electrolyte, which results in a change in the electrode microstructure. Due to this, the first electrode expansion physics should be adopted, and further microstructural changes must be characterized. Finally, the developed EIS model can be used to calculate its overall electrochemical performance.

From the research perspective, LBM can scan many different electrolyte types to see their effect on manufacturing. Furthermore, LBM can simulate all the LIB cell formats to improve the electrolyte infiltration process for the cells. Finally, the obtained results can be imported to a machine learning program to optimize both electrolyte design and infiltration.

Abbreviations

| | |
|------|--|
| EIS | Electrochemical impedance spectroscopy |
| NMC | $\text{Li}(\text{Ni}_{1/3}\text{Mn}_{1/3}\text{Co}_{1/3})\text{O}_2$ |
| PVdF | Polyvinylidene fluoride |
| CB | Carbon black |
| CBD | Carbon-binder domain |
| AM | Active material |
| CGMD | Coarse-grained molecular dynamics |
| MD | Molecular dynamics |
| C45 | Carbon black Timcal Super 45 |
| CMC | Carboxymethyl cellulose |
| DEC | Diethyl carbonate |
| DMC | Dimethyl carbonate |
| EC | Ethylene carbonate |
| LCO | LiCoO_2 |
| LFP | LiFePO_4 |
| LIB | Lithium-ion battery |
| LMO | LiMn_2O_4 |
| LTO | $\text{Li}_4\text{Ti}_5\text{O}_{12}$ |
| NCA | $\text{LiNi}_x\text{Co}_y\text{Al}_z\text{O}_2$ |

| | |
|------|---|
| NCM | $\text{LiNi}_x\text{Mn}_y\text{Co}_z\text{O}_2$ |
| PC | Propylene carbonate |
| PVDF | Polyvinylidene fluoride |
| SBR | Styrene-butadiene rubber |
| LBM | Lattice Boltzmann Method |
| SEI | Solid electrolyte interphase |
| LMFP | $\text{LiMn}_x\text{Fe}_{1-x}\text{PO}_4$ |
| REV | Representative elementary volumes |
| AI | Artificial Intelligence |
| ML | Machine learning |
| DNN | Deep Neural Networks |
| CNN | Convolutional Neural Network |
| MLP | Multi layers perceptron |
| PSD | Pore size distribution |
| MSE | Mean square error |
| DEM | Discrete Element Method |
| FEM | Finite element method |

Bibliography

- [1] The Average Cost of Solar Panel System in 2021 | Solar.com, (n.d.). <https://www.solar.com/learn/solar-panel-cost/> (accessed June 14, 2021).
- [2] Global EV Outlook 2020 – Analysis - IEA, (n.d.). <https://www.iea.org/reports/global-ev-outlook-2020> (accessed June 14, 2021).
- [3] Primary direct energy consumption by source, World, (n.d.). https://ourworldindata.org/grapher/primary-energy-consumption-by-source?country=~OWID_WRL (accessed June 14, 2021).
- [4] L. Batteries, Lithium Ion Batteries State and Technology, 2007.
- [5] F. Mezei, Basics Concepts, 2011. <https://doi.org/10.1002/9780470933886.ch1>.
- [6] Image of alessandro volta's letter to the royal society, 20 march 1800. by Science & Society Picture Library, (n.d.). <https://www.scienceandsociety.co.uk/results.asp?image=10319203> (accessed June 14, 2021).
- [7] P.A. Nelson, K.G. Bloom, D.W. Dees, P.A. Nelson, K.G. Gallagher, I. Bloom, D.W. Dees, Modeling the performance and cost of lithium-ion batteries for electric-drive vehicles, Electrochemical Energy Storage Theme, Chemical Sciences and Engineering division, Argonne National Laboratory, Septem, (2011) 121.
- [8] D.A. Aikens, Electrochemical methods, fundamentals and applications, 2009. <https://doi.org/10.1021/ed060pa25.1>.
- [9] B. Scrosati, J. Garche, Lithium batteries: Status, prospects and future, Journal of Power Sources. 195 (2010) 2419–2430. <https://doi.org/10.1016/j.jpowsour.2009.11.048>.
- [10] G. Ertl, The nobel prize in chemistry, Nobel Lectures: Chemistry: 2006 - 2010. (2014) 37–38. https://doi.org/10.1142/9789814635660_0002.
- [11] A.A. Franco, Rechargeable Lithium Batteries: From Fundamentals to Applications, Elsevier Inc., 2015. <https://doi.org/10.1016/C2013-0-16455-0>.
- [12] P. PbSO, N. Koh, -e -, V. Li Si, S. LiX, PbO 2 H 2 O H 2 SO 4 /H 2 O H + PbSO 4 SO 4 2- +-e-2.0 V Lead-acid Li 1-x CoO 2 LiPF 6 EC-DMC LiPF 6 EC-DMC Lithium ion Future batteries? Lithium ion based on nanomaterials Ionic liquids Lithium metal Lithium-air Lithium-based electrolytes, Nature. 451 (2008) 652–657.
- [13] M. Armand, Nature Lithium Battery, Nature. 414 (2001) 359–367.
- [14] S. Jeschke, P. Johansson, Supervised Machine Learning-Based Classification of Li–S Battery Electrolytes, Batteries & Supercaps. (2021). <https://doi.org/10.1002/batt.202100031>.
- [15] F. Makhlooghiyazad, C. Pozo-Gonzalo, P. Johansson, M. Forsyth, Electrolytes for Sodium Batteries, in: Na-ion Batteries, Wiley, 2021: pp. 205–241. <https://doi.org/10.1002/9781119818069.ch5>.

- [16] K. Pfeifer, S. Arnold, J. Becherer, C. Das, J. Maibach, H. Ehrenberg, S. Dsoke, Can Metallic Sodium Electrodes Affect the Electrochemistry of Sodium-Ion Batteries? Reactivity Issues and Perspectives, *ChemSusChem*. 12 (2019) 3312–3319. <https://doi.org/10.1002/cssc.201901056>.
- [17] K. Pfeifer, M.F. Greenstein, D. Aurbach, X. Luo, H. Ehrenberg, S. Dsoke, Interaction between Electrolytes and Sb₂O₃-Based Electrodes in Sodium Batteries: Uncovering the Detrimental Effects of Diglyme, *ChemElectroChem*. 7 (2020) 3487–3495. <https://doi.org/10.1002/celec.202000894>.
- [18] G. Yan, S. Mariyappan, G. Rousse, Q. Jacquet, M. Deschamps, R. David, B. Mirvaux, J.W. Freeland, J.M. Tarascon, Higher energy and safer sodium ion batteries via an electrochemically made disordered Na₃V₂(PO₄)₂F₃ material, *Nature Communications*. 10 (2019) 1–12. <https://doi.org/10.1038/s41467-019-08359-y>.
- [19] L.C. Loaiza, L. Monconduit, V. Seznec, Si and Ge-Based Anode Materials for Li-, Na-, and K-Ion Batteries: A Perspective from Structure to Electrochemical Mechanism, *Small*. 16 (2020) 1905260. <https://doi.org/10.1002/sml.201905260>.
- [20] A. Torayev, P.C.M.M. Magusin, C.P. Grey, C. Merlet, A.A. Franco, Text mining assisted review of the literature on Li-O₂ batteries, *Journal of Physics: Materials*. 2 (2019) 044004. <https://doi.org/10.1088/2515-7639/ab3611>.
- [21] Roadmap - Battery 2030, (n.d.). <https://battery2030.eu/research/roadmap/> (accessed April 16, 2021).
- [22] D. Castelvechi, E. Stoye, Chemistry Nobel honours world-changing batteries, *Nature*. 574 (2019) 308–308. <https://doi.org/10.1038/d41586-019-02965-y>.
- [23] A.A. Franco, A. Rucci, D. Brandell, C. Frayret, M. Gaberscek, P. Jankowski, P. Johansson, Boosting Rechargeable Batteries R&D by Multiscale Modeling: Myth or Reality?, *Chemical Reviews*. 119 (2019) 4569–4627. <https://doi.org/10.1021/acs.chemrev.8b00239>.
- [24] U. Pa, First principles simulations of sodium-based battery materials, (2019).
- [25] M.S. Whittingham, Lithium batteries and cathode materials, *Chemical Reviews*. 104 (2004) 4271–4301. <https://doi.org/10.1021/cr020731c>.
- [26] J. Asenbauer, T. Eisenmann, M. Kuenzel, A. Kazzazi, Z. Chen, D. Bresser, The success story of graphite as a lithium-ion anode material-fundamentals, remaining challenges, and recent developments including silicon (oxide) composites, *Sustainable Energy and Fuels*. 4 (2020) 5387–5416. <https://doi.org/10.1039/d0se00175a>.
- [27] D. Aurbach, B. Markovsky, I. Weissman, E. Levi, Y. Ein-Eli, On the correlation between surface chemistry and performance of graphite negative electrodes for Li ion batteries, *Electrochimica Acta*. 45 (1999) 67–86. [https://doi.org/10.1016/S0013-4686\(99\)00194-2](https://doi.org/10.1016/S0013-4686(99)00194-2).
- [28] M. Widmaier, K. Pfeifer, L. Bommer, V. Presser, Valence-Tuned Lithium Titanate Nanopowder for High-Rate Electrochemical Energy Storage, *Batteries & Supercaps*. 1 (2018) 11–26. <https://doi.org/10.1002/batt.201700007>.

- [29] K. Mizushima, P.C. Jones, P.J. Wiseman, J.B. Goodenough, Li_xCoO_2 ($0 < x < 1$): A new cathode material for batteries of high energy density, *Materials Research Bulletin*. 15 (1980) 783–789. [https://doi.org/10.1016/0025-5408\(80\)90012-4](https://doi.org/10.1016/0025-5408(80)90012-4).
- [30] M. Sathiya, K. Ramesha, G. Rousse, D. Foix, D. Gonbeau, A.S. Prakash, M.L. Doublet, K. Hemalatha, J.M. Tarascon, High performance $\text{Li}_2\text{Ru}_{1-y}\text{Mn}_y\text{O}_3$ ($0.2 \leq y \leq 0.8$) cathode materials for rechargeable lithium-ion batteries: Their understanding, *Chemistry of Materials*. 25 (2013) 1121–1131. <https://doi.org/10.1021/cm400193m>.
- [31] Z. Lu, Z. Chen, J.R. Dahn, Lack of cation clustering in $\text{Li}[\text{Ni}_x\text{Li}_{1/3-2x/3}\text{Mn}_{2/3-x/3}]\text{O}_2$ ($0 < x \leq 1/2$) and $\text{Li}[\text{Cr}_x\text{Li}_{(1-x)/3}\text{Mn}_{(2-2x)/3}]\text{O}_2$ ($0 < x < 1$), *Chemistry of Materials*. 15 (2003) 3214–3220. <https://doi.org/10.1021/cm030194s>.
- [32] M.J. Lee, S. Lee, P. Oh, Y. Kim, J. Cho, High performance LiMn_2O_4 cathode materials grown with epitaxial layered nanostructure for Li-Ion batteries, *Nano Letters*. 14 (2014) 993–999. <https://doi.org/10.1021/nl404430e>.
- [33] A.K. Padhi, K.S. Nanjundaswamy, J.B. Goodenough, Phospho-olivines as Positive-Electrode Materials for Rechargeable Lithium Batteries, *Journal of The Electrochemical Society*. 144 (1997) 1188–1194. <https://doi.org/10.1149/1.1837571>.
- [34] Y. Ge, X. Yan, J. Liu, X. Zhang, J. Wang, X. He, R. Wang, H. Xie, An optimized Ni doped LiFePO_4/C nanocomposite with excellent rate performance, *Electrochimica Acta*. 55 (2010) 5886–5890. <https://doi.org/10.1016/j.electacta.2010.05.040>.
- [35] L.X. Yuan, Z.H. Wang, W.X. Zhang, X.L. Hu, J.T. Chen, Y.H. Huang, J.B. Goodenough, Development and challenges of LiFePO_4 cathode material for lithium-ion batteries, *Energy and Environmental Science*. 4 (2011) 269–284. <https://doi.org/10.1039/c0ee00029a>.
- [36] P. Sharma, C. Das, S. Indris, T. Bergfeldt, L. Mereacre, M. Knapp, U. Geckle, H. Ehrenberg, M.S.D. Darma, Synthesis and characterization of a multication doped Mn spinel, $\text{LiNi}_{0.3}\text{Cu}_{0.1}\text{Fe}_{0.2}\text{Mn}_{1.4}\text{O}_4$, as 5 v positive electrode material, *ACS Omega*. 5 (2020) 22861–22873. <https://doi.org/10.1021/acsomega.0c02174>.
- [37] G. Åvall, J. Wallenstein, G. Cheng, K.L. Gering, P. Johansson, D.P. Abraham, Highly Concentrated Electrolytes: Electrochemical and Physicochemical Characteristics of LiPF_6 in Propylene Carbonate Solutions, *Journal of The Electrochemical Society*. 168 (2021) 050521. <https://doi.org/10.1149/1945-7111/abfdc3>.
- [38] C.J. Franko, C.-H. Yim, F. Årén, G. Åvall, P.S. Whitfield, P. Johansson, Y.A. Abu-Lebdeh, G.R. Goward, Concentration Dependent Solution Structure and Transport Mechanism in High Voltage LiTFSI –Adiponitrile Electrolytes, *Journal of The Electrochemical Society*. 167 (2020) 160532. <https://doi.org/10.1149/1945-7111/abcf17>.
- [39] R. Zettl, S. Lunghammer, B. Gadermaier, A. Boulaoued, P. Johansson, H.M.R. Wilkening, I. Hanzu, High Li^+ and Na^+ Conductivity in New Hybrid Solid Electrolytes based on the Porous MIL-121 Metal Organic Framework, *Advanced Energy Materials*. 11 (2021) 2003542. <https://doi.org/10.1002/aenm.202003542>.

- [40] M. Marcinek, J. Syzdek, M. Marczewski, M. Piszcz, L. Niedzicki, M. Kalita, A. Plewa-Marczewska, A. Bitner, P. Wieczorek, T. Trzeciak, M. Kasprzyk, P. Łęzak, Z. Zukowska, A. Zalewska, W. Wieczorek, Electrolytes for Li-ion transport - Review, *Solid State Ionics*. 276 (2015) 107–126. <https://doi.org/10.1016/j.ssi.2015.02.006>.
- [41] C. Forestier, Thèse de Doctorat, Amiens, 2017.
- [42] L.U.D.E. Picardie, J. Verne, G. Sudant, Thèse de Doctorat par, (2004).
- [43] L.S. Kremer, A. Hoffmann, T. Danner, S. Hein, B. Prifling, D. Westhoff, C. Dreer, A. Latz, V. Schmidt, M. Wohlfahrt-Mehrens, Manufacturing Process for Improved Ultra-Thick Cathodes in High-Energy Lithium-Ion Batteries, *Energy Technology*. 8 (2020). <https://doi.org/10.1002/ente.201900167>.
- [44] R.P. Cunha, T. Lombardo, E.N. Primo, A.A. Franco, Artificial Intelligence Investigation of NMC Cathode Manufacturing Parameters Interdependencies, *Batteries & Supercaps*. 3 (2020) 60–67. <https://doi.org/10.1002/batt.201900135>.
- [45] E.N. Primo, M. Touzin, A.A. Franco, Calendering of $\text{Li}(\text{Ni}_{0.33}\text{Mn}_{0.33}\text{Co}_{0.33})\text{O}_2$ -Based Cathodes: Analyzing the Link Between Process Parameters and Electrode Properties by Advanced Statistics, *Batteries & Supercaps*. (2021) batt.202000324. <https://doi.org/10.1002/batt.202000324>.
- [46] A. Ngandjong, T. Lombardo, E. Primo, M. Chouchane, A. Shodiev, O. Arcelus, A. Franco, Investigating electrode calendering and its impact on electrochemical performance by means of a new discrete element method model: Towards a digital twin of Li-Ion battery manufacturing, (n.d.). <https://doi.org/10.1016/j.jpowsour.2020.229320i>.
- [47] A. Shodiev, E. Primo, O. Arcelus, M. Chouchane, M. Osenberg, A. Hilger, I. Manke, J. Li, A.A. Franco, Insight on electrolyte infiltration of lithium ion battery electrodes by means of a new three-dimensional-resolved lattice Boltzmann model, *Energy Storage Materials*. 38 (2021) 80–92. <https://doi.org/https://doi.org/10.1016/j.ensm.2021.02.029>.
- [48] T. Knoche, F. Surek, G. Reinhart, A Process Model for the Electrolyte Filling of Lithium-ion Batteries, *Procedia CIRP*. 41 (2016) 405–410. <https://doi.org/10.1016/j.procir.2015.12.044>.
- [49] H. Heimes, A. Kampker, C. Lienemann, M. Locke, C. Offermanns, S. Michaelis, E. Rahimzei, Lithium-ion battery cell production process, (2018) ISBN: 978-3-947920-03-7.
- [50] Home | Artistic, (n.d.). <https://www.erc-artistic.eu/> (accessed January 22, 2021).
- [51] J. Li, Z. Du, R.E. Ruther, S.J. An, L.A. David, K. Hays, M. Wood, N.D. Phillip, Y. Sheng, C. Mao, S. Kalnaus, C. Daniel, D.L. Wood, Toward Low-Cost, High-Energy Density, and High-Power Density Lithium-Ion Batteries, *JOM*. 69 (2017) 1484–1496. <https://doi.org/10.1007/s11837-017-2404-9>.
- [52] B. Tjaden, D.J.L. Brett, P.R. Shearing, Tortuosity in electrochemical devices: a review of calculation approaches, *International Materials Reviews*. 63 (2018) 47–67. <https://doi.org/10.1080/09506608.2016.1249995>.

- [53] J. Landesfeind, J. Hattendorff, A. Ehrl, W.A. Wall, H.A. Gasteiger, Tortuosity Determination of Battery Electrodes and Separators by Impedance Spectroscopy, *Journal of The Electrochemical Society*. 163 (2016) A1373–A1387. <https://doi.org/10.1149/2.1141607jes>.
- [54] R. Zahn, M.F. Lagadec, V. Wood, Transport in Lithium Ion Batteries: Reconciling Impedance and Structural Analysis, *ACS Energy Letters*. 2 (2017) 2452–2453. <https://doi.org/10.1021/acsenergylett.7b00740>.
- [55] F. Pouraghajan, H. Knight, M. Wray, B. Mazzeo, R. Subbaraman, J. Christensen, D. Wheeler, Quantifying Tortuosity of Porous Li-Ion Battery Electrodes: Comparing Polarization-Interrupt and Blocking-Electrolyte Methods, *Journal of The Electrochemical Society*. 165 (2018) A2644–A2653. <https://doi.org/10.1149/2.0611811jes>.
- [56] U. Tröltzsch, O. Kanoun, Generalization of transmission line models for deriving the impedance of diffusion and porous media, *Electrochimica Acta*. 75 (2012) 347–356. <https://doi.org/10.1016/j.electacta.2012.05.014>.
- [57] R. Kant, M.B. Singh, Theory of the Electrochemical Impedance of Mesostructured Electrodes Embedded with Heterogeneous Micropores, *The Journal of Physical Chemistry C*. 121 (2017) 7164–7174. <https://doi.org/10.1021/acs.jpcc.7b01287>.
- [58] M. Itagaki, Y. Hatada, I. Shitanda, K. Watanabe, Complex impedance spectra of porous electrode with fractal structure, *Electrochimica Acta*. 55 (2010) 6255–6262. <https://doi.org/10.1016/j.electacta.2009.10.016>.
- [59] M. Musiani, M. Orazem, B. Tribollet, V. Vivier, Impedance of blocking electrodes having parallel cylindrical pores with distributed radii, *Electrochimica Acta*. 56 (2011) 8014–8022. <https://doi.org/https://doi.org/10.1016/j.electacta.2010.12.004>.
- [60] Q.-A. Huang, Y. Li, K.-C. Tsay, C. Sun, Changping Yang, L. Zhang, J. Zhang, Multi-scale impedance model for supercapacitor porous electrodes: Theoretical prediction and experimental validation, *Journal of Power Sources*. 400 (2018) 69–86. <https://doi.org/https://doi.org/10.1016/j.jpowsour.2018.07.108>.
- [61] S.J. Cooper, A. Bertei, D.P. Finegan, N.P. Brandon, Simulated impedance of diffusion in porous media, *Electrochimica Acta*. 251 (2017) 681–689. <https://doi.org/10.1016/j.electacta.2017.07.152>.
- [62] S. Malifarge, B. Delobel, C. Delacourt, Determination of Tortuosity Using Impedance Spectra Analysis of Symmetric Cell, *Journal of The Electrochemical Society*. 164 (2017) E3329–E3334. <https://doi.org/10.1149/2.0331711jes>.
- [63] J. Landesfeind, A. Eldiven, H.A. Gasteiger, Influence of the Binder on Lithium Ion Battery Electrode Tortuosity and Performance, *Journal of The Electrochemical Society*. 165 (2018) A1122–A1128. <https://doi.org/10.1149/2.0971805jes>.
- [64] R. Morasch, J. Landesfeind, B. Suthar, H.A. Gasteiger, Detection of Binder Gradients Using Impedance Spectroscopy and Their Influence on the Tortuosity of Li-Ion Battery Graphite

- Electrodes, *Journal of The Electrochemical Society* . 165 (2018) A3459–A3467. <https://doi.org/10.1149/2.1021814jes>.
- [65] N. Ogihara, S. Kawauchi, C. Okuda, Y. Itou, Y. Takeuchi, Y. Ukyo, Theoretical and Experimental Analysis of Porous Electrodes for Lithium-Ion Batteries by Electrochemical Impedance Spectroscopy Using a Symmetric Cell, *Journal of The Electrochemical Society* . 159 (2012) A1034–A1039. <https://doi.org/10.1149/2.057207jes>.
- [66] A.N. Mistry, P.P. Mukherjee, Probing spatial coupling of resistive modes in porous intercalation electrodes through impedance spectroscopy, *Physical Chemistry Chemical Physics*. 21 (2019) 3805–3813. <https://doi.org/10.1039/c8cp05109g>.
- [67] A.N. Mistry, K. Smith, P.P. Mukherjee, Secondary-Phase Stochastics in Lithium-Ion Battery Electrodes, *ACS Applied Materials and Interfaces*. 10 (2018) 6317–6326. <https://doi.org/10.1021/acsami.7b17771>.
- [68] M. Chouchane, A. Rucci, A.A. Franco, A Versatile and Efficient Voxelization-Based Meshing Algorithm of Multiple Phases, *ACS Omega*. 4 (2019) 11141–11144. <https://doi.org/10.1021/acsomega.9b01279>.
- [69] M. Chouchane, A. Rucci, T. Lombardo, A.C. Ngandjong, A.A. Franco, Lithium ion battery electrodes predicted from manufacturing simulations : Assessing the impact of the carbon-binder spatial location on the electrochemical performance, *Journal of Power Sources*. 444 (2019) 227285. <https://doi.org/10.1016/j.jpowsour.2019.227285>.
- [70] M. Chouchane, A. Rucci, A.A. Franco, A Versatile and Efficient Voxelization-Based Meshing Algorithm of Multiple Phases, *ACS Omega*. 4 (2019) 11141–11144. <https://doi.org/10.1021/acsomega.9b01279>.
- [71] T. Pajkossy, R. Jurczakowski, Electrochemical impedance spectroscopy in interfacial studies, *Current Opinion in Electrochemistry*. 1 (2017) 53–58. <https://doi.org/10.1016/j.coelec.2017.01.006>.
- [72] J.E. Vogel, M.M. Forouzan, E.E. Hardy, S.T. Crawford, D.R. Wheeler, B.A. Mazzeo, Electrode microstructure controls localized electronic impedance in Li-ion batteries, *Electrochimica Acta*. 297 (2019) 820–825. <https://doi.org/10.1016/j.electacta.2018.11.204>.
- [73] A.C. Ngandjong, A. Rucci, M. Maiza, G. Shukla, J. Vazquez-Arenas, A.A. Franco, Multiscale Simulation Platform Linking Lithium Ion Battery Electrode Fabrication Process with Performance at the Cell Level, *Journal of Physical Chemistry Letters*. 8 (2017) 5966–5972. <https://doi.org/10.1021/acs.jpcclett.7b02647>.
- [74] A. Rucci, A.C. Ngandjong, E.N. Primo, M. Maiza, A.A. Franco, Tracking variabilities in the simulation of Lithium Ion Battery electrode fabrication and its impact on electrochemical performance, *Electrochimica Acta*. 312 (2019) 168–178. <https://doi.org/https://doi.org/10.1016/j.electacta.2019.04.110>.
- [75] A.C. Ngandjong, T. Lombardo, E.N. Primo, M. Chouchane, A. Shodiev, O. Arcelus, A.A. Franco, Investigating electrode calendaring and its impact on electrochemical performance

- by means of a new discrete element method model: Towards a digital twin of Li-Ion battery manufacturing, *Journal of Power Sources*. 485 (2021) 229320. <https://doi.org/10.1016/j.jpowsour.2020.229320>.
- [76] H. Zheng, R. Yang, G. Liu, X. Song, V.S. Battaglia, Cooperation between active material, polymeric binder and conductive carbon additive in lithium ion battery cathode, *Journal of Physical Chemistry C*. 116 (2012) 4875–4882. <https://doi.org/10.1021/jp208428w>.
- [77] M. Widmaier, K. Pfeifer, L. Bommer, V. Presser, Valence-Tuned Lithium Titanate Nanopowder for High-Rate Electrochemical Energy Storage, *Batteries & Supercaps*. 1 (2018) 2–2. <https://doi.org/10.1002/batt.201800036>.
- [78] H. Chen, M. Ling, L. Hencz, H.Y. Ling, G. Li, Z. Lin, G. Liu, S. Zhang, Exploring Chemical, Mechanical, and Electrical Functionalities of Binders for Advanced Energy-Storage Devices, *Chemical Reviews*. 118 (2018) 8936–8982. <https://doi.org/10.1021/acs.chemrev.8b00241>.
- [79] M.F. Lagadec, M. Ebner, R. Zahn, V. Wood, Communication—Technique for Visualization and Quantification of Lithium-Ion Battery Separator Microstructure, *Journal of The Electrochemical Society*. 163 (2016) A992–A994. <https://doi.org/10.1149/2.0811606jes>.
- [80] J. Landesfeind, J. Hattendorff, A. Ehrl, W.A. Wall, H.A. Gasteiger, Tortuosity Determination of Battery Electrodes and Separators by Impedance Spectroscopy, *Journal of The Electrochemical Society*. 163 (2016) A1373–A1387. <https://doi.org/10.1149/2.1141607jes>.
- [81] H. Wang, L. Pilon, Intrinsic limitations of impedance measurements in determining electric double layer capacitances, *Electrochimica Acta*. 63 (2012) 55–63. <https://doi.org/10.1016/j.electacta.2011.12.051>.
- [82] B.A. Mei, O. Munteshari, J. Lau, B. Dunn, L. Pilon, Physical Interpretations of Nyquist Plots for EDLC Electrodes and Devices, *Journal of Physical Chemistry C*. 122 (2018) 194–206. <https://doi.org/10.1021/acs.jpcc.7b10582>.
- [83] COMSOL, Introduction to COMSOL Multiphysics 5.3, Manual. (2014) 168.
- [84] J. Landesfeind, M. Ebner, A. Eldiven, V. Wood, H.A. Gasteiger, Tortuosity of Battery Electrodes: Validation of Impedance-Derived Values and Critical Comparison with 3D Tomography, *Journal of The Electrochemical Society*. 165 (2018) A469–A476. <https://doi.org/10.1149/2.0231803jes>.
- [85] M.A. Valle, A.M. Ramírez, L.A. Hernández, F. Armijo, F.R. Díaz, G.C. Arteaga, Influence of the Supporting Electrolyte on the Electrochemical Polymerization of 3, 4-Ethylenedioxythiophene. Effect on p - and n -Doping / Undoping, Conductivity and Morphology, 11 (2016) 7048–7065. <https://doi.org/10.20964/2016.08.46>.
- [86] Y. Chen, C. Wang, X. Zhang, A.M. Sastry, Porous cathode optimization for lithium cells : Ionic and electronic conductivity , capacity , and selection of materials, 195 (2010) 2851–2862. <https://doi.org/10.1016/j.jpowsour.2009.11.044>.

- [87] C.-F. Chen, A. Verma, P.P. Mukherjee, Probing the Role of Electrode Microstructure in the Lithium-Ion Battery Thermal Behavior, *Journal of The Electrochemical Society*. 164 (2017) E3146–E3158. <https://doi.org/10.1149/2.0161711jes>.
- [88] D.P. Abraham, S. Kawauchi, D.W. Dees, Modeling the impedance versus voltage characteristics of $\text{LiNi}_{0.8}\text{Co}_{0.15}\text{Al}_{0.05}\text{O}_2$, *Electrochimica Acta*. 53 (2008) 2121–2129. <https://doi.org/10.1016/j.electacta.2007.09.018>.
- [89] COMSOL, Introduction to COMSOL Multiphysics 5.3, Manual. (2014) 168.
- [90] T. Pajkossy, Impedance spectroscopy at interfaces of metals and aqueous solutions — Surface roughness, CPE and related issues, *Solid State Ionics*. 176 (2005) 1997–2003. <https://doi.org/https://doi.org/10.1016/j.ssi.2004.06.023>.
- [91] P. Córdoba-Torres, T.J. Mesquita, R.P. Nogueira, Relationship between the Origin of Constant-Phase Element Behavior in Electrochemical Impedance Spectroscopy and Electrode Surface Structure, *The Journal of Physical Chemistry C*. 119 (2015) 4136–4147. <https://doi.org/10.1021/jp512063f>.
- [92] M. Gaberscek, J. Moskon, B. Erjavec, R. Dominko, J. Jamnik, The Importance of Interphase Contacts in Li Ion Electrodes: The Meaning of the High-Frequency Impedance Arc, *Electrochemical and Solid-State Letters*. 11 (2008) A170–A174. <https://doi.org/10.1149/1.2964220>.
- [93] J. Bisquert, G. Garcia-Belmonte, F. Fabregat-Santiago, A. Compte, Anomalous transport effects in the impedance of porous film electrodes, *Electrochemistry Communications*. 1 (1999) 429–435. [https://doi.org/https://doi.org/10.1016/S1388-2481\(99\)00084-3](https://doi.org/https://doi.org/10.1016/S1388-2481(99)00084-3).
- [94] J. Huang, J. Zhang, Theory of Impedance Response of Porous Electrodes: Simplifications, Inhomogeneities, Non-Stationarities and Applications, *Journal of The Electrochemical Society*. 163 (2016) A1983–A2000. <https://doi.org/10.1149/2.0901609jes>.
- [95] T. Sharma, T. Holm, J.A. Diaz-Real, W. Mérida, Experimental verification of pore impedance theory: Drilled graphite electrodes with gradually more complex pore size distribution, *Electrochimica Acta*. 317 (2019) 528–541. <https://doi.org/https://doi.org/10.1016/j.electacta.2019.05.119>.
- [96] S. Hein, A. Latz, Influence of local lithium metal deposition in 3D microstructures on local and global behavior of Lithium-ion batteries, (2016).
- [97] K. Kuchler, D. Westhoff, J. Feinauer, T. Mitsch, I. Manke, V. Schmidt, Stochastic model for the 3D microstructure of pristine and cyclically aged cathodes in Li-ion batteries, *Modelling and Simulation in Materials Science and Engineering*. 26 (2018). <https://doi.org/10.1088/1361-651X/aaa6da>.
- [98] M.F. Lagadec, M. Ebner, R. Zahn, V. Wood, Communication — Technique for Visualization and Quantification of Lithium-Ion Battery Separator Microstructure, 163 (2016) 992–994. <https://doi.org/10.1149/2.0811606jes>.

- [99] M.J. Bleda-Martínez, D. Lozano-Castelló, D. Cazorla-Amorós, E. Morallón, Kinetics of Double-Layer Formation: Influence of Porous Structure and Pore Size Distribution, *Energy & Fuels*. 24 (2010) 3378–3384. <https://doi.org/10.1021/ef901521g>.
- [100] G. Gourdin, T. Jiang, P. Smith, D. Qu, The effects of cell assembly compression on the performance of carbon electrochemical double-layer capacitor electrodes, *Journal of Power Sources*. 215 (2012) 179–187. <https://doi.org/https://doi.org/10.1016/j.jpowsour.2012.04.046>.
- [101] A. Shodiev, E.N. Primo, M. Chouchane, T. Lombardo, A.C. Ngandjong, A. Rucci, A.A. Franco, 4D-resolved physical model for Electrochemical Impedance Spectroscopy of Li(Ni_{1-x-y}Mn_xCo_y)O₂-based cathodes in symmetric cells: Consequences in tortuosity calculations, *Journal of Power Sources*. (2020) 227871. <https://doi.org/10.1016/j.jpowsour.2020.227871>.
- [102] J. Landesfeind, A. Eldiven, H.A. Gasteiger, Influence of the Binder on Lithium Ion Battery Electrode Tortuosity and Performance, *Journal of The Electrochemical Society*. 165 (2018) A1122–A1128. <https://doi.org/10.1149/2.0971805jes>.
- [103] F.L.E. Usseglio-Viretta, A. Colclasure, A.N. Mistry, K.P.Y. Claver, F. Pouraghajan, D.P. Finegan, T.M.M. Heenan, D. Abraham, P.P. Mukherjee, D. Wheeler, P. Shearing, S.J. Cooper, K. Smith, Resolving the Discrepancy in Tortuosity Factor Estimation for Li-Ion Battery Electrodes through Micro-Macro Modeling and Experiment, *Journal of The Electrochemical Society*. 165 (2018) A3403–A3426. <https://doi.org/10.1149/2.0731814jes>.
- [104] C. Meyer, H. Bockholt, W. Haselrieder, A. Kwade, Characterization of the calendaring process for compaction of electrodes for lithium-ion batteries, *Journal of Materials Processing Technology*. 249 (2017) 172–178. <https://doi.org/10.1016/j.jmatprotec.2017.05.031>.
- [105] N. Besnard, A. Etienne, T. Douillard, O. Dubrunfaut, P. Tran-Van, L. Gautier, S. Franger, J.C. Badot, E. Maire, B. Lestriez, Multiscale Morphological and Electrical Characterization of Charge Transport Limitations to the Power Performance of Positive Electrode Blends for Lithium-Ion Batteries, *Advanced Energy Materials*. 7 (2017). <https://doi.org/10.1002/aenm.201602239>.
- [106] F. Cadiou, A. Etienne, T. Douillard, F. Willot, O. Valentin, J.-C. Badot, B. Lestriez, E. Maire, Numerical Prediction of Multiscale Electronic Conductivity of Lithium-Ion Battery Positive Electrodes, *Journal of The Electrochemical Society*. 166 (2019) A1692–A1703. <https://doi.org/10.1149/2.1221908jes>.
- [107] S.J. Cooper, D.S. Eastwood, J. Gelb, G. Damblanc, D.J.L. Brett, R.S. Bradley, P.J. Withers, P.D. Lee, A.J. Marquis, N.P. Brandon, P.R. Shearing, Image based modelling of microstructural heterogeneity in LiFePO₄ electrodes for Li-ion batteries, *Journal of Power Sources*. 247 (2014) 1033–1039. <https://doi.org/https://doi.org/10.1016/j.jpowsour.2013.04.156>.
- [108] M. Armand, J.M. Tarascon, Building better batteries, *Nature*. 451 (2008) 652–657. <https://doi.org/10.1038/451652a>.

- [109] J. Li, Z. Du, R.E. Ruther, S.J. An, L.A. David, K. Hays, M. Wood, N.D. Phillip, Y. Sheng, C. Mao, S. Kalnaus, C. Daniel, D.L. Wood, Toward Low-Cost, High-Energy Density, and High-Power Density Lithium-Ion Batteries, *JOM*. 69 (2017) 1484–1496. <https://doi.org/10.1007/s11837-017-2404-9>.
- [110] S. Ahmed, I. Bloom, A.N. Jansen, T. Tanim, E.J. Dufek, A. Pesaran, A. Burnham, R.B. Carlson, F. Dias, K. Hardy, M. Keyser, C. Kreuzer, A. Markel, A. Meintz, C. Michelbacher, M. Mohanpurkar, P.A. Nelson, D.C. Robertson, D. Scofield, M. Shirk, T. Stephens, R. Vijayagopal, J. Zhang, Enabling fast charging – A battery technology gap assessment, *Journal of Power Sources*. 367 (2017) 250–262. <https://doi.org/10.1016/j.jpowsour.2017.06.055>.
- [111] D.L. Wood, M. Wood, J. Li, Z. Du, R.E. Ruther, K.A. Hays, N. Muralidharan, L. Geng, C. Mao, I. Belharouak, Perspectives on the relationship between materials chemistry and roll-to-roll electrode manufacturing for high-energy lithium-ion batteries, *Energy Storage Materials*. 29 (2020) 254–265. <https://doi.org/10.1016/J.ENSMS.2020.04.036>.
- [112] D. Parikh, T. Christensen, J. Li, Correlating the influence of porosity, tortuosity, and mass loading on the energy density of LiNi_{0.6}Mn_{0.2}Co_{0.2}O₂ cathodes under extreme fast charging (XFC) conditions, *Journal of Power Sources*. 474 (2020). <https://doi.org/10.1016/J.JPOWSOUR.2020.228601>.
- [113] Z. Du, D.L. Wood, C. Daniel, S. Kalnaus, J. Li, Understanding limiting factors in thick electrode performance as applied to high energy density Li-ion batteries, *Journal of Applied Electrochemistry*. 47 (2017) 405–415. <https://doi.org/10.1007/s10800-017-1047-4>.
- [114] A. Nadeina, P. Rozier, V. Seznec, Facile Synthesis of a Common Na-Ion Battery Cathode Material Na₃V₂(PO₄)₂F₃ by Spark Plasma Sintering, *Energy Technology*. 8 (2020) 1901304. <https://doi.org/10.1002/ente.201901304>.
- [115] W.B. Hawley, J. Li, Electrode manufacturing for lithium-ion batteries—Analysis of current and next generation processing, *Journal of Energy Storage*. 25 (2019) 100862. <https://doi.org/10.1016/j.est.2019.100862>.
- [116] C.L. Cobb, M. Blanco, Modeling mass and density distribution effects on the performance of co-extruded electrodes for high energy density lithium-ion batteries, *Journal of Power Sources*. 249 (2014) 357–366. <https://doi.org/10.1016/j.jpowsour.2013.10.084>.
- [117] B. Delattre, R. Amin, J. Sander, J. De Coninck, A.P. Tomsia, Y.-M. Chiang, Impact of Pore Tortuosity on Electrode Kinetics in Lithium Battery Electrodes: Study in Directionally Freeze-Cast LiNi_{0.8}Co_{0.15}Al_{0.05}O₂ (NCA), *Journal of The Electrochemical Society*. 165 (2018) A388–A395. <https://doi.org/10.1149/2.1321802jes>.
- [118] W. Pfleging, A review of laser electrode processing for development and manufacturing of lithium-ion batteries, *Nanophotonics*. 7 (2017) 549–573. <https://doi.org/10.1515/nanoph-2017-0044>.
- [119] D. Parikh, T. Christensen, J. Li, Correlating the influence of porosity, tortuosity, and mass loading on the energy density of LiNi_{0.6}Mn_{0.2}Co_{0.2}O₂ cathodes under extreme fast

- charging (XFC) conditions, *Journal of Power Sources*. 474 (2020) 228601. <https://doi.org/10.1016/j.jpowsour.2020.228601>.
- [120] C. Mao, R.E. Ruther, J. Li, Z. Du, I. Belharouak, Identifying the limiting electrode in lithium ion batteries for extreme fast charging, *Electrochemistry Communications*. 97 (2018) 37–41. <https://doi.org/10.1016/j.elecom.2018.10.007>.
- [121] A.C. Ngandjong, T. Lombardo, E.N. Primo, M. Chouchane, A. Shodiev, O. Arcelus, A.A. Franco, Investigating electrode calendaring and its impact on electrochemical performance by means of a new discrete element method model: Towards a digital twin of Li-Ion battery manufacturing, *Journal of Power Sources*. 485 (2021) 229320. <https://doi.org/10.1016/j.jpowsour.2020.229320>.
- [122] Optimizing Areal Capacities through Understanding the Limitations of Lithium-Ion Electrodes, (n.d.). <https://doi.org/10.1149/2.0321602jes>.
- [123] M.E. Ferraro, B.L. Trembacki, V.E. Brunini, D.R. Noble, S.A. Roberts, Electrode Mesoscale as a Collection of Particles: Coupled Electrochemical and Mechanical Analysis of NMC Cathodes, *Journal of The Electrochemical Society*. 167 (2020) 013543. <https://doi.org/10.1149/1945-7111/ab632b>.
- [124] M. Chouchane, O. Arcelus, A.A. Franco, Heterogeneous Solid Electrolyte Interphase in Graphite Electrodes Assessed by 4D-Resolved Computational Simulations, *Batteries & Supercaps*. (2021) batt.202100030. <https://doi.org/10.1002/batt.202100030>.
- [125] M.R. Roberts, A. Madsen, C. Nicklin, J. Rawle, M.G. Palmer, J.R. Owen, A.L. Hector, Direct observation of active material concentration gradients and crystallinity breakdown in LiFePO₄ electrodes during charge/discharge cycling of lithium batteries, *Journal of Physical Chemistry C*. 118 (2014) 6548–6557. <https://doi.org/10.1021/jp411152s>.
- [126] D.A. Cogswell, M.Z. Bazant, Theory of coherent nucleation in phase-separating nanoparticles, *Nano Letters*. 13 (2013) 3036–3041. <https://doi.org/10.1021/nl400497t>.
- [127] Causes and effects of inhomogeneity in lithium-ion battery modules: A physicochemical modelling approach, n.d.
- [128] J. Landesfeind, J. Hattendorff, A. Ehrl, W.A. Wall, H.A. Gasteiger, Tortuosity Determination of Battery Electrodes and Separators by Impedance Spectroscopy, *Journal of The Electrochemical Society*. 163 (2016) A1373–A1387. <https://doi.org/10.1149/2.1141607jes>.
- [129] J. Landesfeind, A. Eldiven, H.A. Gasteiger, Influence of the Binder on Lithium Ion Battery Electrode Tortuosity and Performance, *Journal of The Electrochemical Society*. 165 (2018) A1122–A1128. <https://doi.org/10.1149/2.0971805jes>.
- [130] M. Duquesnoy, T. Lombardo, M. Chouchane, E.N. Primo, A.A. Franco, Data-driven assessment of electrode calendaring process by combining experimental results, in silico mesostructures generation and machine learning, *Journal of Power Sources*. 480 (2020) 229103. <https://doi.org/10.1016/j.jpowsour.2020.229103>.

- [131] S. Beucher, C. Lantuejoul, Use of Watersheds in Contour Detection, International Workshop on Image Processing: Real-Time Edge and Motion Detection/Estimation. (1979) 12–21.
- [132] F.L.E. Usseglio-viretta, K. Smith, Quantitative Microstructure Characterization of a NMC Electrode Transportation and Hydrogen Systems Center , National Renewable Energy Laboratory , Golden , Colorado 80401-3305 , USA Performance of lithium-ion batteries (LIBs) is strongly influenced by , 77 (2017) 1095–1118.
- [133] C. Gaya, Y. Yin, A. Torayev, Y. Mammeri, A.A. Franco, Investigation of bi-porous electrodes for lithium oxygen batteries, *Electrochimica Acta*. 279 (2018) 118–127. <https://doi.org/10.1016/J.ELECTACTA.2018.05.056>.
- [134] T.T. Nguyen, A. Demortière, B. Fleutot, B. Delobel, C. Delacourt, S.J. Cooper, The electrode tortuosity factor: why the conventional tortuosity factor is not well suited for quantifying transport in porous Li-ion battery electrodes and what to use instead, *Npj Computational Materials*. 6 (2020) 1–12. <https://doi.org/10.1038/s41524-020-00386-4>.
- [135] R. Elango, M.M. Morcrette, Thick binder free electrodes for Li-ion battery using Spark Plasma Sintering and templating approach, <Http://Www.Theses.Fr>. (2018).
- [136] M. Gaberscek, J. Moskon, B. Erjavec, R. Dominko, J. Jamnik, The importance of interphase contacts in Li ion electrodes: The meaning of the high-frequency impedance arc, *Electrochemical and Solid-State Letters*. 11 (2008). <https://doi.org/10.1149/1.2964220>.
- [137] J. Moškon, M. Gaberšček, Transmission line models for evaluation of impedance response of insertion battery electrodes and cells, *Journal of Power Sources Advances*. 7 (2021) 100047. <https://doi.org/10.1016/J.POWERA.2021.100047>.
- [138] Y. Li, L. Wang, K. Zhang, F. Liang, M. Yuan, H. Zhang, Y. Yao, An encapsulation of phosphorus doped carbon over LiFePO₄ prepared under vacuum condition for lithium-ion batteries, *Vacuum*. 184 (2021) 109935. <https://doi.org/10.1016/J.VACUUM.2020.109935>.
- [139] R. Borah, F.R. Hughson, J. Johnston, T. Nann, On battery materials and methods, *Materials Today Advances*. 6 (2020) 100046. <https://doi.org/https://doi.org/10.1016/j.mtadv.2019.100046>.
- [140] D.L. Wood, J. Li, S.J. An, Formation Challenges of Lithium-Ion Battery Manufacturing, *Joule*. 3 (2019) 2884–2888. <https://doi.org/https://doi.org/10.1016/j.joule.2019.11.002>.
- [141] A. Davoodabadi, J. Li, Y. Liang, D.L. Wood, T.J. Singler, C. Jin, Analysis of electrolyte imbibition through lithium-ion battery electrodes, *Journal of Power Sources*. 424 (2019) 193–203. <https://doi.org/10.1016/j.jpowsour.2019.03.115>.
- [142] D.L. Wood, J. Li, C. Daniel, Prospects for reducing the processing cost of lithium ion batteries, *Journal of Power Sources*. 275 (2015) 234–242. <https://doi.org/10.1016/j.jpowsour.2014.11.019>.
- [143] D.L. Wood, J. Li, S.J. An, Formation Challenges of Lithium-Ion Battery Manufacturing, *Joule*. 3 (2019) 2884–2888. <https://doi.org/https://doi.org/10.1016/j.joule.2019.11.002>.

- [144] D.H. Jeon, Wettability in electrodes and its impact on the performance of lithium-ion batteries, *Energy Storage Materials*. 18 (2019) 139–147. <https://doi.org/10.1016/j.ensm.2019.01.002>.
- [145] T. Knoche, F. Surek, G. Reinhart, A Process Model for the Electrolyte Filling of Lithium-ion Batteries, *Procedia CIRP*. 41 (2016) 405–410. <https://doi.org/10.1016/j.procir.2015.12.044>.
- [146] A. Davoodabadi, J. Li, H. Zhou, D.L. Wood, T.J. Singler, C. Jin, Effect of calendaring and temperature on electrolyte wetting in lithium-ion battery electrodes, *Journal of Energy Storage*. 26 (2019) 101034. <https://doi.org/10.1016/j.est.2019.101034>.
- [147] S.G. Lee, D.H. Jeon, B.M. Kim, J.H. Kang, C.-J. Kim, Lattice Boltzmann Simulation for Electrolyte Transport in Porous Electrode of Lithium Ion Batteries, *Journal of the Electrochemical Society*. 160 (2013) H258–H265. <https://doi.org/10.1149/2.017306jes>.
- [148] A. Davoodabadi, C. Jin, D.L. Wood, T.J. Singler, J. Li, On electrolyte wetting through lithium-ion battery separators, *Extreme Mechanics Letters*. 40 (2020). <https://doi.org/10.1016/j.eml.2020.100960>.
- [149] F.J. Günter, C. Burgstaller, F. Konwitschny, G. Reinhart, Influence of the Electrolyte Quantity on Lithium-Ion Cells, 166 (2019). <https://doi.org/10.1149/2.0121910jes>.
- [150] W.J. Weydanz, H. Reisenweber, A. Gottschalk, M. Schulz, T. Knoche, G. Reinhart, M. Masuch, J. Franke, R. Gilles, Visualization of electrolyte filling process and influence of vacuum during filling for hard case prismatic lithium ion cells by neutron imaging to optimize the production process, *Journal of Power Sources*. 380 (2018) 126–134. <https://doi.org/https://doi.org/10.1016/j.jpowsour.2018.01.081>.
- [151] A. Schilling, S. Wiemers-Meyer, V. Winkler, S. Nowak, B. Hoppe, H.H. Heimes, K. Dröder, M. Winter, Influence of Separator Material on Infiltration Rate and Wetting Behavior of Lithium-Ion Batteries, *Energy Technology*. 8 (2020) 1900078. <https://doi.org/10.1002/ente.201900078>.
- [152] S. Beyer, O. Kobsch, D. Pospiech, F. Simon, C. Peter, K. Nikolowski, M. Wolter, B. Voit, Influence of surface characteristics on the penetration rate of electrolytes into model cells for lithium ion batteries, *Journal of Adhesion Science and Technology*. 34 (2020) 849–866. <https://doi.org/10.1080/01694243.2019.1686831>.
- [153] C. Peter, K. Nikolowski, S. Reuber, M. Wolter, A. Michaelis, Chronoamperometry as an electrochemical in situ approach to investigate the electrolyte wetting process of lithium-ion cells, *Journal of Applied Electrochemistry*. 50 (2020) 295–309. <https://doi.org/10.1007/s10800-019-01383-2>.
- [154] T. Knoche, V. Zinth, M. Schulz, J. Schnell, R. Gilles, G. Reinhart, In situ visualization of the electrolyte solvent filling process by neutron radiography, *Journal of Power Sources*. 331 (2016) 267–276. <https://doi.org/10.1016/j.jpowsour.2016.09.037>.

- [155] A. Davoodabadi, J. Li, Y. Liang, D.L. Wood, T.J. Singler, C. Jin, Analysis of electrolyte imbibition through lithium-ion battery electrodes, *Journal of Power Sources*. 424 (2019) 193–203. <https://doi.org/10.1016/j.jpowsour.2019.03.115>.
- [156] S.G. Lee, D.H. Jeon, B.M. Kim, J.H. Kang, C.-J. Kim, Lattice Boltzmann Simulation for Electrolyte Transport in Porous Electrode of Lithium Ion Batteries, *Journal of the Electrochemical Society*. 160 (2013) H258–H265. <https://doi.org/10.1149/2.017306jes>.
- [157] T. Knoche, V. Zinth, M. Schulz, J. Schnell, R. Gilles, G. Reinhart, In situ visualization of the electrolyte solvent filling process by neutron radiography, *Journal of Power Sources*. 331 (2016) 267–276. <https://doi.org/10.1016/j.jpowsour.2016.09.037>.
- [158] A. Schilling, P. Gümbel, M. Möller, F. Kalkan, F. Dietrich, K. Dröder, X-ray Based Visualization of the Electrolyte Filling Process of Lithium Ion Batteries, *Journal of The Electrochemical Society*. 166 (2019) A5163–A5167. <https://doi.org/10.1149/2.0251903jes>.
- [159] A. Davoodabadi, J. Li, Y. Liang, R. Wang, H. Zhou, D.L. Wood, T.J. Singler, C. Jin, Characterization of Surface Free Energy of Composite Electrodes for Lithium-Ion Batteries, *Journal of The Electrochemical Society*. 165 (2018) A2493–A2501. <https://doi.org/10.1149/2.0341811jes>.
- [160] H78177.pdf, (n.d.).
- [161] M. Quadrio, C. Pipolo, S. Corti, R. Lenzi, F. Messina, C. Pesci, G. Felisati, Review of computational fluid dynamics in the assessment of nasal air flow and analysis of its limitations, *European Archives of Oto-Rhino-Laryngology*. 271 (2014) 2349–2354. <https://doi.org/10.1007/s00405-013-2742-3>.
- [162] M. Quadrio, C. Pipolo, S. Corti, R. Lenzi, F. Messina, C. Pesci, G. Felisati, Review of computational fluid dynamics in the assessment of nasal air flow and analysis of its limitations, *European Archives of Oto-Rhino-Laryngology*. 271 (2014) 2349–2354. <https://doi.org/10.1007/s00405-013-2742-3>.
- [163] S. Takenaka, K. Suga, T. Kinjo, S. Hyodo, Flow Simulations in a Sub-Micro Porous Medium by the Lattice Boltzmann and the Molecular Dynamics Methods, *ASME Conference Proceedings*. 2009 (2009) 927–936.
- [164] E.M. Viggen, *The lattice Boltzmann method: Fundamentals and acoustics*, 2014. [https://doi.org/ISBN 978-82-326-0037-3](https://doi.org/ISBN%20978-82-326-0037-3).
- [165] L. Chen, Q. Kang, Y. Mu, Y.L. He, W.Q. Tao, A critical review of the pseudopotential multiphase lattice Boltzmann model: Methods and applications, *International Journal of Heat and Mass Transfer*. 76 (2014) 210–236. <https://doi.org/10.1016/j.ijheatmasstransfer.2014.04.032>.
- [166] C. Pan, M. Hilpert, C.T. Miller, Lattice-Boltzmann simulation of two-phase flow in porous media, *Water Resources Research*. 40 (2004) 1–14. <https://doi.org/10.1029/2003WR002120>.

- [167] C. Pan, M. Hilpert, C.T. Miller, Lattice-Boltzmann simulation of two-phase flow in porous media, *Water Resources Research*. 40 (2004) 1–14. <https://doi.org/10.1029/2003WR002120>.
- [168] S.G. Lee, D.H. Jeon, Effect of electrode compression on the wettability of lithium-ion batteries, *Journal of Power Sources*. 265 (2014) 363–369. <https://doi.org/10.1016/j.jpowsour.2014.04.127>.
- [169] S.G. Lee, D.H. Jeon, Effect of electrode compression on the wettability of lithium-ion batteries, *Journal of Power Sources*. 265 (2014) 363–369. <https://doi.org/10.1016/j.jpowsour.2014.04.127>.
- [170] A. Davoodabadi, J. Li, Y. Liang, R. Wang, H. Zhou, D.L. Wood, T.J. Singler, C. Jin, Characterization of Surface Free Energy of Composite Electrodes for Lithium-Ion Batteries, *Journal of The Electrochemical Society*. 165 (2018) A2493–A2501. <https://doi.org/10.1149/2.0341811jes>.
- [171] M. Duquesnoy, T. Lombardo, M. Chouchane, E.N. Primo, A.A. Franco, Data-driven assessment of electrode calendaring process by combining experimental results, in silico mesostructures generation and machine learning, *Journal of Power Sources*. 480 (2020) 229103. <https://doi.org/10.1016/j.jpowsour.2020.229103>.
- [172] A.C. Ngandjong, A. Rucci, M. Maiza, G. Shukla, J. Vazquez-Arenas, A.A. Franco, Multiscale Simulation Platform Linking Lithium Ion Battery Electrode Fabrication Process with Performance at the Cell Level, *Journal of Physical Chemistry Letters*. 8 (2017) 5966–5972. <https://doi.org/10.1021/acs.jpcllett.7b02647>.
- [173] M. Duquesnoy, T. Lombardo, M. Chouchane, E.N. Primo, A. Alejandro, Accelerating Battery Manufacturing Optimization by Combining Experiments , In Silico Electrodes Generation and Machine Learning, *ChemRxiv*. Preprint. (2020) 1–33. <https://doi.org/https://doi.org/10.26434/chemrxiv.12473501.v>.
- [174] F. Wilde, M. Ogurreck, I. Greving, J.U. Hammel, F. Beckmann, A. Hipp, L. Lottermoser, I. Khokhriakov, P. Lytaev, T. Dose, H. Burmester, M. Müller, A. Schreyer, Micro-CT at the imaging beamline P05 at PETRA III, *AIP Conference Proceedings*. 1741 (2016) 10–14. <https://doi.org/10.1063/1.4952858>.
- [175] P. Coupe, P. Yger, S. Prima, P. Hellier, C. Kervrann, C. Barillot, An optimized blockwise nonlocal means denoising filter for 3-D magnetic resonance images, *IEEE Transactions on Medical Imaging*. 27 (2008) 425–441. <https://doi.org/10.1109/TMI.2007.906087>.
- [176] Y.H. Qian, D. D’Humières, P. Lallemand, Lattice bgk models for navier-stokes equation, *Epl*. 17 (1992) 479–484. <https://doi.org/10.1209/0295-5075/17/6/001>.
- [177] D.A. Perumal, A.K. Dass, A Review on the development of lattice Boltzmann computation of macro fluid flows and heat transfer, *Alexandria Engineering Journal*. 54 (2015) 955–971. <https://doi.org/10.1016/j.aej.2015.07.015>.

- [178] X. Shan, H. Chen, Lattice Boltzmann model for simulating flows with multi phases and components Shan, X., & Chen, H. (1993). Lattice Boltzmann model for simulating flows with multi phases and components. *Physical Review E*, 47(3), 1815–1819. <https://doi.org/10.1103/PhysRevE.47.1815>.
- [179] D.A. Perumal, A.K. Dass, A Review on the development of lattice Boltzmann computation of macro fluid flows and heat transfer, *Alexandria Engineering Journal*. 54 (2015) 955–971. <https://doi.org/10.1016/j.aej.2015.07.015>.
- [180] C. Pan, M. Hilpert, C.T. Miller, Lattice-Boltzmann simulation of two-phase flow in porous media, *Water Resources Research*. 40 (2004) 1–14. <https://doi.org/10.1029/2003WR002120>.
- [181] Y. Cha, S.S. Park, K. Kim, M. Byeon, C.A. Stow, *Water Resources Research*, (2014) 5375–5377. <https://doi.org/10.1002/2013WR014979>.Reply.
- [182] J. Zhu, J. Ma, Extending a Gray Lattice Boltzmann Model for Simulating Fluid Flow in Multi-Scale Porous Media, *Scientific Reports*. 8 (2018) 1–19. <https://doi.org/10.1038/s41598-018-24151-2>.
- [183] X. Shan, G. Doolen, Multicomponent lattice-Boltzmann model with interparticle interaction, *Journal of Statistical Physics*. 81 (1995) 379–393. <https://doi.org/10.1007/BF02179985>.
- [184] H. Huang, D.T. Thorne, M.G. Schaap, M.C. Sukop, Proposed approximation for contact angles in Shan-and-Chen-type multicomponent multiphase lattice Boltzmann models, *Physical Review E - Statistical, Nonlinear, and Soft Matter Physics*. 76 (2007) 1–6. <https://doi.org/10.1103/PhysRevE.76.066701>.
- [185] N.S. Martys, H. Chen, Simulation of multicomponent fluids in complex three-dimensional geometries by the lattice Boltzmann method, *Physical Review E - Statistical Physics, Plasmas, Fluids, and Related Interdisciplinary Topics*. 53 (1996) 743–750. <https://doi.org/10.1103/PhysRevE.53.743>.
- [186] X. Shan, H. Chen, Lattice Boltzmann model for simulating flows with multi phases and components Shan, X., & Chen, H. (1993). Lattice Boltzmann model for simulating flows with multi phases and components. *Physical Review E*, 47(3), 1815–1819. <https://doi.org/10.1103/PhysRevE.47.1815>.
- [187] X. Shan, G. Doolen, Multicomponent lattice-Boltzmann model with interparticle interaction, *Journal of Statistical Physics*. 81 (1995) 379–393. <https://doi.org/10.1007/BF02179985>.
- [188] J. Latt, O. Malaspinas, D. Kontaxakis, A. Parmigiani, D. Lagrava, F. Brogi, M. Ben Belgacem, Y. Thorimbert, S. Leclaire, S. Li, F. Marson, J. Lemus, C. Kotsalos, R. Conradin, C. Coreixas, R. Petkantchin, F. Raynaud, J. Beny, B. Chopard, Palabos: Parallel Lattice

- Boltzmann Solver, *Computers and Mathematics with Applications*. (2020). <https://doi.org/10.1016/j.camwa.2020.03.022>.
- [189] M. Waseem Khan, A Survey: Image Segmentation Techniques, *International Journal of Future Computer and Communication*. (2014) 89–93. <https://doi.org/10.7763/ijfcc.2014.v3.274>.
- [190] F.L.E. Usseglio-Viretta, D.P. Finegan, A. Colclasure, T.M.M. Heenan, D. Abraham, P. Shearing, K. Smith, Quantitative Relationships Between Pore Tortuosity, Pore Topology, and Solid Particle Morphology Using a Novel Discrete Particle Size Algorithm, *Journal of The Electrochemical Society*. 167 (2020) 100513. <https://doi.org/10.1149/1945-7111/ab913b>.
- [191] L. Holzer, B. Muench, M. Wegmann, P. Gasser, R.J. Flatt, FIB-nanotomography of particulate systems - Part I: Particle shape and topology of interfaces, *Journal of the American Ceramic Society*. 89 (2006) 2577–2585. <https://doi.org/10.1111/j.1551-2916.2006.00974.x>.
- [192] B. Geveci, ParaView: An End-User Tool for Large Data Visualization ParaViewWeb View project, 836 (2005).
- [193] M. Duquesnoy, T. Lombardo, M. Chouchane, E.N. Primo, A.A. Franco, Data-driven assessment of electrode calendaring process by combining experimental results, in silico mesostructures generation and machine learning, *Journal of Power Sources*. 480 (2020) 229103. <https://doi.org/10.1016/j.jpowsour.2020.229103>.
- [194] F.L.E. Usseglio-Viretta, D.P. Finegan, A. Colclasure, T.M.M. Heenan, D. Abraham, P. Shearing, K. Smith, Quantitative Relationships Between Pore Tortuosity, Pore Topology, and Solid Particle Morphology Using a Novel Discrete Particle Size Algorithm, *Journal of The Electrochemical Society*. 167 (2020) 100513. <https://doi.org/10.1149/1945-7111/ab913b>.
- [195] E.N. Primo, M. Chouchane, M. Touzin, P. Vasquez, A.A. Franco, Understanding the calendaring processability of Li(Ni_{0.33}Mn_{0.33}Co_{0.33})O₂-based cathodes, *Journal of Power Sources*. (2020).
- [196] A. Torayev, A. Rucci, P.C.M.M. Magusin, A. Demortière, V. De Andrade, C.P. Grey, C. Merlet, A.A. Franco, Stochasticity of Pores Interconnectivity in Li-O₂ Batteries and its Impact on the Variations in Electrochemical Performance, *Journal of Physical Chemistry Letters*. 9 (2018) 791–797. <https://doi.org/10.1021/acs.jpcclett.7b03315>.
- [197] A. Torayev, P.C.M.M. Magusin, C.P. Grey, C. Merlet, A.A. Franco, Importance of Incorporating Explicit 3D-Resolved Electrode Mesostructures in Li-O₂ Battery Models, *ACS Applied Energy Materials*. 1 (2018) 6433–6441. <https://doi.org/10.1021/acsaem.8b01392>.
- [198] D.L. Wood, J. Li, S.J. An, Formation Challenges of Lithium-Ion Battery Manufacturing, *Joule*. 3 (2019) 2884–2888. <https://doi.org/https://doi.org/10.1016/j.joule.2019.11.002>.

- [199] M.F. Lagadec, V. Wood, Microstructure of Celgard® PP1615 Lithium-Ion Battery Separator, (2018).
- [200] H. Banda, S. Périé, B. Daffos, L. Dubois, O. Crosnier, P. Simon, P.L. Taberna, F. Duclairoir, Investigation of ion transport in chemically tuned pillared graphene materials through electrochemical impedance analysis, *Electrochimica Acta*. 296 (2019) 882–890. <https://doi.org/10.1016/j.electacta.2018.11.122>.
- [201] T. Danner, S. Eswara, V.P. Schulz, A. Latz, Characterization of gas diffusion electrodes for metal-air batteries, *Journal of Power Sources*. 324 (2016) 646–656. <https://doi.org/10.1016/j.jpowsour.2016.05.108>.
- [202] J.E. Harlow, X. Ma, J. Li, E. Logan, Y. Liu, N. Zhang, L. Ma, S.L. Glazier, M.M.E. Cormier, M. Genovese, S. Buteau, A. Cameron, J.E. Stark, J.R. Dahn, A Wide Range of Testing Results on an Excellent Lithium-Ion Cell Chemistry to be used as Benchmarks for New Battery Technologies, *Journal of The Electrochemical Society*. 166 (2019) A3031–A3044. <https://doi.org/10.1149/2.0981913jes>.
- [203] R. Borah, F.R. Hughson, J. Johnston, T. Nann, On battery materials and methods, *Materials Today Advances*. 6 (2020) 100046. <https://doi.org/https://doi.org/10.1016/j.mtadv.2019.100046>.
- [204] D.H. Jeon, Wettability in electrodes and its impact on the performance of lithium-ion batteries, *Energy Storage Materials*. 18 (2019) 139–147. <https://doi.org/10.1016/j.ensm.2019.01.002>.
- [205] W.J. Weydanz, H. Reisenweber, A. Gottschalk, M. Schulz, T. Knoche, G. Reinhart, M. Masuch, J. Franke, R. Gilles, Visualization of electrolyte filling process and influence of vacuum during filling for hard case prismatic lithium ion cells by neutron imaging to optimize the production process, *Journal of Power Sources*. 380 (2018) 126–134. <https://doi.org/https://doi.org/10.1016/j.jpowsour.2018.01.081>.
- [206] J.E. Santos, D. Xu, H. Jo, C.J. Landry, M. Prodanović, M.J. Pyrcz, PoreFlow-Net: A 3D convolutional neural network to predict fluid flow through porous media, *Advances in Water Resources*. 138 (2020). <https://doi.org/10.1016/j.advwatres.2020.103539>.
- [207] A. Mistry, A.A. Franco, S.J. Cooper, S.A. Roberts, V. Viswanathan, How Machine Learning Will Revolutionize Electrochemical Sciences, *ACS Energy Letters*. 39 (2021) 1422–1431. <https://doi.org/10.1021/acsenerylett.1c00194>.
- [208] A. Mistry, A.A. Franco, S.J. Cooper, S.A. Roberts, V. Viswanathan, How Machine Learning Will Revolutionize Electrochemical Sciences, *ACS Energy Letters*. 14 (2021) 1422–1431. <https://doi.org/10.1021/acsenerylett.1c00194>.
- [209] H. El-Bousiydy, T. Lombardo, E.N. Primo, M. Duquesnoy, M. Morcrette, P. Johansson, P. Simon, A. Grimaud, A.A. Franco, What Can Text Mining Tell Us About Lithium-Ion Battery Researchers' Habits?, *Batteries & Supercaps*. (2021) batt.202000288. <https://doi.org/10.1002/batt.202000288>.

- [210] S. Kumar, S. Tan, L. Zheng, D.M. Kochmann, Inverse-designed spinodoid metamaterials, *Npj Computational Materials*. 6 (2020) 1–10. <https://doi.org/10.1038/s41524-020-0341-6>.
- [211] D.S. Marks, L.J. Colwell, R. Sheridan, T.A. Hopf, A. Pagnani, R. Zecchina, C. Sander, Protein 3D structure computed from evolutionary sequence variation, *PLoS ONE*. 6 (2011). <https://doi.org/10.1371/journal.pone.0028766>.
- [212] Deep neural networks for object detection | Proceedings of the 26th International Conference on Neural Information Processing Systems - Volume 2, (n.d.). <https://dl.acm.org/doi/10.5555/2999792.2999897> (accessed April 8, 2021).
- [213] M. Yang, S. Wang, J. Bakita, T. Vu, F.D. Smith, J.H. Anderson, J.M. Frahm, Re-thinking CNN frameworks for time-sensitive autonomous-driving applications: Addressing an industrial challenge, in: Proceedings of the IEEE Real-Time and Embedded Technology and Applications Symposium, RTAS, Institute of Electrical and Electronics Engineers Inc., 2019: pp. 305–317. <https://doi.org/10.1109/RTAS.2019.00033>.
- [214] S. Yue, Imbalanced Malware Images Classification: a CNN based Approach, *ArXiv*. (2017).
- [215] R. Barth, J. Hemming, E.J. Van Henten, Improved Part Segmentation Performance by Optimising Realism of Synthetic Images using Cycle Generative Adversarial Networks, 2018.
- [216] H. Wei, S. Zhao, Q. Rong, H. Bao, Predicting the effective thermal conductivities of composite materials and porous media by machine learning methods, *International Journal of Heat and Mass Transfer*. 127 (2018) 908–916. <https://doi.org/10.1016/j.ijheatmasstransfer.2018.08.082>.
- [217] A. Rabbani, M. Babaei, Hybrid pore-network and lattice-Boltzmann permeability modelling accelerated by machine learning, *Advances in Water Resources*. 126 (2019) 116–128. <https://doi.org/10.1016/j.advwatres.2019.02.012>.
- [218] J.A. Benediktsson, M. Pesaresi, K. Arnason, Classification and feature extraction for remote sensing images from urban areas based on morphological transformations, *IEEE Transactions on Geoscience and Remote Sensing*. 41 (2003) 1940–1949. <https://doi.org/10.1109/TGRS.2003.814625>.
- [219] N. Alqahtani, F. Alzubaidi, R.T. Armstrong, P. Swietojanski, P. Mostaghimi, Machine learning for predicting properties of porous media from 2d X-ray images, *Journal of Petroleum Science and Engineering*. 184 (2020) 106514. <https://doi.org/10.1016/j.petrol.2019.106514>.
- [220] O. Sudakov, E. Burnaev, D. Koroteev, Driving Digital Rock towards Machine Learning: predicting permeability with Gradient Boosting and Deep Neural Networks, *Computers and Geosciences*. 127 (2018) 91–98. <https://doi.org/10.1016/j.cageo.2019.02.002>.
- [221] V.L. Deringer, Modelling and understanding battery materials with machine-learning-driven atomistic simulations, *Journal of Physics: Energy*. 2 (2020) 041003. <https://doi.org/10.1088/2515-7655/abb011>.

- [222] F.L.E. Usseglio-Viretta, K. Smith, Quantitative Microstructure Characterization of a NMC Electrode, *ECS Transactions*. 77 (2017) 1095–1118. <https://doi.org/10.1149/07711.1095ecst>.
- [223] L. Holzer, B. Muench, M. Wegmann, P. Gasser, R.J. Flatt, FIB-Nanotomography of Particulate Systems—Part I: Particle Shape and Topology of Interfaces, *Journal of the American Ceramic Society*. 89 (2006) 2577–2585. <https://doi.org/https://doi.org/10.1111/j.1551-2916.2006.00974.x>.
- [224] A. Torayev, A. Rucci, P.C.M.M. Magusin, A. Demortière, V. De Andrade, C.P. Grey, C. Merlet, A.A. Franco, Stochasticity of Pores Interconnectivity in Li-O₂ Batteries and its Impact on the Variations in Electrochemical Performance, *Journal of Physical Chemistry Letters*. 9 (2018) 791–797. <https://doi.org/10.1021/acs.jpcclett.7b03315>.
- [225] Z.A. Khan, P.A.G. Salaberri, T.M.M. Heenan, R. Jervis, P.R. Shearing, D. Brett, A. Elkamel, J.T. Gostick, Probing the Structure-Performance Relationship of Lithium-Ion Battery Cathodes Using Pore-Networks Extracted from Three-Phase Tomograms, *Journal of The Electrochemical Society*. 167 (2020) 40528. <https://doi.org/10.1149/1945-7111/ab7bd8>.
- [226] C.R. Harris, K.J. Millman, S.J. van der Walt, R. Gommers, P. Virtanen, D. Cournapeau, E. Wieser, J. Taylor, S. Berg, N.J. Smith, R. Kern, M. Picus, S. Hoyer, M.H. van Kerkwijk, M. Brett, A. Haldane, J.F. del Río, M. Wiebe, P. Peterson, P. Gérard-Marchant, K. Sheppard, T. Reddy, W. Weckesser, H. Abbasi, C. Gohlke, T.E. Oliphant, Array programming with NumPy, *Nature*. 585 (2020) 357–362. <https://doi.org/10.1038/s41586-020-2649-2>.
- [227] C. Sullivan, A. Kaszynski, PyVista: 3D plotting and mesh analysis through a streamlined interface for the Visualization Toolkit (VTK), *Journal of Open Source Software*. 4 (2019) 1450. <https://doi.org/10.21105/joss.01450>.
- [228] W. Schroeder, K. Martin, B. Lorensen, The Visualization Toolkit (VTK), *Open Source*. (2018) 558.
- [229] T. Masters, S.D. New, Y. Boston, *Practical Neural Network Recipes in C++*, n.d.
- [230] A. Saltelli, Making best use of model evaluations to compute sensitivity indices, *Computer Physics Communications*. 145 (2002) 280–297. [https://doi.org/10.1016/S0010-4655\(02\)00280-1](https://doi.org/10.1016/S0010-4655(02)00280-1).
- [231] Y. Gan, Q. Duan, W. Gong, C. Tong, Y. Sun, W. Chu, A. Ye, C. Miao, Z. Di, A comprehensive evaluation of various sensitivity analysis methods: A case study with a hydrological model, *Environmental Modelling and Software*. 51 (2014) 269–285. <https://doi.org/10.1016/j.envsoft.2013.09.031>.
- [232] A. Maurel, M. Armand, S. Grugeon, B. Fleutot, C. Davoisne, H. Tortajada, M. Courty, S. Panier, L. Dupont, Poly(Ethylene Oxide)–LiTFSI Solid Polymer Electrolyte Filaments for Fused Deposition Modeling Three-Dimensional Printing, *Journal of The Electrochemical Society*. 167 (2020) 070536. <https://doi.org/10.1149/1945-7111/ab7c38>.

Résumé développé de la thèse en Français

(Summary in French)

Le développement de la batterie lithium-ion (LIB) a commencé pendant la crise pétrolière des années 1970. Dans le cadre de ses recherches sur les matériaux pour semi-conducteurs, Stanley Whittingham a conçu une batterie au lithium riche en énergie, qui a ensuite été perfectionnée par ses collègues lauréats du prix Nobel John B. Goodenough et Akira Yoshino, qui ont amélioré la technologie en remplaçant la cathode et l'anode par de l'oxyde de cobalt et du graphite, respectivement. Depuis la première LIB commerciale en 1991, le monde a connu un boom de l'électronique portable, des véhicules électriques à grande autonomie et de la possibilité de servir d'accumulateur pour des sources renouvelables comme l'énergie solaire et éolienne. Dans ce sens, des études d'optimisation sont encore nécessaires pour améliorer les performances électrochimiques des LIB et diminuer leur coût.

Cette thèse se concentre sur le développement d'une compréhension de la physique régissant la propagation de l'électrolyte dans les électrodes poreuses pendant l'étape d'imprégnation. Cette physique est fortement dépendante de la chimie des matériaux constituant l'électrode (matière active, agrégats de carbone, liant polymère), déterminant la mouillabilité des pores, et les propriétés texturales (porosité et tortuosité) dépendant du niveau de calandrage des électrodes.

La première partie de la thèse a consisté à développer un modèle d'impédance électrochimique pour caractériser les cellules électrochimiques symétriques. Le modèle EIS 3D pour la cellule symétrique a été développé et des expériences ont été menées pour valider le modèle. Le modèle doit également valider le résultat de différentes structures générées par la dynamique moléculaire à grain fin, les électrodes générées de manière stochastique et les électrodes obtenues par tomographie expérimentale.

La deuxième partie du travail a consisté à développer des modèles basés sur la méthode Lattice Boltzmann pour simuler la propagation de l'électrolyte dans les mésostructures d'électrodes obtenues par différentes sources. Le modèle doit capturer l'imprégnation de l'électrolyte et la physique de la pression externe appliquée à un niveau 3D. Des recherches expérimentales doivent être menées pour la validité du modèle.

Dans le deuxième chapitre, un modèle physique 4D (3D dans l'espace + temps) a été utilisé avec succès pour simuler et analyser les spectres EI de cellules symétriques basées sur des cathodes NMC simulées pour l'évaluation de leur facteur de tortuosité. Les résultats ont été comparés et validés avec des spectres EI expérimentaux acquis en interne sur des cathodes NMC réelles. Le modèle électrochimique 4D considère explicitement les trois phases de l'électrode (c'est-à-dire les particules AM et CBD et les pores remplis d'électrolyte) ainsi que la physique distincte pour la conduction des électrons et des ions à l'intérieur de celles-ci.

Dans la première partie de ce travail, les caractéristiques générales de l'EI ont été discutées : Le **Figure 6** en fournit un bon résumé. On a constaté que, contrairement à la TLM utilisée pour l'interprétation des spectres, la région des hautes et moyennes fréquences s'écarte d'une pente de 45° et qu'une région incurvée à haute fréquence apparaît, tant dans les cas simulés qu'expérimentaux. La possibilité d'analyser chaque paramètre de l'électrode à la fois a permis de conclure que ces écarts par rapport à la "TLM idéale" sont liés aux temps caractéristiques d'accès à chaque région de l'électrode poreuse en fonction de la fréquence. Le fait que notre modèle considère une diffusion/conduction ionique corrigée par Bruggeman de l'électrolyte au sein de la phase poreuse de la DBC et des conductivités électroniques différentes pour l'AM et la DBC, s'est avéré être une stratégie efficace pour l'interprétation des spectres EI dans les cellules symétriques.

Dans la deuxième partie, les principales limitations pour le calcul des cathodes à base de NMC à partir des expériences d'EI en cellule symétrique ont été analysées. La comparaison d'électrodes avec différentes compositions NMC/CBD à la fois simulées et expérimentales a révélé que l'EIS, qui provient de la conductivité ionique effective de l'électrolyte, produit des valeurs et des tendances qui ne sont pas celles attendues. Bien que toutes les méthodologies de calcul aient leurs limites et leurs hypothèses, pour le cas des électrodes poreuses dans lesquelles l'AM n'est pas un bon conducteur électronique, la cellule symétrique EI peut produire des résultats erronés. Néanmoins, notre modèle explicite 4D a aidé à comprendre cette question car nous avons pu comparer les valeurs provenant de deux méthodologies indépendantes pour la même structure d'électrode.

Dans le troisième chapitre, un nouveau LBM tridimensionnel a été développé pour simuler le remplissage d'électrolyte dans différentes mésostructures de cathodes LIB et cellules complètes.

Le LBM simule l'écoulement fluide instationnaire et l'évolution de l'interface biphasique (électrolyte et air) pendant le passage de l'électrolyte à travers les mésostructures. Ce modèle nous a permis de visualiser la pénétration de l'électrolyte et de caractériser le degré de mouillabilité avec un très haut degré de détail. Les électrodes provenant de trois sources différentes (stochastique, tomographie, CGMD) ont été utilisées dans cette étude de simulation.

Les résultats indiquent que la mouillabilité des électrodes poreuses est fortement liée à leur porosité, à la distribution de la taille des pores, au facteur de tortuosité et à l'organisation du réseau de pores. De plus, l'effet du calandrage sur la mouillabilité s'avère très significatif. Les études ont également révélé que les pores géométriquement isolés jouent un rôle majeur dans la mauvaise mouillabilité des électrodes. L'étude de la configuration de la cellule complète a démontré que le degré de pénétration de l'électrolyte dans chaque électrode dépend aussi fortement de l'emplacement des gouttes d'électrolyte initiales. L'extension de cette étude à d'autres configurations de montage pourrait donner des suggestions précises sur l'emplacement de l'entrée initiale de l'électrolyte pour un remplissage optimal, mais cela dépasse le cadre de la présente étude. Des simulations électrochimiques ont également été réalisées pour évaluer l'effet de la mouillabilité sur les performances globales de l'électrode positive. Ces simulations montrent qu'une mauvaise mouillabilité entraîne une résistance ionique accrue et une intercalation inhomogène du lithium, ce qui se traduit par une capacité plus faible que dans le cas où l'électrolyte est censé remplir entièrement les pores de l'électrode, comme cela est généralement supposé dans de nombreux modèles mathématiques de performance dans la littérature. L'outil de simulation présenté dans ce travail est destiné à être intégré dans le flux de travail informatique global de notre projet ARTISTIC qui simule toutes les étapes du processus de fabrication des électrodes LIB, y compris la boue d'électrode, le revêtement, le séchage, le calandrage, l'infiltration de l'électrolyte et la performance électrochimique qui en résulte.

Dans le quatrième chapitre, nous présentons un modèle innovant d'apprentissage automatique basé sur une architecture de perceptron multicouches (MLP), pour prédire l'infiltration d'électrolyte dans les électrodes poreuses NMC. La structure hôte de l'électrode poreuse NMC a été obtenue expérimentalement par des mesures tomographiques aux rayons X (micro-CT). Le MLP a été entraîné avec des données provenant d'un modèle LBM 3D basé sur la physique et des réseaux de

pores extraits de la tomographie aux rayons X (micro-CT). Les résultats de prédiction du réseau neuronal ont été comparés et validés par des simulations LBM 3D.

Le MLP formé peut généraliser les problèmes d'écoulement pour prédire le taux de saturation et le temps de remplissage dans les électrodes poreuses. En outre, il peut prédire avec précision la direction de l'écoulement du fluide, la saturation totale et le temps de remplissage de l'électrode. Les prédictions ont également montré la même tendance asymptotique que le modèle LBM basé sur la physique pour la courbe de saturation. En outre, une analyse de sensibilité systématique a été réalisée pour démêler la relation spatiale entre la forme complexe des pores de l'électrode, l'emplacement des pores, le volume des pores, la connexion entre les autres pores et la pression externe appliquée sur les caractéristiques globales prédites du processus d'infiltration, telles que les degrés de saturation et les temps de remplissage, entre autres.

En outre, le MLP entraîné a prédit avec précision des exemples de géométries et de pressions appliquées variables en moins d'une seconde de calcul sur un ordinateur de bureau, alors que les simulations LBM basées sur la physique ont pris plusieurs jours (2-5) sur un serveur à forte puissance de calcul. En outre, notre modèle ML ne génère qu'environ 10 Mo de données à comparer aux 50 à 200 Go générés lors des simulations LBM, ce qui permet d'économiser de l'espace de stockage de données et rend le post-traitement rapide et abordable. Tous les avantages mentionnés ci-dessus permettent au modèle de passer rapidement en revue différentes architectures d'électrodes et les propriétés possibles de l'électrolyte dans le cadre d'un jumeau numérique de la fabrication des batteries. Par conséquent, il sert d'outil essentiel pour optimiser le processus d'infiltration de l'électrolyte. Enfin, cette méthode peut être utilisée plus avant dans différents domaines où intervient l'écoulement de fluides à travers des milieux poreux.